Deciphering the dynamics of the Milky Way bar and spiral arms with Gaia

Yassin Rany Khalil

Université de Strasbourg

Observatoire astronomique de Strasbourg | ObAS

École doctorale Physique, chimie-physique ED 182 Université de Strasbourg

UNIVERSITÉ DE STRASBOURG

ÉCOLE DOCTORALE DE PHYSIQUE ET CHIMIE-PHYSIQUE

Observatoire Astronomique de Strasbourg (UMR 7550)

THÈSE présentée par

Yassin Rany KHALIL

soutenue le: **30 septembre 2025**

pour obtenir le grade de: **Docteur de l'Université de Strasbourg**
Discipline/Spécialité: Physique

Deciphering the dynamics of the Milky Way bar and spiral arms with Gaia

THÈSE dirigée par:

M. FAMAEY Benoit	Directeur de Recherche, Observatoire Astronomique de Strasbourg

RAPPORTEURS:

M. LAVALLE Julien	Directeur de Recherche, Laboratoire Univers et Particules de Montpellier
Mme RECIO-BLANCO Alejandra	Astronome, Observatoire de la Côte d'Azur

---

AUTRES MEMBRES DU JURY:

M. BOILY Christian	Professeur, Observatoire Astronomique de Strasbourg
M. FOUVRY Jean-Baptiste	Chargé de Recherche, Institut d'Astrophysique de Paris
Mme KRALJIC Katarina	Chargée de recherche, Observatoire Astronomique de Strasbourg
M. MONARI Giacomo	Astronome adjoint, membre invité, Observatoire Astronomique de Strasbourg
M. NAVORET Laurent	Maître de Conférence, membre invité, Institut de Recherche Mathématique Avancée, Université de Strasbourg

Abstract

Français

Cette thèse utilise les données de la mission Gaia pour modéliser la dynamique de la Voie lactée, incluant la barre et les bras spiraux. Un potentiel Galactique paramétrique est ajusté aux données via une méthode d'intégration rétrograde pour évaluer la fonction de distribution stellaire à quatre dimensions d'espace des phases dans le plan Galactique. Nous avons ainsi été les premiers (et les seuls à ce jour) à réaliser un ajustement direct au champ de vitesses radiales médianes du disque tel que mesuré par Gaia. Il s'agit du modèle dynamique non-axisymétrique le plus réaliste à ce jour pour la Voie Lactée. Ce modèle est ensuite généralisé en trois dimensions spatiales avec des simulations particules tests, ce qui permettra d'étudier les perturbations verticales et le halo de matière noire. Cette approche permettra, à terme, une comparaison étoile par étoile dans l'étude des populations stellaires de la Voie Lactée.

English

This thesis uses Gaia data to model the dynamics of the Milky Way, including the bar and spiral arms. A parametric Galactic potential is fitted to the data via a backward integration method to evaluate the four-dimensional phase-space stellar distribution function in the Galactic plane. This allowed me to be the first (and only to date) to achieve a direct fit to the median radial velocity field of the disk as measured by Gaia. This is therefore the most realistic non-axisymmetric dynamical model of the Milky Way to date. This model is then generalized in three spatial dimensions with test particle simulations, which should enable us to study vertical perturbations or the dark matter halo. This approach will eventually enable star-by-star comparisons in the study of stellar populations.

Avertissement au lecteur

Warning to the reader

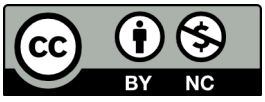

Summary

This thesis uses Gaia data to model the dynamics of the Milky Way, including the bar and spiral arms. The unprecedented precision of Gaia's astrometric and kinematic measurements has enabled me to reveal the non-axisymmetric velocity field of the Galactic disk in detail, providing the basis for building models that extend beyond the traditional axisymmetric framework. A parametric Galactic potential is fitted to the data via a backward integration method, which makes use of the conservation of the stellar distribution function as governed by the Vlasov equation. By integrating orbits backward in time to an axisymmetric equilibrium state, I was able to evaluate the four-dimensional phase-space stellar distribution function in the Galactic plane, directly constrained by Gaia observations.

This allowed me to achieve the first direct fit to the median radial velocity field of the disk as measured by Gaia, across a large portion of the Galactic plane. This is therefore the most realistic non-axisymmetric dynamical model of the Milky Way to date, simultaneously capturing the role of the bar and the spiral arms. The model reveals multiple spiral arm components with distinct pattern speeds and, despite being purely dynamical, it recovers the locations of several photometrically detected spiral over-densities. In particular, it identifies the Scutum–Local–Outer arms as slowly rotating and the Sagittarius–Carina–Perseus arms as having a somewhat higher pattern speed. It also naturally reproduces smaller-scale phase-space structures, such as the moving groups observed in the extended Solar neighborhood.

I then generalized this model in three spatial dimensions with test-particle simulations, making it possible for future investigations to explore vertical perturbations and to investigate the link with the Galactic dark matter halo. These simulations provide a framework for studying the connection between disk dynamics, vertical disequilibrium such as phase-space spirals, and the long-term role of non-axisymmetric structures in galactic evolution. This approach will eventually enable detailed star-by-star comparisons in the study of stellar populations, representing a step toward a comprehensive dynamical model of the Milky Way that unifies its structure, kinematics, and chemical evolution.

Résumé

Cette thèse utilise les données de Gaia pour modéliser la dynamique de la Voie lactée, en particulier la barre et les bras spiraux. La précision inédite des mesures astrométriques et cinématiques de Gaia m'a permis de mettre en évidence en détail le champ de vitesses non axisymétrique du disque galactique, base nécessaire à la construction de modèles dépassant le cadre axisymétrique traditionnel. Un potentiel galactique paramétrique est ajusté aux données à l'aide d'une méthode d'intégration rétrograde, fondée sur la conservation de la fonction de distribution stellaire décrite par l'équation de Vlasov. En intégrant les orbites en arrière dans le temps jusqu'à un état d'équilibre axisymétrique, j'ai pu évaluer la fonction de distribution stellaire à quatre dimensions de l'espace des phases dans le plan galactique, directement contrainte par les observations de Gaia. Cela m'a conduit au premier ajustement direct du champ de vitesses radiales médian du disque tel que mesuré par Gaia, sur une large portion du plan galactique. Il s'agit du modèle dynamique non axisymétrique le plus réaliste de la Voie lactée à ce jour, intégrant simultanément les effets de la barre et des bras spiraux. Le modèle révèle plusieurs composantes spirales à vitesses de rotation distinctes et, bien qu'étant purement dynamique, retrouve les positions de surdensités spirales identifiées photométriquement. En particulier, il associe les bras Scutum–Local–Outer à une rotation lente et les bras Sagittaire–Carina–Persée à une rotation légèrement plus rapide. Il reproduit aussi des structures de plus petite échelle, comme les groupes en mouvement observés dans le voisinage solaire. J'ai ensuite généralisé ce modèle en trois dimensions à l'aide de simulations de particules tests, permettant d'étudier les perturbations verticales et leur lien avec le halo de matière noire galactique. Ces simulations offrent un cadre pour relier la dynamique du disque, les déséquilibres verticaux comme les spirales de l'espace des phases, et le rôle à long terme des structures non axisymétriques dans l'évolution galactique. Cette approche ouvrira la voie à des comparaisons étoile par étoile des populations stellaires et constitue une étape vers un modèle dynamique global de la Voie lactée unifiant structure, cinématique et évolution chimique.

Remerciements

Je voudrais tout d'abord exprimer ma plus profonde reconnaissance à mon directeur de thèse, Benoit Famaey. Je tiens à le remercier de m'avoir accueilli avec un beau projet qui m'a introduit à la dynamique galactique et qui a fait naître en moi un véritable enthousiasme pour ce domaine et ses multiples horizons. Je lui suis également reconnaissant pour tout le soutien, la compréhension et la bienveillance envers moi et mes proches. Je suis profondément reconnaissant pour tout le temps qu'il m'a toujours accordé, pour chaque échange et discussion, pour toutes les idées inspirantes et les précieux conseils, j'en ai appris énormément. Je suis aussi reconnaissant pour sa patience et sa gentillesse avec moi tout au long de cette expérience formatrice. Je ne saurais exprimer toute ma gratitude ni l'honneur que j'ai eu de réaliser ce doctorat sous son encadrement, et j'espère honorer cela en poursuivant ma carrière avec l'intuition, la rigueur et la créativité scientifique nourries au fil de ces années.

Je remercie énormément Laurent Navoret pour son suivi attentif de mes progrès au fil de ces années, pour la richesse de nos échanges et de ses idées, ainsi que pour les cours et séminaires interdisciplinaires qu'il organisait, dont j'ai beaucoup bénéficié. Je remercie également Giacomo Monari, avec qui j'ai beaucoup appris sur la dynamique. Je suis reconnaissant pour nos échanges et pour ses conseils, ainsi que son enthousiasme face aux avancées des projets et ses encouragements à concrétiser mes idées, ont été particulièrement importants pour moi. Je tiens à remercier profondément Rodrigo Ibata pour son inestimable soutien depuis le début. Nos échanges m'ont été très marquants, et ses idées ainsi que ses commentaires constructifs au long de ces années m'ont été d'une grande valeur. Je tiens également à remercier Jonathan Freundlich pour les nombreuses discussions stimulantes, ainsi que pour les moments conviviaux et de partage. Je lui suis aussi reconnaissant pour ses encouragements dans la réalisation de mes projets et pour l'opportunité qui m'a été donnée de co-encadrer des étudiants lors de leur stage. Je remercie également Florent Renaud pour tous les moments toujours si agréables, les discussions intéressantes et pour sa bienveillance avec l'ensemble des doctorants et pour ses nombreux conseils.

Je tiens à remercier sincèrement Nalini Anantharaman pour sa grande compréhension de ma situation personnelle avant le début de ma thèse, ainsi que pour son soutien, qui a été essentiel pour me permettre de réaliser cette thèse dans le cadre de l'Institut Thématique Interdisciplinaire IRMIA++. Je remercie également Pierre-Alain Duc pour son accueil à l'Observatoire et Nicolas Martin pour son accueil au sein de l'équipe GALHECOS, ainsi que pour leur bienveillance et leur sollicitude.

Je remercie chaleureusement l'ensemble des membres du jury de ma thèse de doctorat pour avoir gentiment accepté d'en faire partie et pour tout leur temps et pour l'intérêt qu'ils portent à ce travail de thèse.

Je remercie toutes les personnes avec qui j'ai eu le plaisir de collaborer : Marcel Bernet, Guillaume Thomas, Pau Ramos, Teresa Antoja, Chengdong Li, Simon Rozier, Mercè Romero-Gómez, Alexandre Bougakov et Alicia Rivero Batista. Je remercie en particulier Pau Ramos de m'avoir permis de présenter sa formule pour la localisation des résonances de barre dans l'espace des vitesses en appendice. Je tiens également à exprimer ma gratitude à Pedro Palicio, Sebastian Keller, Francesca Fragkoudi, Julien Hiegel et Axel Widmark pour les échanges stimulants et enrichissants.

Je tiens également à remercier les membres de mon comité de suivi individuel, Catherine Allamel-Raffin, Jean-Baptiste Fouvry et Jonathan Freundlich, pour leur attention et leur bienveillance, ainsi que pour l'intérêt qu'ils ont porté à mon travail de doctorat et pour leurs commentaires constructifs et suggestions particulièrement précieuses.

Je remercie vivement Katarina Kraljic, Arnaud Siebert, Nicolas Martin, Christian Boily, Paolo Bianchini et Laurent Chemin, avec qui j'ai eu la chance de partager de bons moments et d'échanger des idées qui m'ont beaucoup stimulé. J'aimerais bien aussi exprimer ma gratitude à Ada Nebot-Gomez-Moran, Philippe Vonflie, Mark Allen, Caroline Bot, Pierre-Alain Duc, Frédéric Marin, Alex Oancea et Ariane Lançon pour les moments partagés à l'Observatoire et l'Irma et pour les discussions toujours enrichissantes.

Je voudrais également remercier mes collègues et amis de l'Observatoire pour tous les moments partagés qui colorent mes souvenirs de ces années passées : Srikanth, Mathias, Mei, Lucie, Thibault, Clément, Anirudh, Chengdong, Samuel, Thomas, Hamza, Marie, Simon, Diana, Wassim, Elisabeth, Radi, Baptiste, Claire, Gauri, Amel, Julie, Adrien, Cédric et Thibaut. Je remercie également Matteo, Clarisse, Clément et Romain, que j'ai eu le plaisir de co-encadrer, dans une expérience que j'espère avoir été aussi enrichissante pour eux que cela a été pour moi.

Je profite de l'occasion pour remercier chaleureusement Sandrine Langenbacher et Véronique

Trimbour de l'ObAS pour toute leur attention et leur excellence dans l'accompagnement des démarches administratives. Je voudrais également exprimer ma gratitude envers toutes les personnes impliquées dans le fonctionnement pratique de l'Observatoire, en particulier je remercie Philippe et Rachid pour les discussions spontanées et toujours agréables. J'adresse aussi mes remerciements à l'ensemble des responsables de l'École doctorale chimie et physique-chimie de Strasbourg pour toutes les démarches administratives de la thèse. Je remercie également les responsables de l'UFR Mathématiques, notamment pour les démarches liées à la formation complémentaire Diplôme d'Université « Mathématiques et applications : recherche et interactions ».

Je remercie également Laurène Préhaut, Chloé Thibaudeau et Geoffroy Domenech de l'ITI IRMIA++ pour leur soutien dans les démarches administratives liées à la thèse. Je les remercie également pour leur soutien au dispositif Budget Jeunes Chercheurs, auquel j'ai eu le plaisir de contribuer avec mes collègues, notamment Claire Schnoebelen, à travers des projets marquants, destinés à l'ensemble des jeunes chercheurs de l'ITI IRMIA++. Un grand merci également à Margot Zinck, du Jardin des Sciences, pour m'avoir rendu possible de donner une conférence grand public au CASF de Bischwiller, une expérience qui m'a profondément marqué.

Je suis aussi reconnaissant à Thomas Keller et Mathilde Dembront pour toute leur patience et compréhension dans leur assistance informatique et aussi pour leurs discussions sympas. Je suis également reconnaissant à Jérôme Pansanel et Vincent Legoll pour leur attention et pour m'avoir confié l'accès aux ressources numériques de la plateforme SCIGNE à l'Institut pluridisciplinaire Hubert Curien. Mes remerciements vont également à Michel Ringenbach et David Brusson, du Centre de Calcul de l'Université de Strasbourg, pour toute l'attention qu'ils m'ont accordée. J'exprime aussi ma gratitude envers les différents intervenants du Très Grand Centre de Calcul du CEA pour leur assistance.

Je tiens enfin à remercier mes amis et ma famille, toujours présents dans mon cœur bien qu'éparpillés à travers le monde, pour leur bienveillance, leur soutien et pour toujours partager mon enthousiasme à mieux comprendre notre Univers.

Je conclus ces remerciements sans trouver de mots à la hauteur de ma reconnaissance envers mon père et mes grands-parents, qui ont partagé mon rêve à chaque étape, et à la mémoire desquels je dédie cette thèse. J'adresse enfin ma plus profonde gratitude à ma précieuse mère, à qui je dédie ce travail en son honneur.

Ce travail a été soutenu par l'Institut thématique interdisciplinaire IRMIA++, dans le cadre du programme ITI 2021-2028 de l'Université de Strasbourg, du CNRS et de l'Inserm, a été soutenu par IdEx Unistra (ANR-10-IDEX-0002) et par le projet SFRI-STRAT'US (ANR-20-SFRI-0012) dans le cadre du programme français Investissements d'avenir. Ce travail a bénéficié d'un accès aux ressources HPC de l'IDRIS dans le cadre de l'allocation 2025-AD010415956. Certains résultats présentés dans cet article ont été calculés sur la plateforme SCIGNE. Nous remercions l'équipe informatique de SCIGNE pour son soutien technique et pour avoir mis à notre disposition ses installations informatiques et de stockage. Certains calculs ont été effectués au Centre de Calcul de l'Université de Strasbourg.

Contents

List of Publications

First Author

Khalil, Y. R. et al. (Dec. 2023). "Can we decipher the dynamics of the Milky Way Disk from Gaia ?" In: *SF2A-2023: Proceedings of the Annual meeting of the French Society of Astronomy and Astrophysics*, pp. 91–94.

Khalil, Y. R. et al. (July 2025a). "A non-axisymmetric potential for the Milky Way disk". In: A&A 699, A263, A263. arXiv: 2411.12800 [astro-ph.GA].

Collaborations

Bougakov, A. et al. (Sept. 2025). "The variation of galactic tides affecting the long-term dynamics of distant trans-Neptunian objects". In: *EPSC-DPS Joint Meeting 2025*. EPSC-DPS2025-1586. Helsinki, Finland.

Rivero, A. et al. (June 2025). "Age-Metallicity distributions of Moving Groups in the Solar-Neighbourhood". poster at European Astronomical Society Annual Meeting.

Posters

Khalil, Y. R. (Mar. 2024a). "Can we decipher the dynamics of the Milky Way Disk from Gaia ?" poster at Congress of PhD Students of ED 182.

Khalil, Y. R. et al. (June 2025c). "Deciphering the Galactic bar and spiral arms dynamics with Gaia." poster at European Astronomical Society Annual Meeting.

Softwares

Khalil, Y. R. et al. (July 2025d). *SPIBACK: Backward-integration-based non-axisymmetric models of the Milky Way disk*. Astrophysics Source Code Library, record ascl:2507.027.

Outreach

Khalil, Y. R. and M. Palanque (Oct. 2022). *Dynamical systems and astrophysics*. Published in the DU IRMIA++ students' journal. URL: https://irmiapp.unistra.fr/fr/formation/le-journal-des-etudiants-du-du-irmia#c65070 (visited on 08/09/2025).

List of Figures

List of Tables

Chapter 1

Introduction

1.1 Overview of the Milky Way Galaxy

1.1.1 Context

If we pause for a moment, in order to picture in our imagination where we are located, we can quickly start imagining ourselves 'as seen from above us'. As we move further and further away, we imagine seeing the Earth, then the Earth-moon system, then the full Solar system, then the Solar neighborhood with our nearest stars brightening the sight, until we reach a point far enough to imagine seeing our whole Galactic disk: the Milky Way (MW) disk, with its 200 billion stars mostly following nearly-circular orbits around the Galactic center. If we keep this exercise going, we would then picture the Local Group, with the MW and Andromeda galaxies and their streams and satellites. Moving further away, we would then picture the Local (or Virgo) Supercluster, which contains approximately 100 galaxy groups. Then we would start seeing the full 'cosmic web', filling the whole observable Universe.

While it is fun to imagine observing the Universe in this manner, in practice, such a view is only inferred from models, as our real view of the Universe is fundamentally different: we actually detect light emitted by distant sources, collected by ground-based and space-based telescopes, which allow us to observe extragalactic systems with an ever increasing depth and resolution. Observations of these extragalactic systems reveal a remarkable diversity in the morphological properties of galaxies, as illustrated in Fig. 1.1. Paradoxically, studying our own MW galaxy, however, presents significant challenges precisely due to our position within it. Therefore, unraveling the structure of the MW required a considerable time, careful investigations, and transformative insights to establish its nature as a barred spiral disk galaxy.

However, even today, the detailed structure of the MW, particularly its bar and spiral arms, remains remarkably poorly known. Nevertheless, the precision of the data that we can nowadays obtain in the MW is so exquisite that it allows us to model it with details that we cannot hope to achieve in other galaxies. In particular, a better understanding of the secular evolution of disk galaxies needs a better understanding of the origin and nature of spiral arms, as well as their role in the evolution of galaxy disks. For this, the MW galaxy is a perfect laboratory, and unraveling the detailed structure of its spiral arms from a dynamical point of view will be the main topic of the present thesis. Another long term goal is to establish a full reference Galactic gravitational potential for the MW, that could have a long-lasting impact on the community's understanding of the Galactic disk dynamics, but also of all the Galactic components and (sub)-structures (see Fig 1.2), including the mysterious halo of putative dark matter, the nature of which remaining the most fundamental question in the context of Galactic dynamics.

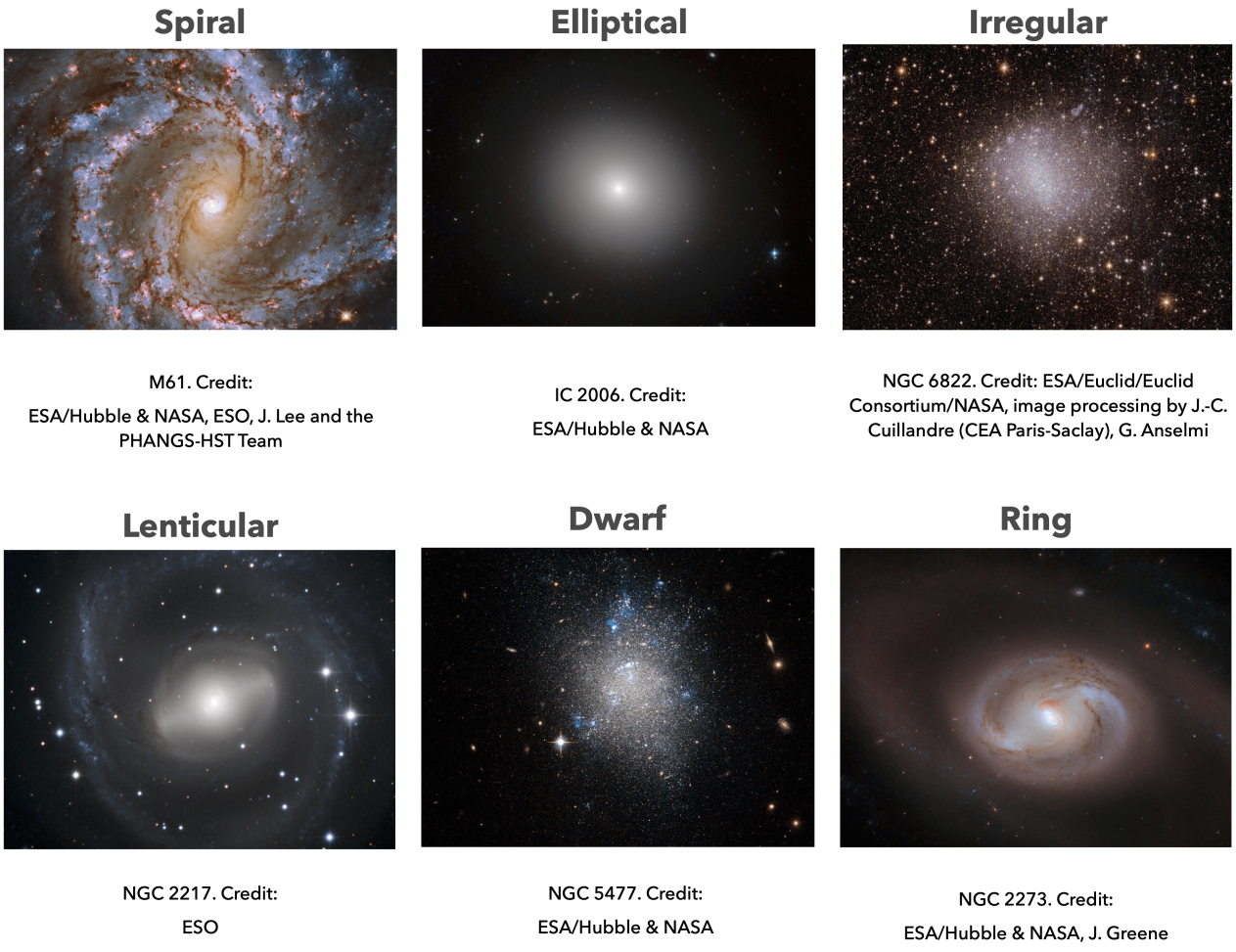

Figure 1.1: Examples of observed galaxies and their respective morphology. Copyrights are indicated below each image

To leading order, the MW is composed of $\sim 2 \times 10^{11}$ stars and interstellar gas, mostly residing in a disk with a total baryonic mass of $\sim 6 \times 10^{10}$ Solar masses. The stellar disk can be decomposed into a thin and a thick component. In the central parts, there is a bulge component, which is nowadays thought to be mostly related to the bar (a boxy-peanut "pseudo-bulge"). Surrounding the disk is a spheroidal stellar halo, composed of rather old stars, mostly irrelevant in terms of total mass but holding invaluable clues on the history of the Galaxy and also containing excellent dynamical tracers such as stellar streams (see Fig 1.2). Much more importantly in terms of mass, the disk is also surrounded by a putative massive dark matter halo, whose mass is not very well determined but is typically estimated between a few times 10^{11} and 10^{12} Solar masses. Most available information on stellar populations of the Galaxy were put together in a dynamically coherent model in a series of papers of the mid-1980s, by astronomers from Besançon Observatory (Robin and Creze, 1986; Bienayme et al., 1987). This model, known as the Besançon Galaxy Model (BGM) has been continuously updated since then, and remains up to this day a reference model for the structure of the Galaxy (Robin et al., 2003; Lagarde et al., 2017; Robin et al., 2022). Despite discussions of the MW disk hosting spiral arms dating back to the earliest discussions on the nature of the MW as a galaxy, it was only with the work of Morgan et al. (1952) that some of these arms were identified by studying the distribution of HII regions. The existence of the MW bar on the other hand, was originally hypothesized from the observations of gas kinematics (de Vaucouleurs, 1964; Peters, 1975; Gerhard and Vietri, 1986; Binney et al., 1991) and confirmed from (near-) infrared observations (e.g., Blitz and Spergel, 1991; Sellwood, 1993; Weiland et al., 1994; Binney et al., 1997) as well as bulge stellar kinematics (e.g., Zhao et al., 1994).

Recent advances in our understanding of the structure and dynamics of the MW have arisen from major theoretical developments together with increasingly precise observations and numerical computations. Space-based telescopes, in particular, inaugurated the era of precision astrometry, playing a key role in refining our understanding of the MW. Building on these advances, this thesis aims to construct and fit a reference non-axisymmetric gravitational potential to the MW (including a detailed account of its bar and spiral arms), in particular to its disk kinematics using the recent ESA *Gaia* mission's most comprehensive and precise stellar position and motion data. The next sections discuss the *Hipparcos* and *Gaia* space missions, which form the observational foundations for this thesis work. Section 1.2 then introduces essential concepts in Galactic dynamics, forming the basis for the modeling and subsequent analysis in this thesis. Then, Section 1.3 focuses more in detail on the Galactic bar and spiral

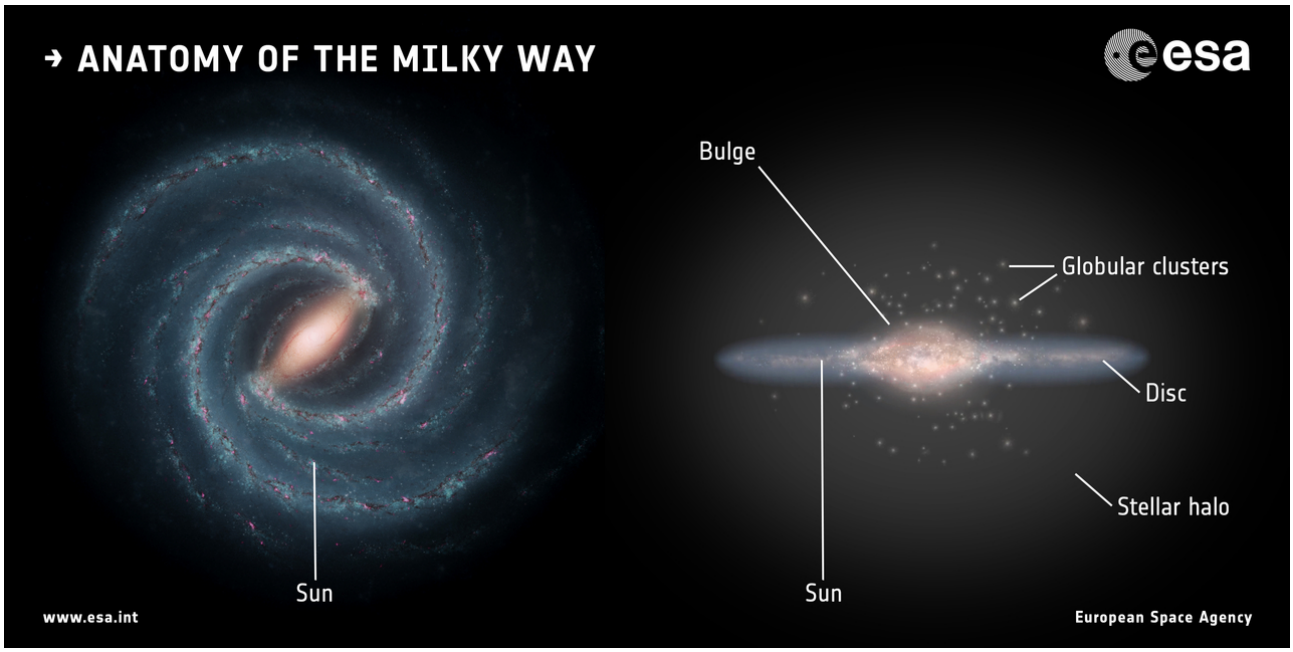

Figure 1.2: Illustration of some of the main Galactic components. The left panel depicts the disk structure of the MW, indicating the presence of the bar in the central region and of the spiral arms around. The right panel illustrates the Sun's position, the disk, stellar bulge, and stellar halo, as well as globular clusters. Copyright: Left: NASA/JPL-Caltech; right: ESA; layout: ESA/ATG medialab

arms.

1.1.2 Astrometry

Astrometry is the part of astronomy that deals with precise measurements of the position and motion of stars (and of other celestial bodies). It can be traced back to the work of Babylonian astronomers (around 500 BC) and Hipparchus (around 190 BC) who actually discovered the consequences of the precession of the Earth (although it was not interpreted in this way at the time) with astrometry. Astrometry nowadays also yields the most precise measurements of the distance of stars since when observing a star from two different points on the Earth's heliocentric orbit, its position appears to shift relative to much more distant background sources on the sky, whose own positions are too far away for their changes to be perceivable. Measuring this apparent shift yields the parallax angle p, which is related to the distance d by $\tan(p) = \frac{1\text{AU}}{d(\text{AU})}$, where the Astronomical Unit (AU) is the distance from the Earth to the Sun (about 1.5×10^8 km). In practice, p is very small, typically less than one arcsecond, so the equation is usually simplified to $p \simeq \frac{1\text{AU}}{d(\text{AU})}$ (in radians). The distance corresponding to one arcsecond is called a parsec, pc, which is about 206265 AU. If we measure the parallax in milliarcsecond (mas), one has that $d(\text{kpc}) = \frac{1}{p(\text{mas})}$.

Besides parallax, which is only an apparent stellar motion, observations of the same star over a period of time make it possible to measure its proper motion, i.e., its actual angular displacement on the sky, which, together with the distance, can be translated into the transverse velocity. The remaining third component of a star's velocity, the line-of-sight velocity, can be obtained through spectroscopic measurements, where one looks for the Doppler effect, a shift in frequency, on characteristic spectral lines — usually strong and sharp absorption lines.

1.1.3 The Hipparcos era: unraveling the dynamics of the Solar neighborhood

In 1967, Pierre Lacroute, while at the Strasbourg astronomical Observatory, proposed to the *Centre national d'études spatiales* (CNES) to build an astrometric space mission. This proposal ultimately led to the advent of the first satellite designed for astrometry by the European Space Agency (ESA): the HIgh Precision PARallax COllecting Satellite (*Hipparcos*, Clausen and Perryman, 1990; Perryman, 1991), launched in 1989 and that has been actively observing until 1993. One of its main scientific motivations was to investigate the structure and kinematics of the Solar neighborhood in the MW, through unprecedented precision on stellar positions, parallaxes, and two-dimensional on-sky velocities.

After the mission's observational period, the final *Hipparcos* catalogue was published in 1997 (Perryman et al., 1997), featuring 118 218 sources with both astrometry and photometry, achieving an outstanding milliarcsecond (mas) precision in parallax and in proper motion. Larger but less precise catalogues complemented the *Hipparcos* catalogue, first with Tycho (Høg et al., 1997) and later with Tycho-2 (Høg et al., 2000), including about 2.5 million sources with precision from tens to hundreds of mas in parallax and about 2.5 mas in proper motion. Note that *Hipparcos* yielded only 5-dimensional phase-space information, lacking radial velocity for a full 6-dimensional characterization of position and velocity. This led to multiple complementary spectroscopic observations, in particular with the two photoelectric cross-correlation spectrometers CORAVEL (Baranne et al., 1979; Mayor, 1985) operated at the Swiss 1-m telescope at Observatoire de Haute-Provence (OHP, France) and at the Danish 1.5-m telescope at La Silla (ESO, Chile), whose data were published in Nordström et al. (2004) and Famaey et al. (2005).

Building on the availability of these rich datasets, several remarkable scientific advances followed. Most major contributions up to 2012 can be consulted in Perryman (2012). For instance, in García-Sánchez et al. (1999), the *Hipparcos* data were combined with line-of-sight

velocities to search for stars expected to come closest to the Sun, potentially affecting the small bodies in the Solar System. *Hipparcos* also helped refining estimates of the Sun's distance to the Galactic center, with values ranging from 7.8 kpc to 9.3 kpc (see Table 9.1 in Perryman, 2012) and heights above the plane rangig from 9 pc (Pham, 1997) and 8 pc (Holmberg et al., 1997) with F-stars and red giants, to 24 pc (Maíz-Apellániz, 2001) with younger O-B5 stars.

An important advance was the dynamical estimate of the local matter density (including dark matter) at the Solar position. Crézé et al. (1998) and Holmberg and Flynn (2000) both assumed that the vertical phase-space distribution only depends on the vertical energy and could adjust the shape of the vertical potential and hence the local matter density, obtaining values ranging from 0.076 to 0.1 $M_{\odot}pc^{-3}$ depending on the parametrization of the local vertical potential. The value of Holmberg and Flynn (2000) was confirmed in Siebert et al. (2003) and used in Famaey and Dejonghe (2003), where Stäckel potentials (the most general type of potential for which stellar motion is fully separable with three exact analytic integrals of the motion) for the MW with different forms and features were fitted, ensuring that they satisfy various observational constraints, including the local matter density. These constraints on the local matter density, especially those of Holmberg and Flynn (2000), have not really improved since then, the main reason being that *Gaia* data have later revealed vertical disequilibria, rendering the accuracy of the estimate less reliable despite the even better astrometric data that we have today. With the local baryon budget accounting for about 0.085 $M_{\odot}pc^{-3}$, this implies a local dark matter density of 0.015 $M_{\odot}pc^{-3}$ (see also de Salas and Widmark, 2021, for more recent estimates), a value which is particularly important for dark matter direct detection experiments, in combination with constraints on the possible dark matter velocity distribution (e.g. Lacroix et al., 2018).

Of high relevance for the investigations in the present thesis were the first detailed determination of the local velocity distribution of stars in the Solar neighborhood by Dehnen (1998), as illustrated in Fig. 1.3. In Famaey et al. (2005), *Hipparcos* data were combined with CORAVEL line-of-sight velocities to obtain full 6-dimensional information on nearly 7000 Giant stars, which revealed that the overdensities in local velocity space known as moving groups (the Hercules, Sirius and Hyades/Pleiades moving groups), spanned a large range of ages, demonstrating their dynamical origin, which was confirmed by the detailed studies of Famaey et al. (2007) and Famaey et al. (2008). This corroborated the hypothesis that these groups of stars are in resonant orbits, affected by dynamical interactions with the bar, the spiral arms, or both, as proposed for instance in the work of Dehnen (2000) linking the Hercules moving group to

the outer Lindblad resonance of the Galactic bar, using the backward integration method of Vauterin and Dejonghe (1997) which we will also use in our work, or in Quillen and Minchev (2005) associating the Pleiades and Hyades moving groups with one class of orbits in resonance with a spiral arm.

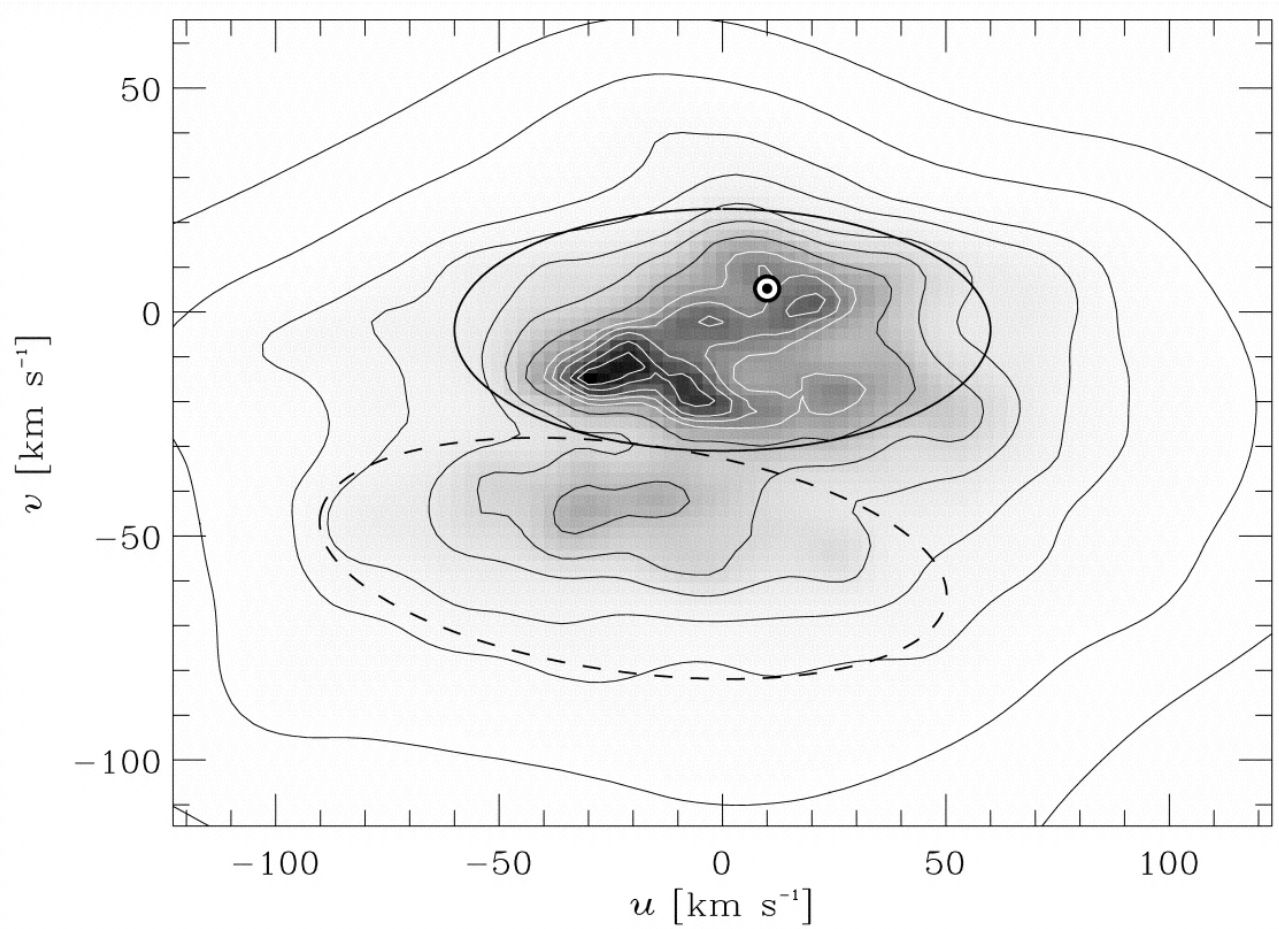

Figure 1.3: Figure extracted from Dehnen (1998). The figure illustrates the velocity distribution of 6018 stars from the Solar neighborhood, using *Hipparcos* data. The (u, v) velocity plane shown is defined such that the 'Local Standard of Rest' (supposedly corresponding to a frame in circular motion) has 0 kms^{-1}, with u being toward the Galactic center (hence with the opposite sign to Galactocentric V_R) and v in the direction of Galactic rotation (same direction as V_φ). The solid and dashed eclipses represent, respectively, the regions where most stars are early-type or late-type. The gray scale of the contour lines represents the percentage of stars, ranging from 2% to 99.9%.

Other important studies of the *Hipparcos* era discussed the origin of the stellar halo of the MW (e.g., Chiba and Yoshii, 1998), which represents only a small fraction of the total mass of the Galaxy (less than 1%) but holds important clues about its formation. It was shown that this component of the Galaxy may have formed *in situ* or may have been accreted, but most probably results from both processes. On the other hand, a crucial advance on our understanding of the so-called thick disk component of the MW was made by Reddy et al.

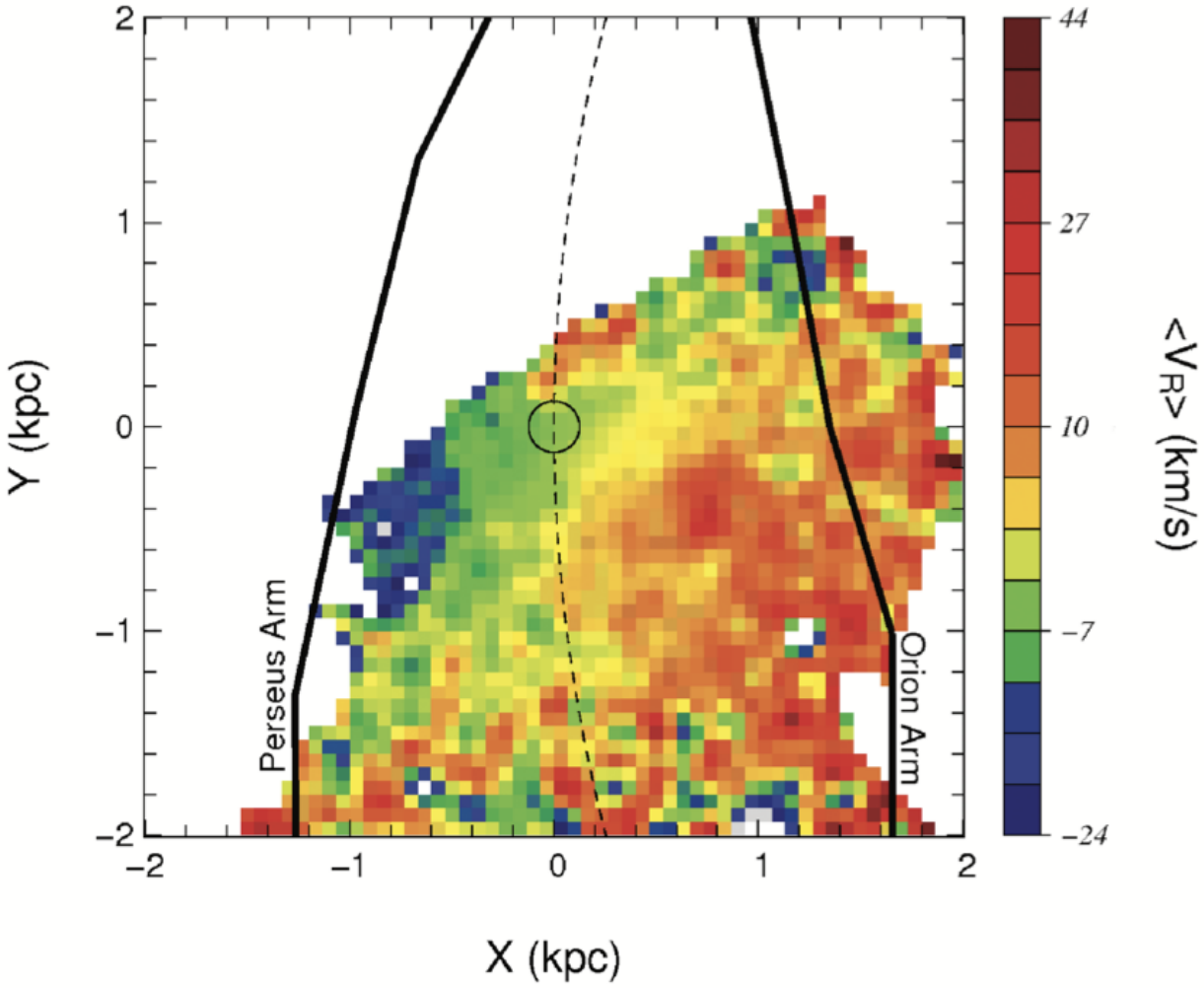

Figure 1.4: Figure extracted from Siebert et al. (2011). Mean Galactocentric radial velocity $\langle V_R \rangle$ on the Galactic plane within > 1 kpc from the Sun, with X axis positive in the direction of the Galactic center, and Y positive towards the Galactic rotation. The sample of 213713 is from the Radial Velocity Experiment (RAVE), with measured line-of-sight velocities complemented with astrometric parameters from three catalogues: PPMX, UCAC2, and Tycho-2. The locations of the nearest spiral arms are indicated from gas mapping of Englmaier et al. (2011), and the open circle indicates the location of the Sun.

(2006), who showed convincingly — thanks to high resolution spectroscopy complementary to *Hipparcos* data — that this Galactic component, first put forward from star counts by Gilmore and Reid (1983), was actually composed of stars with a clear enhancement of the ratio of α-elements (O, Mg, Si, Ca and Ti) to iron compared to the thin disk. This led to an actual re-definition of what the thick disk actually is, namely an old stellar population that can be purely chemically characterized, and that happens to be thicker and hotter than the thin disk populations. Questions about its connection with *in situ* halo stellar populations then emerged, and are still alive up to this day.

1.1.4 The post-Hipparcos era: spectroscopic surveys and the Solar suburbs

After $\sim$ 2005, drastic improvements in acquisition of massive amounts of spectroscopic data outside of the close Solar neighborhood (hence moving away to the "suburbs") have then been made, through various large surveys such as SEGUE, SEGUE-2 and APOGEE, as part of the Sloan Digital Sky Survey (SDSS, taking data since 2000, York et al., 2000), as well as RAVE (Steinmetz et al., 2006) and the *Gaia*-ESO survey (Gilmore et al., 2012), whilst proper motion catalogues such as PPMX (Röser et al., 2008) complemented the *Hipparcos*/Tycho-2 catalogues. Of high relevance for the investigations in the present thesis were the first-ever maps of the non-axisymmetric Galactocentric radial velocity field of the MW by Siebert et al. (2011) with RAVE data, as illustrated in Fig. 1.4. This allowed Siebert et al. (2012) to make use of the density wave formalism to fit a 2-armed spiral model with a contrast surface density of 14%, a pitch angle of 10 degrees and a pattern speed of 18.6 $\mathrm{kms}^{-1}\mathrm{kpc}^{-1}$, whilst Monari et al. (2014) showed that the bar could also have a significant effect on this radial velocity map. At the same time, observations from SDSS (Widrow et al., 2012) allowed to measure a 10% North-South asymmetry in the density of stars in a 1 kpc-wide cylinder around the Sun, whilst complementary measurements of radial velocities with SEGUE revealed that the mean vertical motion of stars could reach up to 10 km/s at heights of 1.5 kpc above the plane. It was speculated that such vertical perturbations could be excited by the recent passage of a satellite galaxy in the plane, such as the Sagittarius dwarf. Such non-zero mean vertical motions were also detected with RAVE (Williams et al., 2013), which ultimately revealed that the Solar neighborhood is apparently located in a transition zone between the inner disk affected mainly (but not solely) by vertical "breathing modes" (with non-zero vertical velocities, but plane-

symmetric), and the outer disk dominated by "bending modes" (where the whole disk tends to oscillate). Exploring the effect of spiral arms in 3D, Faure et al. (2014) were able to show, using test-particle simulations, and solving the linearized Jeans equations for a cold fluid, that breathing modes could be explained by the gravitational effect of internal non-axisymmetries, while only bending modes would need an external perturbation of the disk.

In parallel, a pioneering high-resolution spectroscopic study of nearby stars (Nissen and Schuster, 2010) revealed clearly, for the first time, that halo stars definitely fall into two distinct populations, clearly separated in [α/Fe]. The high-α halo stars were understood as an *in situ* population, either from an ancient disk population heated to halo kinematics or as the first stars formed during the collapse of a proto-Galactic gas cloud, whilst the kinematics of the low-α halo stars suggested that they were *ex situ* accreted stars. This new picture of the stellar halo is actually still well and alive today. While the thick disk-halo transition is still a matter of active research today, it is also the case of the thin disk-thick disk transition. A founding study for this connection was performed thanks to the high-resolution *Gaia*-ESO survey (Recio-Blanco et al., 2014), where it became clear that the thick disc in the [α/Fe] vs. [Fe/H] plane smoothly connects with the thin disk at high metallicities, hence that it lays in progressively thinner and thinner layers as the metallicity increases and the [α/Fe] decreases with time, until it fully merges with the thin disk. With APOGEE (Hayden et al., 2015), it was then shown that the location of the high-α sequence in the [α/Fe] vs. [Fe/H] plane is nearly constant across the disk and indeed smoothly connects with the low-α sequence at high metallicities, but that the high-α stars completely disappear beyond distances of 11 kpc from the Galactic center, while the morphology of the low-α sequence changes with the location in the Galactic disk. The latter is therefore assumed to have been subject to inside-out formation while the former has probably been formed faster before a quenching event occurred, possibly related to its heating and thickening. The role of mergers, the connection with the dual sequence of halo stars, and the role of non-axisymmetric structures of the disk such as the bar and spiral arms in this complex history of the disk are not yet fully settled today. Indeed, following the seminal work of Sellwood and Binney (2002), it became clear that spiral arms can actually play a crucial role in the history of the disk by radially mixing it, i.e. exchanging angular momenta at the spiral arms' corotation radii while not excessively heating the disk. Such a radial migration mechanism was later shown to be greatly enhanced in the joint presence of a bar and spiral arms (Minchev and Famaey, 2010). Therefore, the high metallicity dispersion in the local age-metallicity distribution has been understood as a consequence of this mechanism, meaning

that stars that can be considered as truly resulting of the chemical evolution at the Solar circle have a rather restricted metallicity range (Haywood, 2008). All these results argue for a better understanding of the non-axisymmetries of the MW disk not only to decipher its present-day structure but also to understand its secular evolution.

1.1.5 The Gaia era: dynamics of the whole Milky Way

As a follow-up to the immensely successful *Hipparcos* mission, ESA began developing the *Gaia* astrometric mission in 2000 (Gaia Collaboration et al., 2016b). The mission includes on-board spectroscopic determination of line-of-sight velocities and the ability to observe much fainter stars than *Hipparcos*. *Gaia*'s core scientific goals are the structure, dynamics, formation, and evolution of the MW. Launched on December 19, 2013, it entered a heliocentric orbit at Lagrange point L2, and obtained full-sky astrometric, photometric, and spectroscopic data until the conclusion of its science operations on January 15, 2025, before deactivation on March 27, 2025. Over its 11 years of operation, the *Gaia* spacecraft collected an impressive three trillion observations—covering approximately 2 billion sources—and, producing the largest, most complete, and homogeneous astrometric MW catalogue ever.

The final *Gaia* mission catalogue is expected to be released by the end of ∼2030. The first *Gaia* Data Release (DR1, Gaia Collaboration et al., 2016a) was essentially only a more precise upgrade of data for *Hipparcos* sources in terms of astrometric measurements—position, parallax, and proper motion. *Gaia* Data Release 2 (DR2) was then released two years later (Gaia Collaboration et al., 2018b) and was a true revolution for the field, with an impressive 1.3 billion sources having full astrometric measurements, together with seven million line-of-sight velocities. The Early Third Data Release (EDR3), published another two years later (Gaia Collaboration et al., 2021a), featured 1.4 billion sources with full astrometric measurements, with improved calibration and precision as well as better completeness for faint sources. The Data Release 3 (DR3), the latest *Gaia* catalogue, was then published another two years later (Gaia Collaboration et al., 2023c). Introducing new data products such as distances, metallicity, temperatures, gravities, and extinction for nearly 470 million sources, it also includes classifications for about 1.6 billion sources. Thirty-three million line-of-sight velocities are provided, with average uncertainties around $1\,\mathrm{km s^{-1}}$. Uncertainties are as low as 0.01 mas for position and parallax and 0.01 $\mathrm{mas yr^{-1}}$ for proper motion for most sources. The sources with radial velocities reach beyond the Galactic center by a few kiloparsecs and climb a dozen kiloparsecs in height in the inner halo. This gives the *Gaia* DR3 subsample with full

6-dimensional phase-space information great value for Galactic dynamics and discoveries. In addition, *Gaia* DR3 contains the largest chemical catalogue to date, with detailed abundances for up to 13 chemical elements for over 5.6 million stars. These are derived from the General Stellar Parametriser-Spectroscopy (GSP-Spec) module using *Gaia* RVS spectra (Recio-Blanco et al., 2023). Another data release (DR4) is expected at the end of 2026, bringing anticipated major improvements, particularly in source number and data product quality and diversity.

Gaia's unprecedented high-precision parallaxes still require care in inferring stellar distances: about 100 million sources have top-tier astrometry with very high SNR but selecting only these high-SNR sources introduces a bias (Luri et al., 2018). To estimate distances using *Gaia* parallaxes, several approaches have been developed. In Bailer-Jones et al. (2018a), a galaxy model was used to infer the distances of *Gaia* DR2 sources from a probability distribution fundamentally based only on parallax, position, and uncertainty—but not source astrophysical parameters. Adding this and more information is possible, as done for *Gaia* EDR3 with color and magnitude (Bailer-Jones et al., 2021), and *Gaia* DR3 with proper motion (Bailer-Jones, 2023), using a mock *Gaia* catalogue from Rybizki et al. (2020). Alternatively, some of the most accurate distance estimates for *Gaia* DR2 (Anders et al., 2019) and EDR3 (Anders et al., 2022) were inferred using *Gaia* parallaxes and multi-band photometry from other surveys, enabling per-star estimation of age, mass, and extinction. This is the `StarHorse` catalogue that we will use in this thesis.

The upcoming *Gaia* data releases (DR4 in mid-2026, DR5 hopefully in 2030) will provide full 6-dimensional stellar phase-space information for an even larger MW volume and introduce new data unlocking fresh research avenues. Other surveys strongly complement *Gaia*'s research on Galactic dynamics. So far a dozen of photometric and spectroscopic ground-based surveys mentioned are used in many works in combination with *Gaia*. Additional surveys, such as WEAVE (Jin et al., 2024), 4MOST (de Jong et al., 2019), LSST (Ivezić et al., 2019), SDSS-V MWM (Kollmeier et al., 2017), and MOONS (Cirasuolo et al., 2020), are anticipated to nicely complement *Gaia* data.

The impact of the *Gaia* mission spans a wide range of topics, including stellar physics and evolution, stellar variability, exoplanets, binaries, and the Solar System. But above all, *Gaia* has enabled breakthroughs in refining our understanding of the structure, kinematics, dynamics, and evolution of the MW. An example of a topic at the border between Galactic dynamics and Solar System physics, following up on García-Sánchez et al. (1999), is the work of Berski and Dybczyński (2016) predicting Gliese 710, a K-dwarf star, to pass 0.6 pc from

us in 1.35 Myr, with the largest predicted impact on the Oort cloud. This is an active field, with many examples, but so far, all using axisymmetric gravitational potentials for the MW, including the systematic approach by Bailer-Jones et al. (2018b) on 7.2 million stars, finding about 700 of them approaching the Sun in less than 5 pc within 15 Myr. Our present thesis establishing a reference non-axisymmetric potential for the MW could therefore be immensely useful for this field.

Regarding the history of the assembly of the MW, a milestone from *Gaia* has been the confirmation of the picture already hinted at by Nissen and Schuster (2010), with the discovery of the remnant of a major accretion event involving a massive dwarf galaxy, approximately 8 Gyr to 11 Gyr ago, known as *Gaia*-Sausage-Enceladus (GSE), and making up most of the *ex situ* stellar halo (Belokurov et al., 2018; Helmi et al., 2018; Haywood et al., 2018). The MW globular clusters data from *Gaia* were investigated by Myeong et al. (2018) and Massari et al. (2019) to identify some of them that were brought by GSE in the merger event, before a comprehensive dynamical characterization of the Galactic halo in terms of stellar streams, globular clusters, and satellite galaxies was performed in Malhan et al. (2022). In this work, membership in different mergers was investigated, along with orbital and chemical characterizations, providing an important reference for understanding the properties of our Galaxy in the context of studying general galaxy evolution and formation. Among many other developments in this active field, more recently, in Skúladóttir et al. (2025), chemo-kinematical observational evidence is shown to support several passages of the then-merging dwarf galaxy. This investigation, in particular, reveals that GSE stars with high kinematic energy are associated with earlier passages and originate from the outer region of GSE, as they are found to be less chemically evolved. On the other hand, stars with low kinematic energy are associated with later passages, and with the inner and more chemically evolved region of the merging dwarf galaxy. These findings enhance our understanding of galaxy mergers and position GSE as a key benchmark in hierarchical galaxy formation. The role that the GSE merger might have played in the quenching and heating event leading to the current kinematical structure of the thick disk is still actively discussed.

The *Gaia* mission has also proven to be an extraordinary goldmine for the discovery of new stellar streams, mostly originating from tidally disrupted golbular clusters, in the stellar halo, with up to $\sim$ 90 thin stellar streams (Ibata et al., 2024) discovered thanks to the STREAMFINDER algorithm (Malhan and Ibata, 2018) applied to *Gaia* data. Such streams nearly trace orbits and are thus invaluable probes of the 3D potential of the Galaxy, for which

they were used for instance in Malhan and Ibata (2019) and Ibata et al. (2024), providing excellent constraints on the enclosed mass within 20 kpc. Interestingly, *Gaia* has also allowed for the first time ever to detect streams of *open* clusters within the disk (Jerabkova et al., 2021), which offers new sets of constraints on the structure and pattern speed of non-axisymmetric structures such as the bar (Thomas et al., 2023). In the halo, the best constraints at very large distances come from the Sagittarius stream (Ibata et al., 2001), the tidal stream of the Sagittarius dwarf galaxy (Ibata et al., 1994), whose data have led to the current best time-dependent MW gravitational potential (Vasiliev et al., 2021) in which an infalling massive Large Magellanic Cloud (LMC), representing more than 10% of the mass of the MW, plays a crucial role. The dynamical effects of this infalling massive LMC on the density and kinematics of the stellar halo are also actively investigated (e.g., Rozier et al., 2022). However, the model of Vasiliev et al. (2021) cannot by itself explain the presence of a bifurcation in the Sagittarius stream, in the form of a faint branch running parallel to the main brighter branch. Such a bifurcation could be understood as precession of the stream with successive wraps, but would impose a very nearly spherical potential which would contradict the current best-fit time-dependent model. A possible solution to this conundrum was however offered by Oria et al. (2022) who proposed that the faint branch originates in a (now disappeared) disk component of the Sagittarius dwarf, that was nearly perpendicular to both the MW disk and Sagittarius orbital plane.

The Sagittarius dwarf was already suspected (among other possible vertical perturbers) by Widrow et al. (2012) to be responsible for the vertical waves discovered in the Galactic disk, and this suspicion grew to another level with the staggering *Gaia* DR2 discovery of a one-armed phase-spiral in the local $z - V_z$ plane (Antoja et al., 2018), a signature of on-going phase-mixing clearly indicating that the disk is in vertical disequilibrium, and thereby complicating the local vertical force analyses based on the assumption of equilibrium (Haines et al., 2019; Salomon et al., 2020). Simulations and dynamical models have shown how one could, indeed, relate the local one-armed phase-spiral to the interaction of the Sagittarius dwarf with the MW disk (e.g., Binney and Schönrich, 2018; Laporte et al., 2019), but the discovery of a two-armed phase spiral for stars with lower angular momenta (e.g., Li et al., 2023) has on the other hand reinforced the idea that the Solar neighborhood could be located in a transition zone between the inner disk affected mainly (but not solely) by plane-symmetric "breathing modes" (including the two-armed phase-spiral) and the outer disk dominated by asymmetric "bending modes" (including the one-armed phase-spiral). While it has been suggested that the two-armed phase spiral could be related to internal non-axisymmetries, in particular to a decelerating bar (Li et al., 2023), the

exact origins of both the one-armed and two-armed phase spirals are still under a heavy debate (e.g., Khoperskov et al., 2019; Hunt et al., 2022; Grand et al., 2023; Widrow, 2023; Tremaine et al., 2023; Frankel et al., 2024) and their relation with large-scale vertical wave patterns of the disk is still unclear. Indeed, already with *Gaia* DR1, Schönrich and Dehnen (2018) and Carrillo et al. (2018) confirmed that the outer disk is vertically warped and accompanied by some sort of wave-like pattern in vertical velocities, a pattern which was further investigated in Poggio et al. (2025), and whose exact dynamical origin is still a matter of ongoing research. Furthermore, it was observed in Gaia Collaboration et al. (2023a), that the Galactic disk exhibits an overall strong chemo-kinematical vertical symmetry and a pronounced flaring with a higher scale height than previously measured. Compounding the disk flaring, the warping of the Galactic disk beyond about 7 kpc was characterized kinematically in Schönrich and Dehnen (2018). In Skowron et al. (2019), vertical velocities of the warp are quite significant, ranging from 10 to 20 kms^{-1} with both extremities moving away from the disk in opposite directions. The warp itself was confirmed as a dynamical precession structure in Poggio et al. (2020).

Perhaps related to these non-equilibrium features, one should note the current debates about the outer rotation curve of the MW as deduced from *Gaia* data and its possible surprising consequences for the dark matter content of the Galaxy. While the best models based on stellar streams (e.g., Ibata et al., 2024), especially the one reproducing the Sagittarius stream in the presence of a massive LMC (Vasiliev et al., 2021), as well as all estimates of the mass of the MW based on the escape speed curve (Monari et al., 2018; Roche et al., 2024a) point to virial masses between $\sim 7 \times 10^{11}\,\mathrm{M}_\odot$ and $10^{12}\,\mathrm{M}_\odot$, the most recent estimates from the rotation curve computed from Jeans modeling of the outer disk can be as low as $\lesssim 2 \times 10^{11}\,\mathrm{M}_\odot$ (Jiao et al., 2023; Ou et al., 2024), which would make it only twice the mass of the LMC. In our work, we will adopt a dark matter halo mass in between those values. It is, in any case, perhaps more advisable to fit phase-space distribution functions (see next section) to *Gaia* data in order to construct axisymmetric models of the MW, rather than using Jeans modeling in the outer disk. Such a relevant axisymmetric self-consistent model for the MW using *Gaia* DR2 was presented in Binney and Vasiliev (2023). With *Gaia* DR3, this model was extended in Binney and Vasiliev (2024) to include chemical parameters, and a new parametrization of the Galactic bulge.

Regarding non-axisymmetries, and in particular spiral arms, *Gaia* has allowed to trace them in configuration space, from different stellar populations, both young stars (e.g., Gaia Collaboration et al., 2023b; Poggio et al., 2021; Drimmel et al., 2024) and more evolved ones

(e.g., Khanna et al., 2024). In Poggio et al. (2022), the *Gaia* chemical information was used to distinguish different samples of young bright stars, allowing for a detailed mapping of the chemical distribution of stars in a large part of the MW disk. This is found to be remarkably correlated with the location of spiral arms, as traced by the over-densities of young stars in Poggio et al. (2021). Barbillon et al. (2025) in turn investigated in detail the chemical radial and azimuthal distribution of young and old stars. Notably, significant azimuthal variations in metallicity were found, particularly for young stellar populations. These variations are smaller for older stars, suggesting that spiral arms play a role in shaping the recent chemical structure of the disk. In Gaia Collaboration et al. (2023a), the GSP-Spec parameters allowed a precise sampling of the stellar population, enabling, in particular, to reveal very clearly, in stellar density and in metallicity, the spiral arms segments nearest to the Sun with massive stars. Another topic, related to the role played by spiral arms in the secular evolution of the disk, is the measure of heating versus radial migration that was obtained by Frankel et al. (2020) from *Gaia*-APOGEE data, namely that radial heating is an order of magnitude lower than angular momentum diffusion. This led to some debate as to whether this is even possible with our current understanding of radial migration from spiral arms (Hamilton et al., 2024b; Sellwood and Binney, 2025), knowing that including the effect of the bar should make things worse, with a general agreement that, in any case, this leaves *zero* room for any additional significant radial heating from other external perturbers (which could have consequences for various dark matter models). Finally, in Widmark and Naik (2024), a local dynamical (Jeans) analysis revealed that the Orion (Local) arm is the most striking over-density in the vicinity of the Sun, while Palicio et al. (2023) also identified spiral arm structures in the disk by considering the distribution of actions as a function of position. More highlights are discussed in detail in the following section 1.3. Regarding the bar, several observations at the Solar radius (Monari et al., 2019a; Monari et al., 2019b; Binney, 2020; D'Onghia and Aguerri, 2020; Lucchini et al., 2024), in the bulge region from proper motion data from the VVV survey calibrated on *Gaia* (e.g., Clarke et al., 2019; Sanders et al., 2019), in the stellar halo kinematics (Dillamore et al., 2024) and with the chemistry of the disk (Haywood et al., 2024; Khoperskov et al., 2024) have all converged on a pattern speed between $\sim$ 35-40 km s^{-1} kpc^{-1}, although possible sudden variations of the pattern speed are also possible (Hilmi et al., 2020). More highlights are discussed in detail in the following section 1.3.

More generally, the exquisite data from *Gaia* DR2 and DR3 (e.g., Gaia Collaboration et al., 2018a; Gaia Collaboration et al., 2023b) have revealed a particularly rich information contained

solely within the in-plane motions of disk stars. In particular, the map of local velocity space (Fig. 1.3) and the Galactocentric radial mean (or median) velocity field (Fig. 1.4) have been staggeringly refined. The moving groups can now also be traced as a function of radius and azimuth (e.g., Ramos et al., 2018; Bernet et al., 2022; Bernet et al., 2024). However, prior to this thesis, no global model reproducing these features has been produced, meaning that the rich information contained solely within the in-plane motions of stars had not been fully exploited yet. This is the topic of the present thesis. But before getting into the construction of such a model, we will first review below some basic notions of Galactic dynamics.

1.2 Galactic dynamics

Modeling the MW can be broadly categorized into two approaches: "top-down" and "bottom-up" (Famaey, 2024). "Top-down" models simulate MW-like galaxies, typically with hydrodynamical simulations, from cosmological initial conditions, and then compare these simulations to observed data. Conversely, "bottom-up" models construct the Galaxy directly from Galactic data. There are also many intermediate approaches, such as idealized simulations, that do not directly fit the data but can be tailored to resemble them. While 'top-down" models reveal physical processes across scales, they struggle by design with actually observed fine details, especially with cutting-edge large catalogues, such as those provided by *Gaia*. Both approaches are indeed complementary, and in particular, the "top-down" approach can help validate the "bottom-up" results.

"Bottom-up" modeling consists in simultaneously adjusting the phase-space distribution of stars, dark matter (and gas) as well as the gravitational potential to the data. We will mainly be considering stellar dynamics hereafter, and ignore gas dynamics for the time being. Broadly speaking, any N-particle system (with N being, for us, the number of stars — or even the number of stars and dark matter particles — in the MW) is described by a probability distribution function (PDF) in a large phase space of $6N$ dimensions, P_N. While each individual particle moves according to Hamilton's equations, the full phase-space PDF, P_N, is strictly conserved along trajectories, according to Liouville's theorem. The Bogoliubov–Born–Green–Kirkwood–Yvon (BBGKY) hierarchy then allows us to provide a statistical description of the system only via the one-particle distribution function (DF), which we will simply denote as F. The equation obeyed by F in a system governed by a long-range force such as gravity, in which the relaxation time is long, is the collisionless Boltzmann equation,

or Vlasov equation, which together with the Poisson equation for the gravitational potential, forms the fundamental equations of Galactic dynamics, at the core of "bottom-up" modeling methods. We will now review these concepts more in depth.

1.2.1 Hamilton's equations

In Hamiltonian dynamics, the evolution in time t, for each stellar particle from a system of N particles, of index $0 \leq i \leq N$, with masses μ_i, positions $\boldsymbol{x}_i$, and momenta $\mu_i \boldsymbol{v}_i$ is fully determined by the Hamilton's equations:

$$\mu_i \frac{d\boldsymbol{x}_i}{dt} = \frac{\partial H}{\partial \boldsymbol{v}_i} \qquad \text{and} \qquad \mu_i \frac{d\boldsymbol{v}_i}{dt} = -\frac{\partial H}{\partial \boldsymbol{x}_i} \tag{1.1}$$

with H being the Hamiltonian, which can be interpreted for most applications as being the total energy of the system, including kinetic and potential energy. The Hamiltonian can depend on the full system positions and velocities at each time, $H = H(\boldsymbol{x}, \boldsymbol{v}, t)$, with $(\boldsymbol{x}, \boldsymbol{v})$ denoting all particles' position $\boldsymbol{x} \equiv (\boldsymbol{x}_0, \ldots, \boldsymbol{x}_N)$, and all particles' velocities $\boldsymbol{v} \equiv (\boldsymbol{v}_0, \ldots, \boldsymbol{v}_N)$.

In the case of an idealized gravitationally bound system of N identical particles of equal mass μ, the Hamiltonian is explicitly given by:

$$H(\boldsymbol{x}, \boldsymbol{v}, t) = \frac{\mu}{2} \sum_{i}^{N} \boldsymbol{v}_i^2 + \mu^2 \sum_{i<j}^{N} U(|\boldsymbol{x}_i - \boldsymbol{x}_j|) \tag{1.2}$$

with $U(r) = -\frac{G}{r}$. But since a galaxy like the MW has more than 10^{11} stars, such a "per particle" approach is however impractical, and a statistical approach is better suited to such a case.

1.2.2 From Liouville's equation to Vlasov equation

In this context, it is useful to introduce the phase-space PDF of the system (e.g., Fouvry et al., 2016), $P_N(\Gamma_i, \ldots, \Gamma_N, t)$, with $\Gamma_i \equiv (\boldsymbol{x}_i, \boldsymbol{v}_i)$ the phase-space position of each particle i. The function P_N describes the probability of finding, at time t, the N particles of the system in a particular configuration $\Gamma \equiv (\boldsymbol{x}, \boldsymbol{v})$, where each particle of index i is located in phase-space at

Γ_i. The function P_N evolves in time according to the Liouville's equation:

$$\frac{\partial P_N}{\partial t} + \sum_{i=1}^{N} \left[\boldsymbol{v_i} \cdot \frac{\partial P_N}{\partial \boldsymbol{x_i}} + \mu \boldsymbol{\mathcal{F}}_i^{tot} \cdot \frac{\partial P_N}{\partial \boldsymbol{v_i}} \right] = 0 \tag{1.3}$$

where $\boldsymbol{\mathcal{F}}_i^{tot} = \sum_{j \neq i}^{N} \boldsymbol{\mathcal{F}}_{ij}$ is the total force applied by the system particles $j \neq i$ on the particle i. Variables of the $\boldsymbol{\mathcal{F}}_i^{tot}$ and P_N functions are generally $(\Gamma_i, \ldots, \Gamma_N, t)$, but are omitted here for readability, as in the following equations.

We can now also rewrite the Liouville's equation as a chain of equations known as the Bogoliubov – Born – Green – Kirkwood – Yvon (BBGKY) hierarchy. This will indeed allow for a more adaptable framework. First, let us remind that, by definition, the total integration of P_N across the whole phase-space must result in unity:

$$\int P_N(\Gamma_1, \ldots, \Gamma_N, t) d\Gamma_1 \ldots d\Gamma_N = 1, \tag{1.4}$$

then let us define the reduced PDF considering all subsystems of 1 to n particles, with $n \leq N$:

$$P_n(\Gamma_1, \ldots, \Gamma_n, t) \equiv \int P_N(\Gamma_1, \ldots, \Gamma_N, t) d\Gamma_{n+1} \ldots d\Gamma_N, \tag{1.5}$$

and then define the associated reduced phase-space density DF

$$F_n(\Gamma_1, \ldots, \Gamma_n, t) \equiv \mu^n \frac{N!}{(N-n)!} P_n(\Gamma_1, \ldots, \Gamma_n, t) \tag{1.6}$$

with F_1 denoting the single-particle $n = 1$ case, which we will simply denote F.

Integrating Liouville's equation (1.3) on the variables (Γ_{n+1}, Γ_N) leads to the BBGKY hierarchy given by:

$$\frac{\partial F_n}{\partial t} + \sum_{i=1}^{n} \boldsymbol{v_i} \cdot \frac{\partial F_n}{\partial \boldsymbol{x_i}} + \sum_{i=1}^{n} \sum_{k=1, k \neq i}^{n} \mu \boldsymbol{\mathcal{F}}_{ik} \cdot \frac{\partial F_n}{\partial \boldsymbol{v_i}} + \sum_{i=1}^{n} \int d\Gamma_{n+1} \boldsymbol{\mathcal{F}}_{i,n+1} \cdot \frac{\partial F_{n+1}}{\partial \boldsymbol{v_i}} = 0 \tag{1.7}$$

For each n, the corresponding equation in the hierarchy (1.7) depends on $(\Gamma_1, \ldots, \Gamma_n, t)$. These N equations are hierarchical as they are coupled: the solution for n needs knowledge of the $n+1$ solution. Despite being quite complicated, only the rightmost term involves the next order, $n+1$ in the hierarchy, which accounts for the collision terms of the up to n-particle subsystems. In particular, the BBGKY hierarchy for the lowest order, $n = 1$, where $F_1(\Gamma_1, t)$

is the one-particle phase-space density in terms of mass, writes as:

$$\frac{\partial F_1}{\partial t} + \boldsymbol{v_1} \cdot \frac{\partial F_1}{\partial \boldsymbol{x_1}} + \int \boldsymbol{\mathcal{F}}_{1,2} \cdot \frac{\partial F_2}{\partial \boldsymbol{v_1}} d\Gamma_2 = 0 \tag{1.8}$$

An approach to simplify these equations is to consider a simplification of the next order DF, $F_2(\Gamma_1, \Gamma_2, t)$. This can be done using the definition of the 2-body correlation function $g_2(\Gamma_1, \Gamma_2)$, such that:

$$F_2(\Gamma_1, \Gamma_2, t) = F_1(\Gamma_1, t) F_1(\Gamma_2, t) + g_2(\Gamma_1, \Gamma_2) \tag{1.9}$$

with this definition, the BBGKY hierarchy for $n = 1$ can be rewritten as:

$$\frac{\partial F_1}{\partial t} + \boldsymbol{v_1} \cdot \frac{\partial F_1}{\partial \boldsymbol{x_1}} + \left[\int F_1(\Gamma_2, t) \boldsymbol{\mathcal{F}}_{12} d\Gamma_2 \right] \cdot \frac{\partial F_1}{\partial \boldsymbol{v_1}} + \int \boldsymbol{\mathcal{F}}_{12} \cdot \frac{\partial g_2(\Gamma_1, \Gamma_2, t)}{\partial \boldsymbol{v_1}} d\Gamma_2 = 0 \tag{1.10}$$

From (1.4) and (1.6) it follows that, at any t:

$$\int F_1(\Gamma_1, t) d\Gamma_1 = \mu N \equiv M \qquad \text{and} \qquad \int g_2(\Gamma_1, \Gamma_2, t) d\Gamma_1 d\Gamma_2 = -\mu^2 N \equiv -M^2/N \tag{1.11}$$

where M is the total mass of the system.

Importantly, we can immediately notice from equations (1.11), that the respective orders of magnitude of the positive continuously differentiable functions F_1 and g_2, are related by $|g_2| \sim \frac{|F_1|}{N}$. This scaling for g_2 notably encompasses (but not only) the notion of "diluting encounters", where the impact of individual stellar encounters becomes increasingly negligible compared to the single-particle DF as the system grows in number of particles N, ultimately becoming effectively collisionless.

A way to check for this effective dilution of stellar encounters in the large N limit is to compute the system's relaxation time, τ_{relax}, estimating how long it takes close stellar encounters to change a star's velocity by about an order of magnitude compared to the mean field. It can be described by $\tau_{relax} = n_{relax} t_{cross}$, where t_{cross} is the typical time for a star to cross the Galaxy, and n_{relax} is the number of encounters needed to change a star's velocity by an order of magnitude. With simple assumptions, Binney and Tremaine (2008) find:

$$\tau_{relax} \approx \frac{N}{10 \ln N} t_{cross}, \tag{1.12}$$

which obviously goes to infinity in the infinite N limit. In the MW, we can estimate $t_{cross} \approx$

$R_{\rm disk}/V$, with $R_{\rm disk}$ some characteristic radius of the disk, and V the velocity of a typical orbit. Even when adopting a high value for the typical velocity, 300 $\rm kms^{-1}$, and a small characteristic radius of 1 kpc for the MW stellar disk, we would need much less than 10^8 stars for the relaxation time to fall below the age of the Universe. However, this sole notion of diluting encounters is an oversimplification of what is really encapsulated in the g_2 term, since individual orbits can also resonantly interact from far away, and not only in close encounters. Considering these $1/N$ resonant effects, we can actually use the BBGKY hierarchy (Heyvaerts, 2010) to derive what is known as the Balescu–Lenard equation (see also, e.g., Fouvry et al., 2016), which does take into account the secular evolution of the single-particle DF in the finite N case. However, going back to equation (1.10), and strictly taking the limit $N \to \infty$, we have

$$\int d\Gamma_2 \boldsymbol{\mathcal{F}}_{12} \cdot \frac{\partial g_2(\Gamma_1, \Gamma_2)}{\partial \boldsymbol{v_1}} \to 0 \tag{1.13}$$

enabling to further simplify the BBGKY hierarchy for $n = 1$ (1.10), in the limit $N \to \infty$, to

$$\frac{\partial F_1}{\partial t} + \boldsymbol{v_1} \cdot \frac{\partial F_1}{\partial \boldsymbol{x_1}} + \left[\int d\Gamma_2 F_1(\Gamma_2, t) \boldsymbol{\mathcal{F}}_{12} \right] \cdot \frac{\partial F_1}{\partial \boldsymbol{v_1}} = 0 \tag{1.14}$$

which is, in fact, known as the collisionless Boltzmann equation, or Vlasov equation, as in plasma physics. Stellar dynamics and plasma physics have a similar historical origin, namely from classical kinetic theory and statistical mechanics. Nowadays, they are separate fields, with different terminology, applications, and research interests, but that sometimes overlap, and benefit each other mutually (e.g., Bois et al., 2020; Hamilton and Fouvry, 2024; Hamilton et al., 2024a). The Vlasov equation fully describes the evolution of the single-particle DF for a strictly collisionless ($N \to \infty$) stellar system.

In (1.14), the fact that we can neglect stellar encounters means that we can also approximate the gravitational field of the system with a mean smooth gravitational potential $\Phi(\boldsymbol{x}, t)$ governed by the Poisson equation, which, in the absence of gas, relates the potential to the DF

$$\nabla^2 \Phi(\boldsymbol{x}, t) = 4\pi G \int d^3\boldsymbol{v} F_1(\boldsymbol{x}, \boldsymbol{v}, t), \tag{1.15}$$

where $\int d^3\boldsymbol{v} F_1(\boldsymbol{x}, \boldsymbol{v}, t) \equiv \rho(\boldsymbol{x}, t)$ is the density of the system. With this mean field hypothesis, a star's force is given by the gradient of a function, avoiding the need to know all particle positions:

$$-\frac{\partial \Phi}{\partial \boldsymbol{x}} = \int d\Gamma_2 F_1(\Gamma_2, t) \boldsymbol{\mathcal{F}}_{12}. \tag{1.16}$$

By substituting equation (1.16) into equation (1.14) we obtain an equation that, together with Poisson equation (1.15), forms the Vlasov-Poisson system for the gravitational potential Φ and the DF F of the stellar system:

$$\begin{cases} \frac{\partial F}{\partial t} + \boldsymbol{v} \cdot \frac{\partial F}{\partial \boldsymbol{x}} - \frac{\partial \Phi}{\partial \boldsymbol{x}} \cdot \frac{\partial F}{\partial \boldsymbol{v}} = 0 \\ \nabla^2 \Phi = 4\pi G \int d^3\boldsymbol{v} F \end{cases} \tag{1.17}$$

with $F = F(\boldsymbol{x}, \boldsymbol{v}, t)$, $\Phi = \Phi(\boldsymbol{x}, t)$, and we omit the index on F_1, as from now on we only consider the 1-particle 6-dimensional DF.

As a side note, taking the velocity moments of the Vlasov equation leads to the Jeans equations, that we referred to a few times in the previous section on *Gaia* results. Unlike when fully specifying the DF, Jeans' modeling only describes velocity moments and may sometimes result in an unphysical negative DF in certain parts of phase space.

1.2.3 Integrals of motion and action-angle variables

Each stellar orbit in the gravitational potential has at each time t a specific phase-space position, $\Gamma(t) = (\boldsymbol{x}(t), \boldsymbol{v}(t))$. Some functions are known to be constant along the trajectories of orbits in phase-space. For each orbit, it is known as a constant of motion, $C(\Gamma(t_1), t_1) = C(\Gamma(t_2), t_2)$ for any t_1 and t_2. A particularly important case is when the constant of motion does not explicitly depend on time. Such a function $I(\Gamma)$, which depends only on phase-space coordinates, is called an integral of motion, $I(\Gamma(t_1)) = I(\Gamma(t_2))$ for any t_1 and t_2. The integral of motion satisfies by definition:

$$\frac{dI}{dt} = \frac{\partial I}{\partial \boldsymbol{x}} \frac{\partial \boldsymbol{x}}{\partial t} + \frac{\partial I}{\partial \boldsymbol{v}} \frac{\partial \boldsymbol{v}}{\partial t} = 0. \tag{1.18}$$

Hence, we immediately see that, if the DF does not explicitly depend on time, it is itself an integral of motion, or said otherwise, depends on other integrals of the motion, which is known as Jeans' theorem. A gravitational potential can indeed have many integrals of motion, but only 5 independent ones. To check for independence, we can test each pair, such as I_1 and I_2, to see if they are in involution—meaning their Poisson brackets are zero:

$$\{I_1, I_2\} = \sum_{i=1}^{d} \frac{\partial I_1}{\partial x_i} \frac{\partial I_2}{\partial v_i} - \frac{\partial I_1}{\partial v_i} \frac{\partial I_2}{\partial x_i} = 0 \tag{1.19}$$

with $d = 3$, and $\boldsymbol{x} = (x_1, x_2, x_3)$ and $\boldsymbol{v} = (v_1, v_2, v_3)$. The maximum number of integrals of motion is $w = 2d - 1$, which effectively confines the motion to 1 dimension in phase-space.

From Noether's theorem, each symmetry of the system is associated to an integral of the motion: a time-independent gravitational potential is time-symmetric and leads to the conservation of energy (or of the Hamiltonian), while each component of angular momentum is conserved in a spherical gravitational potential. In an axisymmetric time-independent potential, like the potential of the MW to leading order (before considering perturbations from the bar and spiral arms), two obvious integrals of the motion are the energy per unit mass E and the component of the angular momentum (per unit mass too) L_z along the symmetry axis.

Independent integrals of motion help to solve the equations of motion for an orbit. For a system with w independent integrals of motion, the equations of motion are of dimension $2d-w$. When a system has $w = d$ integrals of motion, it is referred to as integrable, namely the fact that no orbits are chaotic (they are all regular). It turns out that typical axisymmetric gravitational potential for galaxies are always close to integrable, meaning that we can numerically check that most non-resonant orbits do have three independent integrals of the motion (Binney and Tremaine, 2008). These integrals are E, L_z and a third integral which is numerical, and related to the fact that typical galactic potentials are relatively close to Stäckel potentials (e.g., Famaey and Dejonghe, 2003).

In the Vlasov-Poisson equations (1.17), the evolution in time of the DF is set by the time derivative, and if the DF does not evolve in time, it satisfies $\partial F/\partial t = 0$, meaning that F represents a steady state stellar system, i.e, a system in equilibrium. For such systems, Jeans' theorem states that the equilibrium DF solution to the collisionless Boltzmann equation depends on the phase-space coordinates $F = F(\boldsymbol{x}, \boldsymbol{v})$ only through three independent integrals of motion in the given integrable potential. Said otherwise, for a galaxy at equilibrium, having most of its orbits as regular non-resonant orbits, the DF can always be written as $F = F(I_1, I_2, I_3)$.

Now, rather than using quantities with different dimensions such as energy and angular momentum, it would be even more convenient if the integrals of the motion are chosen to be phase-space coordinates themselves. Since each integral of the motion is associated to some symmetry of the system (for instance, in axisymmetry the Hamiltonian does not depend on the azimuthal angle of cylindrical coordinates), wisely choosing the phase-space coordinates should allow for the Hamiltonian to not depend on *any* of those wisely chosen "positions", meaning that the associated momenta would themselves be integrals of the motion from Hamilton's equations. These generalized momenta are known as *action* coordinates $\boldsymbol{J}$ (with the same dimension as angular momenta) and the generalized positions as (dimensionless) *angle* coordinates $\boldsymbol{\theta}$. Indeed, while positions and velocities—such as in Galactocentric cartesian coordinates—are often prac-

tical, for theoretical work, generalized phase-space coordinates $(\boldsymbol{q}, \boldsymbol{p})$ are more useful. These can include the Cartesian coordinates with positions $\boldsymbol{q} = \boldsymbol{x}$ and momenta $\boldsymbol{p} = \mu \boldsymbol{v}$, but these coordinates can be canonically transformed to any other ones as long as Hamilton's equations stay invariant under the coordinate transformation. This requires *canonical transformations*. After the transformation from positions and velocities to angles and actions, we have from Hamilton's equations:

$$\begin{cases} \dfrac{d\boldsymbol{J}}{dt} = -\dfrac{\partial H}{\partial \boldsymbol{\theta}} = 0 \\ \dfrac{d\boldsymbol{\theta}}{dt} = \dfrac{\partial H}{\partial \boldsymbol{J}} = \boldsymbol{\Omega}(\boldsymbol{J}) \end{cases} \tag{1.20}$$

where the fundamental frequencies $\boldsymbol{\Omega}$ describe how quickly the angle variables change, as $\boldsymbol{\theta} = \boldsymbol{\theta}_0 + \boldsymbol{\Omega}(\boldsymbol{J})t$, with each angle periodically defined on $[0, 2\pi]$ interval. Said otherwise, each triplet of actions fully characterizes a regular orbit, both in terms of the 3-dimensional volume of phase-space that it fills, that is an actual three-torus, and in terms of the frequencies with which stars move on that torus. Angles are simply labeling where a given star is at a given time on its torus. Each regular orbit therefore maps to a three-torus in phase-space, illustrated in Fig. 1.5. The geometry of such three-tori enables a formula for the actions:

$$J_i = \frac{1}{2\pi} \oint_{\Gamma_i} \boldsymbol{p} \cdot d\boldsymbol{q} \tag{1.21}$$

with Γ_i a path along the tori in phase-space where the angle θ_i is constant.

To get physical intuition on the meaning of the action variables, we can consider the case of quasi-circular orbits in an axisymmetric disk potential. These can be reasonably well approximated by the so-called epicyclic approximation, illustrated in Fig 1.6:

$$\begin{aligned} R(t) &= R_g + \mathrm{A} cos(\kappa \mathrm{t} + \alpha) \\ \varphi(t) &= \varphi_0 + \Omega(R_g)t - 2\frac{A\Omega(R_g)}{\kappa R_g} sin(\kappa \mathrm{t} + \alpha) \\ z(t) &= \mathrm{B} cos(\nu \mathrm{t} + \beta) \end{aligned} \tag{1.22}$$

with (R, φ, z) as the Galactic cylindrical coordinates, A, B, α, β, φ_0, as constants of each orbit, and $\mathrm{R_g}$, the guiding radius. The guiding radius is the radius of a circular orbit corresponding to the orbit angular momentum L_z, which is conserved in the axisymmetric potential. The

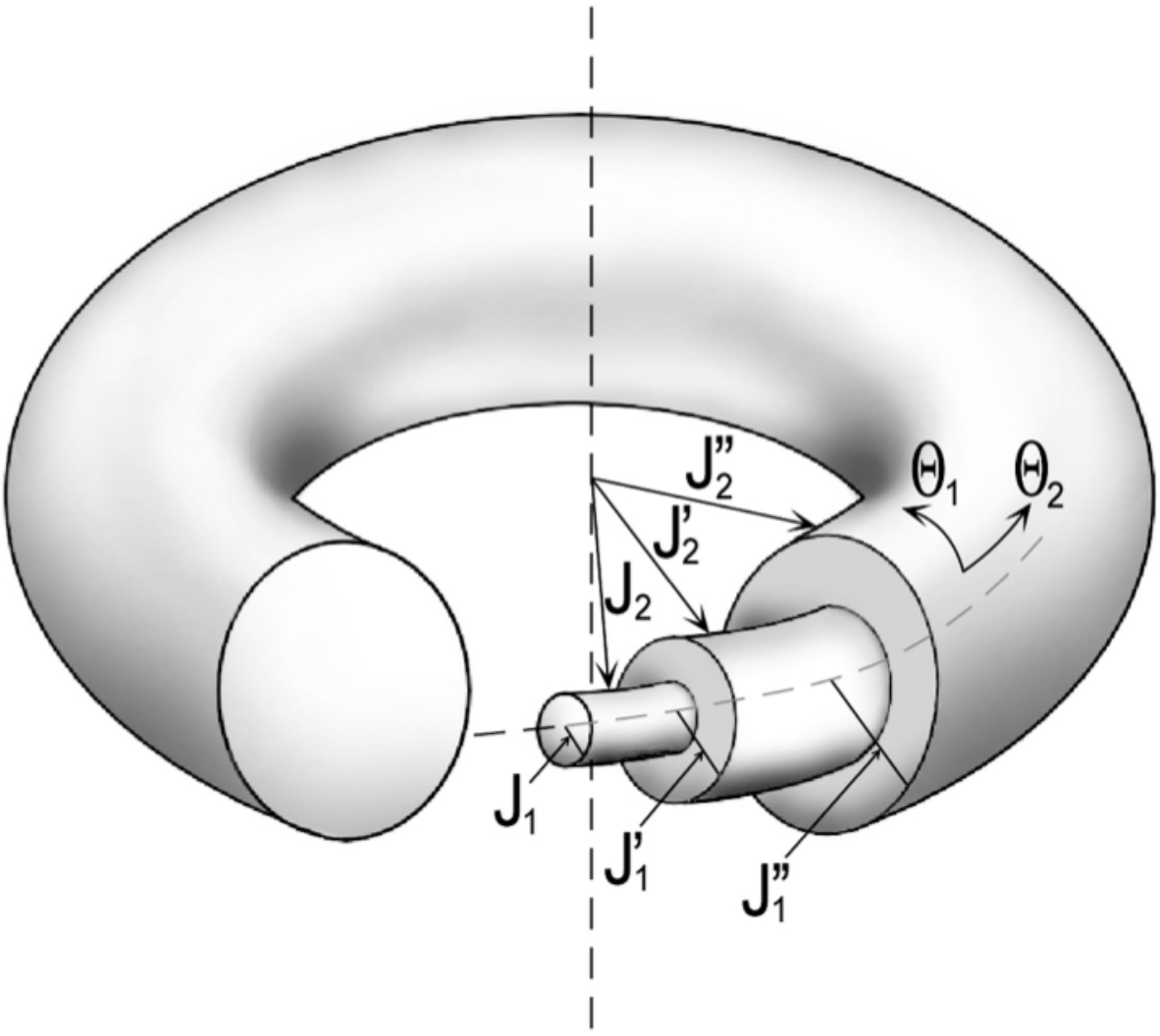

Figure 1.5: Figure extracted from (Masoliver and Ros, 2011). Illustration of a 2-dimensional orbital torus in action-angle variables within 4-dimensional phase-space (for instance, within a Galactic disk, neglecting the vertical direction). The nested torii represent different regular orbits, distinguished by their actions. The stellar trajectory lies on the torus surface and is mapped by the angles that evolve linearly in time.

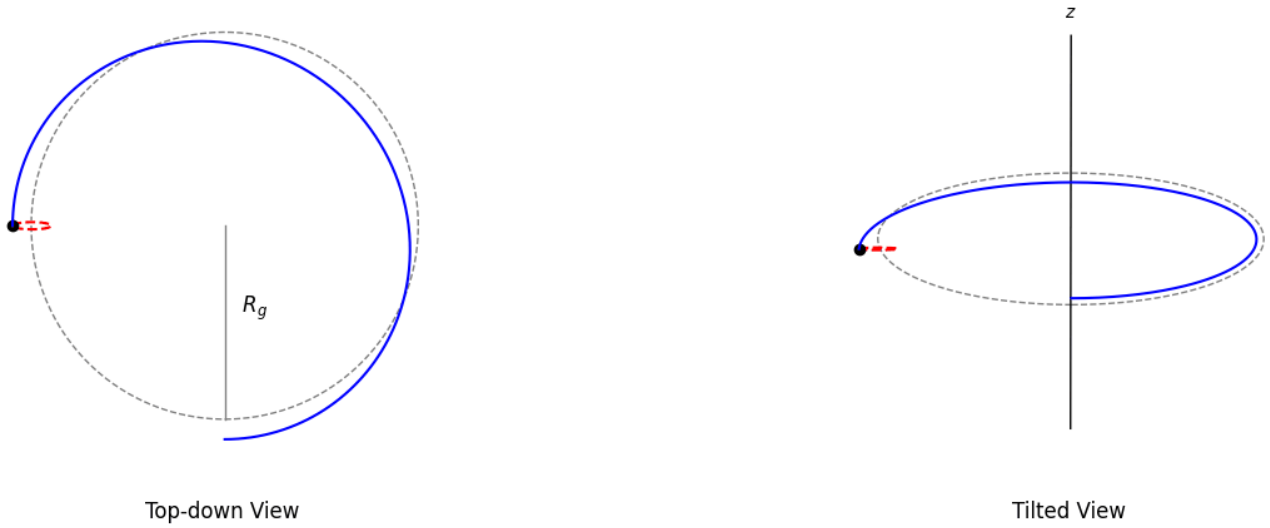

Figure 1.6: Illustration of the epicyclic approximation for orbits in an axisymmetric potential. The orbit is approximated by a retrograde motion on an ellipse, whose guiding center is in prograde motion along the guiding radius.

frequencies are evaluated at $z = 0$ and defined by:

$$\begin{aligned} \Omega^2 &= \frac{1}{R_g}\left.\frac{\partial \Phi}{\partial R}\right|_{R=R_g} \\ \kappa^2 &= \left.\frac{\partial^2 \Phi}{\partial R^2}\right|_{R=R_g,z=0} + \frac{3}{R_g}\left.\frac{\partial \Phi}{\partial R}\right|_{R=R_g} \\ \nu^2 &= \left.\frac{\partial^2 \Phi}{\partial z^2}\right|_{R=R_g}. \end{aligned} \tag{1.23}$$

Clearly, the radial and vertical motions of such small perturbations around a circular orbit are two separate harmonic oscillators, with radial energy $E_R = \frac{1}{2}\kappa^2 A^2$ and vertical energy $E_z = \frac{1}{2}\nu^2 B^2$. Within this approximation, three actions can be defined as (Binney and Tremaine, 2008)

$$\begin{aligned} J_R &= \frac{1}{2}\kappa(R_g)A^2 = \frac{E_R}{\kappa} \\ J_\varphi &= \Omega(R_g)R_g^2 = L_z \\ J_z &= \frac{1}{2}\nu(R_g)B^2 = \frac{E_z}{\nu}, \end{aligned} \tag{1.24}$$

which shows how the azimuthal action is just the vertical component of the angular momentum, while the radial and vertical actions are directly related to the radial and vertical energies of the stars.

Now to conclude the discussion on the action-angle formalism so far, it is essential to mention

the analytical action-angle solution for the integrable Stäckel potentials (see, e.g., Famaey and Dejonghe, 2003). The axisymmetric Stäckel potentials are expressed in a spheroidal coordinate system, which is defined at any given position by a focal distance Δ_2 (a geometric parameter describing the shape of the ellipsoids):

$$\Delta_2 = z^2 - R^2 + 3\left[3z\frac{\partial\Phi}{\partial R} - 3R\frac{\partial\Phi}{\partial_z} + Rz\left(\frac{\partial^2\Phi}{\partial R^2} - \frac{\partial^2\Phi}{\partial z^2}\right)\right]\left(\frac{\partial^2\Phi}{\partial R\partial z}\right)^{-1} \tag{1.25}$$

One can then use the actual Galactic potential at any given position, instead of the Stäckel potential, to compute an equivalent focal distance as if the potential were locally of Stäckel form. This focal distance enables calculation of the (quasi-)integrals of motion and corresponding actions in the true potential. This approach is known as the "Stäckel fudge" (Binney, 2012; Sanders and Binney, 2016) and gives an approximation for transforming stellar positions and velocities into actions in the Galactic potential. A fast and accurate computation for Δ_2 is fully implemented in the Action-based Galaxy Modeling Architecture library (Vasiliev, 2018; Vasiliev, 2019, `AGAMA`), which is used for evaluating the action-angle variables in the present thesis. Action variables are especially suitable as arguments of equilibrium DFs because volume is conserved under coordinate transformation. Since every triplet of actions simply labels a given regular orbit in the Galaxy, devising an equilibrium DF that depends on actions corresponds to filling the whole phase space with regular orbits, each with their own weight corresponding to the value of the DF. Our focus will now shift to DFs based on actions for constructing axisymmetric MW models.

1.2.4 Equilibrium axisymmetric distribution functions

The MW is not strictly integrable in principle, but a large portion of phase space is filled by regular orbits. We can therefore apply the framework described so far to model the MW's stellar populations with action-based DFs, making use of the Stäckel fudge. Indeed, as we have seen above, from Jeans theorem, for a galaxy at equilibrium, the DF can always be written as $F = F(\mathbf{J})$.

While the stellar DF parameters can, in principle, be constrained from direct astrometric observations, the DF for the DM component cannot be constrained in this way, since there is no direct tracer for the putative dark matter particles. Within the context of the Vlasov-Poisson equations, the DF and gravitational potential solutions for all components are coupled. Therefore, a good knowledge of the stellar DF and of the total gravitational potential can

allow, with some underlying symmetry and/or isotropy assumptions, to constrain the DF of the DM halo. Relevant axisymmetric self-consistent models for the MW using *Gaia* data were, for instance, presented in Binney and Vasiliev (2023) and Binney and Vasiliev (2024).

In general such self-consistent axisymmetric models are built iteratively from inversion methods, such as the isotropic Eddington formula (see, e.g Lacroix et al., 2018; Lacroix et al., 2020), where spherical symmetry and an isotropic velocity field are assumed, hence with a DF that depends only on the relative energy. An extension to isotropic Eddington inversion is the axisymmetric inversion method, tested in cosmological simulations of spiral galaxies (Petač et al., 2021), which assumes axisymmetry and allows for anisotropic velocity structures.

In this thesis, the initial focus will be on the stellar Galactic disk and constraining its non-axisymmetric structures (bar and spiral arms). No specific DF will be implemented for the DM halo. However, this PhD thesis is only a first step towards building a full non-axisymmetric self-consistent model of the MW, hence the non-axisymmetric potential developed hereafter could later be used to develop a more holistic dynamical model of the Galaxy, ideally fully self-consistent, including both stellar and DM components. This model could potentially be applied in investigating astrophysical predictions for direct and indirect DM searches and Galactic structures and substructures investigations (Lavalle and Magni, 2015; Stref et al., 2019). Finally, having a reference non-axisymmetric potential for the MW could perhaps help in investigating further possible hypothetical DM non-axisymmetric structures, as a shadow bar (Petersen et al., 2016) and DM spiral arms (Bernet et al., 2025).

Since our modeling approach hereafter will focus solely on the stellar disk, it is important to choose an adequate equilibrium DF for the tracer stellar populations within the disk. The quasi-isothermal disk DF is a suitable choice. Notably, to allow for a simple and tractable form of the DF by a simple linear combination for the thin and thick disks:

$$F_{\rm disk}(J_R, J_\varphi, J_z) = (1-\chi)F_{\rm thin} + \chi F_{\rm thick} \tag{1.26}$$

with a small value of χ. The quasi-isothermal disk DF has the particularity of depending exponentially on radial action J_r and vertical action J_z. It is given (Binney, 2010; Binney and McMillan, 2011) by

$$F_{\rm thick/thin} = \eta \frac{\Omega(J_\varphi)\nu(J_\varphi)}{\kappa(J_\varphi)\tilde{\sigma}_R^2(J_\varphi)\tilde{\sigma}_z^2(J_\varphi)} \exp\left(-\frac{R_{\rm g}(J_\varphi)}{h_R}\right) \exp\left(-\frac{J_R\kappa(J_\varphi)}{\tilde{\sigma}_R^2(J_\varphi)}\right) \exp\left(-\frac{J_z\nu(J_\varphi)}{\tilde{\sigma}_z^2(J_\varphi)}\right), \tag{1.27}$$

where

$$\tilde{\sigma}_R(R_{\rm g}(J_\varphi)) = \tilde{\sigma}_R(R_0)\exp\left(-\frac{R_{\rm g}(J_\phi)-R_0}{h_{\sigma,R}}\right) \qquad \tilde{\sigma}_z(R_{\rm g}(J_\varphi)) = \tilde{\sigma}_z(R_0)\exp\left(-\frac{R_{\rm g}(J_\phi)-R_0}{h_{\sigma,z}}\right), \tag{1.28}$$

with the same variables as defined in the epicyclic approximation, but evaluated more generically with the Stäckel fudge. Beyond the frequencies that are directly defined by the axisymmetric background potential (including the potential of the DM halo), it has some other parameters, such as R_0, the Sun's Galactocentric radius, h_R, the disk population scale length, η, the normalization factor (in units of surface density, or number of stars per length squared, such that the DF has the units of a phase-space density) of the tracer population, and finally all parameters defining the evolution of the radial and vertical velocity dispersion as a function of the guiding radius, $\tilde{\sigma}_R(R_{\rm g}(J_\varphi))$ and $\tilde{\sigma}_z(R_{\rm g}(J_\varphi))$.

1.2.5 Instabilities and the growth of non-axisymmetric structures

As we have seen, from Jeans theorem, a DF written as $F = F(\mathbf{J})$ for an axisymmetric galaxy describes a time-independent equilibrium, and is automatically a solution of the Vlasov equation. However, there is absolutely no guarantee that such an axisymmetric equilibrium is stable. Moreover, we know that the real MW disk does display prominent non-axisymmetric structures, such as the bar and the spiral arms. Understanding what drives these perturbations of the axisymmetric equilibrium remains today an area of active research.

The past history of the MW seems to have been relatively calm. The largest external perturbation was probably the GSE merger, which occurred approximately 8 Gyr ago. Only now are we starting to have a new similar major interaction with the LMC. Smaller perturbations still happen, with an ongoing example being the Sagittarius dwarf interaction, which is definitely a source of vertical perturbations of the MW disk, although probably not the only one. But, in any case, even in the absence of such external perturbations, if the axisymmetric equilibrium is unstable, even the tiniest internal kick, related to local perturbations (formation of star clusters, etc.) can destabilize the axisymmetric equilibrium. Broadly speaking, if the equilbrium is stable, the system will wobble but reach a final state with properties similar to its initial state, while if unstable, it can respond by developing new features, like the bar and spiral arms, that ultimately profoundly alter the system and its secular evolution (through heating, radial mixing, etc.).

The Vlasov-Poisson system of equations can actually be used to study the linear response

of an equilibrium system described by an equibilibrium DF, $F(\mathbf{J})$, to a small perturbation potential ψ^e. The response DF will be a small additive perturbation, $f(\boldsymbol{\theta}, \mathbf{J})$, which itself leads to a small potential perturbation ψ^s. This can be used in (1.17), with action-angle coordinates, to linearize the collisionless Boltzmann equation (see, e.g., Rozier et al., 2022; Hamilton and Fouvry, 2024; Famaey, 2024)

$$\begin{gathered} \frac{\partial f}{\partial t} + \boldsymbol{\Omega}(\boldsymbol{J}) \cdot \frac{\partial f}{\partial \boldsymbol{\theta}} - \frac{\partial(\psi_e + \psi_s)}{\partial \boldsymbol{\theta}} \cdot \frac{\partial F}{\partial \boldsymbol{J}} = 0 \\ \nabla^2 \psi^s = 4\pi G \int d^3\boldsymbol{v} f. \end{gathered} \tag{1.29}$$

Since any function of the angles is 2π-periodic, we can expand both the perturbing potential $\psi = \psi_e + \psi_s$ and the perturbed DF, f, as Fourier series on the angles $\boldsymbol{\theta}$:

$$\psi(\boldsymbol{\theta}, \mathbf{J}, t) = \sum_{\mathbf{n}} \psi_{\mathbf{n}}(\mathbf{J}, t)\, e^{i\mathbf{n}\cdot\boldsymbol{\theta}}, \quad f(\boldsymbol{\theta}, \mathbf{J}, t) = \sum_{\mathbf{n}} f_{\mathbf{n}}(\mathbf{J}, t)\, e^{i\mathbf{n}\cdot\boldsymbol{\theta}} \tag{1.30}$$

The equation (1.29) can then be separated into equations for each Fourier coefficient of the series, as

$$\frac{\partial f_{\mathbf{n}}}{\partial t} + \mathrm{i}\, \mathbf{n} \cdot \boldsymbol{\Omega}\, f_{\mathbf{n}} - \mathrm{i}\, \mathbf{n} \cdot \frac{\partial F}{\partial \mathbf{J}}\, \psi_{\mathbf{n}} = 0. \tag{1.31}$$

One can now Fourier transform this equation in time, going from time t to complex frequency ω, as

$$\hat{f}_{\mathbf{n}}(\mathbf{J}, \omega) = \frac{\mathbf{n} \cdot \partial F / \partial \mathbf{J}}{\mathbf{n} \cdot \boldsymbol{\Omega} - \omega}\, \hat{\psi}_{\mathbf{n}}(\mathbf{J}, \omega) \tag{1.32}$$

where the hat denotes the temporal Fourier transform. From this form of the $\mathbf{n}$-th Fourier coefficient of the response DF, it is already clear that the values are going to explode for certain orbits that have $\mathbf{n} \cdot \boldsymbol{\Omega} - \omega = 0$, called resonances.

So far, this description focused on the linearized collisionless Boltzmann equation in (1.29). The Poisson equation in (1.29), on the other hand, relates the DF perturbation f to the potential perturbation ψ^s. To avoid having to go back and forth between cartesian coordinates, where the Poisson equation is best treated, and the angle-action pahse-space coordinates, it is best to decompose the problem into potential-density pairs that are known in advance, as in Kalnajs' matrix method (Kalnajs, 1977). In this method, densities and potentials are projected on a bi-orthogonal basis of functions, formed of potentials, $\psi^{(p)}$ and densities $\rho^{(p)}$ that are pairs of solutions to the Poisson equation and obey a bi-orthogonality condition:

$$\nabla^2 \psi^{(p)} = 4\pi G \rho^{(p)} \qquad \int d\mathbf{x}\, \psi^{(p)}(\mathbf{x}) \rho^{(q)*}(\mathbf{x}) = -\delta^q_p, \tag{1.33}$$

where δ_p^q is the Kronecker delta. Using these functions, we can write the perturbing potential in vector form in the basis, namely

$$\psi^s(\mathbf{x},t) = \sum_p a_p(t)\psi^{(p)}(\mathbf{x}) \quad \psi^e(\mathbf{x},t) = \sum_p b_p(t)\psi^{(p)}(\mathbf{x}), \tag{1.34}$$

which we can simply summarize as two vectors $\mathbf{a}$ for the self-consistent response potential and $\mathbf{b}$ for the initial perturbation. Making use of the bi-orthogonality condition, we can obtain the vector decomposition of the self-gravitating response by simply taking the inner product of the perturbed density and each of the basis elements, $a_{\mathbf{p}}(t) = -\int \mathrm{d}\mathbf{x} \int \mathrm{d}\mathbf{v}\, f(\mathbf{x},\mathbf{v},t)\, \psi^{(\mathbf{p})*}(\mathbf{x})$, which can be canonically transformed into an integral over actions and angles after making use of the Fourier series of equation (1.30):

$$a_p(t) = -(2\pi)^3 \sum_{\mathbf{n}} \int \mathrm{d}\mathbf{J}\, f_{\mathbf{n}}(\mathbf{J},t)\, \psi_{\mathbf{n}}^{(p)*}(\mathbf{J}). \tag{1.35}$$

Fourier transforming this, and making use of equation (1.32), we have:

$$\hat{a}_p(\omega) = \sum_q \underbrace{\left\{ (2\pi)^3 \sum_{\mathbf{n}} \int \mathrm{d}\mathbf{J}\, \frac{\mathbf{n}\cdot\partial F/\partial \mathbf{J}}{\omega - \mathbf{n}\cdot\mathbf{\Omega}}\, \psi_{\mathbf{n}}^{(p)*}(\mathbf{J})\, \psi_{\mathbf{n}}^{(q)}(\mathbf{J}) \right\}}_{\hat{M}_{pq}} \Big(\hat{a}_q(\omega) + \hat{b}_q(\omega) \Big). \tag{1.36}$$

which can be understood as the application of a response matrix $\hat{M}_{pq}(\omega)$, corresponding to the first bracket hereinabove, on the vector of the total perturbation $\mathbf{a} + \mathbf{b}$:

$$\hat{\mathbf{a}} = \hat{\mathbf{M}} \cdot (\hat{\mathbf{a}} + \hat{\mathbf{b}}) \tag{1.37}$$

which can be further written as

$$\hat{\mathbf{a}} = \Big([\mathbf{I} - \hat{\mathbf{M}}]^{-1} - \mathbf{I} \Big) \cdot \hat{\mathbf{b}}. \tag{1.38}$$

From there, the temporal evolution of the response vector $\mathbf{a}(t)$ can be obtained from the reverse Fourier transform

$$\mathbf{a}(t) = \frac{1}{2\pi} \int_{-\infty}^{+\infty} d\omega\, ([\mathbf{I} - \hat{\mathbf{M}}]^{-1} - \mathbf{I}) \cdot \hat{\mathbf{b}}(\omega) e^{-i\omega t} = -i \sum_k \mathbf{a}_k e^{-i\omega_k t}, \tag{1.39}$$

making use of the residue theorem, where the label k is labeling each pole of the integrand in the upper half of the complex plane, and $\mathbf{a}_k$ is the residue of the integrand at the complex pole

$\omega = \omega_k$. The poles correspond to where $[\mathbf{I} - \hat{\mathbf{M}}]^{-1}$ is singular, hence where

$$\det(\mathbf{I} - \hat{\mathbf{M}}(\omega)) = 0, \tag{1.40}$$

namely all the frequencies ω_k such that $\hat{\mathbf{M}}(\omega)$ has an eigenvalue of 1, with the residue vector $\mathbf{a}_k$ being simply proportional to the corresponding eigenvector. This residue vector $\mathbf{a}_k$ is then defining the shape of the instability mode (a bar, a spiral arm, etc.), while the real part of the pole defines the pattern speed or oscillation frequency $\mathrm{Re}(\omega_\mathrm{k}) = \omega_\mathrm{p,k}$ and its imaginary part defines the growth rate. We do have an unstable mode that grows to form a bar or a spiral arms, or any other instability, when $\mathrm{Im}(\omega_k) > 0$. The fastest evolution will be associated with the largest value of $\mathrm{Im}(\omega_k)$.

This matrix method provides an insightful and efficient framework for identifying global instabilities and their growth rates only in the regimes of small perturbations. After forming, for example, a bar or spiral arms, the final distribution could still not be predicted by this method, especially because of the non-linear evolution of the DF driven by the resonances. It was already clear from the equations above for the response matrix that resonances are crucial features for the instability modes to appear, but they are also the main drivers of the evolution of the system.

An orbit labelled by actions $\mathbf{J}$ in a given axisymmetric background potential is said to be resonant with a perturbation mode of oscillation frequency ω_p if $\mathbf{n} \cdot \boldsymbol{\Omega}(\mathbf{J}) - \omega_p = 0$. Let us now consider a bi-symmetric perturbation, such as a bar, that has developed within the Galactic plane with oscillation frequency $\omega_p = 2\Omega_p$ (where Ω_p is the true pattern speed, taking into account the bisymmetry of the perturbation), and let us consider only in-plane motions. Considering the Fourier mode $\mathbf{n} = (l, m)$ with $m = 2$, the resonant condition becomes

$$l\Omega_R + m(\Omega_\varphi - \Omega_p) = 0. \tag{1.41}$$

The most notable resonances are the co-rotation (CR) for $l = 0$, where stars move at the same angular speed as the rotating potential, the Outer Lindblad Resonance (OLR) for $l = 1$, where stars' orbital motion lags behind the rotating potential $[(\Omega_\varphi - \Omega_p) < 0]$, and the Inner Lindblad Resonance (ILR) for $l = -1$, where stars move ahead of the rotating potential $[(\Omega_\varphi - \Omega_p) > 0]$. If enough stars with orbits in resonance are observed, they may exhibit distinct features in the data, making resonances a very insightful tool for studying Galactic structure and dynamics. In particular, stars trapped in resonance can exchange angular momentum with the spiral or bar

pattern. This process produces specific orbital configurations and also fuels the redistribution of mass and angular momentum across the disk.

We have been working in the action-angle variables of the unperturbed axisymmetric system, but such variables cannot, in principle, be used in resonant zones. Indeed, if the resonance remains present for a very long time, the response grows towards infinity in the linear response of the original action-angle coordinates (e.g. Monari et al., 2016a; Al Kazwini et al., 2022). Therefore modeling the resonances with action-angle variables actually requires quite a sophisticated treatment, as shown in, e.g., Monari et al. (2017a), Laporte et al. (2020), Binney (2020), and Hamilton et al. (2023). For a bar in the Galactic disk, Monari et al. (2017a) for instance introduced an approach to model orbits in a given resonant zone and construct a DF, F_b, perturbing an initial equilibrium disk DF, F. The idea is to perform two canonical transformations in a row, in order to find the relevant action-angle variables to use in the resonant region, and then to simply populate the new tori by phase-averaging the original unperturbed DF over the new resonant tori. The first canonical transformation is going from actions (J_R, J_φ) and angles $(\theta_R, \theta_\varphi)$ to the "slow" and "fast" variables:

$$\theta_s = l\theta_R + m(\theta_\varphi - \Omega_p t) \qquad J_\varphi = mJ_s \tag{1.42}$$

$$\theta_f = \theta_R \qquad J_R = lJ_s + J_f \tag{1.43}$$

with Ω_p the pattern speed of the bar, (J_s, θ_s) and (J_f, θ_f), respectively the slow and fast action-angles. Then, after averaging over the fast motion, the Hamiltonian near the resonances is equivalent to that of a pendulum. In this analogy, the slow action acts like the pendulum's angular momentum. The slow angle represents then the pendulum's position. The pendulum energy defines whether the motion is resonant. It can be similar to a pendulum that swings back and forth (librating, trapped around a fixed point). Alternatively, it can be non-resonant, such as a pendulum that rotates freely (in circulating orbits). The second canonical transformation then makes use of the actual action-angle variables of a pendulum. Once writing the original equilibrium DF in the new action-angle variables, there is a dependency on the pendulum angles, which we can average over to get the new equilibrium DF in the resonant zone. This approach has given some excellent qualitative insights in understanding the nature of the Hercules moving group (e.g., Monari et al., 2019a; Monari et al., 2019b; Laporte et al., 2020) and, far away from the main resonances of another perturber, it could in principle be generalized to include spiral arm modes through linear perturbation on top of this. However, with this method,

each resonant zone needs the computation of its own action-angle variables, and this becomes impossible when resonances of multiple modes do overlap. Such overlapping resonances regions would trigger a chaotic behavior in stellar orbits, increasing the number of chaotic orbits. As a result, modeling the system in a unified manner for the entire phase-space becomes even more challenging.

1.2.6 Backward integration modeling

The lack of an analytical DF to model the response to bar and spiral arm modes of different pattern speeds makes it hard to use *Gaia* data to fit a non-axisymmetric gravitational potential for the MW disk. In contrast, for axisymmetric DFs and potentials, this fitting can be done self-consistently, as in Binney and Vasiliev (2023). To address the challenge in the non-axisymmetric case, backward integration modeling (Vauterin and Dejonghe, 1997) will help us circumvent this issue. This approach is effective because DF values are conserved along orbits. This is a crucial property encoded in the Vlasov equation. Indeed, this conservation property makes the backward integration modeling possible. The key idea behind the method is to numerically characterize the non-axisymmetric DF at each point in phase space by integrating an orbit backward in time from each point. By doing so, we trace the MW's evolution in reverse. We integrate back to a time before the bar and spiral arms formed. At that earlier time, the Galaxy could be modeled as an equilibrium axisymmetric system with a known analytical DF. We then evaluate this DF to recover the value at the current time. Before explaining how this method predicts observables for *Gaia* data, let us first recall some important features encoded in the Vlasov equation (1.17). These features are important for justifying the method and are useful for understanding its application and limitations.

Let us start with the remarkable property of the conservation of DF along the orbits. In the current context of mean-field hypothesis and collisionless system, any point $(\boldsymbol{x}_0, \boldsymbol{v}_0)$ in phase-space, has a unique orbit passing by it, $\Gamma(t) = (\boldsymbol{x}(t), \boldsymbol{v}(t))$, with $\Gamma(t_0) = (\boldsymbol{x}_0, \boldsymbol{v}_0)$ for an initial time t_0. For each point in phase-space, the DF along the associated orbit is given at time t by $F(\boldsymbol{x}(t), \boldsymbol{y}(t), t)$. The first key feature encoded in the Vlasov equation is that the DF

is conserved along orbits. Indeed:

$$\begin{aligned}\frac{d}{dt}F(\boldsymbol{x}(t),\boldsymbol{v}(t),t) &= \frac{\partial F}{\partial t}+\frac{d\boldsymbol{x}}{dt}\cdot\frac{\partial F}{\partial \boldsymbol{x}}+\frac{d\boldsymbol{v}}{dt}\cdot\frac{\partial F}{\partial \boldsymbol{v}}\\ &= \frac{\partial F}{\partial t}+\boldsymbol{v}\cdot\frac{\partial F}{\partial \boldsymbol{x}}-\frac{\partial \Phi}{\partial \boldsymbol{x}}\cdot\frac{\partial F}{\partial \boldsymbol{v}}\\ &= 0\end{aligned} \tag{1.44}$$

The second key feature of the method is actually inherited from Hamiltonian dynamics itself. It is the reversibility in time of the Vlasov equation. This means that the DF evolution is reversible in time. We can evolve it one way or the other, equivalently. In the case of the MW, we can model the DF as if it had evolved from an initial equilibrium, axisymmetric scenario in the past, making the bar and spiral arms evolve slowly, or we can do it the other way around. In practice, for each orbit, it means that if the DF F is a solution of Vlasov equations, then the DF $\tilde{F}$ defined by $\tilde{F}(\boldsymbol{x}(t),\boldsymbol{v}(t),t) = F(\boldsymbol{x}(-t),-\boldsymbol{v}(-t),-t)$ is also a solution.

The third feature encoded in the Vlasov equation is the conservation of phase-space volume during the evolution of a collisionless system. To understand it, we start from the Hamiltonian flow, $\mathcal{F}_t$, that maps each initial point in phase-space to its position on the space-space at time t. We can write it as:

$$\mathcal{F}_t : (\boldsymbol{x}_0,\boldsymbol{v}_0) \mapsto \Gamma(t) = (\boldsymbol{x}(t),\boldsymbol{v}(t)) \tag{1.45}$$

with $\Gamma(t)$, the orbit that has $(\boldsymbol{x}_0,\boldsymbol{v}_0)$ as initial condition. The Hamiltonian flow is differentiable. It is also invertible, from the discussed time-reversibility, and bijective, as mentioned, orbits are unique, and also the entire phase-space is mappable. Now, we can consider an arbitrary volume in phase-space, $\mathcal{V}_0$. Each point in $\mathcal{V}_0$ can be seen as an initial condition that can be mapped, at each time t, by the Hamiltonian flow $\mathcal{F}_t$. We may follow the time evolution of this volume by following the orbits of each point in $\mathcal{V}_0$ with the Hamiltonian flow. At each time t, the volume is then $\mathcal{V}_t = \mathcal{F}_t(V_0)$. The phase-space volume is conserved:

$$\int_{V_t} d\boldsymbol{p}d\boldsymbol{q} = \int_{V_0} d\boldsymbol{p}d\boldsymbol{q}, \quad \text{for any } t \tag{1.46}$$

which is equivalent to stating that the Jacobian of the Hamiltonian flow in phase-space is unitary. The volume $\mathcal{V}_0$ can undergo shape deformation during the system's evolution, particularly to form very fine-scale structures, such as filaments. However, its volume will be conserved. It also means that the probability is conserved in these volumes, which ultimately implies that the total number of particles is also conserved. However, as we discuss briefly below, this does

not prevent some practical problems when dealing with real data. This feature of phase-space volume conservation is related to the volume conservation of canonical transformations. Indeed, let $\mathcal{J}$ be the Jacobian of the transformation between $(\boldsymbol{J}, \boldsymbol{\theta})$ and $(\boldsymbol{x}, \boldsymbol{v})$. Since $\det\mathcal{J} = 1$ for canonical variables (Binney and Tremaine, 2008), the transformation between a DF in $(\boldsymbol{J}, \boldsymbol{\theta})$, $F(\boldsymbol{J}, \boldsymbol{\theta})$, and the corresponding distribution in $(\boldsymbol{x}, \boldsymbol{v})$, $F'(\boldsymbol{x}, \boldsymbol{v})$, can be explicitly written as follows:

$$\begin{aligned} F'(\boldsymbol{x}, \boldsymbol{v}) d\boldsymbol{x} d\boldsymbol{v} &= F(\boldsymbol{J}(\boldsymbol{x}, \boldsymbol{v}), \boldsymbol{\theta}(\boldsymbol{x}, \boldsymbol{v})) d\boldsymbol{J} d\boldsymbol{\theta} \\ &= F(\boldsymbol{J}(\boldsymbol{x}, \boldsymbol{v}), \boldsymbol{\theta}(\boldsymbol{x}, \boldsymbol{v})) d\boldsymbol{x} d\boldsymbol{v} \ |\det\mathcal{J}| \end{aligned} \tag{1.47}$$

which basically means that F' is just F with $\boldsymbol{J}$ and $\boldsymbol{\theta}$ written as functions of $\boldsymbol{x}$ and $\boldsymbol{v}$.

This backward integration method thus allows us, in principle, to give ourselves an equilibrium axisymmetric DF, $F(\mathbf{J})$ at some time in the past before the non-axisymmetric modes have grown, and compute the present-day non-axisymmetric DF in the presence of such modes. There are however a few drawbacks with this method. The first and most obvious one is that the method, at least in the form that we will use in this PhD work, is not self-consistent. Moreover, the observed stellar DF is always measured over finite phase-space volumes, so it is in fact the so-called *coarse-grained* DF. Over time, phase-space elements of high density are stretched out into infinitesimally thin ridges that get mixed with phase-space elements of lower density, so that the "practical" coarse-grained DF does not obey Vlasov. Furthermore, the Nyquist-Shannon sampling theorem imposes limits on the minimum size of thin structures in phase space that can form for a fixed number of particles over time, and this limit is reached on rather short time scales (Beraldo e Silva et al., 2019). Once this limit is reached, the physical system with a finite number of particles cannot form thinner structures, despite the collisionless Boltzmann equation predicting that these structures should form. In practice, this means that, if our backward integration is carried out for too long, the DF tracked by our method will lead to sharp and unsmoothed features in velocity space, where chaotic features will also appear as sharper than in the real world. To circumvent this problem, the integration will have to be carried out only for a relatively limited time, adjusted so that the sharpness of resonant features in velocity space resembles what is observed.

Keeping this in mind, we will use the backward integration modeling to fit a realistic non-axisymmetric potential for the MW disk, including a multi-modal bar and spiral arms of distinct pattern speeds. In the next section, we provide the final introductory details on how the method is applied in order to model the MW. Starting from the axisymmetric components, followed

by the bar, and on the spiral arms. The literature on the axisymmetric gravitational potential is fairly well explored. The weight of the challenge remains on the bar and spiral arms, which are non-axisymmetric structures. We briefly revisit some important insights from the extensive and lively investigations into non-axisymmetric structures, relying on observations, theory, and numerical simulations. These will prove helpful in establishing the fitting procedure and analyzing the results.

1.3 Modeling the Milky Way and its non-axisymmetries

We are now in a position to start our modeling of the MW disk. Our main goal will be to produce the first-ever full direct parametric fit to both the local velocity distribution (see Fig. 1.3) and to the map of the radial velocity field within the Galactic plane (see Fig. 1.4), as measured with the latest data from *Gaia* DR3. Such a parametric non-axisymmetric potential will be a valuable asset for the community. To build our non-axisymmetric model, described in Chapter 2, we must start from an axisymmetric one, and subsequently add a bar and spiral arms as perturbations, defined by several parameters. Within the then steady-state, axisymmetric potential, we use the equilibrium phase-space DF of Eq. (1.27) to describe our tracer population. However, we will make use of a 2D projected version of the DF. To compute the DF $F(\boldsymbol{x}, \boldsymbol{v}, t)$, at current time, at position $(\boldsymbol{x}, \boldsymbol{v})$ of phase-space, we will first backward integrate the orbit whose initial condition is $(\boldsymbol{x}, \boldsymbol{v})$ back to a time t' before the formation of bar and spiral arms. Then, we will compute the DF value when there was no non-axisymmetric structure, and we will be left with only the axisymmetric components of the model, for which we know the DF. Since the DF is conserved along the orbit, by computing it at the time before the formation of the bar and spiral arms, we will obtain the current value for the DF. In practice, assuming that the tracer population is represented by the equilibrium DF, $F(\boldsymbol{J})$, in the axisymmetric background potential at time t', we transform $(\boldsymbol{x}', \boldsymbol{v}')$ to action-angle variables using the "Stäckel Fudge" method coded in `AGAMA`, compute the value of the DF. In fact, the phase-space volume conservation properties of the Vlasov equation and of canonical transformations, allow us to attribute the same value of the DF to the phase-space position $(\boldsymbol{x}, \boldsymbol{v})$ at present time $t = 0$ in the presence of the bar and spirals. In the fitting process, each set of parameters for the gravitational potential will lead to a specific prediction on stellar densities and velocity distributions that can be compared to

Gaia DR3 data. In principle, the observables are obtained from knowing the DF continuously:

$$\begin{aligned}\rho(\boldsymbol{x},t) &= \int F(\boldsymbol{x},\boldsymbol{v},t)d^3\boldsymbol{v} \\ \overline{\boldsymbol{v}}(\boldsymbol{x},t) &= \rho^{-1}(\boldsymbol{x},t)\int \boldsymbol{v}F(\boldsymbol{x},\boldsymbol{v},t)d^3\boldsymbol{v}\end{aligned} \tag{1.48}$$

In practice, however, we need to coarse-grain the DF to compare its observables to binned data. Therefore, we evaluate the DF on grid points. We assume that it is the average value for the cell phase-space volume centered in the grid $\boldsymbol{x}_i$. So we can write for the model as well at each cell position:

$$\begin{aligned}\rho(\boldsymbol{x}_i,t=0) &= \sum_{j=1}^{N_x}\sum_{k=1}^{N_y}\sum_{\ell=1}^{N_z} F\left(\boldsymbol{J}\left(\mathcal{F}_{t'}(\boldsymbol{x}_i,\boldsymbol{v}_{j,k,\ell})\right)\right)\,\Delta v_x\,\Delta v_y\,\Delta v_z \\ \overline{\boldsymbol{v}}(\boldsymbol{x},t=0) = \rho(\boldsymbol{x}_i,t=0)^{-1} &\sum_{j=1}^{N_x}\sum_{k=1}^{N_y}\sum_{\ell=1}^{N_z} \boldsymbol{v}_{j,k,\ell}F\left(\boldsymbol{J}\left(\mathcal{F}_{t'}(\boldsymbol{x},v_{r,j},v_{\phi,k},v_{z,\ell})\right)\right)\,\Delta v_x\,\Delta v_y\,\Delta v_z.\end{aligned} \tag{1.49}$$

As mentioned hereinabove, this poses a few practical problems, but these are not too severe as long as the integration time does not become too long.

Our model predictions can be directly compared to data, both qualitatively and quantitatively. This comparison can be carried out by evaluating how the observed phase-space distribution from *Gaia* matches the model prediction on different projection planes, such as at the velocity distribution in the Solar neighborhood or at different positions across the disk, or the median radial velocity as a function of position. These comparisons form the basis for establishing the fitting procedure to assess data and models. Furthermore, we can compute the distribution of axisymmetric actions using the same approach.

As a final introductory material before delving into our work, we will now review some rather technical details on the properties of the MW bar and spiral arms. This information will prove to be very helpful as a foundation for the underlying hypotheses in our work, for tailoring the fitting procedure, and for the subsequent analysis, which will be explained in detail in Chapter 2.

The Galactic bar

Strikingly, about two-thirds of spiral galaxies in the local Universe are barred (Sheth et al., 2008; Euclid Collaboration et al., 2025). Bars are often associated with spiral arms and with nuclear, inner, outer, or pseudo rings, they are quite often elongated, but do not extend across the whole galaxy. Early-type galaxies tend to have strong bars with nearly constant surface

brightness along their major axis. Late-type galaxies typically exhibit slightly shorter, weaker bars, with brightness profiles that are closer to the exponential profile observed in the disk. In barred galaxies, boxy-peanut-shaped bulges are seen as the inner, vertically thickened regions of the bar. This links the typically observed bulge structure of most disk galaxies directly to the dynamics of the bar. It is important to mention that the physics regulating bar formation and evolution remains poorly understood from the perspective of numerical simulations in a cosmological context. Such simulations indeed struggle to produce large enough bars for a given pattern speed, or even to produce bars at all, a problem, shared by literally all simulations in a cosmological context that have a spatial resolution below 100 pc (e.g., Reddish et al., 2022).

In our own Galaxy, the existence of the MW bar was originally hypothesized from the observations of gas kinematics (de Vaucouleurs, 1964; Peters, 1975; Gerhard and Vietri, 1986; Binney et al., 1991) and confirmed from (near-)infrared observations (e.g., Blitz and Spergel, 1991; Sellwood, 1993; Weiland et al., 1994; Binney et al., 1997) as well as bulge stellar kinematics (e.g., Zhao et al., 1994). It is nowadays clear that a large fraction of stars in the bulge region indeed follow a rotating, barred, boxy/peanut-shaped structure connected to an edge-on bar (Bland-Hawthorn and Gerhard, 2016).

Slightly before the advent of *Gaia* DR2, Portail et al. (2017) produced benchmark models of the Galactic bar, that were fitted to three-dimensional density maps of red clump giants, obtained after extinction and completeness corrections from infrared photometry (VVV, UKIDSS, 2MASS), combined with stellar kinematics from spectroscopic surveys (BRAVA, ARGOS) and astrometric measurements (OGLE) of stars in the bar region. They used a made-to-measure (M2M) modeling method, which is a hybrid method between simulation and orbit-fitting, characterizing the non-axisymmetric DF numerically through a self-consistent N-body simulation (Syer and Tremaine, 1996). In this approach, the mass of particles in the simulation is gradually fine-tuned throughout the system's evolution, providing the advantage of reproducing averaged observables non-parametrically. Although various bar pattern speeds were considered without reaching a firm conclusion, the resulting best-fit mass distribution model of Portail et al. (2017) can be taken as a benchmark model for the MW bar. It also reproduces the disk and dark matter halo gravitational potentials remarkably well: perhaps surprisingly, their best-fit dark matter halo presents a central constant density core, which might present a challenge to understand in a cosmological context. This model will be used as reference in this thesis for the axisymmetric and bar gravitational potential (see also Thomas et al., 2023), as described further in Chapter 2. The models of Portail et al. (2017) were also thoroughly tested

in Clarke et al. (2019) against a comprehensive three-dimensional kinematic map of the bulge and bar regions. These investigations used proper motions from the VVV Infrared Astrometric Catalogue (VIRAC) calibrated on *Gaia* DR2. Later, Clarke and Gerhard (2022) further showed that the models of Portail et al. (2017) reproduce observed features well, despite not being fitted to them, supporting their robustness to overall characterization of the axisymmetric and bar potential, with the limitation though on the exact bar pattern speed estimate. Different models in Portail et al. (2017) also have different bar pattern speeds: models from $\Omega_\mathrm{b} = 37.5$ km s^{-1} kpc^{-1} to $\Omega_\mathrm{b} = 42.5$ km s^{-1} kpc^{-1} all show good compatibility with the data. Varying the pattern speed, Clarke et al. (2019) found the model with $\Omega_\mathrm{b} = 37.5$ km s^{-1} kpc^{-1} to qualitatively best reproduce all observables from the combined VIRAC and *Gaia* DR2 data for the bar and bulge regions. More recently, Clarke and Gerhard (2022) fitted to the same dataset a lower quantitative estimate of $\Omega_\mathrm{b} = 33.29 \pm 1.81$ km s^{-1} kpc^{-1}. This estimate is well below the initial constraint on Ω_b set by Portail et al. (2017). This discrepancy is partly due to differences in data, the fitting methodology, and the error estimates for both the data and the models. Such low pattern speeds have alos recently been reported in terms of signatures of the bar in the stellar halo (Dillamore et al., 2025).

This highlights the sensitivity of pattern speed determinations to both the data and modeling approach. It illustrates the general challenge of measuring pattern speeds of non-axisymmetric Galactic structures. The bar's pattern speed remains a topic of debate until this day. Less than three decades ago, a consensus emerged for a bar pattern speed in the range $\Omega_\mathrm{b} \sim$ 50-60 km s^{-1} kpc^{-1}, based on various lines of evidence. These included hydrodynamical simulations comparing the modeled gas flow to observed Galactic CO and HI longitude-velocity diagrams (Fux, 1999; Englmaier and Gerhard, 1999; Bissantz et al., 2003), the so-called "Tremaine and Weinberg (1984)" method applied to stars in the inner Galaxy (Debattista et al., 2002), or local stellar kinematics (Dehnen, 1999b; Dehnen, 2000; Fux, 2001) positioning the Sun marginally beyond the 2:1 OLR of the bar. The latter argument has been supported by numerous subsequent analyses (e.g., Minchev et al., 2007; Quillen et al., 2011; Antoja et al., 2012; Antoja et al., 2014; Fragkoudi et al., 2019). From 2015 on, however, rival research works presented a revised pattern speed of $\Omega_\mathrm{b} \sim$ 35-40 km s^{-1} kpc^{-1}. This was based on analyses of the density of red clump stars in the disk (Wegg et al., 2015), gas kinematics (Sormani et al., 2015; Li et al., 2016), dynamical modeling of stellar kinematics in the inner Galaxy (Portail et al., 2017, see hereinabove), and proper motion data from the VVV survey (e.g., Clarke et al., 2019, see hereinabove too), including with the Tremaine-Weinberg method (Sanders et al., 2019). Pérez-

Villegas et al. (2017) and Monari et al. (2019a) subsequently demonstrated that the Galactic model adjusted to bulge stellar kinematics by Portail et al. (2017) could effectively replicate several observed features in local velocity space (see also Monari et al., 2019b; Binney, 2020; D'Onghia and Aguerri, 2020; Lucchini et al., 2024). Such a lower bar pattern speed is also consistent with observed overdensities in the stellar halo phase-space (Dillamore et al., 2024), where the best fit can sometimes be even lower (Dillamore et al., 2025), and with the chemistry of the disk (Haywood et al., 2024; Khoperskov et al., 2024). Other intermediate and even much lower pattern speeds have been proposed (Hunt and Bovy, 2018; Horta Darrington et al., 2025). Several studies concluded that stellar kinematics of the disk alone were not sufficient to break the degeneracy (Trick et al., 2021; Trick, 2022; Bernet et al., 2024). On the other hand, today, kinematics of stars in the bar region itself seem to have converged to $\Omega_{\rm b} \sim$ 35-40 km s^{-1} kpc^{-1}. Possible sudden variations of the pattern speed are also possible (Hilmi et al., 2020). A steady decrease of the pattern speed of the bar with time has been tentatively detected (Chiba et al., 2021; Chiba and Schönrich, 2021), although degeneracies with spirals arms should still be checked in detail. A decelerating bar may also explain some aspects of the vertical disequilibrium of the Galactic disk, such as the two-armed phase-spiral in the inner disk (Li et al., 2023), and can partially contribute to the presence of metal-poor stars with prograde planar orbits in the Solar vicinity (Li et al., 2024; Yuan et al., 2024).

The Galactic spiral arms

Spirals in external disk galaxies often display two-armed grand-design features. However, on top of these clear grand-design spirals, there are also smaller numbers with threefold, fourfold, and fivefold symmetries. In contrast, some spirals do not fit these clear patterns and appear flocculent. Notably, depending on the observational tracer, the same galaxy might appear as a grand design on one band and flocculent on another, or even featureless, highlighting a contrast in appearance due to different stellar or interstellar medium tracers. For example, in the near-infrared, arms trace the old stellar backbone of the disk, whereas optical and ultraviolet bands emphasize young stars and H II regions along the arms, resulting in a sharper and more fragmented appearance in gas-rich tracers. Spiral properties further contrast in length, strength, and pitch angle depending on morphological type and bar presence. Additionally, some spiral galaxies may exhibit rings in their inner, outer, or nuclear central regions, and these rings may also be associated with the presence of a bar. Recent observations have added new contrasts to our understanding of spiral properties—such as the possible evolution of pitch angles over

time (about $1°\text{Gyr}^{-1}$ (Yu and Ho, 2020; Reshetnikov et al., 2023)) and the apparent preference of pitch angle values around 12° and 23° with a scatter of $\sim 4°$. While the pitch angle and spiral amplitude do not appear to be correlated, there are however good theoretical reasons to expect a three-fold correlation between the amplitude, pitch angle *and* pattern speed of the spiral arms (Hamilton, 2024), which we will be using as a prior for our own modeling.

The specific location and dynamics of spiral arms in the MW present a less clear observational picture than even that of the bar. Although the idea that the MW could host spiral arms dates back to as early as its classification as a disk galaxy, extinction long obscured clear identification. It was not until the work of Morgan et al. (1952)—who identified these arms through HII region distributions—and the subsequent kinematic analysis of the HI 21-cm line by Oort et al. (1958), that their existence was observationally supported. Using distances to OB associations and HII regions, Georgelin and Georgelin (1976) mapped a four-armed spiral pattern. This view has been consistently confirmed with young or gaseous tracers (e.g. Urquhart et al., 2014); in contrast, older/redder tracers—which should better reveal perturbations in the Galactic potential—do not confirm this structure. Indeed, Drimmel (2000), Drimmel and Spergel (2001), Benjamin et al. (2005), and Churchwell et al. (2009) found with near-infrared and mid-infrared tracers that the MW seemingly hosts two main spiral arms.

Collecting data on HII regions and giant molecular clouds, Hou et al. (2009) showed that models of three-armed and four-armed logarithmic spirals could connect those different spiral tracers, as reviewed in Shen and Zheng (2020). In summary, it is no exaggeration to say that different tracers and observations are far from converging on parameters describing the positions of each spiral arm segment in the MW disk. The so-called Local arm, for example, has been found by Gaia Collaboration et al. (2023b) and Poggio et al. (2021), tracing young stars, to be more extended – and to have an intermediary pitch angle – compared to Vázquez et al. (2008) where this arm rather heads outwards to the Perseus arm, or to Xu et al. (2021) where the Local arm heads inwards to the Carina–Sagittarius arm. Similar debates exist regarding the Perseus arm and the Outer arm with respect to their positions in the disk and pitch angles. Perhaps most strikingly, the pitch angle of the Perseus arm has been found to be $\sim 24°$ in Levine et al. (2006), compatible with results of Poggio et al. (2021) or Drimmel et al. (2024), and $\sim 9°$ in Reid et al. (2019), meaning that the name does not actually always refer to the same observed overdensities in the Galactic plane. The situation regarding the pattern speed of spiral arms is even more confused, as its signature can also depend on their dynamical nature and origin (see Sellwood and Masters, 2022, for a review).

Keeping in mind this range of observations and interpretations, several tentative measurements of the amplitude and pattern speed of spiral arms have been made over time. Originally, Lin et al. (1969) proposed a 2-armed model with pitch angle of 6° and pattern speed of $\Omega_{s,2} \sim 13$ km s^{-1} kpc^{-1} based on the systematic motion of gas and the displacement of moderately young stars in their classical density wave model. A more recent estimate based on the classical Lin and Shu (1964) density wave formalism has been made by Siebert et al. (2012) fitting the mean radial velocity map from the RAVE survey and finding a best-fit 2-armed spiral model with a contrast surface density of 14%, a pitch angle of 10° and a pattern speed of $\Omega_{s,2} \sim 18.6$ km s^{-1} kpc^{-1}. This model, however, neglected the effect of the bar (see, e.g. Monari et al., 2014). On the other hand, Amaral and Lepine (1997) argued for a superposition of a 2-armed and 4-armed spiral, both with a pattern speed of ~ 20 km s^{-1} kpc^{-1} based on tracing back open clusters to their birth place. Such a procedure was recently carried out by Castro-Ginard et al. (2021), finding a declining pattern speed with radius from ~ 50 km s^{-1} kpc^{-1} for the Scutum arm segment to ~ 17 km s^{-1} kpc^{-1} for the Perseus arm segment. Modeling the gas flow in the inner Galaxy, Bissantz et al. (2003) obtained a joint measurement of the bar and 4-armed spiral pattern speeds, with a very high pattern speed for the bar, $\Omega_b \sim 60$ km s^{-1} kpc^{-1}, and a 4-armed spiral pattern speed of $\Omega_{s,4} \sim 20$ km s^{-1} kpc^{-1}. More recently, again neglecting the bar, Eilers et al. (2020) applied a toy model of a logarithmic spiral to *Gaia* DR2 mean Galactocenric radial velocity field to suggest a contrast surface density of $\sim 10\%$, a pitch angle of 12° and a fixed pattern speed of $\Omega_{s,2} = 12$ km s^{-1} kpc^{-1} for a 2-armed spiral corresponding to the Local and Outer arms. Such low pattern speeds had also previously been suggested by, e.g., Sellwood (2010) based on the signature of a spiral ILR in local stellar kinematics (~ 8 km s^{-1} kpc^{-1} for a 2-armed spiral and ~ 15 km s^{-1} kpc^{-1} for a 3-armed spiral). Regarding the amplitude, the most recent determination, based on the vertical Jeans equation, has found the Local arm to be the strongest local overdensity, with a contrast density of roughly 20% (Widmark and Naik, 2024).

Beyond observational approaches, numerical simulations of galactic disks offer multiple perspectives on this topic, from transient corotating structures winding up and disappearing quickly (e.g., Baba et al., 2013; Hunt et al., 2018; Hunt et al., 2019), to multiple modes persisting over a few (or even many) galactic rotations, falsely appearing as very short-lived due to superposition of modes (e.g., Sellwood and Carlberg, 2014). In the following, our modeling procedure will follow two main guidelines.

The first guideline is the current consensus that, when spirals appear as modes in simula-

tions, these are not strictly static as in the classical density wave picture (Lin and Shu, 1964), but are rather made of a recurrent cycle of groove modes (seeded by a depletion of circular orbits in a narrow range of angular momenta, see, e.g. De Rijcke and Voulis, 2016; De Rijcke et al., 2019) that live between their ILR and OLR, where they can create new grooves which set up the recurrent cycle (Sellwood and Carlberg, 2014; Sellwood and Carlberg, 2019). They can also be edge modes (Fiteni et al., 2024). The amplitudes of the individual modes grow and decay, but they are nevertheless genuine standing wave oscillations with fixed shape and pattern speed, detectable over a period of at least one rotation. Complementing this, Hamilton et al. (2024a) presents an analytical framework for studying the dynamics of galactic disks. Building on that, Hamilton et al. (2025) shows that groove modes naturally arise in their unified linear response theory as the long-wavelength limit of the same mechanism that produces density waves and swing amplification. In this picture, a depletion of near-circular orbits seeds a self-gravitating mode confined between its ILR and OLR, capable of amplifying to the order of magnitude of density contrasts observed in galactic disks. This places the recurrent groove modes seen in N-body simulations within a broader, continuous framework of spiral instabilities.

The second guideline that we will follow is that spectrograms of N-body simulations displaying joint bar and spiral perturbations tend to display spiral arms rotating more slowly than the bar; moreover, spiral arms are never present within the CR radius of the bar. These spirals live between their own ILR and OLR but are usually strongest between their ILR and CR (Quillen et al., 2011). Our modeling approach will not account for the possibility of winding spirals over time.

1.4 Outline

The DR3 of the *Gaia* mission now provides full six-dimensional phase-space information on the MW disk for a larger number of stars and over a larger volume than ever before. However, the rich information contained solely within the in-plane motions of stars (e.g., Gaia Collaboration et al., 2018a; Gaia Collaboration et al., 2023b) has not been fully exploited yet. Indeed, these in-plane motions should – in principle – allow us to get a detailed dynamical mapping of the most important non-axisymmetric structures of the MW disk, namely the Galactic bar and the spiral arms. However, such a detailed mapping is still lacking. This is the focus of this thesis.

We will attempt to fully exploit the rich information encoded within the in-plane stellar motions in *Gaia* DR3 (Gaia Collaboration et al., 2023b) to constrain dynamically the non-

axisymmetries of the Galaxy. Previous similar attempts include the more empirical approach of Khoperskov et al. (2020) and Khoperskov and Gerhard (2022), as well as the recent works of Hunter et al. (2024) and Vislosky et al. (2024), with the later comparing three hydrodynamical simulations of galaxies to the velocity maps from *Gaia* in order to get insights on the bar-spiral orientation. Our approach hereafter is complementary since, instead of qualitatively comparing a self-consistent hydrodynamical simulation to the data, we attempt a more quantitative fit to the stellar phase-space data from *Gaia*. For this, we will resort to backward integrations to model the velocity field with a parametric form of the gravitational potential. Our approach is also complementary to the modeling of Khoperskov et al. (2024) and Khoperskov et al. (2025), who only considered the bar but not the effect of spiral arms.

In Chapter 2, we first briefly present the data extracted from the RVS sample of *Gaia* DR3 that we use to constrain the potential from the MW disk kinematics in Section 2.1. The modeling method and the parametrization of the potential are introduced in Section 2.2. The fitting procedure and the fit results are presented in Section 2.3. Since the fit was done in 2D, the three-dimensional extension of the non-axisymmetric potential is then explored in Chapter 3. Chapter 4 explores predictions and applications of the model, including the mapping of spiral arm locations, azimuthal and radial velocity fields, the chemo-dynamics of moving groups, and implications for Solar and stellar orbits. Finally, Chapter 5 summarizes the main findings and outlines some prospects for future work.

Chapter 2

2D non-axisymmetric gravitational potential for the Milky Way

2.1 Data

Since we are planning to use the in-plane motions of disk stars to constrain the non-axisymmetries of the MW, we select a sample of stars with six-dimensional phase-space information from the *Gaia* RVS close to the Galactic plane. We use data from *Gaia* DR3 (Gaia Collaboration et al., 2023d) combined with the StarHorse (Anders et al., 2022) distances, and select 17 414 667 stars within a height of 300 pc from the Galactic plane.

We adopt, for the Sun's position $\boldsymbol{x}_\odot = (x_\odot, y_\odot, z_\odot)$ and velocity $\boldsymbol{v}_\odot = (V_{x_\odot}, V_{y_\odot}, V_{z_\odot})$ in Galactocentric Cartesian coordinates, $\boldsymbol{x}_\odot = (8275, 0, 15.29)$ *pc* and $\boldsymbol{v}_\odot = (-9.3, 251.5, 8.59)\,\mathrm{km\,s^{-1}}$ (Gaia Collaboration et al., 2023b; Portail et al., 2017; Widmark and Monari, 2019), respectively. We then transform the data from equatorial coordinates to Galactocentric coordinates with the Astropy library (Astropy Collaboration et al., 2022) to compute the stars' positions in Galactocentric Cartesian coordinates, $\boldsymbol{x} = (x, y, z)$ and their in-plane velocities in Galactocentric Cylindrical coordinates, $\boldsymbol{v} = (V_R, V_\varphi)$, with the Galactocentric radius $R = \sqrt{x^2 + y^2}$ and azimuth $\varphi = \arctan(y/x)$, defined to be zero at the azimuth of the Sun and positive in the direction of Galactic rotation. The stars are selected within $4\,\mathrm{kpc} < x < 12\,\mathrm{kpc}$ and $-4\,\mathrm{kpc} < y < 4\,\mathrm{kpc}$.

Figure 2.1 shows the local stellar velocity distribution in a cylinder around the Sun, with radius and half-height varying from 100 pc to 300 pc. The left panel, with a 100 pc radius and 1.8×10^5 stars, already reveals some velocity-space ridges. Increasing the height to 200 pc includes 9.1×10^5 stars and enhances these features. At 300 pc, the ridges become well populated

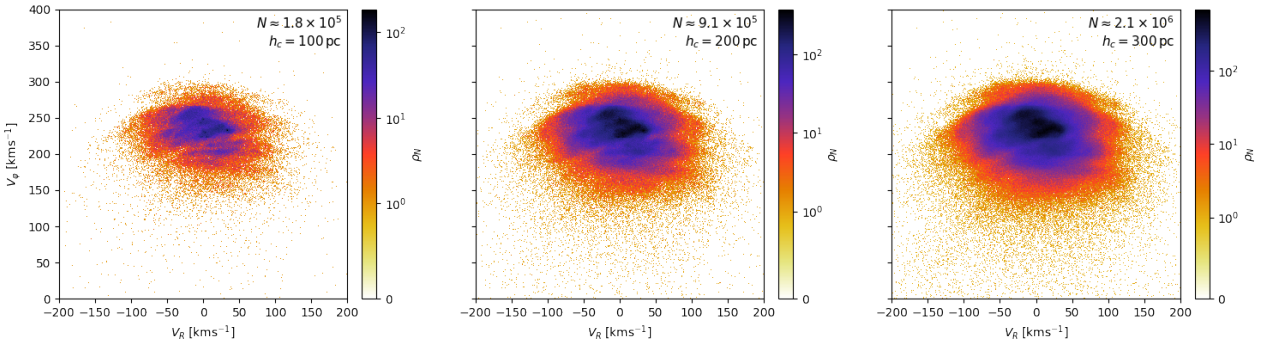

Figure 2.1: 2-dimensional histogram of the number density of stars from the *Gaia* RVS disk sample in the local (V_R, V_φ) plane. For each panel, the stars were selected within cylinders of h_c pc radius and $\pm h_c$ pc height around the Sun. From left to right, $h_c = 100, 200, 300$ pc, respectively, with N indicating the number of stars in the cylinder. The distribution is shown in the (V_R, V_φ) plane defined on a $[-200, 200]$ kms^{-1} $\times [0, 400]$ kms^{-1} grid, binned with (1 kms^{-1})^2 bins.

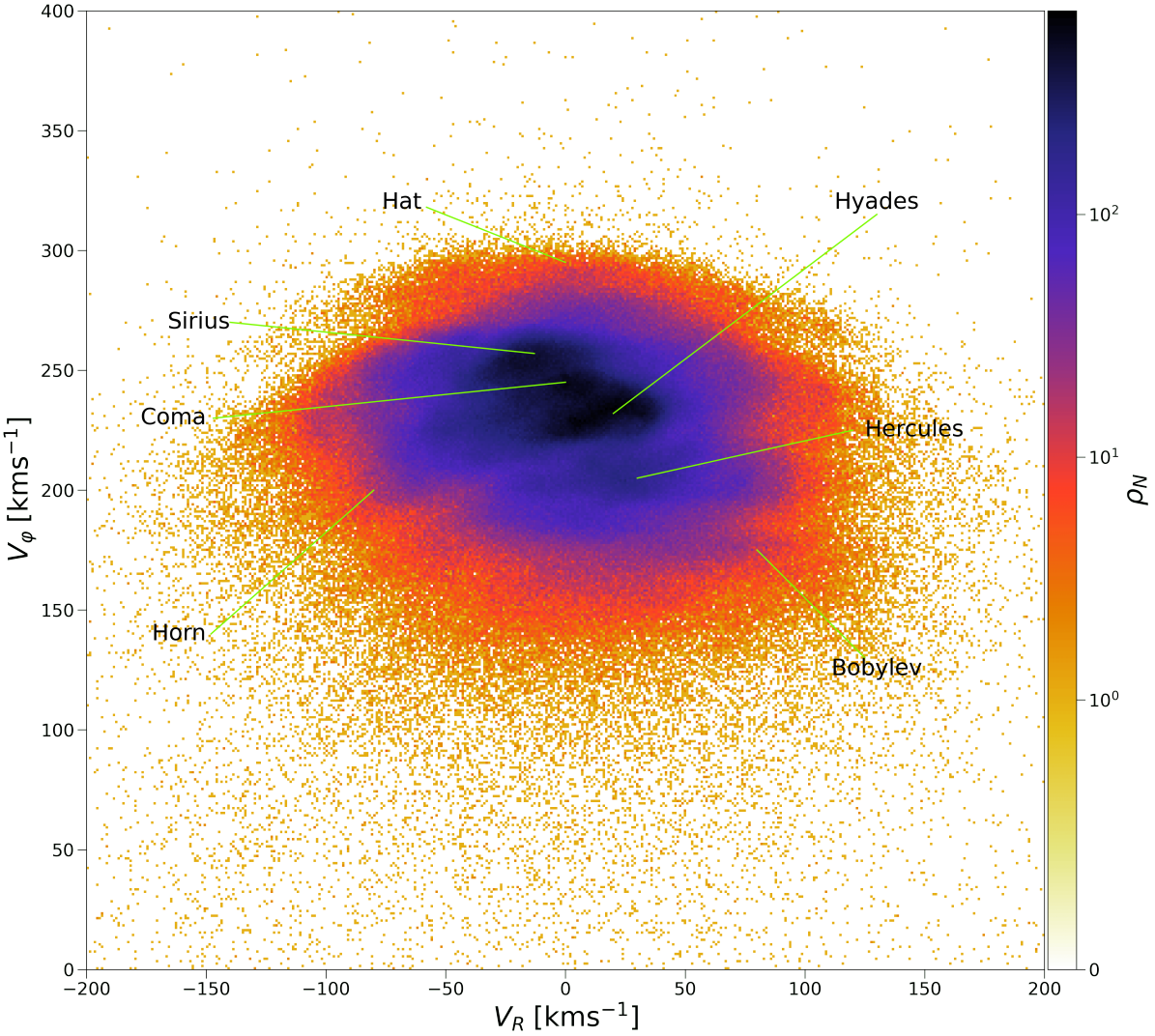

Figure 2.2: Zoomed view of the last panel at right of Fig 2.1 with the locations of the different moving groups. Note that V_R is positive towards the outer Galaxy, hence in the opposite direction from u in Fig. 1.3.

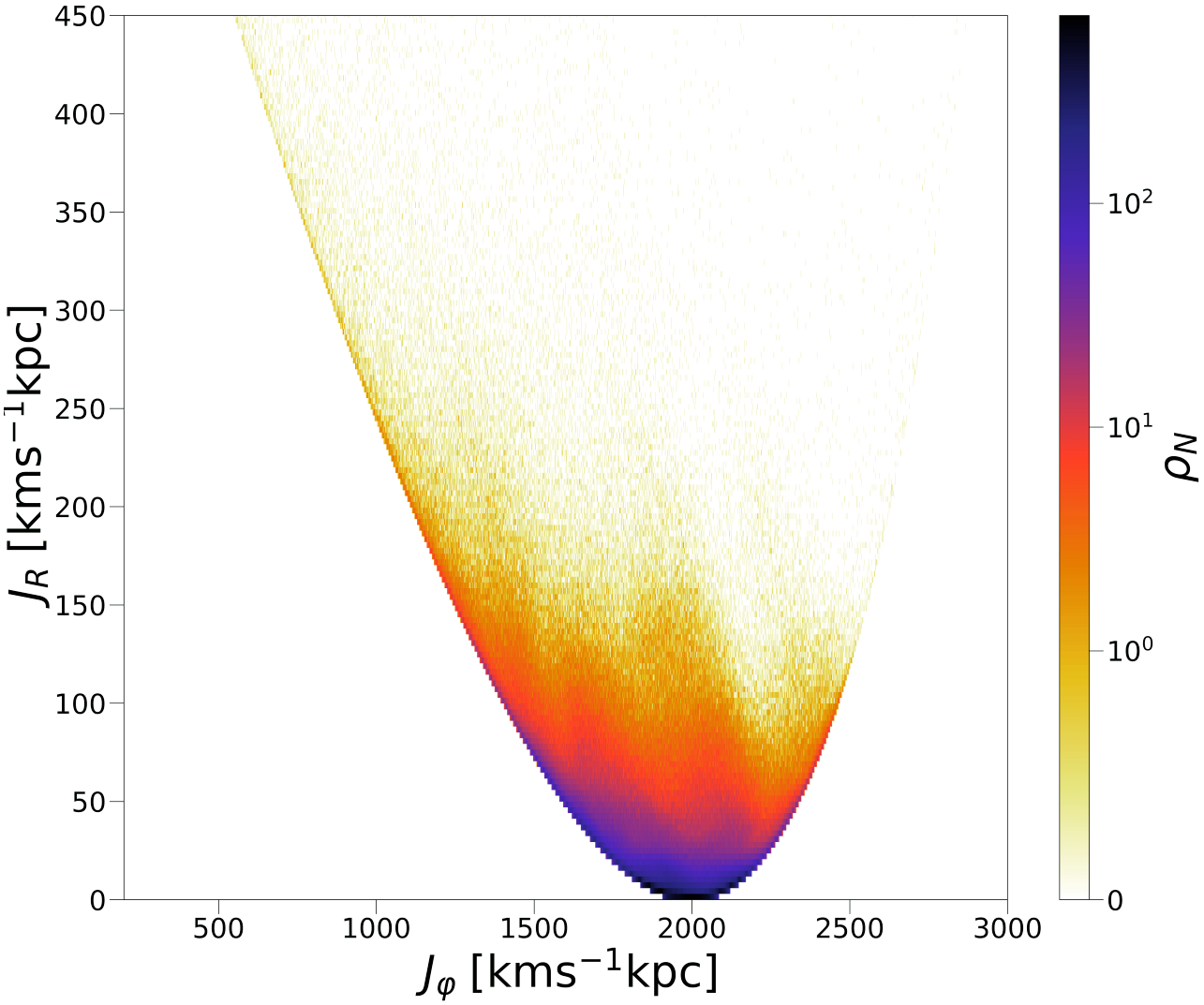

Figure 2.3: Same distribution as in Fig 2.2 on the actions (J_φ, J_R) plane (computed with `AGAMA` in the axisymmetric potential of Table 2.1) defined on a $[0, 600]$ $\mathrm{kms}^{-1}\,\mathrm{kpc}^{-1}$ $\times$ $[200, 3000]$ $\mathrm{kms}^{-1}\,\mathrm{kpc}^{-1}$ grid, binned with $(3 \times 2\,\mathrm{km}^2\,\mathrm{s}^{-2}\,\mathrm{kpc}^{-2})$ bins.

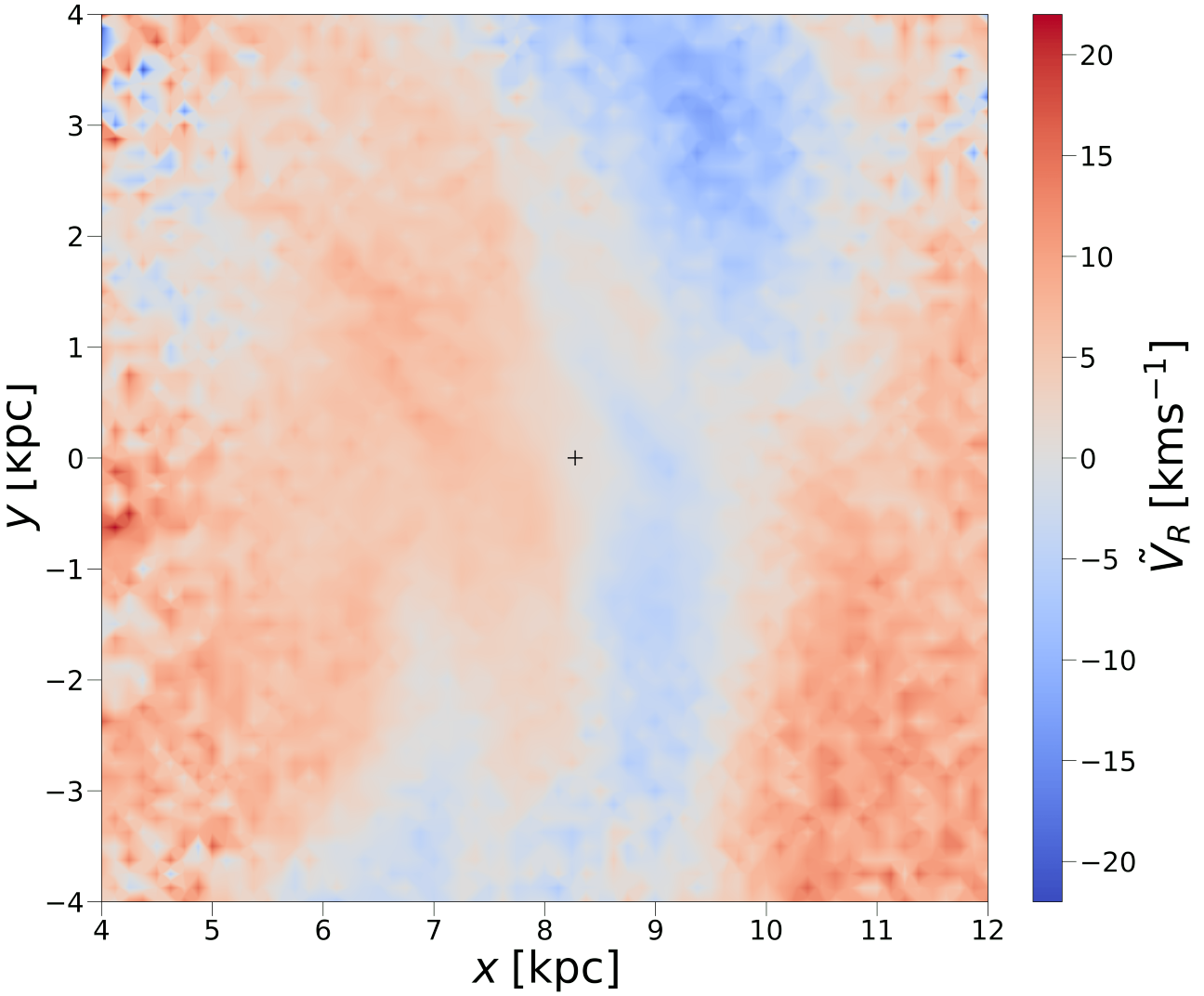

Figure 2.4: Median radial velocity $\tilde{V}_R\,(x, y)$ as a function of the position in the Galactic plane for the full sample of 17 414 667 stars with $|z| < 300$ pc. The grid is defined as $[4, 12]$ kpc $\times$ $[-4, 4]$ kpc, binned with $(125\,\mathrm{pc})^2$ bins. The Galactic center is located at $(x, y) = (0\,\mathrm{kpc}, 0\,\mathrm{kpc})$, the Sun at $(x, y) = (8.275\,\mathrm{kpc}, 0\,\mathrm{kpc})$ is represented with a cross, and the sense of rotation of the Galaxy is anti-clockwise, hence in the opposite sense of rotation compared to Fig. 1.4.

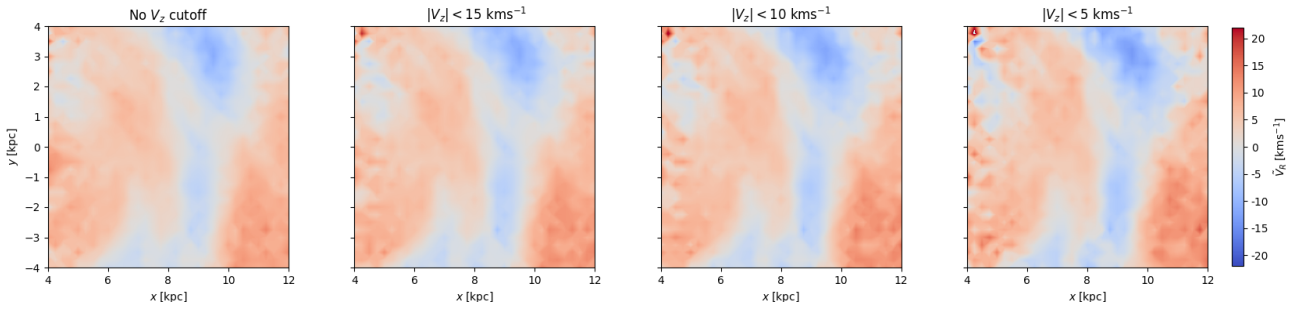

Figure 2.5: Similar to Fig 2.4 for different V_z cutoffs. From left to right: sample without cutoff, as in Fig 2.4, with 17 414 667 stars, followed by maps of samples with cutoffs $|V_z| < 15\,\mathrm{kms}^{-1}$, $|V_z| < 10\,\mathrm{kms}^{-1}$ and $|V_z| < 5\,\mathrm{kms}^{-1}$, respectively, with 11 427 688, 8 583 274 and 4 681 930 stars each.

and defined, as detailed in Fig. 2.2. This configuration, comprising 2.1×10^6 stars, serves as our reference local 2-dimensional velocity distribution for the Gaia RVS disk sample on the local (V_R, V_φ) plane.

In Fig. 2.2, we also indicate the location of several of the well-known moving groups of the Solar neighborhood (e.g., Dehnen, 1998; Famaey et al., 2005; Antoja et al., 2008; Ramos et al., 2018; Bernet et al., 2022). The "Hat" can be seen as the downward concave arch at high V_φ, from $(V_R, V_\varphi) \approx (-100 \ \ \mathrm{kms}^{-1}, 270 \ \ \mathrm{kms}^{-1})$ to $(V_R, V_\varphi) \approx (120 \ \ \mathrm{kms}^{-1}, 260 \ \ \mathrm{kms}^{-1})$; The Sirius moving group (e.g., Famaey et al., 2008) is approximately straight at $V_\varphi \approx 255 \ \ \mathrm{kms}^{-1}$, located between $V_R \approx -50 \ \ \mathrm{kms}^{-1}$ and $V_R \approx 0 \ \ \mathrm{kms}^{-1}$, with a peak at $V_R \approx -15 \ \ \mathrm{kms}^{-1}$; Coma is right below Sirius in azimuthal velocity, around $(V_R, V_\varphi) \approx (0 \ \ \mathrm{kms}^{-1}, 245 \ \ \mathrm{kms}^{-1})$; The Hyades moving group (e.g., Famaey et al., 2007; Pompéia et al., 2011) can be seen as a slightly curved downward arch from the over-density at $(V_R, V_\varphi) \approx (20 \ \ \mathrm{kms}^{-1}, 230 \ \ \mathrm{kms}^{-1})$; The Horn is right next to the Hyades, on the other side in V_R: it appears as an arch going through $(V_R, V_\varphi) \approx (-80 \ \ \mathrm{kms}^{-1}, 200 \ \ \mathrm{kms}^{-1})$; finally, the major Hercules moving group is perceived as a bimodality of the whole velocity-plane, with an under-density, just below the Hyades in azimuthal velocity, separating it from the rest of the distribution. Its bimodality appears clearly, with a second overdensity appearing at low V_φ.

Another way to visualize these arches, which, however, visually erases the asymmetries in radial velocity, is to plot the distribution of stars in the local axisymmetric action space (e.g. Trick et al., 2019; Trick et al., 2021). As a reminder from the previous Chapter, the azimuthal action is simply $J_\varphi = R\,V_\varphi$, whilst the radial action J_R (computed with the Stäckel fudge within the background axisymmetric potential defined in Sect. 2.2) encodes the (Galactocentric) radial excursions of a given orbit. In Fig. 2.3, the arches in local velocity space are now seen as ridges in local action space, characteristic of resonant features (e.g., Monari et al., 2017a; Binney, 2020).

These features of local velocity and action space, traced with exquisite precision, have, however, been known for a long time (see Fig. 1.3). The most interesting added value of *Gaia* data releases has been to expand the volume around the Sun where such dynamical features can be studied (e.g., Ramos et al., 2018; Bernet et al., 2022). In order to adjust the non-axisymmetric components of the Galactic potential in the present work, we will however refrain from using the full phase-space distribution of disk stars, and will rather fit the measure of a central tendency as a function of position in the disk, namely the median Galactocentric radial velocity (Gaia Collaboration et al., 2023b). This map of median radial velocity is displayed in

Fig. 2.4 and will be the main observable adjusted in the present work. We will check only a posteriori the qualitative agreement with the full phase-space distribution of stars.

Since our modeling will be based on a projected 4D phase-space DF (marginalizing equation 1.27 over z and V_z) of the disk stellar populations – a DF that is supposed to take into account stars with non-zero vertical velocities –, we do not make any additional cuts on the vertical velocity in the data. However, while our DF is a projected one, our orbit integrations will be performed only within the plane. Therefore, we also checked that selecting only stars with vertical velocities below $15\,\mathrm{km\,s^{-1}}$, allowing to keep a reasonable number of 11 427 688 stars in the dataset, led to an almost identical median radial velocity map. The maps of median radial velocity for different cutoffs in V_z are show in Fig 2.5. For the important points of the fit, the typical differences are below 0.5 km/s, with a maximum difference of 1 km/s.

2.2 Modeling

To build our non-axisymmetric potential, we start from an axisymmetric one, and we will subsequently add a bar and spiral arms, defined by several parameters as described in the following subsections. Then, to evaluate the DF in this non-axisymmetric potential, we will follow the backward integration modeling introduced in Section 1.2.6. In order to compute the $f(\boldsymbol{x}, \boldsymbol{v}, t)$, at current time $t = 0$, at the phase-space point $(\boldsymbol{x}, \boldsymbol{v})$, in the presence of the bar and spiral arms, we will backward integrate the orbit for a fixed integration time to its phase-space position $(\boldsymbol{x}', \boldsymbol{v}')$ at time $t' < 0$, before the actual appearance of the non-axisymmetric perturbers. Assuming that the tracer population is represented by the equilibrium DF, $F(\boldsymbol{J})$, in the axisymmetric background potential at time t', we transform $(\boldsymbol{x}', \boldsymbol{v}')$ to action-angle variables using the `AGAMA` Stäckel fudge, compute the value of the DF, and since this value in an infinitesimal Lagrangian volume is conserved, we attribute the same value of the DF to the phase-space position $(\boldsymbol{x}, \boldsymbol{v})$ at present time $t = 0$ in the presence of the bar and spirals.

In practice, the orbits are integrated within the plane only, by solving the initial value problem with the Runge-Kutta of order 5 method `odeint` solver from the very efficient `torchdiffeq` library (Chen, 2018) in `PyTorch` (Paszke et al., 2019). Doing this at numerous phase-space locations allows us to compute the median radial velocity as a function of position in the disk, and to adjust the parameters of the non-axisymmetric components in order to fit the observed values. In practice, the median radial velocity at each grid position (sampled every 50 pc in x and y) on the disk is computed after locally integrating the values of the DF in V_φ for a

grid of velocities on which the backward integration is performed at each position. This grid ranges from -79 kms^{-1} to 79 kms^{-1} with a step of 2 kms^{-1} in V_R, and from 110 kms^{-1} to 330 kms^{-1} with a step of 4 kms^{-1} in V_φ. The potential is evaluated on a grid of radii that is subsequently interpolated with a cubic spline in the `torchcubicspline` library in `Pytorch` to improve computational time. Similarly, we also interpolate, with `Scipy` (Virtanen et al., 2020), a cubic spline to the actions computed with `AGAMA`.

There are three caveats with the method, which are worth mentioning (re-mentioning), even though addressing them in detail is far beyond the scope of our present first quantitative approach to the problem. First, we are using the full disk sample described in the previous section without taking into account a detailed selection function, assuming that the high number of stars that we use allows for a good estimate of the true median velocity. This should be the easiest caveat to address in our future invsetigations. The second caveat is that, as we already mentioned, the observed stellar DF is always measured over finite phase-space volumes whilst the backward integration method operates under the assumption that the mean value of the DF within a given phase-space volume is equivalent to its value at the central point, irrespective of how the volume deforms during the system's orbital evolution. In other words, the backward integration method yields the fine-grained DF, which will typically remain unsmoothed at small scales, whilst the measurable DF within observations is the coarse-grained one, which does not obey the collisionless Boltzmann equation (as this coarse-grained DF is smoothed by phase-mixing within finite volumes). The Nyquist-Shannon sampling theorem imposes limits on the minimum size of fine structures in phase space that can form for a fixed number of particles over time, and this limit is reached on rather short time scales, shorter than collisional relaxation (Beraldo e Silva et al., 2019). Once this limit is reached, the system cannot form finer structures, despite the collisionless Boltzmann equation predicting that these structures do form. In practice, this means that, if the integration is carried out for too long, the fine-grained DF tracked by the backward integration method will lead to sharp and unsmoothed features in velocity space, where chaotic features will also appear as sharper than in the real world. To circumvent this problem, the integration must be carried out only for a relatively limited time, adjusted so that the sharpness of resonant features in velocity space resembles what is observed. Luckily, N-body simulations indicating the existence of recurrent cycles of groove modes in galactic disks (Sellwood and Carlberg, 2014; Sellwood and Carlberg, 2019) allow us to consider that current spiral arm modes of the Milky Way are rather recent. This assumption is, of course, not ideal for the bar, but it is reasonable to assume that the location

of the resonant features in local velocity space will not evolve with time, whilst their sharpness will. Hence, we will only deal with the location of resonant features in local velocity space to constrain the pattern speed of the bar, and rely on a parametric form of its potential adjusted to the dynamics of the bulge region (Portail et al., 2017; Thomas et al., 2023) for its amplitude. It would be too costly to resort to a forward integration method within the fitting scheme that we set out to apply in the present Chapter, given the size of the parameter space to explore, and given that each combination of parameters requires a full backward integration of the whole Galactic plane. However, the results obtained in this Chapter will serve as a basis for forward-in-time test-particle simulations, also expanded to three dimensions, that we will present in the next Chapter. Finally, a third and last caveat is that our simulations are, by design, not self-consistent. This simplification is much more efficient for exploring a vast parameter space. However, future improvements of our method might rely on an adaptation of the made-to-measure method (Syer and Tremaine, 1996; Portail et al., 2017) to account for self-consistency, using the results presented hereafter as a basis.

2.2.1 Background axisymmetric potential

As outlined hereinabove, our method makes use of an axisymmetric background potential. In practice, we assume a 3D axisymmetric density profile for this background, and the potential is computed by solving Poisson's equation with `AGAMA`. The density profile is the summed density of each of the following components: stellar disk, gas disk, bulge, and dark matter halo. Then, in the current Chapter, we will only make use of the potential within the Galactic disk when adding on top of it the bar and the spirals.

The axisymmetric stellar and gas disk density profiles are parametrized in Galactocentric cylindrical coordinates (R, z) as:

$$\rho_{\mathrm{disky}}(R,z) = \frac{\Sigma_0}{2h_z}\exp\left(-\left|\frac{z}{h_z}\right|\right)\exp\left(-\frac{R}{h_R}\right), \tag{2.1}$$

with the central surface density Σ_0, scale height h_z (and hence central 3D density $\Sigma_0/2h_z$), and scale length h_R. The spherical density profile for the bulge and dark matter halo is given by:

$$\rho_{\mathrm{spheroidal}}(R,z) = \rho_0\left(\frac{\tilde{r}}{a}\right)^{-\gamma}\left(1+\frac{\tilde{r}}{a}\right)^{\gamma-\beta}\exp\left[-\left(\frac{\tilde{r}}{r_s}\right)^{\alpha}\right], \tag{2.2}$$

with a density normalization ρ_0, a scale radius a, an outer scale radius r_s, and exponents α,

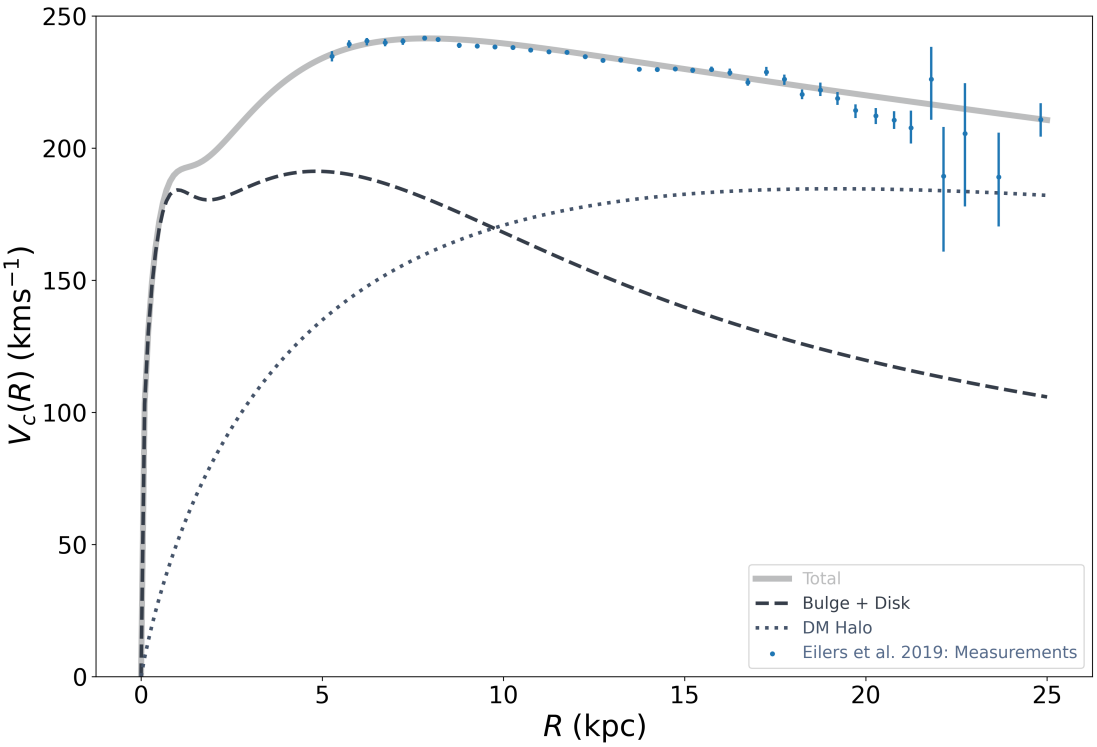

Figure 2.6: The circular velocity curve of the background axisymmetric potential described in Sec. 2.2.1. The scatter points are adapted from Eilers et al. (2019) to the value of the Galactocentric Sun's velocity and position used in this thesis.

β, γ. The ellipsoidal radius is defined as $\tilde{r} = \sqrt{R^2 + \left(\frac{z}{q}\right)^2}$, with q the vertical axis ratio. All parameters are given in Table 2.1. The baryonic mass of the model is $6 \times 10^{10} \mathrm{M}_\odot$ and the dark matter halo is relatively light, with a mass of $3.1 \times 10^{11} \mathrm{M}_\odot$, in between the typical values obtained from circular velocity curve analyses (e.g., Jiao et al., 2023; Ou et al., 2024) and those obtained from escape speed curves, satellite dynamics or stream fitting (e.g., Monari et al., 2018; Callingham et al., 2019; Roche et al., 2024b; Ibata et al., 2024). Only the mass in the inner Galaxy, however, matters for our present modeling: the total enclosed mass (baryons and dark matter) within 20 kpc is $2.2 \times 10^{11} \mathrm{M}_\odot$, roughly in agreement with the Malhan and Ibata (2019) constraint. The local dark matter density at the Sun's position is $1.3 \times 10^{-2} \mathrm{M}_\odot$ pc^{-3}, consistent with most estimates (de Salas and Widmark, 2021, and references therein). In the center, the dark matter halo displays a constant density core (with a central power-law slope of 0) as well as a shallow power-law decline close to the center with a slope of -0.6 at $R = 1$ kpc and of -1 at $R = 3$ kpc. All these background potential parameters could in principle be left free in our fitting procedure hereafter, but to simplify the problem, they have all been fixed

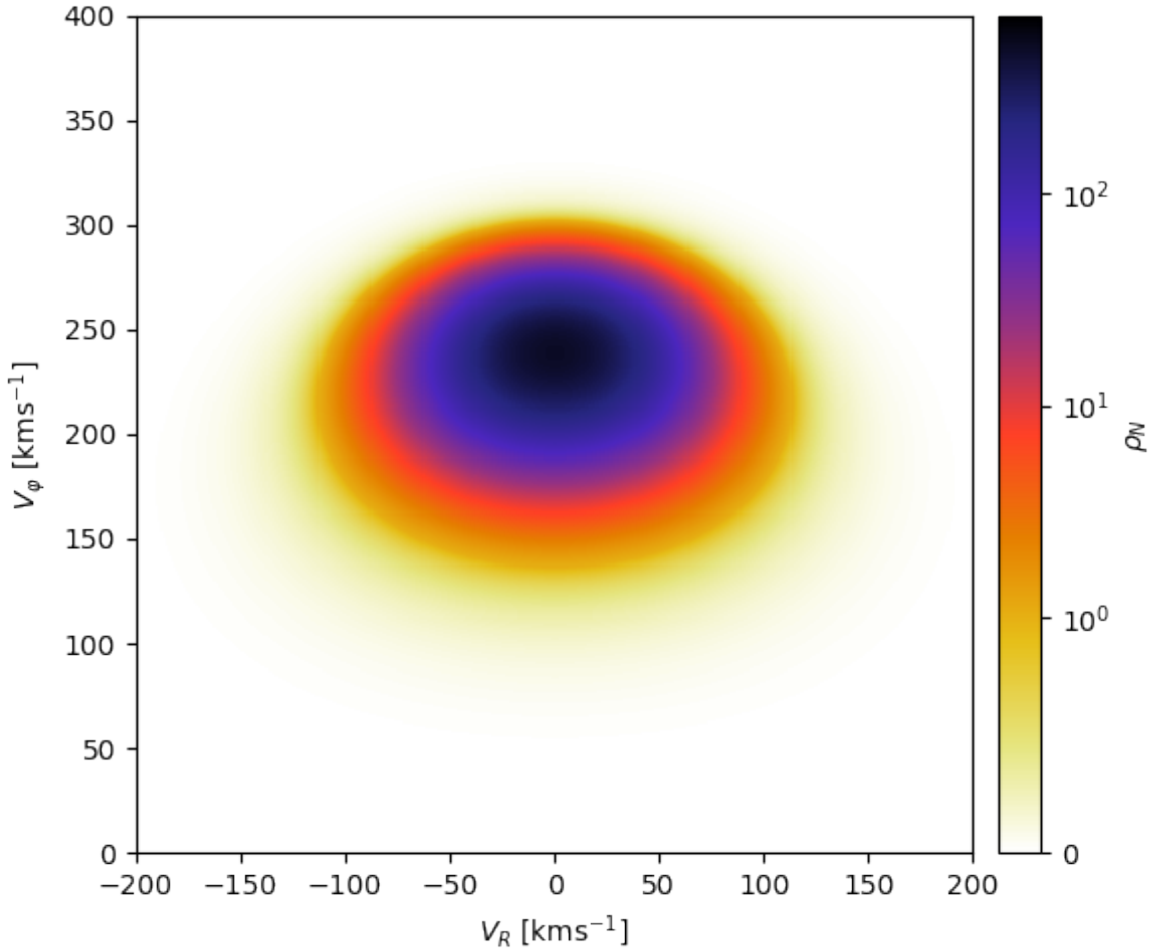

Figure 2.7: The number density ρ_N of stars in velocity space at the Sun's position from the equilibrium DF described in Sec. 2.2.2, for a normalization factor such that the total number in the model at the Sun is the same as found in the data within the 300 pc cylinder around the Sun (as in Fig 2.2).

to resemble closely the axisymmetric part of the model by Portail et al. (2017). The circular velocity curve corresponding to this axisymmetric model is plotted in Fig. 2.2.1. The non-axisymmetric modes that will be added on top of this axisymmetric background will all have zero total mass, meaning that the total mass of the final non-axisymmetric model will be the same as that of the axisymmetric one. Since our orbits will be computed strictly within the plane, we only need hereafter the background potential within the plane, $\Phi_0(R)$.

2.2.2 Axisymmetric equilibrium distribution function

The second step of our procedure consists of choosing an equilibrium DF for the tracer stellar population within the plane. Since we are confined to the plane, we do not attempt here to be fully self-consistent, in order to allow for a simple and tractable form of the DF, namely a simple linear combination of two quasi-isothermal DFs $F_{2D}(J_R, J_\varphi) = F_{\rm thin,2D} + \zeta F_{\rm thick,2D}$, that

Table 2.1: Fixed parameters for the axisymmetric background density.

		Disky density profiles	
Component	Σ_0 ($10^3 M_\odot$ pc^{-2})	h_R (kpc)	h_z (kpc)
Stellar disk	1.19	2.4	0.30
Gas disk	0.07	4.8	0.13

		Spheroidal density profiles					
Component	ρ_0 ($10^{-1} M_\odot$ pc^{-3})	a (kpc)	r_s (kpc)	α	β	γ	q
Bulge	1.08	8.16	0.83	2.0	2.9	1.3	1.0
DM halo	4.56	–	0.65	0.50	0.0	0.0	0.8

1

are two-dimensional in action space, and both adapted from Eq.(1.27) by projecting it onto the plane:

$$F_{2D}(J_R, J_\varphi) = \eta \frac{\Omega(J_\varphi)}{\kappa(J_\varphi)\tilde{\sigma}_R^2(J_\varphi)} \exp\left(-\frac{R_\mathrm{g}(J_\varphi)}{h_R}\right) \exp\left(-\frac{J_R \kappa(J_\varphi)}{\tilde{\sigma}_R^2(J_\varphi)}\right), \tag{2.3}$$

with $\zeta = 0.05$, R_g the guiding radius, Ω, κ the circular and epicyclic frequencies, all three depending on the azimuthal action J_φ, h_R the disk scale length, η the normalization factor (in units of inverse length squared) of the tracer population, and finally the radial velocity dispersion $\tilde{\sigma}_R$ depending on the guiding radius and on $h_{\sigma,R}$, the kinematic scale-length of the tracer population as defined in Eq. 1.28. For $F_{\mathrm{thin,2D}}$, we set the scale length to $h_R = 2.4$ kpc in accordance with the potential, the velocity dispersion at the Sun's position to $\tilde{\sigma}_{R,\mathrm{thin}}(R_0) = 30$ kms^{-1}, and the kinematic scale length to $h_{\sigma_R} = 10$ kpc. For $F_{\mathrm{thick,2D}}$, the only difference is that we set $\tilde{\sigma}_{R,\mathrm{thick}}(R_0) = 55$ kms^{-1}. The latter parametrization is a very rough way of taking into account the thick disk, and should definitely be improved within further works, especially once tagging tracer populations chemically. It is nevertheless good enough for our present, purely dynamical, investigation. Our DF corresponds to a projected four-dimensional DF in phase-space, namely in units of inverse length-squared times inverse velocity-squared, hence corresponding to the 6D DF of the modeled disk populations integrated over heights and vertical velocities. The local velocity distribution at $R = R_0$ corresponding to this axisymmetric DF is displayed in Fig. 2.7. In practice, the normalization factor is adjusted such that the number of stars in the model at the Sun is the same as found in the data within the cylinder of 300 pc radius and ± 300 pc height around the Sun.

2.2.3 Non-axisymmetric potential

The third step of our procedure is to add non-axisymmetric modes on top of the axisymmetric background potential Φ_0. The total potential is obtained by adding to $\Phi_0(R)$ the real part of the following:

$$\Phi_{\rm tot}(R,\varphi,t) = \Phi_0(R) + \sum_m \phi_{{\rm b},m}(R,t)\exp[{\rm i}\,m(\varphi-\varphi_{{\rm b},0}-\Omega_{\rm b}t)] + \sum_m \phi_{{\rm s},m}(R,t)\exp[{\rm i}\,m(\varphi-\varphi_{{\rm s},m,0}-\Omega_{{\rm s},m}t)], \quad (2.4)$$

where the current phase and the pattern speed of the bar are respectively $\varphi_{\rm b,0}$ and $\Omega_{\rm b}$, and those of the spiral arms mode m respectively $\varphi_{{\rm s},m,0}$ (the present-day spiral phase at the Solar position) and $\Omega_{{\rm s},m}$. The amplitude of each mode is given by $\phi_{{\rm b},m}$ and $\phi_{{\rm s},m}$ for the bar and spirals, respectively. The time t is such that currently $t = 0$.

As outlined hereinabove, the amplitude of the modes of the bar potential is fixed to values that fit well the dynamics of the bulge region. Namely, the bar potential is a superposition of three Fourier modes, with the same parametric form as in Thomas et al. (2023), closely resembling the first three even modes of the bar potential derived in Portail et al., 2017. From this same potential, the bar angle phase is fixed to be $\varphi_{\rm b,0} = 28°$. The amplitude of each bar mode m is given by:

$$\phi_{{\rm b},m}(R,t) = G_{\rm b}(t)\,A_{{\rm b},m}(R)\,\Phi_0(R), \quad (2.5)$$

where $G_{\rm b}(t) \leq 1$ is the growth function for the bar, and $A_{{\rm b},m}$ is the relative amplitude of the bar mode given by

$$A_{{\rm b},m}(R) = K_{{\rm b},m}\ (R/R_{\rm b,max})^{a_m-1}(1-R/R_{\rm b,max})^{b_m-1}, \quad (2.6)$$

with $K_{{\rm b},m}$ a global amplitude factor and $R_{\rm b,max}$ the radius at which the mode's amplitude goes to zero. Importantly, we consider that the amplitude has reached a plateau at the present time $G_{\rm b}(t=0) = 1$. The values of $K_{{\rm b},m}$, a_m, and b_m for each of the bar modes are presented in Table 2.2. Only the pattern speed of the bar is adjusted to the location of resonant ridges in local velocity space within our procedure (see the next Section).

The spiral arms potential that we propose is an adaptation of the analytical model of Cox

and Gomez, 2002 described in Monari et al., 2016b, whose amplitude is given by

$$\phi_{\mathrm{s},m}(R,t) = G_{\mathrm{s,m}}(t)\, A_{\mathrm{s},m}(R) \exp\left[\mathrm{i}\, m \frac{\ln(R/R_0)}{\tan p_{\mathrm{s},m}}\right] \Phi_0(R), \tag{2.7}$$

where $G_{\mathrm{s,m}}(t)$ is the growth function for the spiral arms mode m, set to $G_{\mathrm{s,m}}(t=0) = 1$, $p_{\mathrm{s},m}$ is the pitch angle, and $A_{\mathrm{s},m}$ is given by

$$A_{\mathrm{s},m}(R) = \xi_{\mathrm{s},m}(R)\, H_m(R)\, \frac{\Phi_0(R_0)}{\Phi_0(R)}, \tag{2.8}$$

where $\xi_{\mathrm{s},m}$ is the amplitude factor of the mode, normalized to its value $K_{\mathrm{s},m}$ at $R = R_0$ with a radial dependence as follows:

$$\xi_{\mathrm{s},m}(R) = K_{\mathrm{s},m} \frac{(R_0^2 \sin^2 p_{s,m} + m h_{\mathrm{s},m} R_0 \sin p_{s,m} + 0.3 m^2 h_{\mathrm{s},m}^2) \cdot (R^3 \sin p_{s,m} + 0.3 m h_{\mathrm{s},m} R^2)}{(R^2 \sin^2 p_{s,m} + m h_{\mathrm{s},m} R \sin p_{s,m} + 0.3 m^2 h_{\mathrm{s},m}^2) \cdot (R_0^3 \sin p_{s,m} + 0.3 m h_{\mathrm{s},m} R_0^2)} \tag{2.9}$$

This adaptation of the Cox and Gomez, 2002 potential has the advantage of being easily generalizable to 3D. Here, $h_{\mathrm{s},m}$ corresponds to the scale-height of the spiral potential, which we fix to 130 pc. We have checked that our results are not very sensitive to this parameter and are similar for any values between 100 pc and 300 pc. Finally, H_m is a radial cutoff function, parametrized by an inner and an outer cutoff, respectively, $R_{\mathrm{s},m,\mathrm{min}}$ and $R_{\mathrm{s},m,\mathrm{max}}$. The function is simply:

$$H_m(R) = \begin{cases} 1 & \text{if } R_{\mathrm{s},m,\mathrm{min}} \leq R \leq R_{\mathrm{s},m,\mathrm{max}}, \\ 0 & \text{otherwise.} \end{cases} \tag{2.10}$$

This cutoff is chosen for simplicity, in a context where we do not aim for self-consistency. However, in a context where the density-potential pair of a spiral mode is needed at the cut-off, it is desirable to replace the step function by something like $H_m \sim 0.5(1 + \tanh((R - R_{\mathrm{s},m,\mathrm{min}})/\Delta_{\mathrm{cutoff}}))$, where $\Delta_{\mathrm{cutoff}} \to 0$ corresponds to our present case. This will be further explored in Chapter 3. The parameters of the spiral arms (for each mode: amplitude $K_{s,m}$, pitch angle $p_{s,m}$, present-day phase at the Solar position $\varphi_{\mathrm{s},m,0}$, and pattern speed $\Omega_{\mathrm{s},m}$) will be adjusted to the data in the next Section, together with the bar pattern speed Ω_{b}.

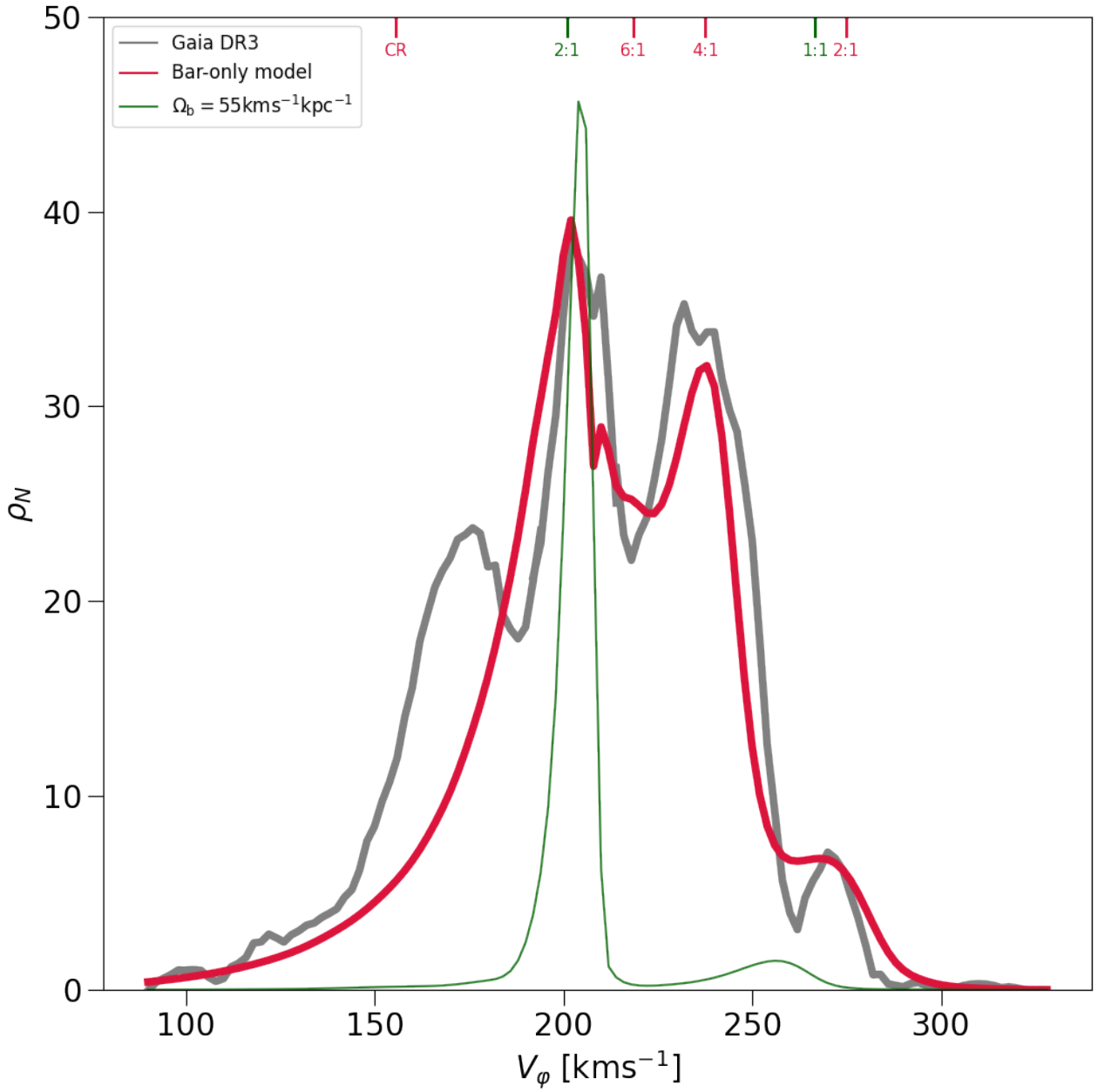

Figure 2.8: 1-Dimensional distribution of the azimuthal velocity of stars in the Solar neighborhood within 99 $\mathrm{kms}^{-1} < V_R < 101$ kms^{-1}, a region of velocity space where the bar impact dominates the distribution (over potential spiral arms signatures). In grey, the stellar distribution from the *Gaia* RVS disk sample in the Solar neighborhood, smoothed with the Savitzky-Golay filter from the `SciPy` library. Red line: the renormalized best bar-only model at $V_R = 100$ kms^{-1}, with pattern speed $\Omega_\mathrm{b} = 37$ $\mathrm{kms}^{-1}\mathrm{kpc}^{-1}$. For reference, we are providing the results for $\Omega_\mathrm{b} = 55$ $\mathrm{kms}^{-1}\mathrm{kpc}^{-1}$ (green line), where only the 1:1 resonance leaves a small signature at higher V_φ than the strong OLR peak. The approximate locations of the different resonances evaluated with Eq. A.5 (described in the Appendix A) represented as red ($\Omega_\mathrm{b} = 37$ $\mathrm{kms}^{-1}\mathrm{kpc}^{-1}$) and green ($\Omega_\mathrm{b} = 55$ $\mathrm{kms}^{-1}\mathrm{kpc}^{-1}$) dashes on top of the plot.

2.3 Fitting procedure and results

2.3.1 Bar-only model

With all the parametric components of the potential defined above, we are now in a position to launch our backward integrations to adjust the parameters to the data. As outlined here-above, the amplitude of the modes and the phase of the bar potential are fixed to values that fit well the dynamics of the bulge region. Only the pattern speed of the bar will now be adjusted to the location of resonant ridges in local velocity space, excluding the spiral arms from the model.

Another hyperparameter to adjust and then fix is the (dummy) integration time, $T_{\rm int}$, within the backward integration context. This will not affect the location of ridges in local velocity space, but will affect their apparent "sharpness". As in Dehnen (2000), we separate the total integration time into two equal-time phases of growth of the bar and plateau of its amplitude, with the following growth function:

$$G_{\rm b}(t) = \begin{cases} 1 & \text{if } -\frac{T_{\rm int}}{2} \leq t \leq 0, \\ \frac{3}{16}\mathcal{T}^5 - \frac{5}{8}\mathcal{T}^3 + \frac{15}{16}\mathcal{T} + \frac{1}{2} & \text{if } -T_{\rm int} < t < -\frac{T_{\rm int}}{2}, \end{cases} \tag{2.11}$$

where $\mathcal{T} \equiv (4t + 3T_{\rm int})/T_{\rm int}$. We choose to adjust those two parameters (pattern speed and dummy integration time) to the 1-dimensional distribution of stars in the Solar neighborhood for azimuthal velocities within 90 $\mathrm{kms}^{-1} < V_\varphi <$ 330 kms^{-1} at $V_R = 100$ kms^{-1}. This distribution is shown in Fig. 2.8. The choice of analyzing the ridges at high V_R prevents them from being "contaminated" by the additional effect of spiral arms since, as we shall see in the next subsection, these distort local velocity space mostly in the central regions of the velocity ellipsoid. This adjustment of the bar pattern speed is made in the Solar neighborhood, which is the most complete volume, so that peaks and valleys are not missing.

Quantitatively, we compare the sum of the squares of the differences of the 1-dimensional distribution of azimuthal velocities in each bin of 2 kms^{-1} between the *Gaia* RVS disk sample and the bar-only model. Only the location of the peaks matters here, so the DF renormalization is applied only in the small V_R range considered in Fig.2.8, instead of the DF normalization applied within the whole local velocity space in all other instances. We find the best match at $\Omega_{\rm b} = 37$ $\mathrm{kms}^{-1}\mathrm{kpc}^{-1}$ for a total (dummy) integration time of 543 Myr, corresponding to 3.2 rotations of the bar. Note however that the velocity peak that can be attributed to Bobylev moving group, or lower part of the Hercules bimodality (at $V_\varphi \sim 160$ kms^{-1} in Fig. 2.8), is not

recovered, and is never so by a bar-only model that also reproduces the hat at large V_φ. Our best value of the pattern speed places the corotation radius of the bar at $R = 6.6$ kpc and its OLR radius at $R = 11$ kpc.

In the first column of Fig. 2.10, we display the distribution of (V_R, V_φ) velocities at the Solar position (setting the value to zero in pixels with no stars in the data within 300 pc from the Sun), of the local (J_φ, J_R) action distribution, as well as the median Galactocentric radial velocity $\tilde{V}_R$ as a function of position within the Galactic plane. Remarkably, the local kinematic distribution corresponding to this bar-only model is already very similar to the observed one, without any additional contribution from spiral arms (see also Monari et al., 2019a, for a less quantitative but similar conclusion). The success of this bar model at producing so many features resembling the observed local kinematic distribution comes from the signatures of the Lindblad resonances of its multiple modes. We confirm this in the Appendix, where we provide a simple formula based on constant energy lines within the improved epicyclic formalism of Dehnen (1999a) in order to evaluate the approximate location of the signature of each bar resonance in local velocity space. At $V_R = 100$ kms^{-1}, these approximate locations of the bar resonances are also indicated as small dashes on top of Fig. 2.8. However, as it also appears clearly in the third row of Fig. 2.10, the bar-only model produces a dipolar structure of median radial velocities within the plane, far from the observed one. This implies that other dynamical ingredients are required to reproduce this median velocity field, which will be the topic of the following subsection. Another clear defect of the bar-only model, locally, is that the Sirius moving group does not stand out in local velocity space. Quantitatively, if one considers the density of stars within a strip of V_φ between 250 kms^{-1} and 260 kms^{-1} in local velocity space, and compares the value at $V_R = -12$ kms^{-1} to that at $V_R = 0$ kms^{-1}, one gets an increase of $\sim$25% in the data at $V_R = -12$ kms^{-1} (the Sirius peak), while one gets a decrease of 11% in the bar-only model (almost identical to the axisymmetric case). This indicates that Sirius is likely caused by spiral arms.

2.3.2 Adding spiral arms

Given the failure of the bar-only model to reproduce the median radial velocity field, the next step is to add non-axisymmetric modes corresponding to spiral arms.

We start by adding a single mode on top of the bar-only model (i.e., with now fixed $\Omega_\mathrm{b} = 37$ kms^{-1}kpc^{-1}), with multiplicity $m \in [1, 2, 3, 4]$. We fix the scale height to be the same as that of the gas component of the background potential, $h_{\mathrm{s},m} = 130$ pc, the outer cut-off to be

the OLR of the spiral, and the inner cut-off to be the larger between the corotation radius of the bar and the ILR of the spiral (so that the spiral lives between its ILR and OLR but does not penetrate within the corotation of the bar). The growth function $G_{\rm s,m}(t)$ has the same form as the bar, and we fix the integration time to exactly one full rotation of the spiral arm mode. In many other attempts, even allowing more than one rotation and a different growth time, the best candidates in the method that follows tend to converge close to the preferred values we found.

The exploration of the whole parameter space with the backward integration method over a large portion of phase-space is computationally very costly, which led us to select the following strategy to fit the Galaxy model to the *Gaia* data. The fit is realized with the differential evolution method of Storn and Price (1997), a global genetic optimization method implemented in the Python `SciPy` library. This algorithm minimizes an objective function, set to be a weighted error function $\mathcal{L} = \sum_i (\tilde{V}_{R,i}^{\rm model} - \tilde{V}_{R,i}^{\rm data})^2/\sigma_i^2$, comparing median radial velocities from model and data on a small selection of points (x_i, y_i) with weights $1/\sigma_i$. The observed median radial velocities $\tilde{V}_{R,i}^{\rm data}$ are calculated within bins of size 250 pc around the selected point (x_i, y_i), whilst the model median radial velocities are the median of the V_R distribution at the selected point, i.e. the model DF values in the (V_R, V_φ) plane integrated over V_φ. The choice of the selected points and their respective weights is a delicate one. The number of points must be limited in order to limit the computation time, but this also means that they must be chosen at 'strategic' positions and not simply on a uniform grid. Moreover, simply weighting them by the number of stars in the data would give too much weight to the Solar vicinity over the entire area of the fit. The first point to which we nevertheless still give the highest weight, $1/\sigma_0$, is the Solar position (x_0, y_0). We then need to choose points which are representative of the variations of the (positive and negative) values of the median radial velocity all over the plane. Adding spiral arms invariably runs the risk of not preserving the roughly correct radial velocity gradient from the bar in the region around $(x_1, y_1) = (7.0\ {\rm kpc}, 3.5\ {\rm kpc})$ and $(x_2, y_2) = (7.0\ {\rm kpc}, 1.0\ {\rm kpc})$, but it is needed to change the sign of $\tilde{V}_R$ at $(x_3, y_3) = (9.0\ {\rm kpc}, 0.0\ {\rm kpc})$. These are our three second-most important points, all with $\sigma_i = 2\sigma_0$. We then choose two pairs of points along constant y axes that encapsulate the positive-negative variations of the median radial velocity field, $(x_4, y_4) = (6.5\ {\rm kpc}, 0.0\ {\rm kpc})$, $(x_5, y_5) = (10.0\ {\rm kpc}, 0.0\ {\rm kpc})$, $(x_6, y_6) = (7.0\ {\rm kpc}, -3.0\ {\rm kpc})$, and $(x_7, y_7) = (10.0\ {\rm kpc}, -3.0\ {\rm kpc})$, with $\sigma_i = 3\sigma_0$. In order to capture the clear spiral feature at the bottom-left of the plane, we also add two points, $(x_8, y_8) = (6.0\ {\rm kpc}, -2.5\ {\rm kpc})$ and $(x_9, y_9) = (7.5\ {\rm kpc}, -2.5\ {\rm kpc})$, with $\sigma_i = 5\sigma_0$. We finally impose a constraint in the outer disk,

$(x_{10}, y_{10}) = (11.5 \text{ kpc}, 1.0 \text{ kpc})$ and $(x_{11}, y_{11}) = (12.0 \text{ kpc}, 0.0 \text{ kpc})$, also with $\sigma_i = 5\sigma_0$. These are the essential points of our fit. We add on top of this a set of low-weight points that will merely help guiding the fit, $(x_{12}, y_{12}) = (9.0 \text{ kpc}, -3.0 \text{ kpc})$, $(x_{13}, y_{13}) = (9.0 \text{ kpc}, 3.5 \text{ kpc})$, $(x_{14}, y_{14}) = (10.0 \text{ kpc}, 3.5 \text{ kpc})$, and $(x_{15}, y_{15}) = (12.0 \text{ kpc}, 3.5 \text{ kpc})$, all with $\sigma_i = 100\sigma_0$. All the selected points are indicated as circles in the bottom-middle panel of Fig. 2.10. This selection of points and their weights hereafter plays the role of a prior on what the most important regions of configuration space are.

For our genetic algorithm, let us now define our population of candidate solutions in parameter space as $\mathbf{a}_{i,g}$, with $1 \leq i \leq n$ and $1 \leq g \leq N$. This means we will consider n candidates for each generation for N generations. In practice, a first generation of candidate solutions is created by picking stochastically many candidate parameters across parameter space by a Latin hypercube sampling, all while trying to cover most of the parameter space within the bounds specified hereafter. This population is then mutated, candidate by candidate, iteratively, thereby establishing a new generation at each iteration. At each generation g, the mutation of each candidate $\mathbf{a}_{i,g}$ is applied according to the "best1bin" strategy with the following steps:

- Select the best parameters candidate (the one minimizing the weighted error function at current generation), $\mathbf{a}_{best,g}$.
- To mutate each candidate $\mathbf{a}_{i,g}$, randomly select two other parameters vector candidates, $\mathbf{a}_{j,g}$ and $\mathbf{a}_{k,g}$.
- Take a fixed multiplication factor (mutation factor $\mathcal{M}$) of their difference in parameters, $\mathcal{M}\left(\mathbf{a}_{j,g} - \mathbf{a}_{k,g}\right)$ to get a vector $\mathbf{v}_i = \mathbf{a}_{best,g} + \mathcal{M}\left(\mathbf{a}_{j,g} - \mathbf{a}_{k,g}\right)$
- The new trial vector $\mathbf{a}_{i,g+1}$ is then built component by component by assigning the value of each parameter either from $\mathbf{v}_i$ or from $\mathbf{a}_{i,g}$ according to if a realization of the binomial function between 0 and 1 is smaller or greater than a chosen recombination value $\mathcal{C}$, respectively.
- Compute the weighted error function for the trial vector $\mathbf{a}_{i,g+1}$: if it performs better in terms of the objective function, it replaces the original candidate in the next generation, otherwise the initial candidate $\mathbf{a}_{i,g}$ remains the same at generation $g + 1$.
- The convergence criteria are met when the standard deviation of the population objective function values at a given generation is smaller than 1% of the mean objective function

value of all candidates in the population in that generation. The final $\mathbf{a}_{best,g=N}$ candidate is kept.

We kept the standard values of the algorithm hyperparameters, notably population size n (15 times the number of parameters), the recombination value $\mathcal{C} = 0.7$, and the mutation factor $\mathcal{M}$, a random variable with values between 0.5 and 1. This method was chosen since it is extremely efficient at converging efficiently over a large parameter space. The selection of points and their weights plays the role of a prior in determining the most important regions of configuration space. However, contrary to a classical Bayesian method, no posterior or well-defined error bars can be given. Therefore, we are not in a position to provide error bars, and we cannot exclude that our best candidate models found hereafter may be local minima in parameter space. Further improvements of the present work should address this question together with taking into account a *Gaia* selection function (e.g., Castro-Ginard et al., 2023).

We first attempted to fit only one spiral arms mode, allowing pitch angles to vary between 6° and 30°, the phase to vary all over 360°, the potential amplitude to vary from zero up to 0.2%, and the pattern speed from 10 $\mathrm{kms^{-1}kpc^{-1}}$ up to the pattern speed of the bar: the mode $m = 2$ performed the best in terms of the objective function among $m \in [1, 2, 3, 4]$, with a pattern speed of 13 $\mathrm{kms^{-1}kpc^{-1}}$. This is the main result of our search, which we will now seek to refine. Indeed, this preferred single mode model clearly produces a distorted local velocity space, especially a very distorted Sirius-like moving group compared to observations. This is not entirely surprising, as local velocity space has not been used to constrain the fit. We then modify the objective function $\mathcal{L}$ with a local constraint, as follows: $\mathcal{L}' = \mathcal{L} + \sum_{i=1}^{i=2}(\Delta_i^{\mathrm{model}} - \Delta_i^{\mathrm{data}})^2/\sigma_\Delta^2$, where Δ_i is the location of the 1-dimensional V_R distribution peak at $V_\varphi = 250\,\mathrm{kms^{-1}}$ $(i = 1)$ and at $V_\varphi = 260\,\mathrm{kms^{-1}}$ $(i = 2)$ at the Sun, and $\sigma_\Delta = 3\sigma_0$ in both cases. Using $\mathcal{L}'$, however, still leads to a best candidate with a distorted Sirius moving group in local velocity space when considering a single $m = 2$ mode, as we illustrate in Fig. 2.9.

Then, in order to possibly improve over this model, we attempt a new fit that adds a second spiral mode with multiplicity $m = 3$ or $m = 4$, together with the first one and the bar. We assume the $m = 2$ spiral to have a range of pattern speeds $10\ \mathrm{kms^{-1}kpc^{-1}} < \Omega_{\mathrm{s},2} < 14\ \mathrm{kms^{-1}kpc^{-1}}$, close to the value found for the single mode fit, which we aim to improve upon. To reduce the parameter space, the amplitude of the second higher mode – whose pattern speed and pitch angle are allowed to vary from 10 $\mathrm{kms^{-1}kpc^{-1}}$ up to the pattern speed of the bar and from 6° to 30° respectively – is fixed with the equation proposed by Hamilton (2024), relating the respective amplitude of both modes to their pattern speed and pitch angle, namely

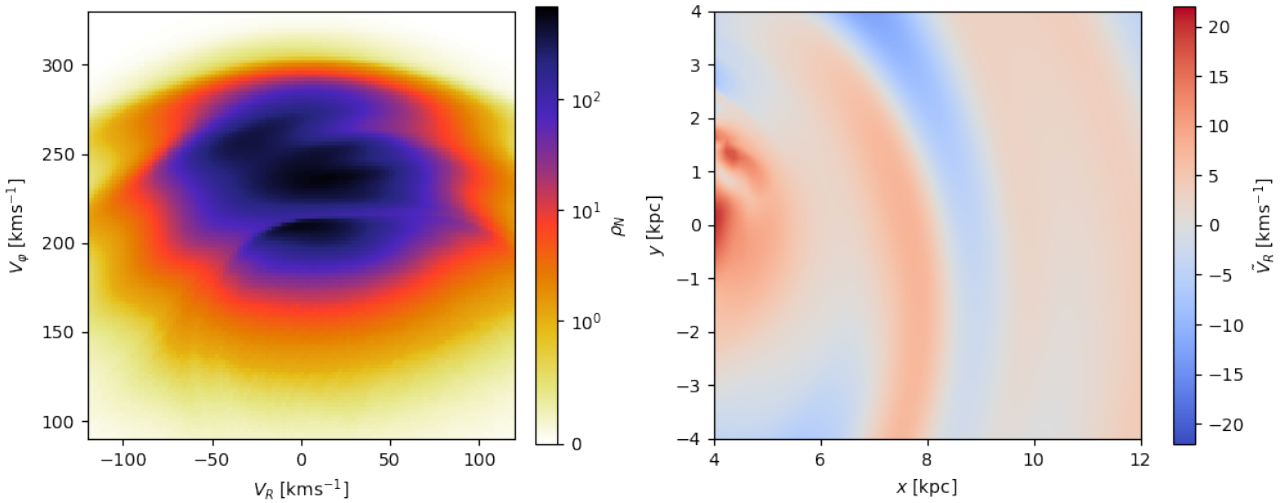

Figure 2.9: Properties of a single $m = 2$ spiral arm added to the bar-only model. In the left panel the distribution the 2-dimensional histogram of stars in the local (V_R, V_φ) plane defined on $[-120, 120]$ kms^{-1}×$[90, 330]$ kms^{-1}, binned with bins of size (2 kms^{-1})^2. In the right panel row, the median $\tilde{V}_R$ (x, y) is shown in the (x, y) plane defined on $[4, 12]$ kpc × $[-4, 4]$ kpc, and binned with bins of size (125 pc)^2.

as being inversely proportional to the product of their pattern speed squared with the tangent of their pitch angle (hence a higher amplitude for lower pattern speed and lower pitch angle). To further reduce parameter space, we impose that the sum of the local density contrasts for both spiral modes is smaller than 35%, checking a posteriori that this limit will not be reached by our best candidate. To compute the surface density contrast of each mode, we take the ratio between the integrated surface density at the Sun of the axisymmetric baryonic component and the spiral arms surface density corresponding to the Cox and Gomez (2002) potential (see also Monari et al., 2016b). In our analysis we found that the secondary $m = 3$ spiral mode does complement the stronger mode better than the $m = 4$ one in terms of the objective function. Adding this second $m = 3$ mode allowed us to taper and regularize the signature of the Sirius moving group in local velocity space while improving slightly the median radial velocity map. To further polish the parameters of this best candidate found with our global optimization method, we then perform a fine search with a gradient descent in a narrow range of parameter space (1 kms^{-1}kpc^{-1} wide in pattern speed, 6° wide in phase, 2° wide in pitch angle and 0.04% wide in potential amplitude $K_{s,2}$) around our best candidate solution, with the Limited-memory Broyden–Fletcher–Goldfarb–Shanno (L-BFGS-B) algorithm implemented in `Scipy`. The solution thus found constitutes our fiducial model.

[1]The parameters are used to compute the background potential, following the definitions in Eq. 2.1 and Eq. 2.2.

[2]The parameters are defined in Eqs (2.6) and (2.8). The surface density contrasts at the Solar radius, Σ_s, are computed from the integrated 3D density equation for spiral arms in Cox and Gomez (2002) over the baryonic

Table 2.2: Parameters of the planar fiducial non-axisymmetric potential fitted in Sect. 2.3.

Bar											
Ω_b	$\varphi_{\mathrm{b},0}$	$R_{\mathrm{b,max}}$	$K_{\mathrm{b},2}$	$K_{\mathrm{b},4}$	$K_{\mathrm{b},6}$	a_2	a_4	a_6	b_2	b_4	b_6
37 $\mathrm{kms^{-1}kpc^{-1}}$	28°	12 kpc	0.25	8.4	210.41	1.8	4.08	5.96	5.08	10.7	16.06

***m*=2 spiral**									
$\Omega_{\mathrm{s},2}$	$K_{\mathrm{s},2}$	$\varphi_{\mathrm{s},2}$	$p_{\mathrm{s},2}$	$R_{\mathrm{s},2,\mathrm{min}}$	$R_{\mathrm{s},2,\mathrm{max}}$	$h_{\mathrm{s},2}$	$\Sigma_{\mathrm{s},2}$	ILR	CR
13.1 $\mathrm{kms^{-1}kpc^{-1}}$	0.15 %	47.8 °	8.1 °	6.6 kpc	26.4 kpc	0.13 kpc	24.9 %	4.1 kpc	17.6 kpc

***m*=3 spiral**									
$\Omega_{\mathrm{s},3}$	$K_{\mathrm{s},3}$	$\varphi_{\mathrm{s},3}$	$p_{\mathrm{s},3}$	$R_{\mathrm{s},3,\mathrm{min}}$	$R_{\mathrm{s},3,\mathrm{max}}$	$h_{\mathrm{s},3}$	$\Sigma_{\mathrm{s},3}$	ILR	CR
16.4 $\mathrm{kms^{-1}kpc^{-1}}$	0.06 %	81.7 °	13.7 °	8.0 kpc	19.6 kpc	0.13 kpc	9.3 %	8.0 kpc	14.4 kpc

2

The final parameters of this fiducial model are presented in Table 2.2, while its local velocity and action space distribution, and median radial velocity map, are presented in the third column of Fig. 2.10. The improvement of the median radial velocity map compared to the bar-only model is striking, but there are also subtle improvements in local velocity space, in particular, a better representation of moving groups close to the center of the velocity ellipsoid. For Sirius, if one reconsiders the density of stars within a strip of V_φ between 250 $\mathrm{kms^{-1}}$ and 260 $\mathrm{kms^{-1}}$, one now gets an increase of 5% at $V_R = -12$ $\mathrm{kms^{-1}}$ compared to $V_R = 0$ $\mathrm{kms^{-1}}$ in the model. This is still a significantly smaller peak than in the data ($\sim$25%), which will require further investigations, but it is a significant improvement upon the decrease of 11% in the bar-only model. In Chapter 4, we will qualitatively compare the predictions of this fiducial model to those of other observables.

2.4 Alternative fitting strategies

In this section, we mention some alternative tools and considerations that could perhaps inspire alternative strategies to improve the fit. Examples include developing fitting strategies that incorporate all axisymmetric parameters and their uncertainties, likely needing to use artificial intelligence techniques, or distinguishing between different chemically-defined stellar populations, or adding constraints from stellar streams on the shape and profile of the dark matter halo. With data from Gaia DR4, as well as from other surveys in the years to come, there will be lots of new opportunities to test the model fitted in this thesis, and also more importantly to enhance it. Hereafter, we mention three alternative tools — two of which we already tested quantitatively on the data, which gave reassuring results compared to the fitted parameters hereinabove.

surface density of the background.

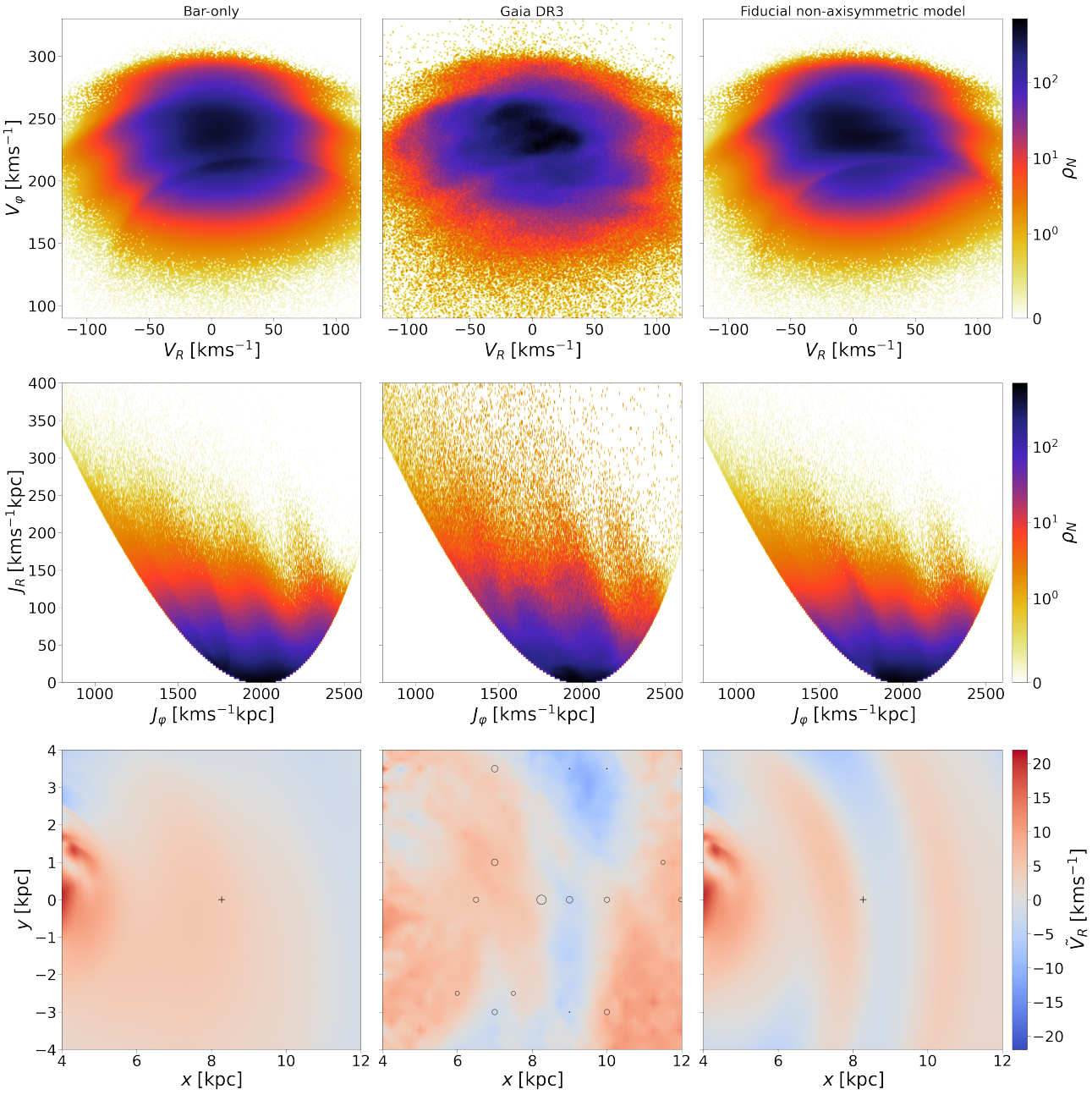

Figure 2.10: From left to right, the columns correspond to the bar-only model, the *Gaia* RVS disk sample, and our fiducial non-axisymmetric model, respectively. Top row: the 2-dimensional histogram of stars in the local (V_R, V_φ) plane defined on $[-120, 120]$ kms$^{-1}\times[90, 330]$ kms^{-1}, binned with bins of size (1 kms^{-1})^2. Middle row: the 2-dimensional histogram of the number density of stars in the (J_R, J_φ) plane defined on $[0, 400]$ kms^{-1}kpc$^{-1}\times[800, 2600]$ kms^{-1}kpc^{-1}, binned with bins of size $(3 \times 2$ km^2 s^{-2}kpc$^{-2})$. For this, the velocities (V_R, V_φ) have been transformed to actions (J_R, J_φ) with `AGAMA`. Bottom row: the median $\tilde{V}_R$ (x, y) is shown in the (x, y) plane defined on $[4, 12]$ kpc $\times$ $[-4, 4]$ kpc, and binned with bins of size (250 pc)^2 for the data and (50 pc)^2 for the models. The cross locates the Sun and circles (with sizes proportional to the weights, the lowest weights being dots) in the middle panel (data) indicate the selected points where the fit has been performed. All panels were smoothed with a bi-linear interpolation.

2.4.1 Markov chain Monte Carlo

An obvious future improvement of our fitting procedure will be to take into account the selection function, for which Bayesian methods are particularly appropriate. As a first exploratory attempt without using any selection function, we performed a Markov Chain Monte Carlo (MCMC) analysis using the `emcee` library (Foreman-Mackey et al., 2013). The fitted non-axisymmetric parameters from Table 2.2 were used as the initial guess, generating a random 7-dimensional box of starting values by perturbing each parameter by a random amount of order 10^{-3} of its fitted value. For the sampling, we employed 14 walkers with a combination of steps, including the "DEMove" differential evolution step algorithm for MCMC proposed by Nelson et al. (2014) and implemented in `emcee`. The error function was reframed as a log-likelihood, and uniform priors were adopted with the same ranges as in the differential evolution fit described in Section 2.3. The resulting posterior distributions, shown in Fig. 2.11, are broadly consistent with the best-fit values from the differential evolution optimization, providing an independent check on the results. However, this procedure is computationally expensive: each iteration is approximately three times more costly than the differential evolution algorithm and requires significantly more iterations to converge. Moreover, the presented corner plot is not long enough, and the chain should be at least four times longer to reach minimum suggested autocorrelation time, which would require an enormous computation time (of much more than 100 000 CPU hours) of computation. So the inferred parameter uncertainties represented in the plot do not necessarily correspond to true physical uncertainties. Such analyses should therefore be interpreted with caution and applied only with careful consideration of their assumptions and limitations. They are however a promising avenue for the future, both in terms of taking a selection function into account and in terms of obtaining reliable error bars on the fitted parameters.

2.4.2 2D measure for the local velocity distribution

We fitted the bar pattern speed on the 1-dimensional distribution of the azimuthal velocity of stars in the Solar neighborhood within 99 $\mathrm{kms}^{-1} < V_R < 101$ kms^{-1}. To use the whole two-dimensional distribution of velocities in the Solar neighborhood, we could use a two-dimensional measure to make an error function, and fit the best parameters by minimizing it non-linearly with a differential evolution algorithm, for example. A suitable choice is the generalized Kull-

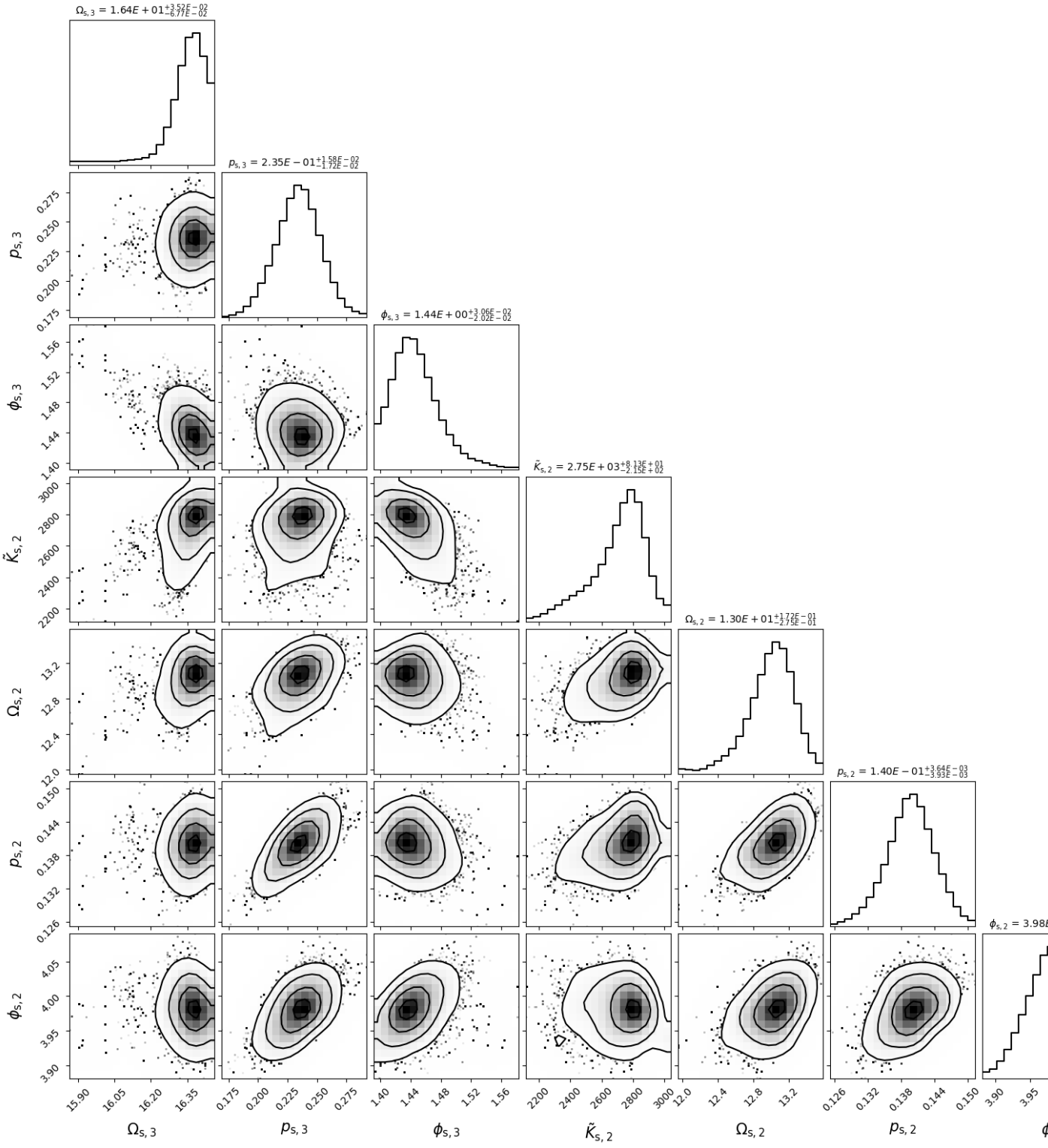

Figure 2.11: Corner plot showing the posterior probability distributions described in Subsection 2.4.1. The diagonal panels display the marginalized distributions, while the off-diagonal panels show covariances between parameters, with contours corresponding to the smoothed 1σ, 2σ, and 3σ credible regions. The one-dimensional histograms have also been smoothed as the chain is not long enough.

back–Leibler divergence (Boyd and Vandenberghe, 2004):

$$\mathrm{KLD}(x,y) = \begin{cases} x\log\left(\frac{x}{y}\right) - x + y, & x > 0,\ y > 0, \\ y, & x = 0,\ y \geq 0, \\ \infty, & \text{otherwise.} \end{cases} \tag{2.12}$$

This measure does not require the data and model to share the same normalization, so the model DF can be given as a probability distribution and compared directly to the observed number density. In practice, the divergence must be symmetrized and bins with zero counts masked, otherwise it returns infinite values. The generalized KL divergence is widely used in information theory, statistics, and optimization, and is implemented in `SciPy`, making it straightforward to apply. Instead of x and y, we use the DF value of the model for each bin or respectively the data number density in each bin, and sum over all bins in the (V_r, V_φ) plane. Surprisingly a quick test returns $\Omega_\mathrm{b} = 37.39$ kms^{-1}kpc^{-1} as the best fit value for a specific region of the (V_r, V_φ) plane, namely for 50 kms^{-1} $\leq V_r \leq$120 kms^{-1} and 150 kms^{-1}$\leq V_\varphi \leq$ 300 kms^{-1}, though this should be treated as exploratory since spiral arms are not included in the model and this value changes dramatically if we change the range of the (V_r, V_φ) grid. The approach can be extended to three dimensions and, in principle, to the Milky Way as a whole, potentially in combination with artificial intelligence methods. However, several drawbacks limit its broader applicability: it is derived under the assumption of Poisson-distributed data (not strictly valid here), it is dominated by high-density regions and thus less sensitive to large-scale gradients, and it is not a true metric, even when symmetrized, it fails the triangle inequality.

2.4.3 Machine Learning methods

Machine Learning methods hold some promises for developing new efficient fitting techniques for the non-axisymmetric gravitational potential of the MW, but balancing computational efficiency and accuracy remains a challenge. In our initial tests, Convolutional Neural Networks (CNNs) have demonstrated some ability to recover the number density distribution function on the (V_R, V_φ) plane, but at significant computational cost. To address this, combining a CNN for fine details with a Transformer for global distribution features, potentially accelerated by GPUs, could be an alternative to improve effectiveness. Additionally, we explored a simple algorithm for Bayesian Optimization approach, using a Gaussian Process surrogate and Probability of Improvement to efficiently navigate parameter space based on a logarithmic Mean Squared

Error objective. While this approach is computationally lighter and more adaptive compared to exhaustive searches, current results have yet to yield accurate parameters recovery, despite requiring longer computation times than differential evolution methods. Nevertheless, Bayesian optimization remains an interesting technique due to its capacity for simultaneous exploration of multiple regions and provision of uncertainty estimates, warranting further investigation.

Chapter 3

3D non-axisymmetric gravitational potential for the Milky Way

In this chapter, we explore 3-dimensional extensions to the 2-dimensional non-axisymmetric gravitational potential fitted in Chapter 2. The axisymmetric potential was already set from the start in three dimensions, while the bar and spiral arm potentials can also easily be extended to three dimensions. This will be the initial discussion of this chapter. We will then focus on a test-particle forward integration approach, to compare to the backward integration method. Such a test-particle approach, while still not being self-consistent, does not suffer from the coarse-grained vs. fine-grained DF problem of the backward integration for long integration times. Here, the test-particles representing pseudo-stars (if going to 2×10^{11} test-particles, which is feasible in principle, they could even represent stars *per se*) are integrated forward in time, following the evolution of the gravitational potential from its axisymmetric initial state to the final non-axisymmetric state. These stars are sampled in 6-dimensional phase-space from the 3-dimensional DF (Eq. 1.27), keeping the planar parameters of the 2D DF (Eq. 2.3) used in Chapter 2, and setting the remaining parameters for the vertical dimension. Although still not self-consistent, this is an important step, as it marks the first steps in adapting the findings of Chapter 2 to more realistic setups, opening new lines of investigation.

3.1 3D extension of the non-axisymmetric potential

We had previously restrained the DF in Eq. (1.27) to the plane to build the planar DF in Eq. (2.3), as used in Chapter 2. To transition back to the 6D phase-space formulation in this chapter, we now apply the full DF with the same parameters as those of the projected DF.

For this, we need to fix the remaining parameters, namely the vertical velocity dispersion at the Sun $\tilde{\sigma}_z(R_0)$ and the vertical kinematical scale-length $h_{\sigma,z}$ (Eq. 1.28). For the latter we set $h_{\sigma,z} = 10$ kpc for both disk components. As for the first, we set $\tilde{\sigma}_{z,\mathrm{thick}}(R_0) = 40$ kms^{-1} for F_{thick}, and $\tilde{\sigma}_{z,\mathrm{thin}}(R_0) = 20$ kms^{-1} for F_{thin}.

Previously, we had also restricted the full potential to the plane in Eq (2.4). Now, in order to generalize it to three dimensions, the 3-dimensional potential can be written as the real part of:

$$\Phi^{\mathrm{3D}}_{\mathrm{tot}}(R,\varphi,z,t) = \Phi^{\mathrm{3D}}_0(R,z) + \sum_m \phi^{\mathrm{3D}}_{\mathrm{b},m}(R,z,t)\exp[\mathrm{i}\,m(\varphi-\varphi_{\mathrm{b},0}-\Omega_{\mathrm{b}}t)] + \sum_m \phi^{\mathrm{3D}}_{\mathrm{s},m}(R,z,t)\exp[\mathrm{i}\,m(\varphi-\varphi_{\mathrm{s},m,0}-\Omega_{\mathrm{s},m}t)], \tag{3.1}$$

The axisymmetric potential is already in 3D, following the definitions of the disky and spheroidal densities in Eq. (2.1) and (2.2), respectively. The axisymmetric parameters are defined in Table 2.1. Continuing the extension, the non-axisymmetric potential parameters fitted in Chapter 2, presented in Table 2.2, will remain the same. For the bar, the parametric form in Thomas et al. (2023) adopted in our work also already includes the vertical dimension. Previously, we had taken its $z = 0$ values. The bar amplitude in 3D is simply the bar amplitude in the plane, $\phi_{\mathrm{b},m}(R,t)$ as in Eq. (2.6), multiplied by a factor depending on z

$$\phi^{\mathrm{3D}}_{\mathrm{b},m}(R,z,t) = \phi_{\mathrm{b},m}(R,t)\left[1+\left(\frac{z}{z_{m,h}(R)}\right)^2\right]^{-1} \tag{3.2}$$

with $z_{m,h}(R) = 0.45R + \Upsilon_m$, and $\Upsilon_m = 0.05$ kpc for $m = 2, 6$ and $\Upsilon_m = 0.025$ kpc for $m = 4$. We notice that, in this formula, the background potential is always evaluated at $z = 0$.

Similarly, the amplitude for the spiral arms, projected on the plane as $\phi_{\mathrm{s},m}(R,t)$ in Eq. (2.7), can also be extended in z by a multiplicative factor. We adapt the version of Monari et al. (2016b) from the solution described in Cox and Gomez (2002).

$$\phi^{\mathrm{3D}}_{\mathrm{s},m}(R,z,t) = \phi_{\mathrm{s},m}(R,t)\left[\mathrm{sech}\left(\frac{K_{\mathrm{s,m}}z}{\beta_{\mathrm{s,m}}}\right)\right]^{\beta_{\mathrm{s,m}}} \tag{3.3}$$

with K and β defined as

$$W_{\mathrm{s,m}} = \frac{m}{R\sin(p_{\mathrm{s,m}})} \tag{3.4}$$

$$\beta_{\mathrm{s,m}} = W_{\mathrm{s,m}}h_{\mathrm{s,m}}\left(1+0.4W_{\mathrm{s,m}}h_{\mathrm{s,m}}\right) \tag{3.5}$$

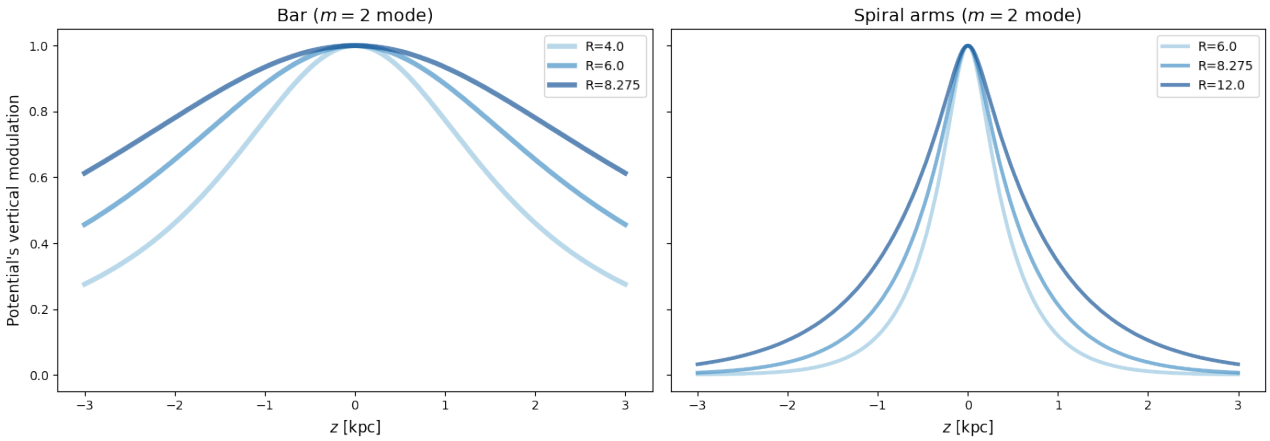

Figure 3.1: Vertical profiles of the bar and spiral arms potentials, as in Eq (3.2) and Eq. (3.3), respectively.

The vertical profile of the bar and spiral arms potential is illustrated in Fig 3.1.

The forward integrations described next are performed entirely with `AGAMA`. The density profiles for the axisymmetric components are described in Chapter 2. These profiles are used by `AGAMA` to solve Poisson's equation to determine the potential by using spherical-harmonic expansion (Multipole) for the bulge and dark matter halo, and azimuthal-harmonic expansion (CylSpline) for the disk components. We also implement the non-axisymmetric components as densities, analytically computing the density expressions corresponding to our bar and spiral potentials with `SAGE` (The Sage Developers, 2025).

We also introduce an additional cutoff to confine the spiral-arm density vertically. For the spiral arms, the density (not the potential) will be limited in z between -1 kpc and 1 kpc using a Heaviside function. We additionally choose a different form than Heaviside (Eq. 2.10 in Section 2.2) for the cutoff in radius. This is important if we want to manipulate the spiral arm densities as well as the spiral potentials, since the density is obviously not defined at the cut-off for the Heaviside case. The cutoff is given by:

$$H'_m(R) = 2^{-2}\left[1 + \tanh\left(\frac{R - R_{\mathrm{s},m,\mathrm{min}})}{\Delta_{\mathrm{m,min}}}\right)\right]\left[1 + \tanh\left(\frac{R_{\mathrm{s},m,\mathrm{max}} - R)}{\Delta_{\mathrm{m,max}}}\right)\right] \tag{3.6}$$

the transition scale is $\Delta_{\mathrm{m,min}}$ and $\Delta_{\mathrm{m,max}}$ around the inner, and outer cutoff radii $R_{\mathrm{s},m,\mathrm{min}}$ and $R_{\mathrm{s},m,\mathrm{max}}$, respectively. A radial cutoff in density, as for the vertical cut-off, would be even more realistic from a physical point of view, but would be further off from our 2D modeling assumptions. Now, to set this new cutoff H'_m, we compare the median radial velocity maps obtained from in-plane ($z = 0$) backward integrations for different transition scales. We set

equal inner and outer scales ($\Delta_{\rm m}$), and keep the cutoff radii as in Table 2.2. For these analyses, we compare Galactocentric radial velocities maps, on a 33×33 (x, y) grid. The goal is to find proper scales that maintain the results close to those in Fig. 2.10 for the Heaviside cutoff. The quantitative comparison is performed with a mean squared error (MSE) function. With this function we build an objective function to fit the best scales minimizing this function with L-BFGS-B optimization. We let scales ranges from 0.01 kpc to 2.00 kpc. Different MSE are available, we test four MSE definitions: (1) the mean squared difference, (2) a structural similarity–based (SSIM) metric from *scikit-image*, (3) squared differences of spatial gradients, and (4) squared deviation from the correlation coefficient. The correlation-based metric (illustrated in Fig. 3.2) best captured the overall spatial similarity. We found in this case $\Delta_{\rm m=2} = 0.3$ kpc and $\Delta_{\rm m=3} = 1.16$ kpc.

3.2 Test-particle simulations: the forward integration framework

We sample $N_{\rm p}$ pseudo-stars in three dimensions from the DF extended to J_z, and integrate their orbits in the axisymmetric potential for 300 Myr to ensure the equilibrium state of these initial conditions. The sampling and the forward integration are fully performed using `AGAMA`. We now aim to integrate for much longer than in the backward integration, since the computation of moments will automatically give the moments of the coarse-grained DF. For the bar growth, we use an interval of 1 Gyr, and for the spiral arms growth, we keep it at one full rotation. The modulation of the amplitude is then similar to Eq. (2.11). The difference is that in formulation of Chapter 2 we considered the current time to be $t_{now} = 0$, while here we start the evolution of the dynamical potential at $t_{start} = 0$, shifting t_{now} for a positive time to be determined in the following analysis. We write it for the bar and spiral arms as:

$$G(t) = \begin{cases} \frac{3}{16}\mathcal{X}^5 - \frac{5}{8}\mathcal{X}^3 + \frac{15}{16}\mathcal{X} + \frac{1}{2} & \text{if } t_1 < t < t_2, \\ 1 & \text{if } t_2 \leq t \leq T_{\rm int} \end{cases} \tag{3.7}$$

where $\mathcal{X} \equiv 2\frac{t-t_1}{t_2-t_1} - 1$, with t_1 being the time where the amplitude start to grow until t_2 after which it stays stable at unitary value. The characteristic times, t_1 and t_2 will be different for each non-axisymmetric structure. The total integration time is $T_{\rm int}$, and for each test-particle setup, we will also save positions and velocities of all particles every few periods of

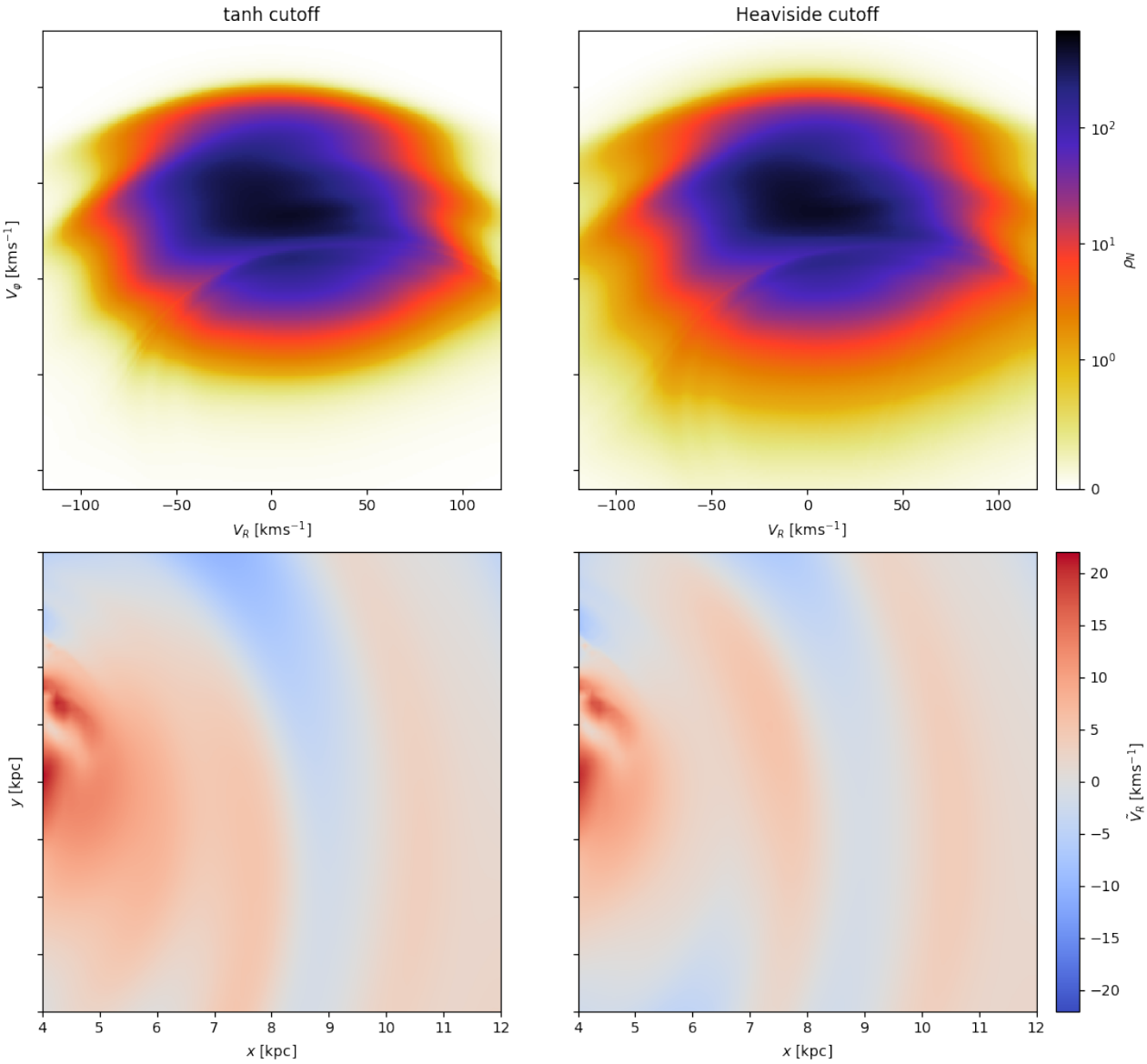

Figure 3.2: In the left panels, results for the backward integration with hyperbolic tangent radius cutoff for spiral arms. In the right panels, the results from Fig. 2.10 for the Heaviside cutoff. Upper panels: the 2-dimensional histogram of stars in the local (V_R, V_φ) plane defined on $[-120, 120]$ kms^{-1}×$[90, 330]$ kms^{-1}, binned with bins of size $(1 \text{ kms}^{-1})^2$. Bottom panels: the median $\tilde{V}_R$ (x, y) is shown in the (x, y) plane defined on $[4, 12]$ kpc × $[-4, 4]$ kpc, and binned with bins of size $(250 \text{ pc})^2$.

time, resulting in a total of N_f frames.

Moreover, as the integrations are longer, it will be interesting to explore a generalization of the bar pattern speed evolution, from constant to decelerating with time. For this, we will have one case of a decelerating bar, where the pattern speed follows the formula adapted from Chiba et al. (2021), used for instance in Dillamore et al. (2024) and Zhang et al. (2025):

$$\Omega_{\rm b}(t) = \begin{cases} \Omega_{\rm b,0}, & t_0^d \leq t < t_1^d, \\ \Omega_{\rm b,0}\left[1 + \frac{1}{2}\varepsilon\,\Omega_{\rm b,0}\dfrac{(t-t_1^d)^2}{t_2^d - t_1^d}\right]^{-1}, & t_1^d \leq t < t_2^d, \\ \Omega_{\rm b,2}\left[1 + \varepsilon\,\Omega_{\rm b,2}(t-t_2^d)\right]^{-1}, & t_2^d \leq t < t_3^d, \\ \Omega_{\rm b,4}\left[1 + \frac{1}{2}\varepsilon\,\Omega_{\rm b,4}\dfrac{(t-t_4^d)^2}{t_3^d - t_4^d}\right]^{-1}, & t_3^d \leq t < t_4^d, \\ \Omega_{\rm b,4}, & t \geq t_4^d. \end{cases} \tag{3.8}$$

with $\Omega_{\rm b,0}$ and $\Omega_{\rm b,4}$ the initial and final pattern speed, respectively. The slowdown rate is $\varepsilon = -\dot{\Omega}\Omega^{-2}$, and $t_0^d, t_1^d, t_2^d, t_4^d$ are free parameters characterizing different deceleration regimes. This function is illustrated in Fig 3.3. Furthermore, the pattern speed $\Omega_{\rm b,2}$ and the characteristic time t_2^d are intermediate. They are defined by:

$$\Omega_{\rm b,2,} = \Omega_{\rm b,0}\left[1 + \tfrac{1}{2}\varepsilon\,\Omega_{\rm b,0}(t_2^d - t_1^d)\right]^{-1} \tag{3.9}$$

$$t_3^d = \frac{2}{\varepsilon\,\Omega_{\rm b,4,}} - \frac{2}{\varepsilon\,\Omega_{\rm b,2,}} + 2t_2^d - t_4^d \tag{3.10}$$

In the case of a decelerating bar, we also re-scale the bar profile radially to $\phi_{{\rm b},m}^{\rm 3D}(\overline{R}, z, t)$ with $\overline{R}$, we do it with the following equation:

$$\overline{R} = \frac{R_{CR}(\Omega_{\rm b})}{R_{CR}(37)} \tag{3.11}$$

with R_{CR} the co-rotation radius satisfying Eq. (1.41) for $l = 0$, numerically solved by finding the scalar root with `Scipy`. Now that we have all elements in place, we will start the next section by finding a correspondence in time between a snapshot of the forward integration and the results of our backward integrations.

3.3 Results

3.3.1 Bar and spiral arms simulated separately

Our main goal here is to find a snapshot in the test-particle simulations that reproduces the results from the backward integrations. The first step for this is to check for the correspondence for each non-axisymmetric component considered individually. For this we setup test-particle simulations for 10^8 particles as described in Table 3.1. In Fig 3.4 we show the median Galactocentric radial velocity maps from the backward integration and forward integration for 3 cases where the potential is solely the axisymmetric potential of Table 2.1 plus one of each non-axisymmetric potential of Table 2.2. For the spiral arms, we use the hyperbolic tangent cutoff of Fig. 3.2. To determine the time at which both results match the best for each structure, we again use the MSE built on the correlation coefficient. We further need to pre-process the frames to follow the rotation of the bar and of each spiral arm, in order to compare backward and forward integration results with the same phase.

We then find that the times when both integration approaches match the best are, respectively, $t = 1210$ Myr for the bar, $t = 850$ Myr for the $m = 2$ spiral mode, $t = 800$ Myr for the $m = 3$ spiral mode. As a reminder, we have started in all three cases the growth of the non-axisymmetric mode at $t = 300$ Myr. The bar ends its growth at $t = 1300$ Myr, hence the best-match is towards the end of the growth of the bar. For these isolated cases, the $m = 2$ spiral mode ends its growth at $t = 780$ Myr (for a 480 Myr growth time) and the $m = 3$ spiral mode ends its growth at $t = 690$ Myr (for a 390 Myr growth time). Hence the best correspondence with the backward integration results would, not very suprisingly, correspond to a young bar and two relatively young spiral modes.

Description	t_1 (Gyr)	t_2 (Gyr)	N_p	T_int (Gyr)
Spiral arms $m = 2$	0.3	0.78	10^8	9.3
Spiral arms $m = 3$	0.3	0.68	10^8	9.3
Bar-only: constant	0.3	1.30	10^8	9.3
Bar-only: decelerating	0.3	1.30	10^7	9.3

Table 3.1: Test-particle simulation parameters for isolated bar and spiral arms.

3.3.2 Behavior for long integration times

It is however interesting to note that these patterns remain particularly stable along the test-particle simulation evolution for the bar case. In Fig. 3.5, we indeed show different snapshots

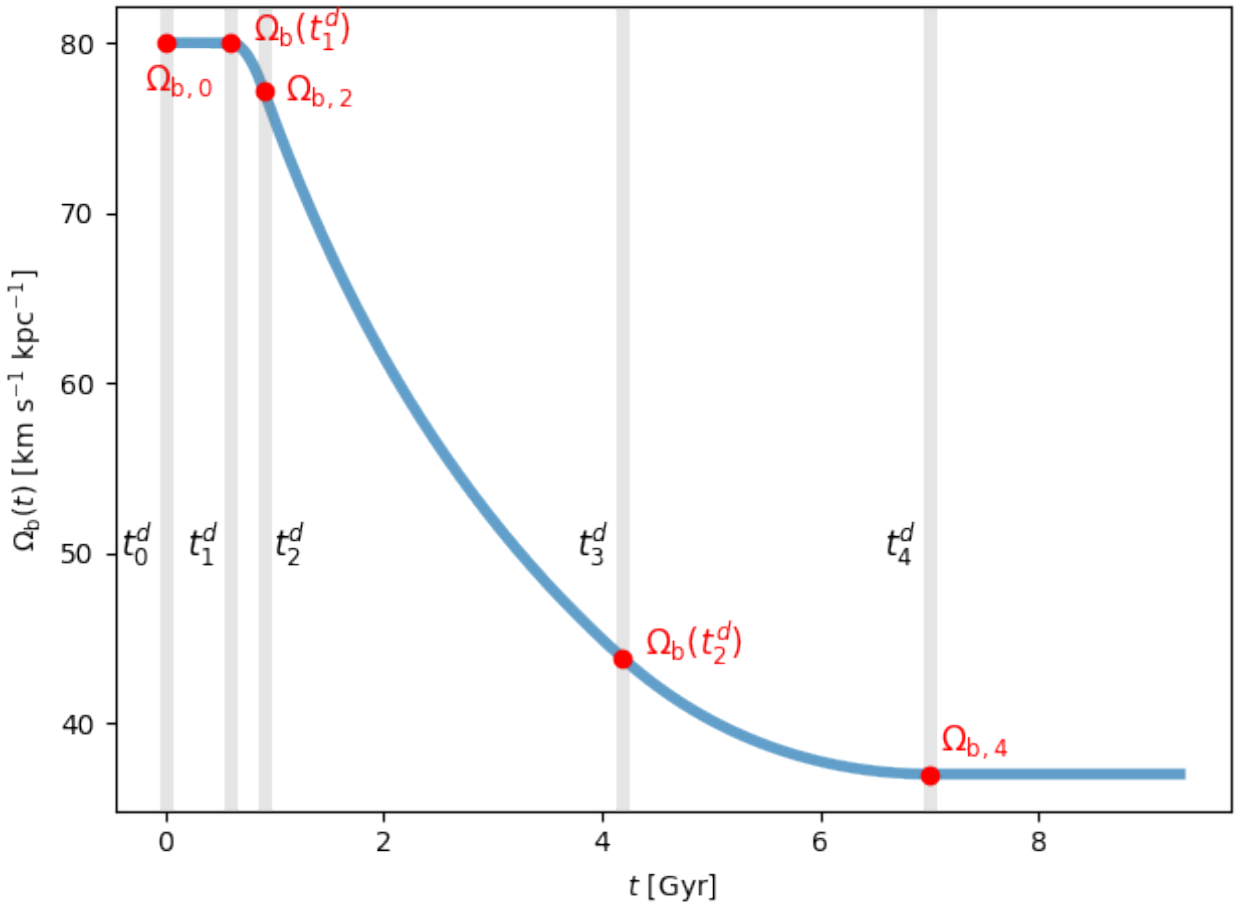

Figure 3.3: The pattern speed deceleration Eq. (3.8) for the parameters used in decelerating bar test-particle setups (see Table 3.1).

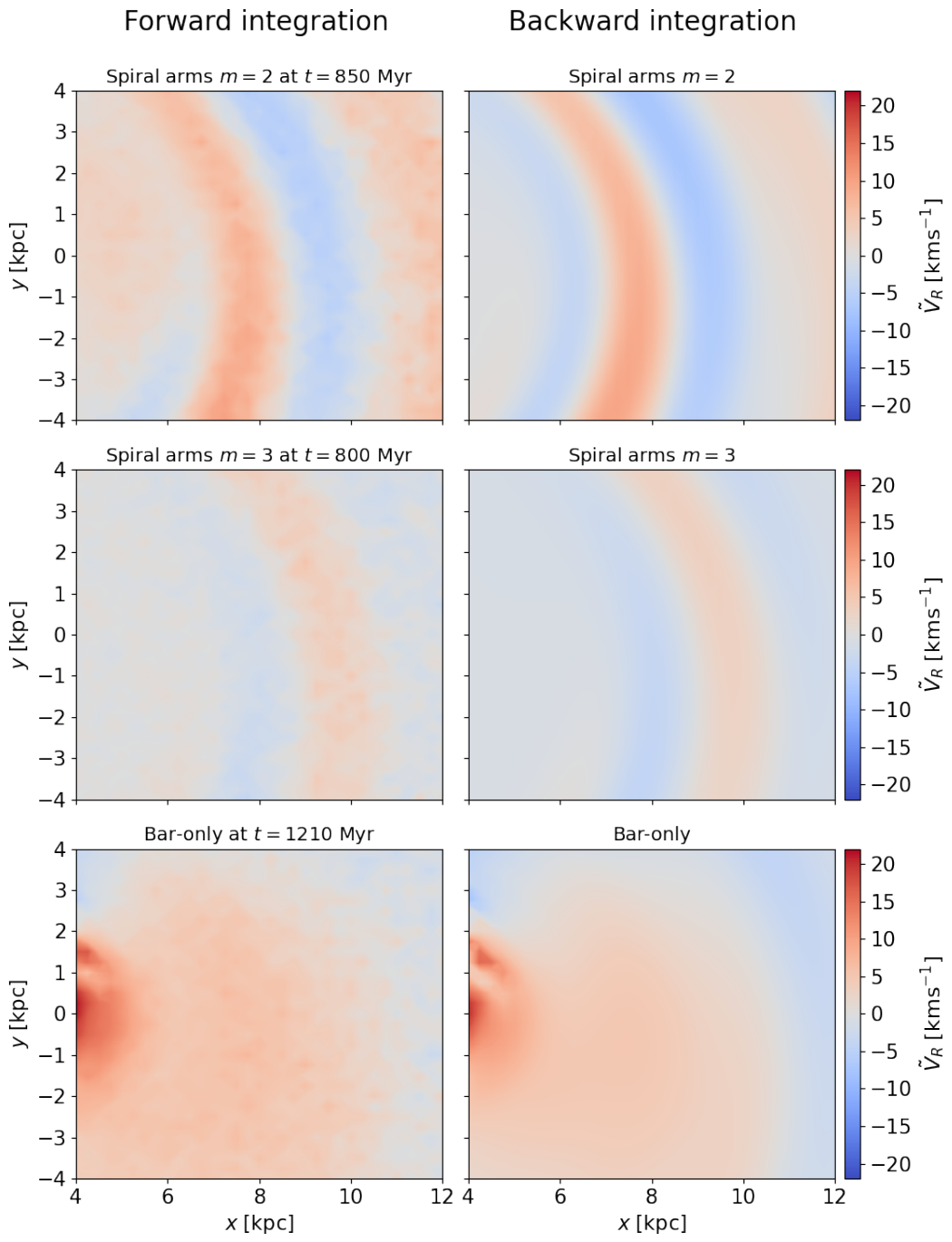

Figure 3.4: Correspondence of backward and forward integration for each non-axisymmetric component on the Galactocentric radial velocity map. The results from forward integrations of 100 million particles are shown in the left column. The results from backward integration are shown in the right column. From top to bottom, we have the spiral arms $m = 2$ mode, followed by $m = 3$ mode, and the bar-only model. The median $\tilde{V}_R$ (x, y) is shown in the (x, y) plane defined on $[4, 12]$ kpc $\times$ $[-4, 4]$ kpc, and binned with bins of size $(250$ pc$)^2$.

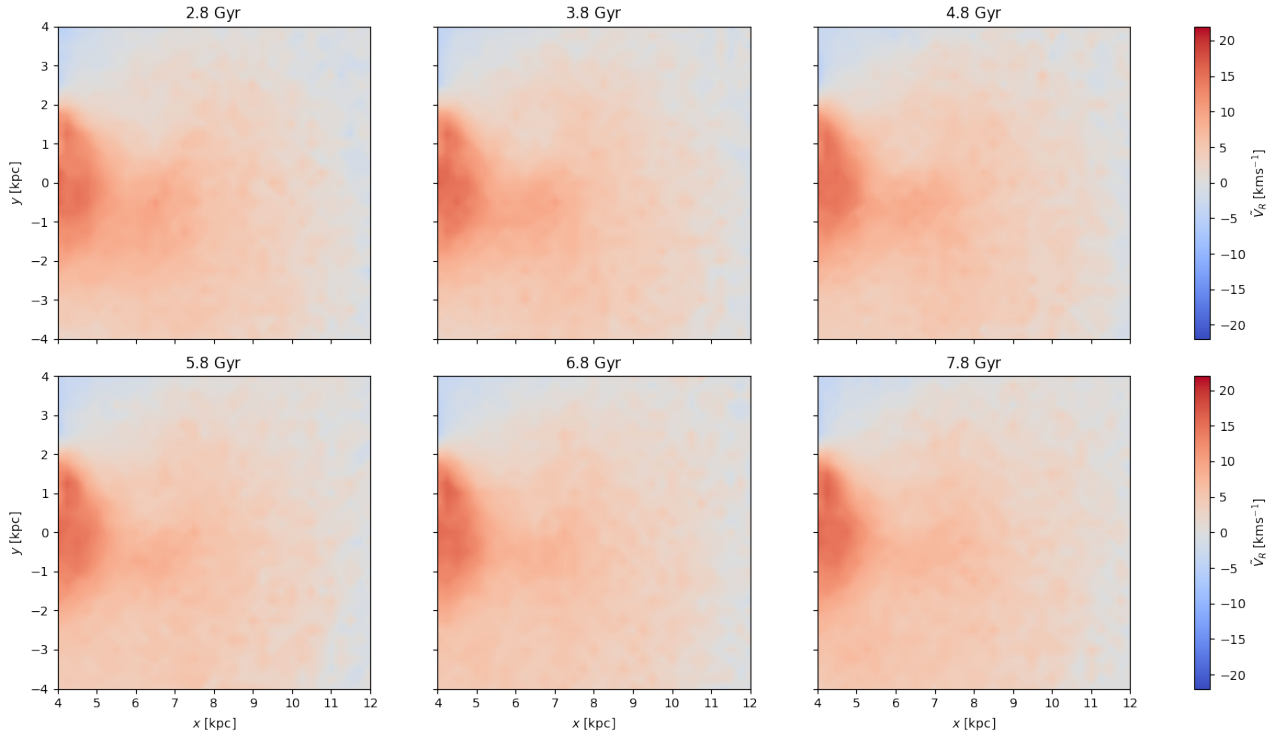

Figure 3.5: Bar-only model test-particle snapshots for constant pattern speed: frames from $\tilde{V}_R$ (x, y) shown in the (x, y) plane defined on $[4, 12]$ kpc $\times$ $[-4, 4]$ kpc, and binned with bins of size $(250\ \mathrm{pc})^2$, always with the same orientation of the bar, at different snapshots. The radial velocity field generated by a constant pattern-speed bar is remarkably stable with time.

of the bar-only model with a constant pattern speed. Overall, the map remains stable. This is re-assuring as it means that the integration time for the backward integration modeling in Chapter 2 was well-chosen for a stable bar. One can however notice some small changes in the amplitude of the median radial velocity for certain regions, notably around $x = 7$ kpc and $y = -1$ kpc. Even the last frame, at 7.8 Gyr, is quite similar to the best frame found previously (see last row in Fig 3.4). Listing the MSE values for all frames, the best match after 7 Gyr is found at 7.5 Gyr, which we will use as the initial time for the first spiral arm to grow in the constant pattern-speed scenario.

As far as a decelerating bar is concerned, the parameters found in, e.g., Dillamore et al. (2024) and Zhang et al. (2025) are for a slightly different evolution periods and not strictly the same axisymmetric and bar-model as used in our work. After exploring some of the parameters for the deceleration, we chose to keep $\varepsilon = 0.003$ as constrained in Chiba et al. (2021). Further, we set the initial pattern speed to be $\Omega_{\mathrm{b},0} = 80.0$ km s^{-1} kpc^{-1} and the final pattern speed as fit in Chapter 2, $\Omega_{\mathrm{b},4} = 37.0$ km s^{-1} kpc^{-1}. The characteristic times defining the different evolutions are $t_0^d = 0$ Gyr, $t_1^d = 0.6$ Gyr, $t_1^d = 0.9$ Gyr, $t_4^d = 7.0$ Gyr, with the pattern speed evolution for these parameters shown in Fig 3.3. The test-particle setup for this case is shown

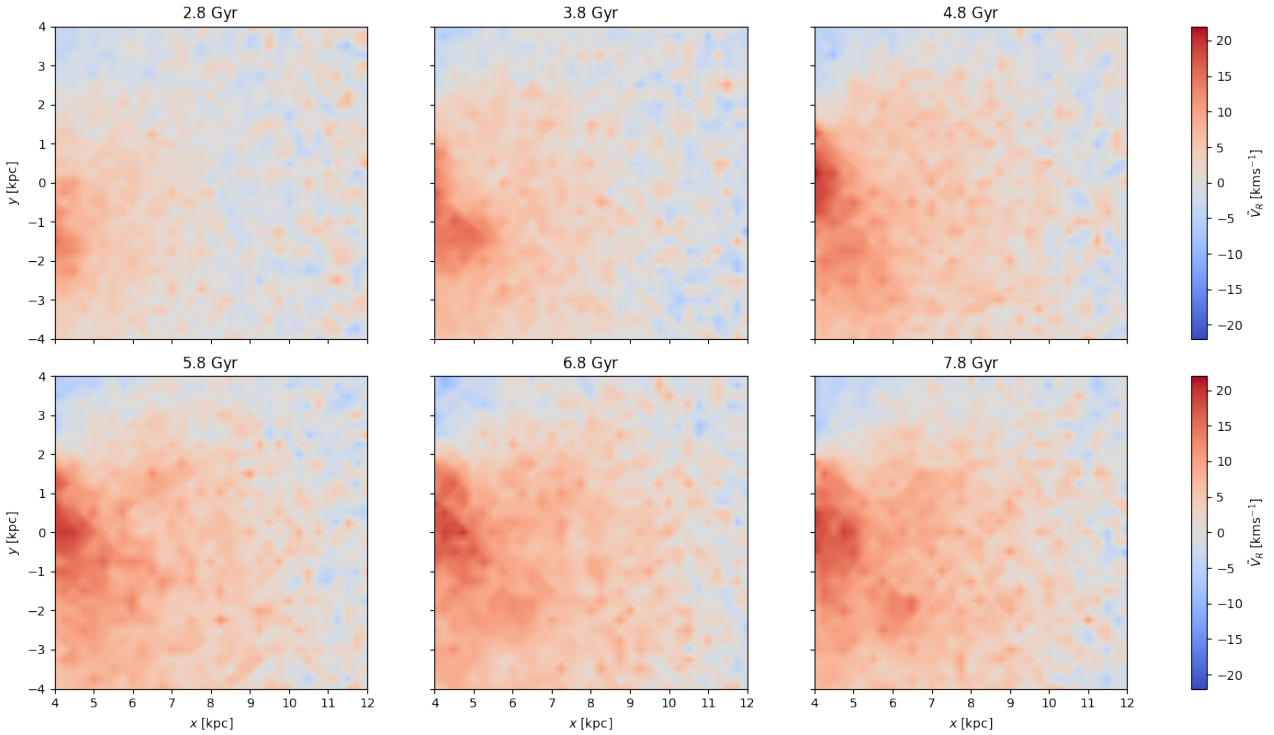

Figure 3.6: Test particle simulation of the bar-only model with decelerating pattern speed of the bar, following Eq (3.8) $\tilde{V}_R\,(x, y)$ shown in the (x, y) plane defined on $[4, 12]$ kpc$\times[-4, 4]$ kpc, and binned with bins of size $(250\text{ pc})^2$.

in the last line of Table 3.1. In Fig. 3.6, we show the results for such a decelerating bar model for different snapshots in time. Listing the MSE values for all frames, we find that the best match with the backward integration for a constant pattern speed after 7 Gyr (once the pattern speed is stabilized to its present-day value) is at 7.57 Gyr, which will serve as the reference initial time for the first spiral arm to grow in the decelerating bar scenario.

3.3.3 Forward-backward correspondence

We now shift the focus to recovering the backward integration radial velocity map in the forward integration approach, for long integration times of the bar (the spiral arms, on the other hand, are considered to be young dynamical features). This time, we increase the number of particles in the sample to 2×10^8 to better populate regions with large Galactocentric radii. We explore four different setups described in Table 3.2, three with constant pattern speed, one with decelerating pattern speed. These setups are simple in the sense that we initially let the bar evolve alone, respectively until 7 500 Myr and 7 570 Myr for the constant pattern speed and decelerating cases. Then we let both spiral arms grow with the same characteristic growth time as in the backward integration modeling of Chapter 2. The mode $m = 3$ is expected to reach

its full amplitude at 7 880 Myr (7 950 Myr in the decelerating scenario), while the stronger $m = 2$ mode is expected to reach its full amplitude at 7 980 Myr (8 050 Myr in the decelerating scenario). These different setups are also a good opportunity to gain a better understanding of the role of the cutoff in the density of the spiral arms.

Spiral arms cutoff	$\Omega_{\rm b}$	$N_{\rm p}$	$T_{\rm int}$ (Gyr)
Heaviside	Constant	2×10^8	9.3
None	Constant	2×10^8	9.3
Hyperbolic tangent	Constant	2×10^8	9.3
Hyperbolic tangent	Decelerating	2×10^8	9.3

Table 3.2: Test-particle simulation parameters for joint old bar and spiral arms.

The frames of test particles simulation for constant bar's pattern speed, described in Table 3.2, are shown in Fig 3.7 for $t = 7.98$ Gyr. This is the time at which both spirals have attained maximum amplitude, and by construction, it is the time when the respective phase of both spiral modes and the bar are exactly the same as in our $t =$ now backward integration scheme. Notably, the result for the Heaviside cutoff is quite similar to the radial median velocity map from the backward integration with Heaviside cutoff. While the amplitudes of the positive median radial velocities appear overall stronger, the negative radial velocity remains stable. On the other hand, the no cutoff case reveals that the Heaviside cutoff introduces a strong negative feature at $x = 6$ kpc and $4 = -4$ kpc, while the hyperbolic tangent nearly blurs it completely, as already seen in the backward integration case. Overall, the three test-particle simulations with constant pattern speed recover fairly well a good portion of the results from backward integration, each with their own limitations. Broadly, it could be said that the hyperbolic tangent cutoff enhances features in at least three regions (upper-left, bottom-middle, bottom-right) while worsening the negative feature between the left and middle region of the bottom part of the plane selection.

In the decelerating bar test-particle simulation, the snapshot for which the respective position of the bar and the two spiral modes is the same as in our $t =$ now backward integration scheme is at 8050 Myr. We show it in Fig 3.8. As this figure illustrates, there are at least cases, such as the one considered here, where the presence of a pattern speed decrease with time for the bar does not change much the present-day radial velocity field of the Galaxy.

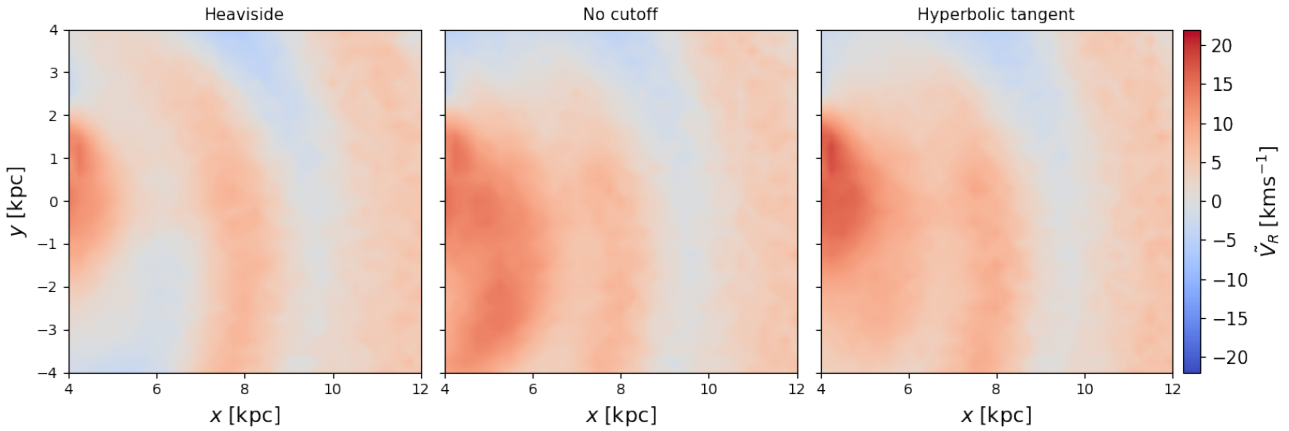

Figure 3.7: Test-particle snapshot at $t = 7.98$ Gyr corresponding to the backward integration median radial velocity map. From left to right, panels of Heaviside, no cutoff, and hyperbolic tangent radial cutoffs for the spiral arms density. Test-particle setups are further described in Table 3.2. $\tilde{V}_R\ (x, y)$ shown in the (x, y) plane defined on $[4, 12]$ kpc $\times$ $[-4, 4]$ kpc, and binned with bins of size $(250\text{ pc})^2$.

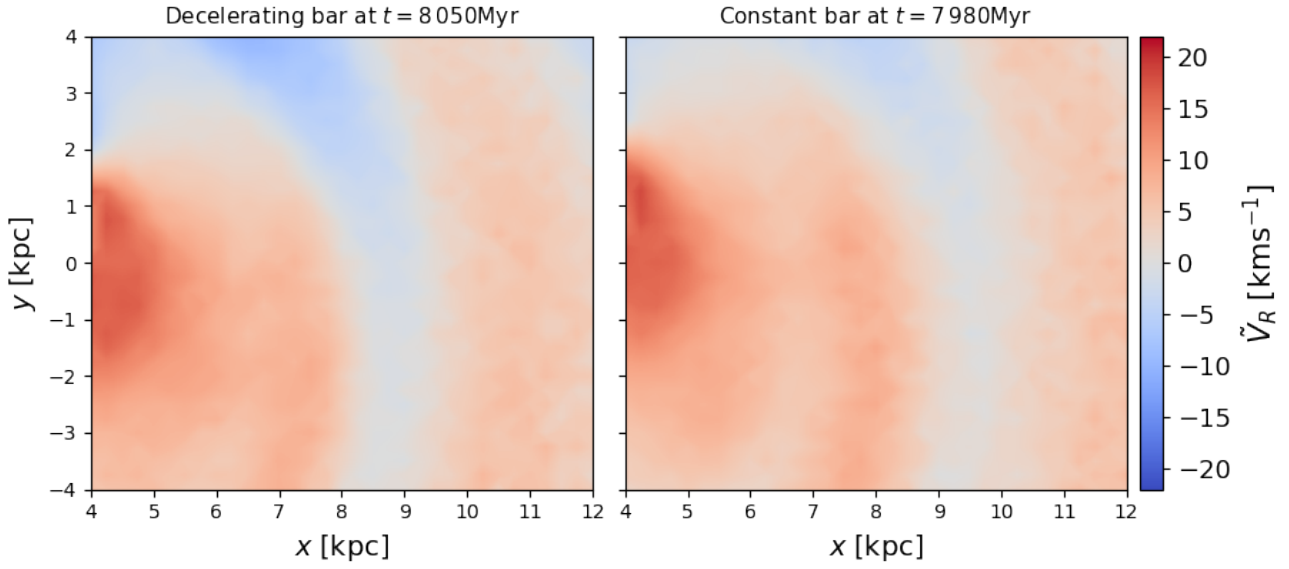

Figure 3.8: Left panel: Snapshot of the decelerating bar test-particle simulation at the time corresponding to the respective phase of the bar and spirals being identical to our fiducial model. Right panel: the constant pattern speed bar simulation is shown also at the snapshot corresponding to the respective phase of the bar and spirals being identical to our fiducial model. The differences are minor. Both simulations are with a tanh cutoff. $\tilde{V}_R\ (x, y)$ shown in the (x, y) plane defined on $[4, 12]$ kpc $\times$ $[-4, 4]$ kpc, and binned with bins of size $(250\text{ pc})^2$.

Chapter 4

Predictions and applications of the models

The work presented in this chapter is mainly based on Khalil et al. (2025a).

In this Chapter, we go back to the 2D fiducial model presented in Table 2.2, which had been adjusted to data with zero prior on the spiral arms locations. We will now check how well the model performs in recovering the position of known spiral arms of the Galaxy, as well as how it fares in reproducing other observables, such as the azimuthal velocity field or the detailed locations of moving groups across the disk.

4.1 Location of spiral arms

In Fig. 4.1, we present the global radial velocity map predicted by our 2D fiducial backward integration model, together with the location of the bar and of the maximum density of the two dynamically-fitted spiral arm modes. The continuous line for each spiral mode in Fig. 4.1 corresponds to the minimum of the spiral potential, and hence to the maximum spiral density, down to the cut-off radius. The correspondence between density and potential is not well defined on the circle corresponding to the cut-off radius, but choosing a smooth function $\sim$ (1+tanh)/2 (Eq. 3.6) instead of a step function (Eq. 2.10) indeed does lead to a sharp density contrast on this circle until the point where the spiral potential reaches zero. This sharp density contrast is marked by the dotted lines in Fig. 4.1.

We also compare the location of those arms to the overdensities of young upper main

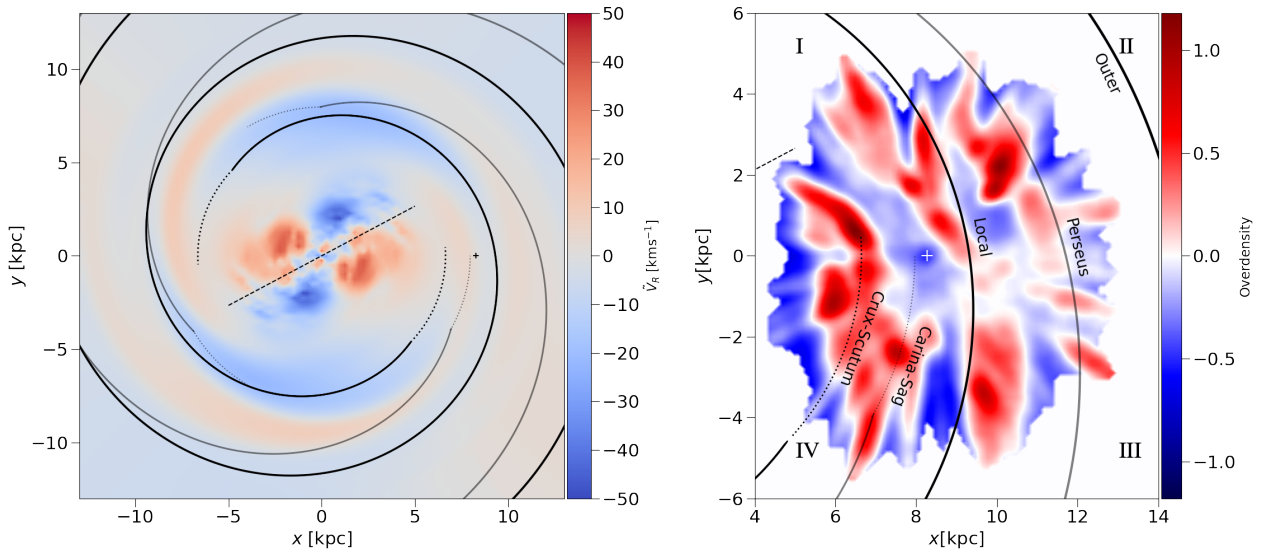

Figure 4.1: Left panel: Median radial velocity $\tilde{V}_R$ for the fiducial non-axisymmetric model in the disk plane (x, y) defined on $[-13, 13]$ kpc $\times$ $[-13, 13]$ kpc binned with $(250 \text{ pc})^2$ bins. Right panel: Adaptation of panel B in figure 1 of Poggio et al., 2021 with over-densities of young upper main sequence stars in red tracing the position of the arms segments. Both panels display the bar position of our fiducial model with dashed black lines, the major $m = 2$ (black) and minor $m = 3$ (grey) spiral locations of our fiducial model as continuous and dotted black and gray lines, respectively. The continuous lines indicate the maximum overdensity of the model spirals as a function of radius from their (negative) potential minimum, down to the cutoff radius. The dotted line then traces an arc of a circle at each cutoff radius, until the point where the spiral potential reaches zero. In both panels, the cross represents the Sun's position. The overdensity maps of young stars following Poggio et al. (2021) are generated from `https://github.com/epoggio/Spiral_arms_EDR3.git`.

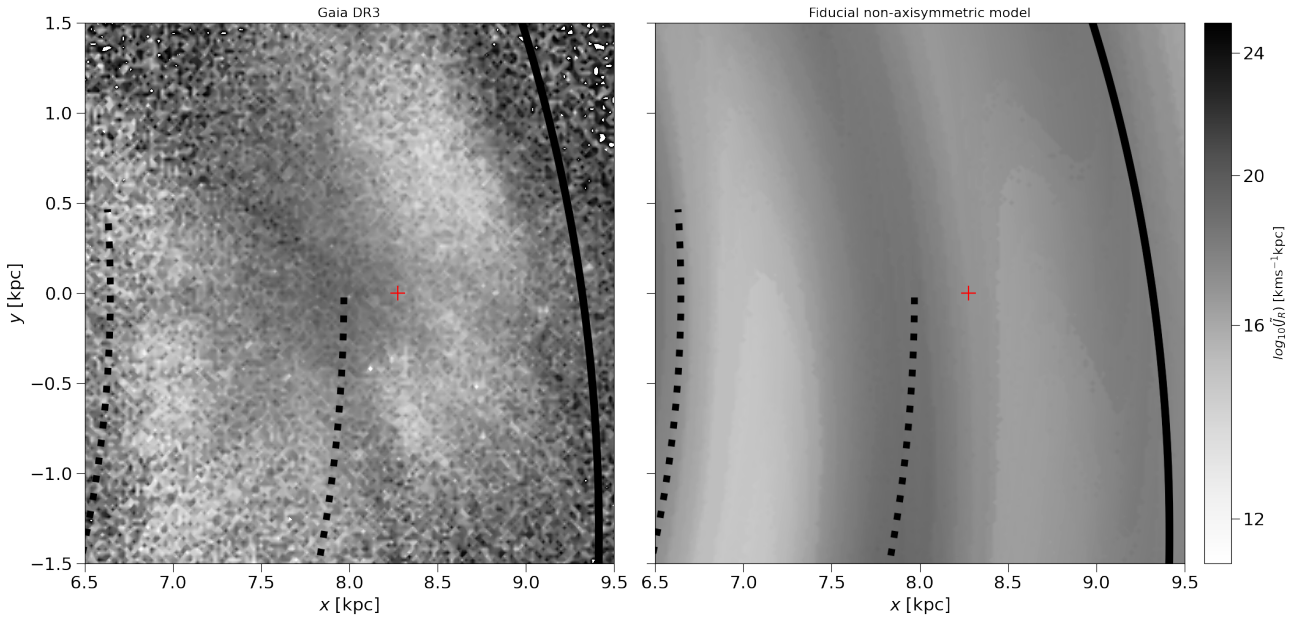

Figure 4.2: The median J_R as a function of position in the data of the extended Solar neighborhood (left panel) and in the model (right panel). The lines indicate the location of spiral arm segments in the model, and the red cross indicates the Sun's position.

sequence stars identified in Poggio et al. (2021). As it appears clearly in the figure, the strongest $m = 2$ mode nicely matches the location of the Crux-Scutum arm close to the Galactic bar (although this arm location is also often labeled as a continuation of the Carina-Sagittarius arm), of the Local arm close to the Sun, and of the Outer arm. However, the distribution of young stars is a consequence of the distribution of the gas, while what we trace is the potential. Therefore, it is most useful to note that our results also appear in line with the findings of Widmark and Naik (2024), who found the Local arm to be a strong local over-density, with a contrast density of roughly 20%, close to the local over-density of 24.9% within our model. Since the pattern speed of the $m = 2$ spiral is smaller than that of the bar, this could be interpreted as a recent disconnection (52.5 Myr ago) from the bar in the Crux-Scutum region, in accordance with the findings of Vislosky et al. (2024). On the other hand, the weaker $m = 3$ spiral nicely matches the location of the Carina-Sagittarius and Perseus arms. It is remarkable that a purely dynamical fit mostly recovers the location of known spiral arm over-densities within the disk.

Another interesting quantity to compare our model predictions with is the median J_R as a function of position in the disk. Indeed, Palicio et al. (2023) identified spiral arm structures in the disk from the median $\tilde{J}_R$ values as a function of position. We reproduce such a map from the *Gaia* RVS data within the extended Solar neighborhood, in Fig. 4.2, and overlay the location of the spiral arms from our fiducial model. We also compute the median axisymmetric $\tilde{J}_R$ values from our model, starting from the same grid of velocities as before at each location in the plane, then computing the corresponding radial actions with `AGAMA` (in the axisymmetric background potential), and computing the median from the DF values. Again, the a posteriori qualitative agreement with the data is remarkable. Note that the increase in median axisymmetric $\tilde{J}_R$ is positively associated with the presence of spiral arms in our model, in accordance with the findings of Debattista et al. (2025) when considering instantaneous axisymmetric actions. In N-body simulations, one typically needs to average actions over a long-enough timescale to even better track the spirals for low values (Debattista et al., 2025) of the median time-averaged radial action. In our case, the important takeaway is the a posteriori qualitative agreement between the data and model for the instantaneous $\tilde{J}_R$, without having used this quantity in the fitting procedure.

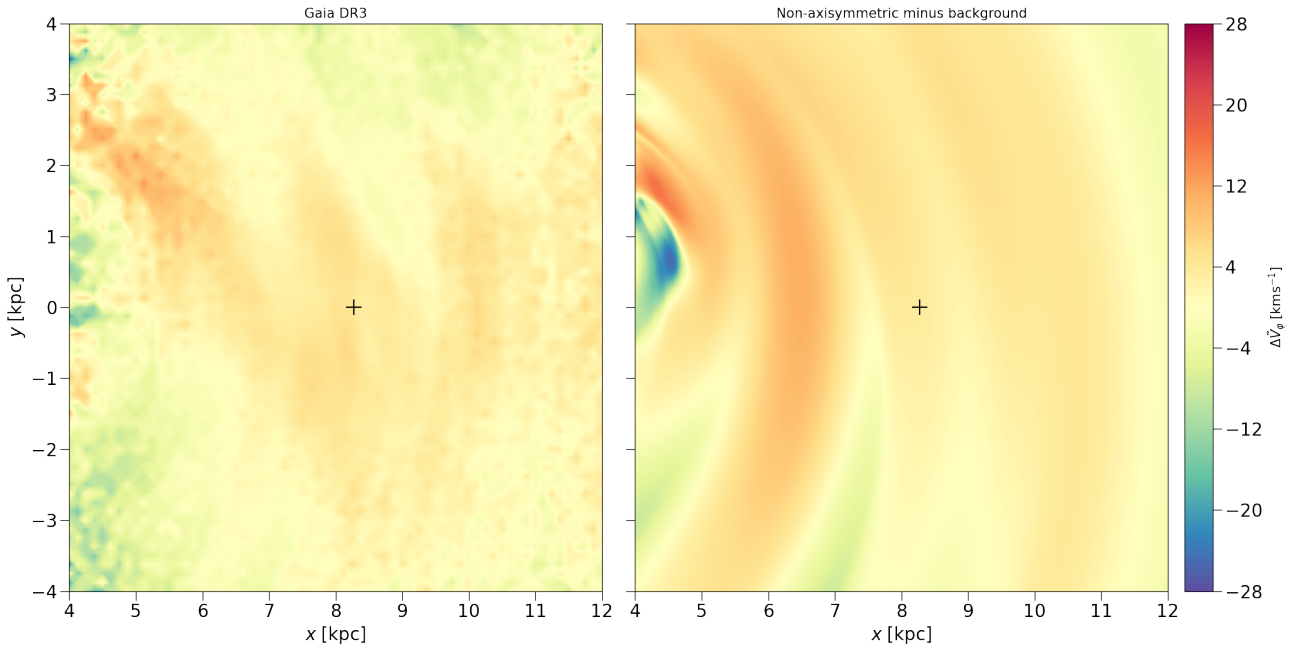

Figure 4.3: Left panel: difference of the median azimuthal velocity compared to its average value at fixed R in the *Gaia* RVS data, $\Delta\tilde{V}_\varphi \equiv \tilde{V}_\varphi(x,y) - \tilde{V}_\varphi(R)$, in the (x,y) plane defined on $[4,12]$ kpc $\times$ $[-4,4]$ kpc, binned with $(125\text{ pc})^2$ bins. Right panel: difference between the median azimuthal velocity of the fiducial model and that of the background axisymmetric DF. In both panels, the black cross indicates the Sun's position.

4.2 Azimuthal velocity field

An interesting quantity to look at in principle is the variation of the median azimuthal velocity at fixed Galactocentric radius, as this is also a clear signature of the non-axisymmetry of the potential. To avoid being dominated by the background DF and axisymmetric potential, one can plot from the data the value

$$\Delta\tilde{V}_\varphi \equiv \tilde{V}_\varphi(x,y) - \tilde{V}_\varphi(R) \tag{4.1}$$

in the (x,y) plane. This is shown in the left panel of Fig. 4.3. One drawback of showing this quantity is that the azimuthal concatenation at fixed R can only be done in the region where data are available, which is why it was not obvious how to implement such a quantity as a target for the fit itself. From our fiducial model, on the other hand, one can directly subtract from the median radial velocity at each position the median radial velocity obtained from the background DF at the same location. Similar trends to the data can be seen in the model, although the two quantities are not straightforward to compare quantitatively.

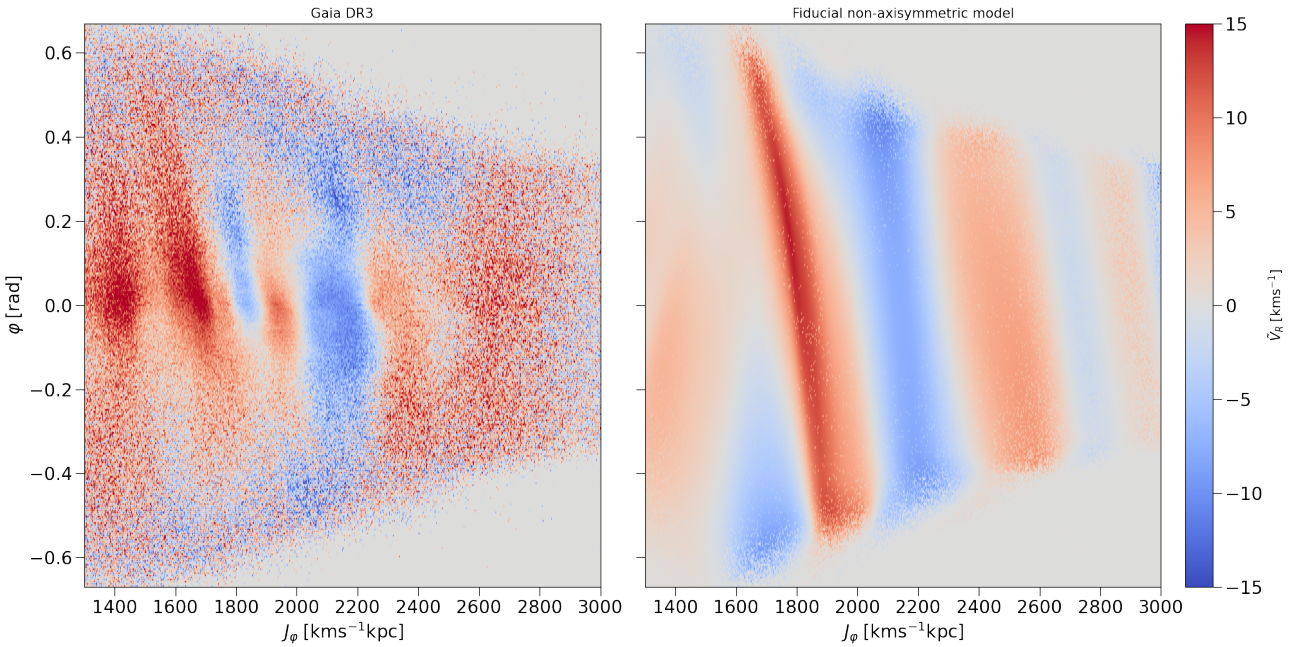

Figure 4.4: Median radial velocity in the (φ, J_φ) plane defined on $[-0.78, 0.78]$ rad $\times$ $[1000, 3000]$ kms^{-1}kpc^{-1}, binned with bins of size $(0.005 \times 2.5$ rad $\times$ kms^{-1}kpc$^{-1})$. Left panel: the *Gaia* RVS disk sample. Right: the fiducial non-axisymmetric model. Points outside 5 kpc $< x <$ 12 kpc and -4 kpc $< y <$ 4 kpc are excluded in both the data and model.

4.3 Median radial velocity in the azimuth-angular momentum plane

An interesting projection of *Gaia* data (see, e.g., Friske and Schönrich, 2019; Monari et al., 2019b; Trick et al., 2021; Chiba et al., 2021) is the structure of median (or mean) radial velocity in the azimuth-angular momentum plane. In Fig. 4.4, we display the median radial velocity in the (J_φ, φ) plane for stars within a box $[1300, 3000]$ kms^{-1} kpc $\times$ $[-0.67, 0.67]$ rad, within $5\,\mathrm{kpc} < x < 12\,\mathrm{kpc}$ and within $-4\,\mathrm{kpc} < y < 4\,\mathrm{kpc}$. To compute the median values in the model, we first fix an azimuth φ_i every 0.01 rad, then consider radii R_j spaced 10 pc from one another. Next, for each point we compute the DF with the backward integration method for different velocities V_R and $V_{\varphi,n} = \frac{J_{\varphi,n}}{R_j}$. We then fix $J_{\varphi,n}$ and sum the values of the DF for all radii R_j, and we compute the median radial velocity for each $(\varphi_i, J_{\varphi,n})$. The qualitative agreement with the data is acceptable, although one can note that the signatures become weak at low J_φ in the model. This can be related to the fact that our non-self-consistent procedure is not particularly reliable in the very inner disk close to the bar region. It could also reveal that our constant pattern speed bar is not enough to explain the richness of the data within this plane (Chiba et al., 2021), that we are missing the effect of vertical perturbations (e.g. Laporte et al., 2019; Laporte et al., 2020), as well as accreted prograde structures, although all

this would require further investigations.

4.4 Moving groups across the disk

In Bernet et al. (2022) and Bernet et al. (2024), a methodology was developed to perform a blind search for moving groups in *Gaia* data across the whole disk, based on the execution of a Wavelet Transform in independent small volumes of the disk followed by a grouping into global structures with the Breadth-first search algorithm from Graph Theory. Fixing a given V_R, one can then, for instance, look at the evolution of the location of moving groups in the (R, V_φ) plane at the azimuth of the Sun, or in the (φ, V_φ) plane at the radius of the Sun. In Fig. 4.6, we overlay the structures found in *Gaia* DR3 on top of the density from our model. The azimuthal distribution of moving groups (right panels of Fig. 4.6) is well in line with the slopes from our model at the Solar radius, while the radial distribution at the Solar azimuth (left panels of Fig. 4.6) also appears globally in line with the data apart from the low $V_\varphi \leq 200$ kms^{-1} region for small $R \leq 6.5$ kpc (the ridges of the model having a much too high slope in that region of phase-space), where the bar self-gravity is probably having a non-negligible effect on the data.

Interestingly, in the model, the Hercules moving group at the Solar radius appears to result from the merging of two ridges at smaller radii, seen as dark regions in Fig. 4.6 in the underlying density of the model, one with a slope compatible with the observed radial gradient of the Hercules moving group, essentially caused by the bar, and another one with a larger slope, mostly due to spiral arms. This is especially clear at positive V_R, where the two ridges are clearly separated at $R < 7$ kpc in the model, while this separation appears to leave a similar signature within the data, too. At $V_R = 0$, the split can also be seen, although it also merges with the inner continuation of the Hyades moving group. At negative V_R, the agreement is less good, though in the region where Hercules is expected to dominate less: the second ridge of Hercules overlaps with the Hyades ridge at $R \sim 7$ kpc in the model, whilst in the data this is only seen as a small upward bend in the Hyades ridge, corresponding to the merging of the ridges in the model. This second Hercules ridge is clearly an effect of spiral arms, while the major Hercules one is produced by the bar alone. The joint effect of the multiple bar modes in the present model, together with the axisymmetric background potential used, might explain the differences with Bernet et al. (2024).

Conversely, we apply the method of Bernet et al. (2022) and Bernet et al. (2024) on the model and overlay in Fig. 4.7 the detected groups on top of *Gaia* data at different radii at the

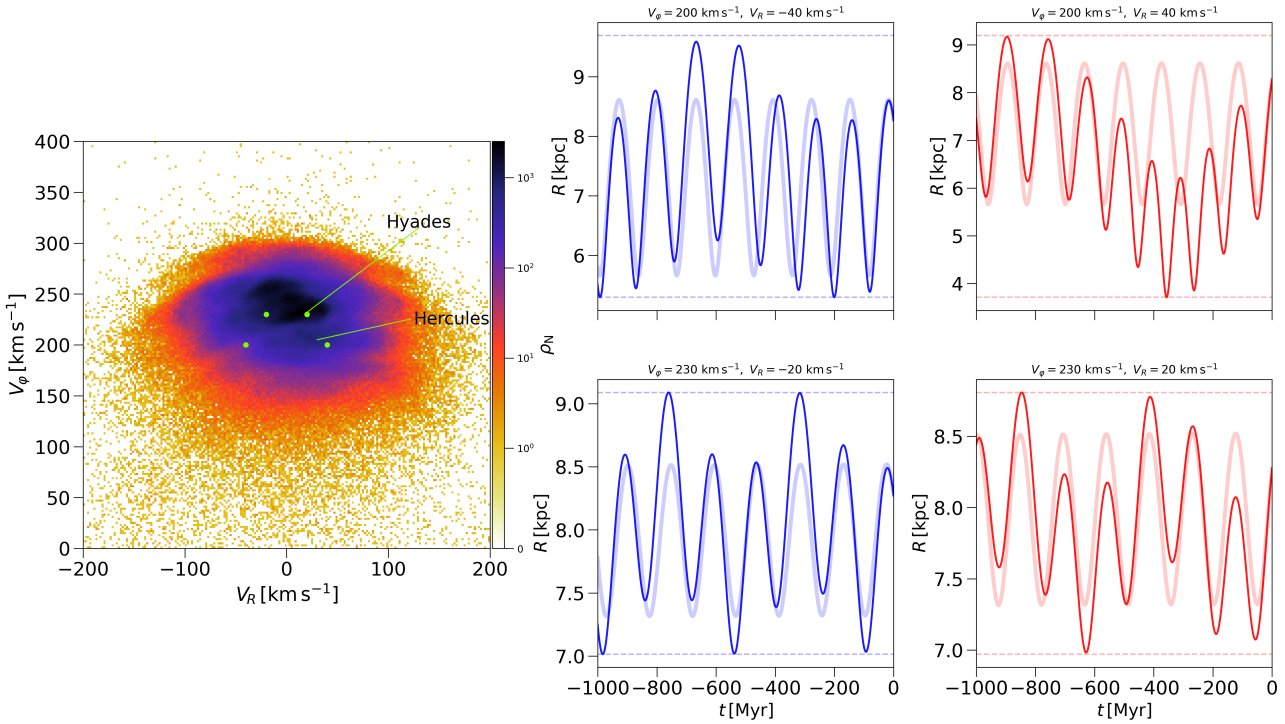

Figure 4.5: In the left panel, the number density of stars in the Solar neighborhood is shown, as described in Fig. 2.1. The lines indicate the positions of the Hyades and Hercules moving groups. In green points selection of two (V_R, V_φ) pairs at same V_φ and opposite sign V_R. At each V_φ, the point of positive V_R is on top of the observed moving group. In the right panels, the orbits from these points are backward integrated using the 2D bar-only model for the strong lines and the axisymmetric model for the lighter lines. The potentials are described in Chapter 2. This indicates interesting features of the moving groups' stellar orbits, and could be used to understand their chemo-dynamical evolution.

azimuth of the Sun, and at different azimuths at the Solar radius. Visually, some features are strikingly similar in the model and data. An interesting point to note is that, even though not clearly visible by eye, the model does seem to recover an overdensity at the Sun's position (bottom-right feature in the second panels from the left in Fig. 4.7) that can be identified with the location of the Bobylev/Hercules-2 bimodality of Hercules, although much less strongly than in the data. We have also started a collaboration with colleagues from the IAC (Rivero et al., 2025), to study the relation between the dynamics of different moving groups and their age-metallicity distribution (work in progress). For this, we compared, in our fiducial model, the orbits of stars found at different locations in the local (V_R, V_φ) plane, as illustrated in Fig. 4.5.

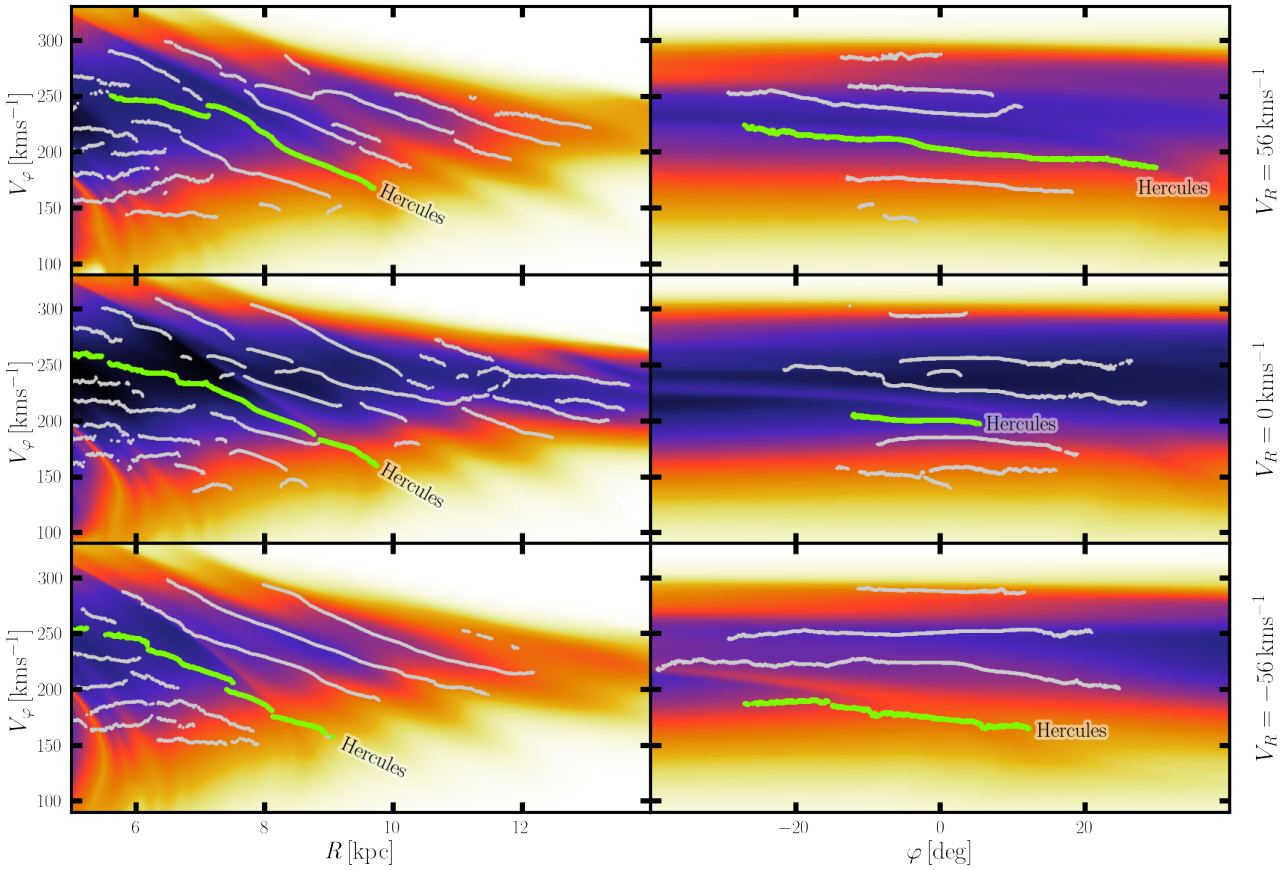

Figure 4.6: At fixed V_R for each row ($V_R = 56$ kms^{-1}, $V_R = 0$ kms^{-1} and $V_R = -56$ kms^{-1}, the white (and green) lines display the main ridges identified in *Gaia* DR3 data with the Wavelet Transform method developed in Bernet et al., 2022; Bernet et al., 2024. Below these lines, we underlay the 2-D histogram distribution of the normalized fiducial model. Left: at fixed azimuth $\varphi = 0°$. Right: at fixed radius $R = R_0$. A thicker green line denotes the Hercules ridge.

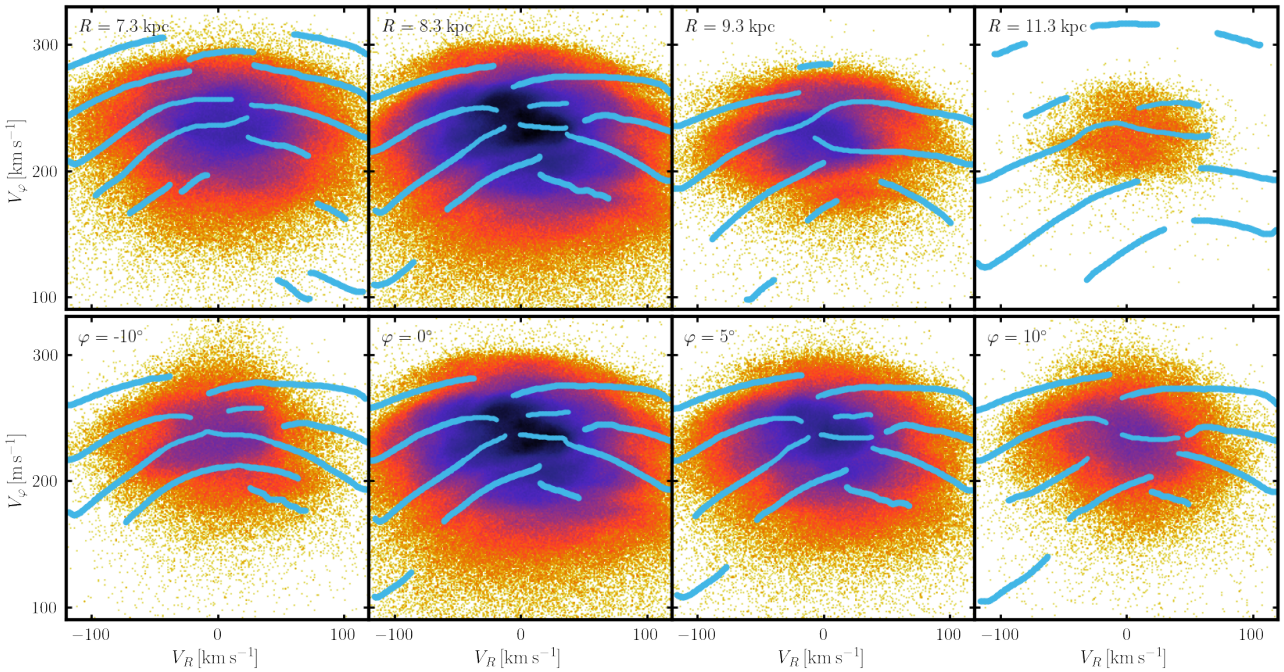

Figure 4.7: 2-D histogram distribution of the *Gaia* RVS disk sample in the (V_R, V_φ) plane for stars within $|\varphi| < 2.4°$ and $|R - R_i| < 300$ pc at different radii $R_i \in [7.3, 8.3, 9.3, 11.3]$ kpc (top row), and for stars within an annulus $|R - R_0| < 300$ pc and $|\varphi - \varphi_j| < \arctan\left(\frac{300}{8275}\right)$ at different azimuthal angles $\varphi_j \in [-10°, 0°, 5°, 10°]$ (bottom row). The colored lines show the peaks identified in our model with the method of Bernet et al. (2022) and Bernet et al. (2024).

4.5 Orbit of the Sun

As an example of application of our model, we propose to compare the in-plane orbit of the Sun in the background axisymmetric model to that in our fiducial non-axisymmetric one. The result is displayed in Fig. 4.8. It is mostly illustrative, and should not be over-interpreted given that the vertical motions are neglected. In the axisymmetric case, the radial period is 161.5 Myr, and the Sun is now close to reaching its pericenter. The time between the last pericentric passage and the one that we are about to reach is a bit smaller in the non-axisymmetric model, namely 154.5 Myr. The previous pericentric passage, which happened a bit later in the non-axisymmetric model, was also closer to the Galactic center than in the axisymmetric case. The last apocenter was very similar in both models, but the next-to-last one was further away in the outer Galaxy in the non-axisymmetric case, for which radial amplitudes are typically larger. If we look at the evolution of the surface density at the Sun's position with time, the picture becomes more complicated. The time between the last surface density maximum and the one that we are about to reach (i.e., still 161.5 Myr in the axisymmetric case) is a bit larger in the non-axisymmetric case, namely 185 Myr, because we will be temporarily following the Local arm overdensity on our journey back to the outer disk. Also, when looking back

at $t \sim -250$ Myr, the apocenter that corresponds to a minimum in the surface density of the axisymmetric model does actually correspond to a local maximum in the non-axisymmetric case, because the Sun was also following a spiral arm at that time. This could have interesting consequences in studying cyclic sedimentation on Earth on long timescales (e.g., Boulila et al., 2018). Since spiral arms are generally expected to arise from a recurrent cycle of groove or edge modes, it is, however, difficult to trace back the Sun's orbit on longer timescales than a few 100 Myr, at least without resorting to detailed (chemo)dynamical modeling of the evolution of the whole Galactic disk. We have started a collaboration on this topic, in particular on the effect of the Galactic potential on the dynamics of the outer Solar system, with colleagues from Paris Observatory (Bougakov et al., 2025, work in progress).

4.6 Orbits of young associations

Young (~ 50 Myr) stellar associations can typically be traced back to their original position by integrating their orbits backward in a given Galactic potential. To illustrate the importance of taking into account the non-axisymmetries of the potential for such a procedure, we integrate forward in time for 50 Myr four archetypal young stellar associations at different positions in the Galactic disk within our fiducial non-axisymmetric model. Each association is represented by 20 stars that are dispersed in velocity and space with Gaussians of standard deviation of 1 kms^{-1} in V_R and V_φ around the circular velocity, and of 2 pc around the positions $(x, y) = (10.6\ \mathrm{kpc}, -2.4\ \mathrm{kpc})$, $(8.7\ \mathrm{kpc}, -0.3\ \mathrm{kpc})$, $(7.1\ \mathrm{kpc}, 0.4\ \mathrm{kpc})$, $(6.0\ \mathrm{kpc}, -0.5\ \mathrm{kpc})$. We then integrate them backward in time, both in the fiducial non-axisymmetric model and in the background axisymmetric model. The associations typically go back to a position that can be erroneous by more than 150 pc in the axisymmetric case, with an elongated shape very different from the true original configuration (Fig. 4.9). This, as well as the previous example on the orbit of the Sun, is just one instance out of the many possible applications of our model to various questions needing an accurate gravitational potential for the Milky Way.

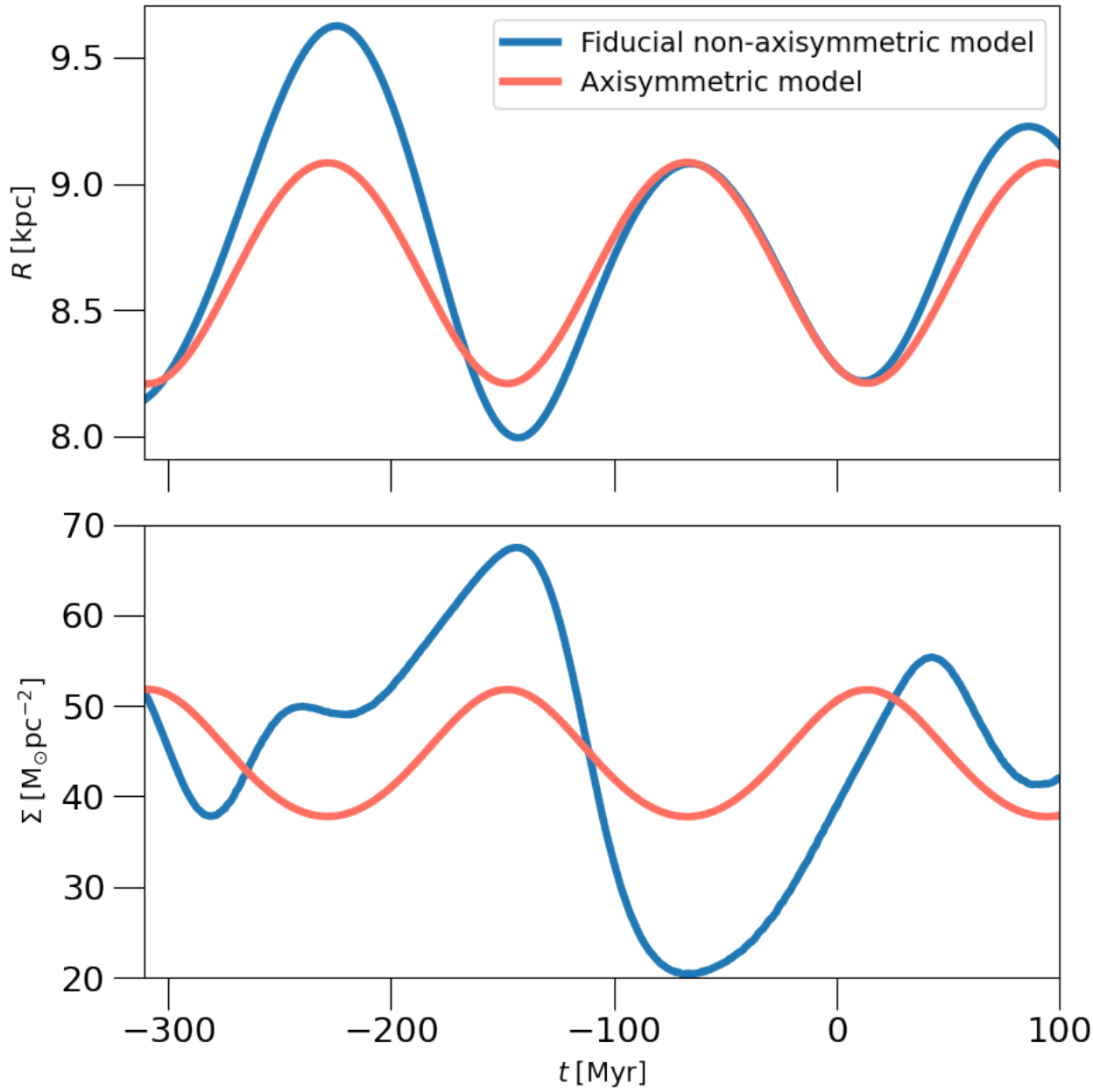

Figure 4.8: Top panel: Galactocentric radius of the Sun as a function of time in the background axisymmetric (orange) and fiducial non-axisymmetric (blue) models. Bottom panel: Evolution of the surface density at the Sun's position with time.

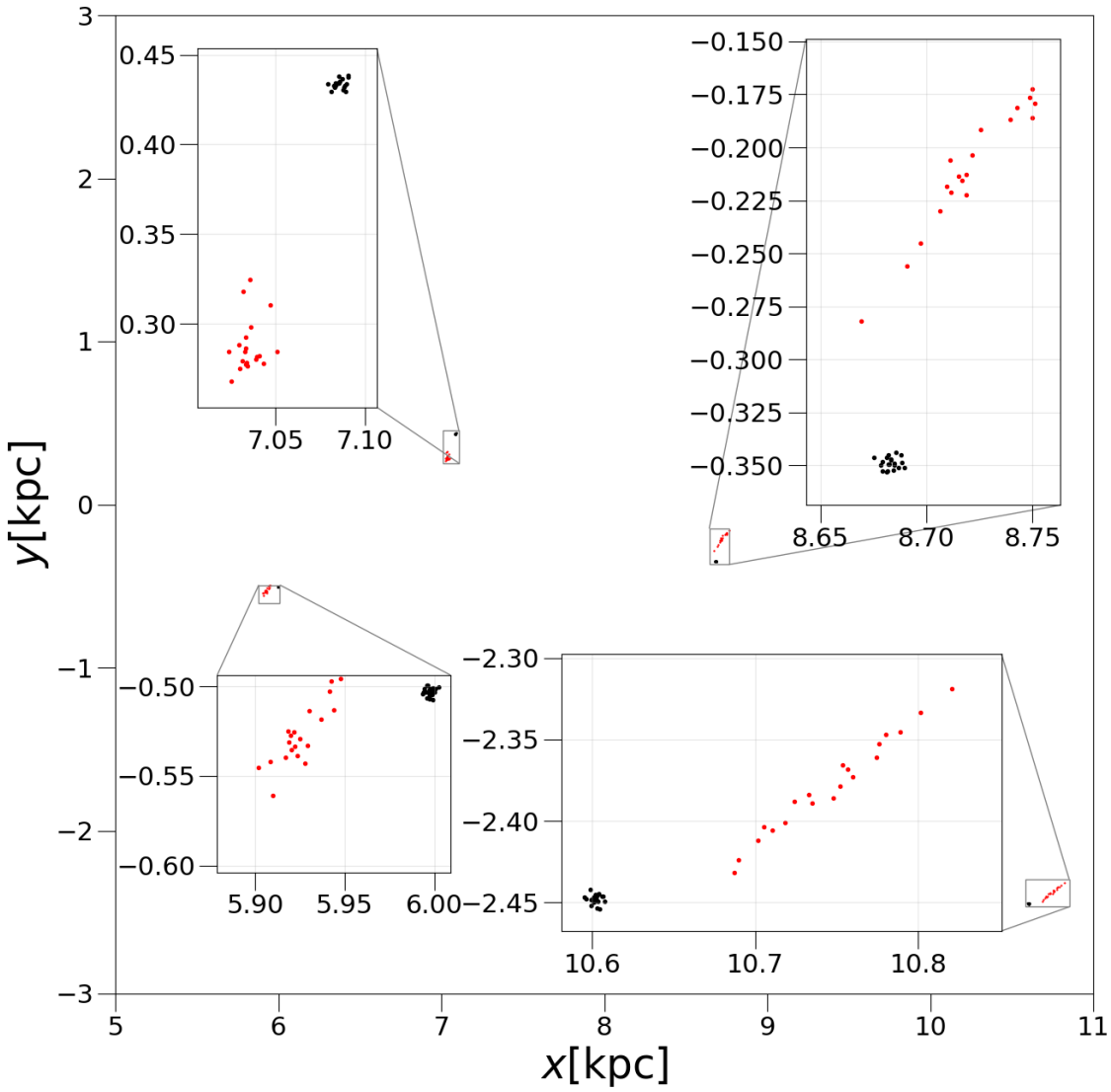

Figure 4.9: The implication of the non-axisymmetries on the orbits of young associations is illustrated by integrating four young associations for 50 Myr forward in the fiducial potential and then backward in time with both the erroneous axisymmetric model (red) and the fiducial one (black). The insets show zoom-ins around the regions of the associations.

Chapter 5

Conclusion and perspectives

In this thesis, I used the in-plane velocities of a large sample of MW disk stars with six-dimensional phase-space information from *Gaia*-`StarHorse` in order to fit a Galactic potential model that includes a detailed parametric shape for the bar and spiral arms, using the backward integration method. The adjusted observable quantities were the median Galactocentric radial velocity, for a selection of points within the Galactic plane, complemented by additional constraints from local velocity space at the Sun's position. This is, to the best of our knowledge, the only such detailed fit of the non-axisymmetric velocity field of the MW that has ever been published in the literature up to now.

All the parameters of the fiducial 2D non-axisymmetric potential are summarized in Table 2.2, within the background axisymmetric potential fixed in Table 2.1. It is remarkable that such a purely dynamical fit recovers many of the known locations of spiral arm over-densities detected from photometry within the disk (Fig. 4.1). These spiral arms can be interpreted as groove or edge modes such as those found in N-body simulations. In the Solar vicinity, I identify the Local arm as a strong gravitational perturbation, in accordance with independent probes of the local non-axisymmetric potential by Widmark and Naik (2024) and by Barbillon et al. (in preparation)[1]. I also recover the observed map of median radial actions in the extended Solar vicinity (Fig. 4.2), as well as a good qualitative agreement with the detailed variation with radius and azimuth of moving groups identified in *Gaia* data (Fig. 4.6). The latter is truly remarkable since the model was not directly fit to these phase-space features. The only (locally) fitted moving group was Sirius, entirely absent from the bar-only model: one can note that it is nevertheless still characterized by a weaker peak in the fiducial model than in the data. While

[1]Preliminary results were presented at the European Astronomical Society Annual Meeting. The talk's slides is available on https://great.ast.cam.ac.uk/Greatwiki/GreatMeet-PM18

my fiducial model may well be a local minimum in parameter space, the latter being particularly vast, especially if letting the parameters of the background axisymmetric density and DF vary too, I nevertheless argued that alternative methods for the fit seem to yield similar fitted parameters and that it can therefore, for the time being, be used as a fiducial non-axisymmetric potential for the Galaxy, for instance in order to confidently integrate in-plane orbits. It can be compared to other recent Galactic potentials such as that of Hunter et al. (2024). The SPIral arms & Bar bACKward integrations `SPIBACK` (Khalil et al., 2025b) tool that I developed in the course of this work to generate local velocity space distributions as well as radial velocity maps is progressively made public. A minimal version is already accesible from my GitHub. A fuller, 3D version of the potential, is available directly within the `AGAMA` library.

The biggest drawback of my analysis has been to neglect the detailed selection function in the fitting procedure, and, partly related to this, the absence of error bars in my computed parameters. In view of this, I have started exploring (Section 2.4.1) how MCMC methods could help one retrieve the fitted parameters. The results are encouraging, but at this stage, they would need much longer computation times to ensure proper error estimates on the fitted parameters. Once this will be fully under control, a proper inclusion of the selection function could then be applied (e.g., Castro-Ginard et al., 2023; Khanna et al., 2024), in order to obtain a proper posterior (and error bars) on the best-fit parameters, while perhaps attempting to separate the stellar populations into distinct DFs.

Another major drawback of the backward integration modeling is that the real observed stellar DF is always measured over finite phase-space volumes, so that it is, in fact, the coarse-grained DF that one measures with data. Over time, phase-space elements of high density are stretched out into infinitesimally thin ridges that get mixed with phase-space elements of lower density, so that the "practical" coarse-grained DF does not actually obey the Vlasov equation. In practice, this means that, if the backward integration is carried out for too long, the fine grained DF tracked by this method would lead to sharp and unsmoothed features in velocity space. To circumvent this problem, the integration was carried out only for a limited time adjusted so that the sharpness of resonant features in velocity space resembles what is observed. Luckily, N-body simulations indicating the existence of recurrent cycles of groove modes in galactic disks allow one to consider that current spiral arm modes of the MW are rather recent. On the other hand, as far as the bar is concerned, I carried out forward-in-time test-particle simulations, also expanded to 3D, that allowed to show how stable the velocity field is with time for a bar with constant pattern speed. This allowed me to show how it is

possible to recover velocity fields such as those fitted with the backward integration method in forward-integrated, finite N, test-particle simulations running over several Gyr with a long-lasting bar and recently grown spiral modes. I also showed that, as far as the median radial velocity field is concerned, a decelerating bar with time does not necessarily change the picture, as illustrated with a model of a decelerating bar in Chapter 3.

From initial estimates, aiming to soon integrate 200 billion test-particles within my 3D non-axisymmetric MW potential seems realistic, which would be, to the best of our knowledge, an unprecedented achievement as this would be the first-ever "star-by-star" dynamical representation of the MW (although not self-consistent). This avenue to enlarge the present PhD work in the coming months will enable a one-to-one comparison of stars with full phase-space information; it will also allow me to devise a detailed study of the different stellar populations, considering measurements such as stellar mass, position in the color-magnitude diagram, age, metallicity, etc. Such a modeling approach would highly benefit from inputs from stellar population synthesis models of the Galaxy such as the BGM (Lagarde et al., 2017; Robin et al., 2022), and would even be perfectly suited for a direct integration within the dynamical part of the BGM itself.

As thoroughly discussed in the introduction of the thesis, *Gaia* data have demonstrated beyond reasonable doubt that the disk of the MW is also vertically perturbed. Test-particle simulations such as those mentioned herinabove are a good tool to make first quick investigations of different possible causes of the perturbations, before moving to self-consistent methods. With a L3 student (Clément Salhi) who I co-supervised, we started exploring the effect on the $z - V_z$ phase-spiral of a vertical kick of the disk, as in Li et al. (2023), within a test-particle simulation including my bar and spiral arms. This is illustrated in Fig. 5.1 for a simple modeling representing the impact on the MW of perturber passage as a Gaussian kick in height and vertical velocity for the whole disk. The phase-space spiral is well visible in vertical motion on the (z, V_z) projection around a more extended neighborhood of the Sun. Scenarios with the non-axisymmetric model and kick were explored, proving to be harder to investigate and interpret, meriting more attention, even with simplification brought by the forward integration. However, such test-particle simulations are not sufficient for studying this problem, as the effect of self-gravity must play a central role (Widrow, 2023) in the development and sustainment of the phase-spiral. I therefore plan to explore this problem numerically and analytically, relying on the action-angle formalism (Binney and Schönrich, 2018) and considering self-gravity. One possibility I envisage would be to use the matrix formalism of linear per-

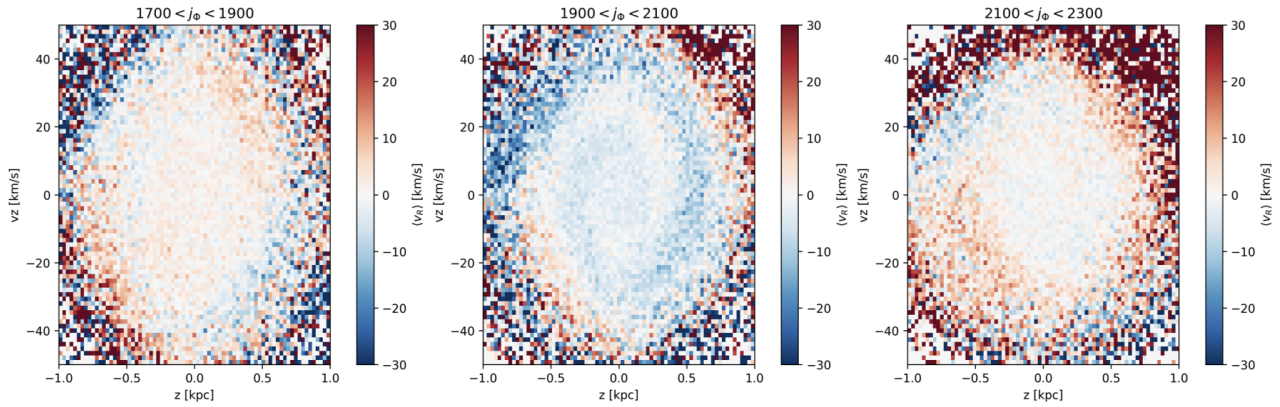

Figure 5.1: Phase-space spirals from a gaussian kick on the disk. Panels show different cutoffs in angular momentum for stars in a perturbed disk. Initially particles were sampled with `AGAMA` for the axisymmetric potential of Table 2.1 and with the DF of Eq. 1.27 and parameters described in Chapter 3. The vertical kick is a Gaussian shift in height, with a Gaussian centered on 400 pc with standard deviation of 150 pc, plus a shift in vertical velocity centered at 5 kms^{-1} with standard deviation of 2 kms^{-1}. The stars are forward integrated within the axisymmetric potential. The kick is done at the time step corresponding to 200 Myr, and the panels are from the 600 Myr snapshot. The observed one arm snail at what correspond to the outer part of the disk is compatible with observations.

turbation theory (see Section 1.2.5) as developed by Simon Rozier and collaborators in the LiRGHaM code (https://github.com/simrozier/LiRGHaM), adapted to thickened disk configurations. More generally, I plan to develop an analytic understanding of different phenomena in non-axisymmetric and vertically perturbed potentials. For instance, relying on the formalism of action-angle variables defined in a resonant zone (see Section 1.2.5, Monari et al., 2017b) of the bar, I am planning to compute analytically the perturbed DF in such a resonant zone when the additional effect of a spiral arm (without first order resonance overlap) is considered, to understand how moving groups generated by bar resonances can be deformed in phase-space in the presence of additional perturbations.

Let us also note that one assumption of the fiducial model was that the spiral arms cannot live inside the corotation resonance of the bar ($R = 6.6$ kpc in the fiducial model), an assumption that could potentially be partially lifted: I already checked that it does not affect much my best candidate model. However, a proper fit of these inner regions of the Galactic disk would require us to make the model self-consistent. The absence of self-consistency can indeed become a serious issue in the innermost parts of the Galaxy, where the bar perturbation is itself the tracer. Some deficiencies of the fiducial model at low radii and low angular momenta have indeed already been identified in Fig. 4.4 and Fig. 4.6. As a first step towards self-consistency, I aim to analyze N-body (or hydro+N-body) simulations of MW-like galaxies, either in an idealized set-up or in a cosmological context (zoom-in) with the same method as in the present

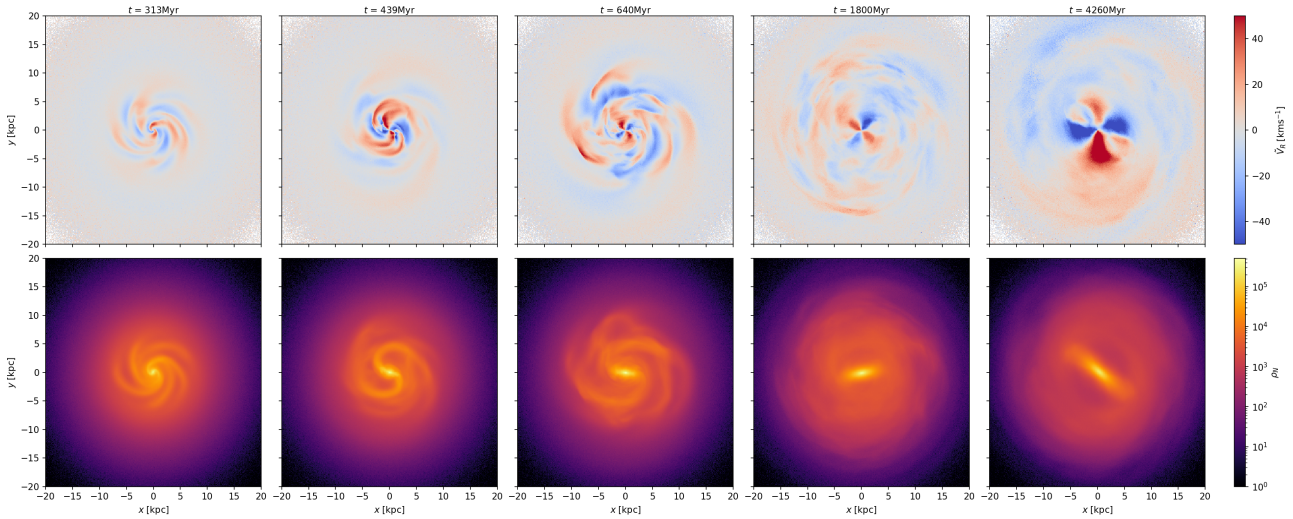

Figure 5.2: Snapshots for stellar particles from a N-body simulation initialized with our axisymmetric potential Table 2.1. The sampling of 835 million particles was done with `AGAMA`. The disk DFs are the same as in Eq. 1.27 with parameters described in Chapter 3. The DF for the bulge and dark matter halo were obtained using Eddington inversion implemented in `AGAMA`. For the gas particles we don't determine the DF, instead we sample the positions from density and assign velocities following the axisymmetric Jeans equation. The top panels show the median radial velocity. Bottom panels show the number density. The non-axisymmetric structures are visible in different snapshots from earlier (left panels) to later frames (right panels). Preliminary analysis shows that the bar formed in this self-consistent simulation has a similar length to the bar model presented in this thesis. The stellar disk, bulge, dark matter halo and gas disk has respectively, 150.3, 16.7, 626.25, 41.75 millions of particles,

work. Such simulations could come from the community/literature, and I have initiated a discussion with Pedro Palicio on this topic with focus on testing the backwards method and action computations, but I am also interested in running my own (idealized) self-consistent simulations. I recently used the axisymmetric potential from Table 2.1 within the `AGAMA` library and assigned each component its own DF, which I sampled with a total of 835 millions of particles. I then integrated these initial conditions in an N-body run — using the SPH-EXA library, designed for large-scale astrophysical simulations — with Ryoanji, a GPU-accelerated module for N-body simulations. It employs the cornerstone octree framework for efficient tree construction, EXAFMM multipole kernels for accurate gravitational interactions, and warp-aware tree traversal inspired by the Bonsai GPU tree code. The density of median radial velocity maps of this simulation are displayed in Fig. 5.2. Using the same simulation code, I could soon relatively easily reach one billion particles within self-consistent tailored simulations similar to those of Naidu et al. (2021), where they explored the merger of GSE with the MW. This could be helpful to characterize and date merger events in the halo and thick disk, as thoroughly discussed in the introduction of the present thesis.

Although definitely beyond the scope of this thesis, future improvements of my modeling methods might rely on an adaptation of the self-consistent made-to-measure method in order to account for self-consistency. This was the method used by Portail et al. (2017) to devise a fiducial model of the Galactic bar, but the methods has never been used for spiral modes. One should also point out that the background model (axisymmetric potential and DF) has not been fitted in this thesis work, and that it could of course in principle also be adjusted to the data. This would vastly increase the parameter space and might require us to use machine learning methods to efficiently explore the full parameter space, using all available information beyond the dynamics of the disk. One obvious such information that would be extremely complementary to the disk velocity field constraints I have used up to now in my Galactic dynamical model would be to include information from stellar streams. These are indeed particularly powerful probes of the gravitational potential far away from the disk (Ibata et al., 2024), but they could also bring complementary information on the non-axisymmetric structures of the disk and their time-evolution. Stellar streams that pass through the disk plane with pericenters smaller than $\sim$ 15 kpc can indeed be significantly affected by the bar and spirals arms, that can lead to resonant confinement of a stream, cause rapid diffusion of a stream as well as the truncation of its length on the leading or trailing side, or can create kinks that make a stream deviate strongly from the orbits of its progenitor. The effect is even stronger for the recently discovered open cluster stellar streams within the disk (Thomas et al., 2023). Halo streams that might already be exhibiting potential signatures of interactions with non-axisymmetric structures of the disk include M92, Ophiuchus, Palomar 5, and Jhelum. Obviously, external perturbations, such as that of the LMC, will also have to be carefully taken into account when considering streams with large apocenters. Another interesting key insight of lumping all these constraints together is that the deceleration of the bar seems to be strongly dependent on the Galactic properties (and consequently on the nature) of the dark matter halo, making it important to explore all these together when fitting a full non-axisymmetric Galactic potential. As a first approach to stellar streams, I have used the spray-particle algorithm of the `AGAMA` library in order to model the tidal stream of Palomar 5 in the presence of my MW bar model, with a L3 student who I co-supervised (Romain Krieger). The developed framework proved to be interesting in understanding the advantages and limitations of the method itself, and also showed great potential and flexibility in testing different scenarios of evolution and parameters for the non-axisymmetric components. The long term goal would be to adjust all these constraints (disk, halo, streams) altogether. As previously noted, the model of Portail et

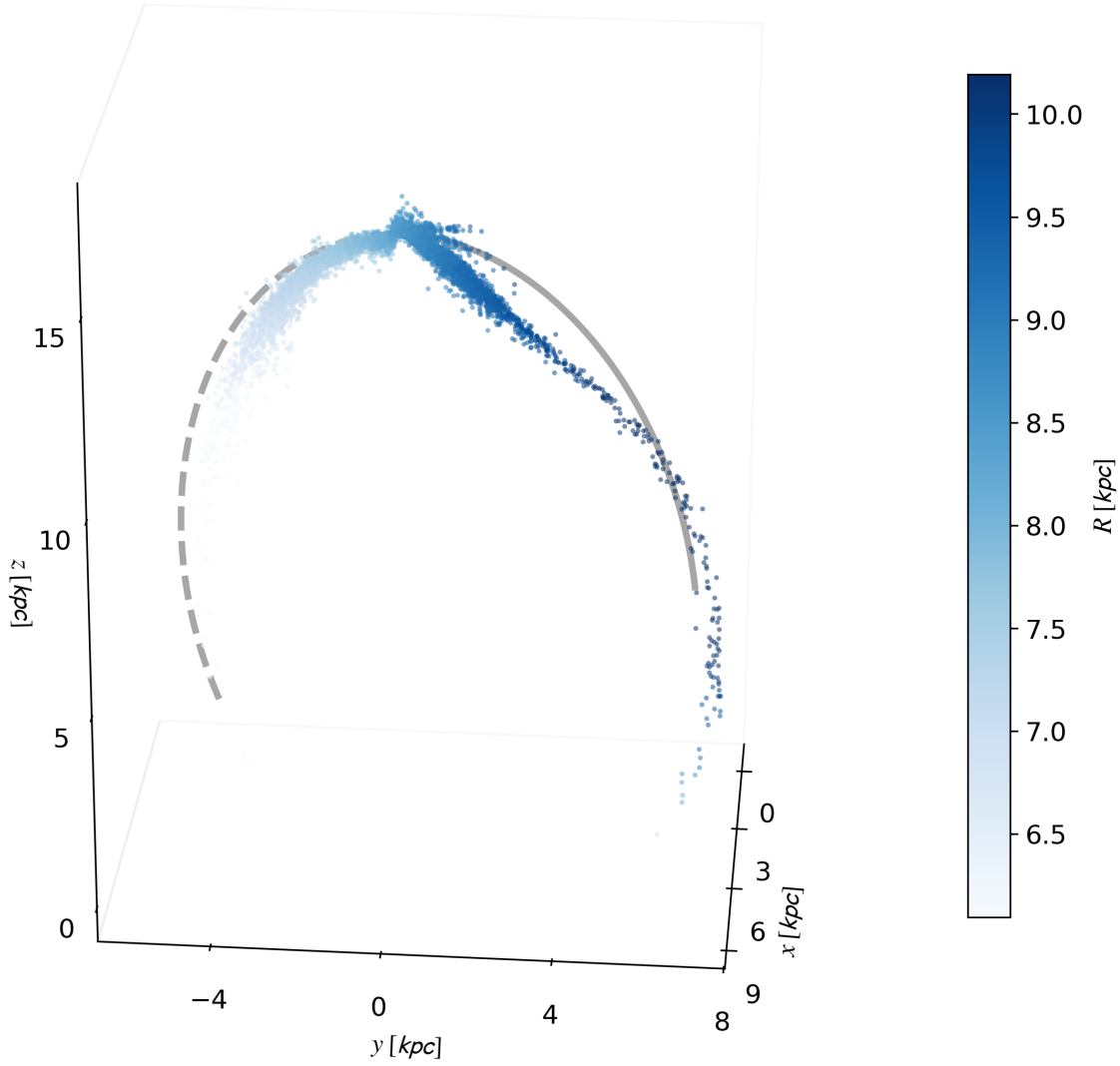

Figure 5.3: Palomar 5 stream modeled with the particle-spray method Fardal et al., 2015 and integrated within the non-axisymmetric bar-only potential described in Table 2.2. The dashed line indicates the future positions and the solid line the past position of the central point of the stream. The stars are colored by their Galactocentric radius. The progenitor is modeled as having $2.5 \times 10^4 M_\odot$ of mass, 4 pc of radius and 10 000 particles. The method generates pairs of stars around the progenitor along its past trajectory over 2 Gyr until its current position. The current position is taken to be $(x, y, z) = (8.2, 0.2, 16.6)$ kpc, and the velocities $(V_x, V_y, V_z) = (-40.7, -89.3, -21.0)$ kms^{-1}.

al. (2017) seems to favor a cored dark matter halo for the MW, and this surprising result would definitely need confirmation with more modern data, as it would have important consequences for the indirect detection of dark matter in the high energy sky towards the Galactic center, and could even bring constraints on the nature of dark matter itself (together with the possible slowing down of the bar).

Finally, as briefly discussed in Section 2.4.3, I am currently examining the conception of new Machine Learning tools for fitting the Galactic potential. It is clear that deep numerical advances are necessary for approaching Galactic Dynamics problems with Artificial intelligence (AI) methods. One frequent barrier I aim to address is a tool to compute actions and angles while satisfying conditions for Automatic Differentiation. Another important barrier is the scale of orbits to be integrated to explore the full parameter space. Recent developments such as SympNets (Jin et al., 2020) and Symplectic Graph Neural Networks (Varghese et al., 2024) designed to learn symplectic maps (mappings that preserve the Hamiltonian structure of dynamical systems) could potentially alleviate this. Indeed, they can potentially be extended to integrate orbits in a known gravitational potential or density distribution efficiently in a larger scale. It could be interesting to advance such research in adequate time and parallel to all the projects mentioned above, as I am persuaded that a full adjustment of the gigantic parameter space to all available data – or even moving towards a full non-parametric inference – will ultimately need to rely on efficient AI methods applied to multi-survey data.

In summary, the main result of this thesis, namely the fiducial model presented in Chapter 2, reproducing a larger amount of observables than ever before, does represent a significant advance in our understanding of the non-axisymmetric structure of the MW disk. However, it is important to recognize its limitations and to continue improving it in order to obtain an even more accurate representation of our Galaxy.

Appendix A

Locating bar resonances in velocity space

The work presented here is from the appendix of Khalil et al. (2025a).

A.1 A simple formula for approximately locating bar resonances in velocity space

In order to evaluate analytically the location of the phase-space resonant zones due to a constant pattern speed bar perturbation, one should define those zones in terms of librating versus circulating orbits after canonically transforming to slow and fast action and angle variables (see Section 1.2.5 and, e.g., Monari et al., 2017a; Binney, 2020). This is a relatively arduous task, and we propose here a less precise but much faster way to roughly estimate the location of resonant ridges in local velocity space, or more accurately, the surfaces of phase-space where the resonant condition is fulfilled. This simple formula will be, by construction, axisymmetric, which means that one cannot use it to model the changes in the morphology of the resonant surfaces with azimuth. The formula relies on locally drawing constant energy lines in the V_R-V_φ plane within the improved epicyclic formalism presented in Dehnen (1999a). For convenience, we reproduce here their equations 28 and 29 for the radial evolution of an orbit:

$$R(\eta) = R_E \left[1 - e\cos(\eta)\right]^{\frac{\gamma}{2}}, \tag{A.1}$$

$$e = \sqrt{1 - \left(\frac{J_\varphi}{J_\varphi^{\rm circ}}\right)^2}, \tag{A.2}$$

where $J_\varphi^{\rm circ}$ and R_E are, respectively, the angular momentum and radius of a circular orbit of the same energy, $\gamma = \gamma(R_E) = 2\Omega(R_E)/\kappa(R_E)$ is the ratio of the circular frequency Ω over the radial epicyclic frequency κ as usual, and e is the eccentricity of the orbit. The phase in radius evolving with time t, namely $\eta(t)$, is the parameter that represents the position along the path of the orbit, and is defined as a function of the eccentricity and the radial epicyclic frequency (see Eq. 28d of Dehnen, 1999a). For simplicity, we consider that $\eta \sim \kappa t$, which in turn means that the radial velocity can be calculated as:

$$V_R = \frac{dR}{d\eta}\frac{d\eta}{dt} \sim \kappa\frac{\gamma}{2}R(\eta)\frac{e\sin(\eta)}{1-e\cos(\eta)} = V_c(R_E)\frac{R}{R_E}\frac{e\sin(\eta)}{1-e\cos(\eta)}. \tag{A.3}$$

The azimuthal velocity, on the other hand, can be written as a function of R simply by the conservation of angular momentum: $V_\varphi = J_\varphi/R(\eta)$. Using Eq. A.1 and Eq. A.2, one then gets a closed form equation that relates the changes of V_R along the orbit to those of R, V_φ, and the circular velocity curve:

$$V_R = V_c(R_E)\left(\frac{R}{R_E}\right)^{\frac{\gamma-2}{\gamma}}\sqrt{2\left(\frac{R}{R_E}\right)^{\frac{2}{\gamma}} - \left(\frac{R}{R_E}\right)^{\frac{4}{\gamma}} - \left(\frac{RV_\varphi}{J_\varphi^{\rm circ}}\right)^2}. \tag{A.4}$$

All that is left is to impose the constraint that stars be on a surface where the resonant condition is met. Under the assumption that frequencies are functions solely of the energy, the resonant condition is preserved as long as stars share the same $J_\varphi^{\rm circ}$ and R_E, and as longs as these are equal to the radius and angular momentum where the circular orbit is $l:m$ resonant. We refer to these as $R_{\rm res}$, such that $l\,\kappa(R_{\rm res}) + m\,[\Omega(R_{\rm res}) - \Omega_b] = 0$, and as $J_\varphi^{\rm res} \equiv R_{\rm res}V_c(R_{\rm res})$, respectively. The final equation for the surfaces of the resonant condition is then:

$$V_\varphi^{\rm res}(R, V_R) = \frac{J_\varphi^{\rm res}}{R}\sqrt{2\left(\frac{R}{R_{\rm res}}\right)^{\frac{2}{\gamma}} - \left(\frac{R}{R_{\rm res}}\right)^{\frac{4}{\gamma}}\left[1 + \left(\frac{R_{\rm res}}{R}\frac{V_R}{V_c(R_{\rm res})}\right)^2\right]}. \tag{A.5}$$

where we reordered the terms to express V_φ as a function of the other phase-space variables.

The application of Eq. A.5 to the V_R-V_φ velocity plane produces for each resonance a curve that is almost identical to Eq. 9 from Dehnen (2000), and is equivalent to drawing lines of constant energy at a given configuration space point, because it is written under the assumption that the orbital frequencies are pure functions of the orbital energy. As can be seen in Fig. A.1, in our best bar model, this formula identifies extremely well the peak of the overdensities produced at $R = R_0$ by the $6:1$, $4:1$, and $2:1$ outer resonances of the bar. For the $(l, m) =$

$(0, 2)$ corotation resonance, the formula fails, probably because the eccentricity becomes too large, and it rather approximately identifies the lower bound of the resonant zone.

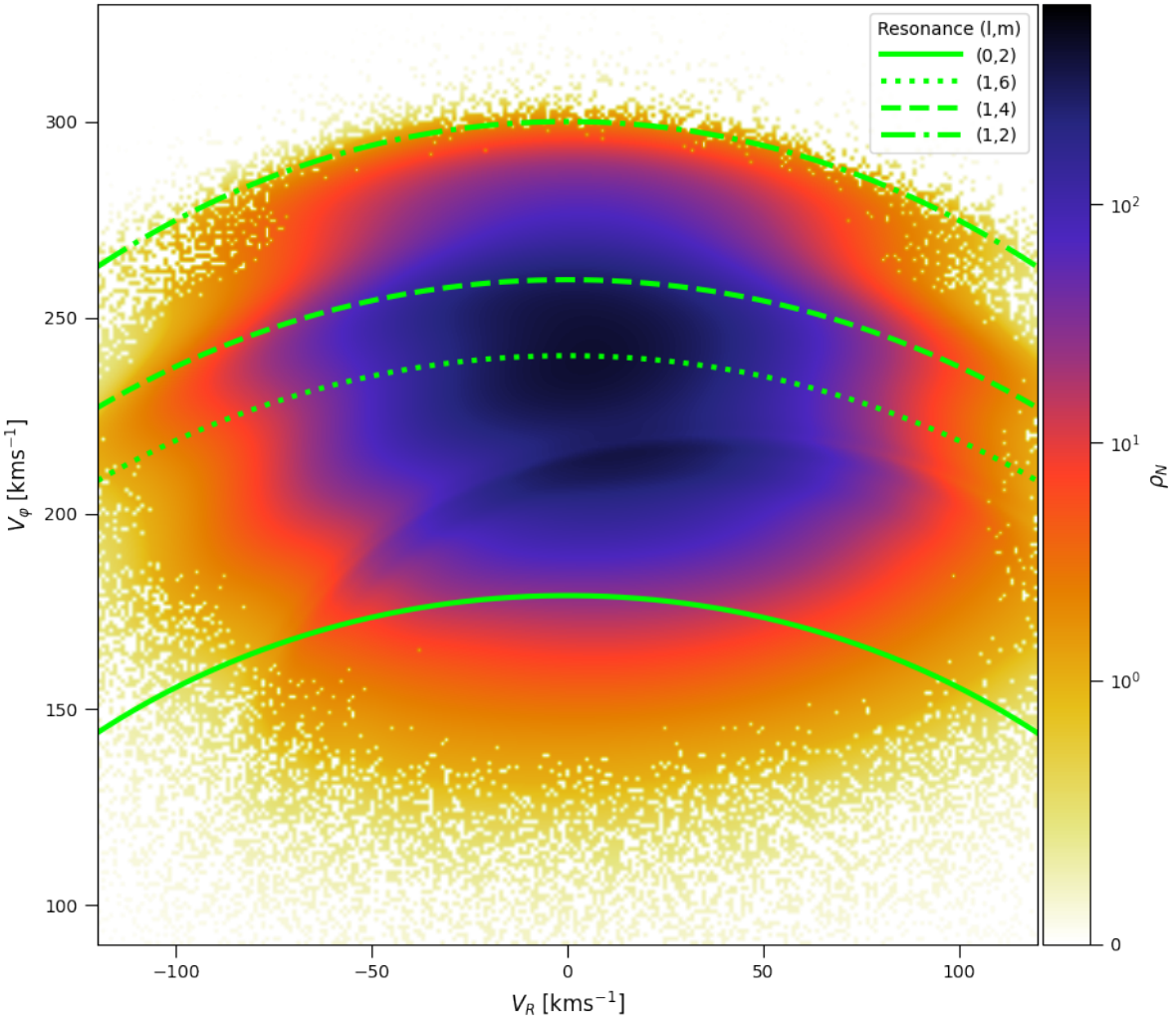

Figure A.1: Resonant lines $V_\varphi^{\rm res}$ as a function of V_R from Eq. A.5 at $R = R_0$, computed with the potential of Table 2.1, for a bar pattern speed of 37 km s^{-1} kpc^{-1}. The lines are overlaid on top of the local velocity space density produced by our preferred bar-only model at the Sun's position.

Appendix B

Un modèle non-axisymétrique pour la Voie Lactée (version française)

B.1 Introduction

La mission Gaia fournit désormais une information complète à 6 dimensions dans l'espace des phases pour le disque de la Voie lactée (VL), concernant un nombre d'étoiles bien plus grand et sur un volume plus étendu que jamais auparavant. Les deuxième (Gaia Collaboration et al., 2018c), début de la troisième (Gaia Collaboration et al., 2021b), et troisième (DR3, Gaia Collaboration et al., 2023d) publications de données de Gaia ont représenté des jalons importants à cet égard (Hunt and Vasiliev, 2025). Alors que les mouvements verticaux des étoiles ont révélé un déséquilibre du disque galactique (Antoja et al., 2018), possiblement lié à une subtile interaction entre perturbations externes et non-axi-symétries internes (e.g., Binney and Schönrich, 2018; Laporte et al., 2019; Li et al., 2023; Tremaine et al., 2023; Frankel et al., 2024), la richesse d'information contenue uniquement dans les mouvements stellaires dans le plan (e.g., Gaia Collaboration et al., 2018a; Gaia Collaboration et al., 2023b) n'a pas encore été pleinement exploitée. En effet, ces mouvements dans le plan devraient — en principe — permettre d'obtenir une cartographie dynamique détaillée des structures non-axi-symétriques les plus importantes du disque de la VL, à savoir la barre galactique et les bras spiraux (Lynden-Bell and Kalnajs, 1972). Cependant, une telle cartographie détaillée fait encore défaut. C'est l'objet de la présente étude.

L'existence de la barre galactique a été initialement supposée à partir d'observations de la cinématique du gaz (de Vaucouleurs, 1964; Peters, 1975; Gerhard and Vietri, 1986; Binney et al., 1991) et confirmée par des observations (proche-)infrarouges (e.g., Blitz and Spergel, 1991; Sellwood, 1993; Weiland et al., 1994; Binney et al., 1997), ainsi que par la cinématique stellaire du bulbe (e.g., Zhao et al., 1994). Il est désormais clair qu'une large fraction des étoiles de la région du bulbe suivent effectivement une structure en rotation, barrée, de forme boxy/peanut, connectée à une barre vue par la tranche (Bland-Hawthorn and Gerhard, 2016), dont le « pattern speed », Ω_b, fait néanmoins encore l'objet de débats. Il y a moins de trois décennies, un consensus s'est établi pour une vitesse de rotation dans la plage $\Omega_b \sim$ 50-60kms^{-1} kpc^{-1}, à partir de divers indices, tels que des simulations hydrodynamiques comparant l'écoulement du gaz modélisé aux diagrammes longitude-vitesse observés en CO et HI (Fux, 1999; Englmaier and Gerhard, 1999; Bissantz et al., 2003), la méthode de Tremaine and Weinberg (1984) appliquée aux étoiles de la Galaxie interne (Debattista et al., 2002), ou la cinématique stellaire locale (Dehnen, 1999b; Dehnen, 2000; Fux, 2001), positionnant le Soleil juste au-delà de la résonance externe 2:1 de Lindblad (OLR) de la barre. Ce dernier argument a été soutenu par de nombreuses analyses

ultérieures (e.g., Minchev et al., 2007; Quillen et al., 2011; Antoja et al., 2012; Antoja et al., 2014; Fragkoudi et al., 2019). À l'inverse, des recherches parallèles sur la densité des étoiles de la branche horizontale rouge dans le disque (Wegg et al., 2015), la cinématique du gaz (Sormani et al., 2015; Li et al., 2016), la modélisation dynamique de la cinématique stellaire dans la Galaxie interne (Portail et al., 2017), et les données de mouvements propres issues du relevé VVV (e.g., Clarke et al., 2019), y compris via la méthode de Tremaine-Weinberg (Sanders et al., 2019), ont collectivement suggéré une vitesse de rotation révisée de $\Omega_b \sim 35$-$40 \mathrm{kms}^{-1}\ \mathrm{kpc}^{-1}$. Pérez-Villegas et al. (2017) et Monari et al. (2019a) ont ensuite démontré que le modèle galactique ajusté à la cinématique stellaire du bulbe par Portail et al. (2017) pouvait effectivement reproduire plusieurs caractéristiques observées dans l'espace des vitesses locales (voir aussi Monari et al., 2019b; Binney, 2020; D'Onghia and Aguerri, 2020; Lucchini et al., 2024). Une telle vitesse de rotation plus faible est également cohérente avec des surdensités observées dans l'espace des phases du halo stellaire (Dillamore et al., 2024) et avec la chimie du disque (Haywood et al., 2024; Khoperskov et al., 2024). D'autres vitesses de rotation intermédiaires ont également été proposées (Hunt and Bovy, 2018), de même que des valeurs beaucoup plus faibles (Horta Darrington et al., 2025), tandis que plusieurs études ont conclu que la cinématique stellaire du disque seule n'était pas suffisante pour lever la dégénérescence (Trick et al., 2021; Trick, 2022; Bernet et al., 2024). Toutefois, la cinématique des étoiles dans la région de la barre elle-même semble avoir convergé vers $\Omega_b \sim 35$-$40 \mathrm{kms}^{-1}\ \mathrm{kpc}^{-1}$, bien que d'éventuelles variations soudaines du « pattern speed » restent possibles (Hilmi et al., 2020). Enfin, une baisse régulière du « pattern speed » de la barre au cours du temps a été tentativement détectée (Chiba et al., 2021; Chiba and Schönrich, 2021), et pourrait expliquer certains aspects du déséquilibre vertical du disque galactique (Li et al., 2023), ainsi que contribuer partiellement à expliquer la présence d'étoiles pauvres en métaux avec des orbites planaires en rotation prograde dans le voisinage solaire (Li et al., 2023; Yuan et al., 2024).

Concernant la localisation et la dynamique des bras spiraux de la VL, la situation observationnelle actuelle est encore moins claire que pour la barre. L'hypothèse que la VL puisse héberger des bras spiraux est aussi ancienne que la reconnaissance de son appartenance à la classe des galaxies à disque, mais, en raison de l'extinction, ce n'est qu'avec le travail de Morgan et al. (1952) que ces bras ont été identifiés, sur la base de la distribution des régions HII, rapidement suivie par l'analyse cinématique de la raie HI à 21 cm par Oort et al. (1958). En se basant sur les distances aux associations OB et aux régions HII, Georgelin and Georgelin (1976) a cartographié un motif spiral à quatre bras, qui a été confirmé à plusieurs reprises par des traceurs jeunes ou gazeux (e.g., Urquhart et al., 2014), mais pas par des traceurs plus anciens et plus rouges, qui devraient mieux révéler les perturbations dans le potentiel galactique. En effet, Drimmel (2000), Drimmel and Spergel (2001), Benjamin et al. (2005) et Churchwell et al. (2009) ont trouvé, grâce à des traceurs en proche infrarouge et en moyen infrarouge, que la VL semblait héberger deux bras spiraux principaux. En collectant des données sur les régions HII et les nuages moléculaires géants, Hou et al. (2009) a montré que des modèles de spirales logarithmiques à trois ou quatre bras pouvaient connecter ces différents traceurs spiraux, comme cela a été passé en revue par Shen and Zheng (2020). En résumé, il n'est pas exagéré de dire que les différents traceurs et observations sont loin de converger sur les paramètres décrivant la position de chaque segment de bras spiral dans le disque de la VL. Le bras dit « Local », par exemple, a été trouvé par Gaia Collaboration et al. (2023b) et Poggio et al. (2021), en retraçant les jeunes étoiles, comme étant plus étendu — et ayant un angle de pitch intermédiaire — comparé à Vázquez et al. (2008), où ce bras se dirige plutôt vers l'extérieur en direction du bras de « Perseus », ou à Xu et al. (2021), où le bras « Local » se dirige vers l'intérieur en direction du bras « Carina-Sagittarius ». Des débats similaires existent à propos du bras de « Perseus » et du bras Externe, concernant leur position dans le disque et leur angle de pitch. Peut-être plus frappant encore, l'angle de pitch du bras de « Perseus » a été trouvé à $\sim 24°$ dans Levine et al. (2006), compatible avec les résultats de Poggio et al. (2021) ou de Drimmel et al. (2024), et à $\sim 9°$ dans Reid et al. (2019), ce qui signifie que ce nom ne fait en réalité pas toujours référence aux mêmes surdensités observées dans le plan galactique. La situation concernant le « pat-

tern speed » des bras spiraux est encore plus confuse, car sa signature peut aussi dépendre de leur nature dynamique et de leur origine (voir Sellwood and Masters, 2022, pour une revue). En effet, les simulations numériques de disques galactiques offrent de multiples perspectives sur ce sujet, allant de structures corotatives transitoires qui s'enroulent et disparaissent rapidement (e.g., Baba et al., 2013; Hunt et al., 2018; Hunt et al., 2019), à de multiples modes persistant sur quelques (voire plusieurs) rotations galactiques, apparaissant à tort comme très éphémères en raison de la superposition de modes (e.g., Sellwood and Carlberg, 2014). Dans la suite, notre procédure de modélisation suivra deux lignes directrices principales. La première est le consensus actuel selon lequel, lorsque les spirales apparaissent comme des modes dans les simulations, celles-ci ne sont pas strictement statiques comme dans le schéma classique des ondes de densité (Lin and Shu, 1964), mais sont plutôt constituées d'un cycle récurrent de modes de sillon (semés par un déficit d'orbites circulaires dans une plage étroite de moments angulaires, voir, e.g., De Rijcke and Voulis, 2016; De Rijcke et al., 2019) qui vivent entre leur résonance interne de Lindblad (ILR) et leur OLR, où elles peuvent créer de nouveaux sillons établissant le cycle récurrent (Sellwood and Carlberg, 2014; Sellwood and Carlberg, 2019). Elles peuvent aussi être des modes de bord (Fiteni et al., 2024). Les amplitudes des modes individuels croissent et décroissent, mais ce sont néanmoins de véritables oscillations d'ondes stationnaires avec une forme fixe et une vitesse de rotation fixe, détectables sur une période d'au moins une rotation. La seconde ligne directrice est que les spectrogrammes de simulations N-corps montrant des perturbations conjointes de barre et de spirale tendent à afficher des bras spiraux qui tournent plus lentement que la barre ; de plus, les bras spiraux ne sont jamais présents à l'intérieur du rayon de corotation de la barre. Ces spirales vivent entre leur propre ILR et OLR, mais sont généralement les plus fortes entre leur ILR et leur corotation (Quillen et al., 2011). Notre approche de modélisation ne prend pas en compte la possibilité de spirales s'enroulant avec le temps.

En gardant à l'esprit toutes les réserves mentionnées ci-dessus, plusieurs mesures provisoires de l'amplitude et du « pattern speed » des bras spiraux ont été effectuées au fil du temps. À l'origine, Lin et al. (1969) a proposé un modèle à deux bras avec un angle de pitch de 6° et une vitesse de rotation de $\Omega_{s,2} \sim 13 \mathrm{kms}^{-1}\ \mathrm{kpc}^{-1}$, basé sur le mouvement systématique du gaz et le déplacement d'étoiles modérément jeunes dans leur modèle classique d'onde de densité. Une estimation plus récente, fondée sur le formalisme classique des ondes de densité de Lin and Shu (1964), a été réalisée par Siebert et al. (2012), en ajustant la carte des vitesses radiales moyennes de l'enquête RAVE, et a abouti à un modèle spiral à deux bras avec une densité de contraste surfacique de 14%, un angle de pitch de 10°, et une vitesse de rotation de $\Omega_{s,2} \sim 18.6 \mathrm{kms}^{-1}\ \mathrm{kpc}^{-1}$. Ce modèle, toutefois, négligeait l'effet de la barre (voir, e.g., Monari et al., 2014). En revanche, Amaral and Lepine (1997) a plaidé pour une superposition d'une spirale à deux bras et d'une spirale à quatre bras, toutes deux avec une vitesse de rotation d'environ $\sim 20 \mathrm{kms}^{-1}\ \mathrm{kpc}^{-1}$, sur la base du retraçage des amas ouverts jusqu'à leur lieu de naissance. Une telle procédure a récemment été réalisée par Castro-Ginard et al. (2021), qui a trouvé une vitesse de rotation décroissante avec le rayon, passant de $\sim 50 \mathrm{kms}^{-1}\ \mathrm{kpc}^{-1}$ pour le segment du bras du Bouclier à $\sim 17 \mathrm{kms}^{-1}\ \mathrm{kpc}^{-1}$ pour le segment du bras de « Perseus ». En modélisant l'écoulement du gaz dans la Galaxie interne, Bissantz et al. (2003) ont obtenu une mesure conjointe des vitesses de rotation de la barre et d'une spirale à quatre bras, avec une vitesse de rotation très élevée pour la barre, $\Omega_b \sim 60 \mathrm{kms}^{-1}\ \mathrm{kpc}^{-1}$, et une vitesse de rotation de $\Omega_{s,4} \sim 20 \mathrm{kms}^{-1}\ \mathrm{kpc}^{-1}$ pour la spirale à quatre bras. Plus récemment, en négligeant de nouveau la barre, Eilers et al. (2020) ont appliqué un modèle simplifié de spirale logarithmique au champ de vitesses radiales galactocentriques moyennes de Gaia DR2, suggérant une densité de contraste surfacique d'environ $\sim 10\%$, un angle de pitch de 12°, et une vitesse de rotation fixe de $\Omega_{s,2} = 12 \mathrm{kms}^{-1}\ \mathrm{kpc}^{-1}$ pour une spirale à deux bras correspondant aux bras « Local » et Externe. De telles vitesses de rotation faibles avaient également été suggérées auparavant, par exemple par Sellwood (2010), sur la base de la signature d'une résonance interne de Lindblad (ILR) spirale dans la cinématique stellaire locale ($\sim 8 \mathrm{kms}^{-1}\ \mathrm{kpc}^{-1}$ pour une spirale à deux bras et $\sim 15 \mathrm{kms}^{-1}\ \mathrm{kpc}^{-1}$ pour une spirale à trois bras). Concernant l'amplitude, la détermination la plus récente, basée sur

l'équation de Jeans verticale, a trouvé que le bras « Local » constitue la surdensité locale la plus marquée, avec une densité de contraste d'environ 20% (Widmark and Naik, 2024).

Ici, nous tentons d'exploiter pleinement la richesse d'information encodée dans les mouvements stellaires dans le plan, issus de Gaia DR3 (Gaia Collaboration et al., 2023b), afin de contraindre dynamiquement les non-axi-symétries de la Galaxie. Des tentatives similaires précédentes incluent l'approche plus empirique de Khoperskov et al. (2020) and Khoperskov and Gerhard (2022), ainsi que le travail récent de Vislosky et al. (2024) comparant trois simulations hydrodynamiques de galaxies aux cartes de vitesses de Gaia, afin d'obtenir des indications sur l'orientation barre-spirale. Notre approche est ici complémentaire puisque, au lieu de comparer qualitativement une simulation hydrodynamique auto-cohérente aux données, nous tentons un ajustement plus quantitatif aux données de l'espace des phases stellaires de Gaia. Pour cela, nous recourons à des intégrations rétrogrades afin de modéliser le champ de vitesses avec une forme paramétrique du potentiel gravitationnel. Notre solution privilégiée pourrait servir de nouveau potentiel paramétrique non-axi-symétrique de référence pour le disque de la VL.

Dans la Section B.2, nous présentons brièvement les données extraites de l'échantillon RVS de Gaia DR3 que nous utilisons pour contraindre le potentiel à partir de la cinématique du disque de la VL. La méthode de modélisation et la paramétrisation du potentiel sont introduites dans la Section B.3, tandis que les résultats sont présentés dans la Section B.4. Des comparaisons a posteriori avec des observables auxquelles le modèle n'a pas été ajusté, ainsi que quelques exemples d'applications de notre potentiel de référence, sont données dans la Section B.5, avant nos conclusions en Section B.6.

B.2 Données

Puisque nous prévoyions d'utiliser les mouvements stellaires dans le plan du disque afin de contraindre les non-axi-symétries de la VL, nous avons sélectionné un échantillon d'étoiles disposant d'une information complète à 6 dimensions dans l'espace des phases, issue du RVS de Gaia, proche du plan galactique. Nous avons utilisé les données de Gaia DR3 (Gaia Collaboration et al., 2023d) combinées aux distances de StarHorse (Anders et al., 2022), et sélectionné 17 414 667 étoiles situées à une hauteur inférieure à 300 pc du plan galactique.

Nous avons adopté, pour la position du Soleil, $\boldsymbol{x}_\odot$, et sa vitesse, $\boldsymbol{v}_\odot$, en coordonnées cartésiennes galactocentriques : $\boldsymbol{x}_\odot = (x_\odot, y_\odot, z_\odot) = (8275, 0, 15.29)$ pc et $\boldsymbol{v}_\odot = (V_{x_\odot}, V_{y_\odot}, V_{z_\odot}) = (-9.3, 251.5, 8.59), \mathrm{km, s^{-1}}$ (Gaia Collaboration et al., 2023b; Portail et al., 2017; Widmark and Monari, 2019), respectivement. Nous avons ensuite transformé les données des coordonnées équatoriales vers les coordonnées galactocentriques à l'aide de la bibliothèque Astropy (Astropy Collaboration et al., 2022), afin de calculer les positions des étoiles en coordonnées cartésiennes galactocentriques, $\boldsymbol{x} = (x, y, z)$, ainsi que leurs vitesses dans le plan en coordonnées cylindriques galactocentriques, $\boldsymbol{v} = (V_R, V_\varphi)$, avec le rayon galactocentrique $R = \sqrt{x^2 + y^2}$ et l'azimut $\varphi = \arctan(y/x)$, défini comme nul à l'azimut du Soleil et positif dans la direction de la rotation galactique. Les étoiles ont été sélectionnées dans la plage $4, \mathrm{kpc} < x < 12, \mathrm{kpc}$ et $-4, \mathrm{kpc} < y < 4, \mathrm{kpc}$.

Dans la Fig.2.2, nous présentons la distribution des vitesses stellaires locales pour un peu plus de 2 millions d'étoiles situées dans un cylindre de rayon 300 pc autour du Soleil, toujours à une hauteur de 300 pc. Dans cette figure, plusieurs des groupes en mouvement bien connus du voisinage solaire (e.g., Dehnen, 1998; Famaey et al., 2005; Antoja et al., 2008; Ramos et al., 2018; Bernet et al., 2022) sont immédiatement visibles. Le « Hat » peut être vu comme l'arche concave vers le bas à grand V_φ, allant de $(V_R, V_\varphi) \approx (-100\,\mathrm{km\,s^{-1}}, 270\ \mathrm{km\,s^{-1}})$ à $(V_R, V_\varphi) \approx (120\ \mathrm{km\,s^{-1}}, 260\ \mathrm{km\,s^{-1}})$. Le groupe en mouvement de « Sirius » (e.g., Famaey et al., 2008) apparaît approximativement droit à $V_\varphi \approx 255\ \mathrm{km\,s^{-1}}$, situé entre $V_R \approx -50\ \mathrm{km\,s^{-1}}$ et $V_R \approx 0\ \mathrm{km\,s^{-1}}$, avec un pic à $V_R \approx -15\ \mathrm{km\,s^{-1}}$. « Coma » se trouve juste en dessous de « Sirius » en vitesse azimutale, autour de $(V_R, V_\varphi) \approx (0\ \mathrm{km\,s^{-1}}, 245\ \mathrm{km\,s^{-1}})$. Le groupe en mouvement des « Hyades » (e.g., Famaey et al., 2007; Pompéia et al., 2011) peut être vu comme une arche légèrement incurvée vers le bas, partant de la surdensité en $(V_R, V_\varphi) \approx (20\ \mathrm{km\,s^{-1}}, 230\ \mathrm{km\,s^{-1}})$. Le « Horn » se trouve juste à côté des « Hyades », de l'autre côté

en V_R : il apparaît comme une arche passant par $(V_R, V_\varphi) \approx (-80\ \mathrm{km\,s^{-1}}, 200\ \mathrm{km\,s^{-1}})$. Enfin, le groupe majeur d'« Hercule » se perçoit comme une bimodalité de tout le plan des vitesses, avec une sous-densité juste en dessous des « Hyades » en vitesse azimutale, le séparant du reste de la distribution. Sa bimodalité apparaît clairement, avec une seconde surdensité apparaissant à faible V_φ.

Une autre façon de visualiser ces arches, qui, toutefois, efface visuellement les asymétries en vitesse radiale, est de représenter la distribution des étoiles dans l'espace des actions axisymétriques locales (e.g., Trick et al., 2019; Trick et al., 2021). En effet, la Galaxie est, à premier ordre, un système quasi-intégrable axisymétrique, et les variables action-angle $(\boldsymbol{J}, \boldsymbol{\theta})$ sont les variables canoniques de l'espace des phases adaptées à l'étude et à la perturbation des systèmes intégrables. Dans ces coordonnées, le Hamiltonien ne dépend que des actions, $\boldsymbol{J}$, qui sont des intégrales du mouvement. Chaque triplet d'actions caractérise alors entièrement une orbite intégrable, tandis que les angles indiquent où se trouve une étoile donnée sur cette orbite particulière. L'action azimutale est simplement $J_\varphi = R, V_\varphi$, tandis que l'action radiale, J_R (calculée dans le potentiel axisymétrique de fond défini dans la Sect.3), encode les excursions radiales (galactocentriques) d'une orbite donnée. Dans la Fig.2.3, les arches dans l'espace des vitesses locales apparaissent désormais comme des crêtes dans l'espace des actions locales, caractéristiques de structures résonantes (e.g., Monari et al., 2017a; Binney, 2020).

Ces caractéristiques de l'espace des vitesses locales et de l'espace des actions, tracées avec une précision remarquable, sont toutefois connues depuis longtemps. La valeur ajoutée la plus intéressante des publications de données de Gaia a été d'élargir le volume autour du Soleil dans lequel de telles structures dynamiques peuvent être étudiées (e.g., Ramos et al., 2018; Bernet et al., 2022). Afin d'ajuster les composantes non axisymétriques du potentiel galactique, nous nous abstenons cependant, dans ce travail, d'utiliser la distribution complète des étoiles du disque dans l'espace des phases, et choisissons plutôt d'ajuster une mesure de tendance centrale en fonction de la position dans le disque, à savoir la vitesse radiale galactocentrique médiane (Gaia Collaboration et al., 2023b). Cette carte de la vitesse radiale médiane est présentée dans la Fig.2.4 et constitue l'observable principale ajustée dans ce travail. Nous ne vérifions qu'a posteriori la concordance qualitative avec la distribution complète des étoiles dans l'espace des phases. Comme notre modélisation repose sur une fonction de distribution (DF) projetée en 4D dans l'espace des phases des populations stellaires du disque — une DF censée tenir compte des étoiles ayant des vitesses verticales non nulles — nous n'appliquons aucune coupure supplémentaire sur la vitesse verticale dans les données. Cependant, bien que notre DF soit une projection, nos intégrations d'orbites sont effectuées uniquement dans le plan. Nous avons donc également vérifié que le fait de ne sélectionner que les étoiles dont la vitesse verticale est inférieure à $15, \mathrm{km, s^{-1}}$, ce qui permet de conserver un nombre raisonnable de 11427 688 étoiles dans l'échantillon, conduit à une carte de la vitesse radiale médiane presque identique. Pour les points importants de l'ajustement, les différences typiques sont inférieures à 0.5 km/s, avec une différence maximale de 1 km/s.

B.3 Modélisation

Pour construire notre potentiel non-axisymétrique, nous sommes partis d'un potentiel axi-symétrique, auquel nous avons ensuite ajouté une barre et des bras spiraux, définis par plusieurs paramètres décrits dans les sous-sections suivantes. À l'intérieur du potentiel axi-symétrique, nous avons utilisé une fonction de distribution dans l'espace des phases, $f(\boldsymbol{x}, \boldsymbol{v})$, pour décrire notre population traceuse. Cette fonction de distribution à une particule est la fonction de densité de probabilité de trouver une étoile au point $(\boldsymbol{x}, \boldsymbol{v})$ de l'espace des phases et, pour un système sans collisions, elle obéit à l'équation de Boltzmann sans collisions (ou de Vlasov). Une telle fonction de distribution, pour tout système stellaire intégrable à l'état stationnaire, devrait uniquement dépendre d'intégrales isolantes du mouvement selon le théorème de Jeans (Binney and Tremaine, 2008). Nous considérons ces intégrales comme étant les actions, $\boldsymbol{J}$. Afin de transformer les positions et vitesses stellaires en actions, on peut utiliser une approximation basée sur les potentiels de Stäckel (voir, e.g., Famaey and Dejonghe, 2003). Les potentiels axi-symétriques de Stäckel sont exprimés dans

un système de coordonnées sphéroïdales, défini par une distance focale, qui est toujours reliée aux dérivées première et seconde du potentiel en une position donnée. Ainsi, en utilisant le potentiel galactique réel en une position donnée, on peut calculer une distance focale équivalente comme si le potentiel était localement de forme de Stäckel, permettant le calcul des intégrales (quasi-)du mouvement et des actions correspondantes. Ce « Stäckel fudge » (Binney, 2012; Sanders and Binney, 2016) est entièrement implémenté dans le code de modélisation galactique basé sur les actions (Vasiliev, 2018; Vasiliev, 2019, `AGAMA`) que nous avons utilisé dans la présente étude.

Nous sommes partis d'une fonction de distribution à l'équilibre, $f(\boldsymbol{J})$, pour la population traceuse définie dans un potentiel axi-symétrique. La première approche pour inclure l'effet de composantes non-axi-symétriques est de les traiter via la théorie des perturbations (e.g., Monari et al., 2016a; Al Kazwini et al., 2022), ce qui, afin d'être véritablement quantitatif, nécessite un traitement particulier des zones résonantes pour une perturbation à vitesse de rotation constante (e.g., Monari et al., 2017a; Laporte et al., 2020; Binney, 2020; Hamilton et al., 2023). Cela devient toutefois pratiquement très compliqué en présence de multiples perturbateurs ayant des vitesses de rotation différentes, dont les résonances se chevauchent. Pour contourner ce problème, on peut heureusement s'appuyer sur la propriété encodée dans l'équation de Boltzmann sans collisions, à savoir que la valeur de la fonction de distribution dans un volume lagrangien infinitésimal est conservée le long de la trajectoire. Cela nous permet d'utiliser la méthode classique des intégrations rétrogrades (Vauterin and Dejonghe, 1997), employée par exemple dans Dehnen (2000), Hunt and Bovy (2018), Hunt et al. (2018), Hunt et al. (2019), Monari et al. (2019a), and Bernet et al. (2024), afin d'explorer la forme de la fonction de distribution.

Afin de calculer $f(\boldsymbol{x}, \boldsymbol{v}, t)$, à l'instant actuel $t = 0$, au point $(\boldsymbol{x}, \boldsymbol{v})$ de l'espace des phases, en présence de la barre et des bras spiraux, nous avons intégré rétrospectivement l'orbite pour un temps d'intégration fixé jusqu'à sa position $(\boldsymbol{x}', \boldsymbol{v}')$ dans l'espace des phases à un instant $t' < 0$, avant l'apparition effective des perturbateurs non-axi-symétriques. En supposant que la population traceuse soit représentée par la fonction de distribution à l'équilibre, $f(\boldsymbol{J})$, dans le potentiel axisymétrique de fond à l'instant t', nous avons transformé $(\boldsymbol{x}', \boldsymbol{v}')$ en variables action-angle en utilisant `AGAMA`, calculé la valeur de la DF[1], et, puisque cette valeur dans un volume lagrangien infinitésimal est conservée, nous avons attribué la même valeur de la DF à la position $(\boldsymbol{x}, \boldsymbol{v})$ de l'espace des phases à l'instant présent $t = 0$ en présence de la barre et des spirales. En pratique, les orbites ont été intégrées uniquement dans le plan, en résolvant le problème de Cauchy avec la méthode de Runge-Kutta d'ordre cinq via le solveur `odeint` de la bibliothèque très performante `torchdiffeq` (Chen, 2018) dans `PyTorch` (Paszke et al., 2019). Faire cela en de nombreux points de l'espace des phases nous permet de calculer la vitesse radiale médiane en fonction de la position dans le disque, et d'ajuster les paramètres des composantes non-axi-symétriques afin de reproduire les valeurs observées. En pratique, la vitesse radiale médiane à chaque position de grille (échantillonnée tous les 50pc en x et y) sur le disque a été calculée après intégration locale des valeurs de la DF en V_φ pour une grille de vitesses sur laquelle l'intégration rétrograde a été effectuée en chaque position. Cette grille s'étend de $-79\,\mathrm{km\,s^{-1}}$ à $79\,\mathrm{km\,s^{-1}}$ avec un pas de $2\,\mathrm{km\,s^{-1}}$ en V_R, et de $110\,\mathrm{km\,s^{-1}}$ à $330\,\mathrm{km\,s^{-1}}$ avec un pas de $4\,\mathrm{km\,s^{-1}}$ en V_φ. Le potentiel a été évalué sur une grille de rayons, ensuite interpolée par une spline cubique dans la bibliothèque `torchcubicspline` de `PyTorch` afin d'améliorer le temps de calcul. De même, nous avons également interpolé, avec `Scipy` (Virtanen et al., 2020), une spline cubique appliquée aux actions calculées avec `AGAMA`.

Il existe trois limites à la méthode, qui méritent d'être mentionnées même si les traiter en détail dépasse largement le cadre de cette première approche quantitative du problème. Premièrement, nous utilisons l'échantillon complet du disque décrit dans la section précédente sans tenir compte d'une fonction de sélection détaillée, en supposant que le grand

[1]Soit $\mathcal{J}$ le jacobien de la transformation entre $(\boldsymbol{J}, \boldsymbol{\theta})$ et $(\boldsymbol{x}, \boldsymbol{v})$. Puisque $\det\mathcal{J} = 1$ pour des variables canoniques (Binney and Tremaine, 2008), la transformation entre une DF dans $(\boldsymbol{J}, \boldsymbol{\theta})$, $f(\boldsymbol{J}, \boldsymbol{\theta})$, et celle dans $(\boldsymbol{x}, \boldsymbol{v})$, $f'(\boldsymbol{x}, \boldsymbol{v})$, est donnée par $f'(\boldsymbol{x}, \boldsymbol{v}) = f(\boldsymbol{J}(\boldsymbol{x}, \boldsymbol{v}), \boldsymbol{\theta}(\boldsymbol{x}, \boldsymbol{v}))\det\mathcal{J} = f(\boldsymbol{J}(\boldsymbol{x}, \boldsymbol{v}), \boldsymbol{\theta}(\boldsymbol{x}, \boldsymbol{v}))$, c.-à-d. que f' est simplement f avec $\boldsymbol{J}$ et $\boldsymbol{\theta}$ écrits comme fonctions de $\boldsymbol{x}$ et $\boldsymbol{v}$.

nombre d'étoiles utilisé permet une bonne estimation de la véritable vitesse médiane. La deuxième limite est que, dans la pratique, la fonction de distribution stellaire observée est toujours mesurée sur des volumes finis de l'espace des phases, tandis que la méthode d'intégration rétrograde repose sur l'hypothèse que la valeur moyenne de la DF dans un volume donné de l'espace des phases est équivalente à sa valeur au point central, indépendamment de la manière dont le volume se déforme au cours de l'évolution orbitale du système. En d'autres termes, la méthode d'intégration rétrograde fournit la DF fine (fine-grained), qui reste généralement non lissée à petite échelle, tandis que la DF mesurable dans les observations est la DF grossière (coarse-grained), qui n'obéit pas à l'équation de Boltzmann sans collisions (car cette DF grossière est lissée par le mélange de phases dans des volumes finis). Le théorème d'échantillonnage de Nyquist-Shannon impose des limites à la taille minimale des structures fines pouvant se former dans l'espace des phases pour un nombre fixe de particules au cours du temps, et cette limite est atteinte sur des échelles de temps assez courtes, plus courtes que la relaxation collisionnelle (Beraldo e Silva et al., 2019). Une fois cette limite atteinte, le système ne peut pas former de structures plus fines, bien que l'équation de Boltzmann sans collisions prévoie leur formation. En pratique, cela signifie que si l'intégration est effectuée trop longtemps, la DF fine suivie par la méthode d'intégration rétrograde donnera lieu à des structures nettes et non lissées dans l'espace des vitesses, où des caractéristiques chaotiques apparaîtront également plus tranchées que dans la réalité. Pour contourner ce problème, l'intégration doit être effectuée uniquement sur un temps relativement limité, ajusté de manière à ce que la netteté des structures résonantes dans l'espace des vitesses ressemble à ce qui est observé. Heureusement, les simulations N-corps indiquant l'existence de cycles récurrents de modes de sillon dans les disques galactiques (Sellwood and Carlberg, 2014; Sellwood and Carlberg, 2019) nous permettent de considérer que les modes de bras spiraux actuels de la VL sont relativement récents. Cette hypothèse n'est bien sûr pas idéale pour la barre, mais il est raisonnable de supposer que la localisation des structures résonantes dans l'espace des vitesses locales n'évolue pas avec le temps, tandis que leur netteté, elle, évolue. Nous nous concentrerons donc uniquement sur la localisation des structures résonantes dans l'espace des vitesses locales pour contraindre le « pattern speed » de la barre, et nous nous appuierons sur une forme paramétrique de son potentiel ajustée à la dynamique de la région du bulbe (Portail et al., 2017; Thomas et al., 2023) pour son amplitude. Il serait trop coûteux de recourir à une méthode d'intégration vers l'avant dans le schéma d'ajustement que nous mettons en œuvre dans cette thèse, étant donné la taille de l'espace des paramètres à explorer, et étant donné que chaque combinaison de paramètres nécessite une intégration rétrograde complète de tout le plan galactique. Cependant, les résultats obtenus ci-après pourraient servir de base à des simulations de particules tests vers l'avant dans le temps, également étendues à trois dimensions, que nous prévoyons de présenter dans un prochain article. Enfin, une troisième et dernière limite est que nos simulations ne sont pas, par conception, auto-cohérentes. Cette simplification est bien plus efficace pour explorer un vaste espace de paramètres. Cependant, de futures améliorations de notre méthode pourraient s'appuyer sur une adaptation de la méthode made-to-measure (Syer and Tremaine, 1996; Portail et al., 2017) afin de tenir compte de l'auto-cohérence, en utilisant les résultats présentés ci-après comme base.

Potentiel axisymétrique de fond

Comme indiqué plus haut, la méthode utilise un potentiel de fond axisymétrique. En pratique, nous avons supposé un profil de densité axisymétrique 3D, et le potentiel a été calculé en résolvant l'équation de Poisson avec `AGAMA`. Le profil de densité est la somme des densités de chacune des composantes suivantes : disque stellaire, disque de gaz, bulbe et halo de matière noire.

Les profils de densité du disque stellaire et du disque de gaz sont paramétrés en coordonnées cylindriques galactocentriques (R, z) dans l'équation 2.1 avec la densité de surface centrale, Σ_0, l'échelle de hauteur, h_z (et donc la densité centrale $\Sigma_0/2h_z$), et l'échelle de longueur, h_R. Le profil de densité sphérique pour le bulbe et le halo de matière noire est donné par l'équation 2.2 avec une normalisation de densité, ρ_0, un rayon d'échelle, a, un rayon d'échelle externe, r_s, et des exposants α, β et γ. Le rayon ellipsoïdal est défini

comme $\tilde{r} = \sqrt{R^2 + \left(\frac{z}{q}\right)^2}$, avec q le rapport d'axe vertical. Tous les paramètres sont donnés dans le Tableau 2.1. La masse baryonique du modèle est de 6×10^{10}M$\odot$ et le halo de matière noire est relativement léger, avec une masse de 3.1×10^{11}M$\odot$, entre les valeurs typiques obtenues à partir d'analyses de courbes de vitesses circulaires (e.g., Jiao et al., 2023; Ou et al., 2024) et celles obtenues à partir des courbes de vitesse d'échappement, de la dynamique des satellites ou de l'ajustement des courants stellaires (e.g., Monari et al., 2018; Callingham et al., 2019; Roche et al., 2024b; Ibata et al., 2024). Seule la masse dans la Galaxie interne, toutefois, importe pour notre modélisation actuelle : la masse totale enfermée (baryons et matière noire) à l'intérieur de 20 kpc est de 2.2×10^{11}M$\odot$, en accord approximatif avec la contrainte de Malhan and Ibata (2019). La densité locale de matière noire à la position du Soleil est de 1.3×10^{-2}M$\odot$ pc^{-3}, cohérente avec la plupart des estimations (de Salas and Widmark, 2021, et références incluses). Au centre, le halo de matière noire présente un cœur de densité constante (avec une pente de loi de puissance centrale de 0) ainsi qu'un déclin peu marqué en loi de puissance près du centre, avec une pente de -0.6 à $R = 1$ kpc et de -1 à $R = 3$kpc. Tous ces paramètres du potentiel de fond pourraient en principe être laissés libres dans notre procédure d'ajustement ci-après, mais afin de simplifier le problème, ils ont tous été fixés pour ressembler étroitement à la partie axisymétrique du modèle de Portail et al. (2017). La courbe de vitesse circulaire correspondant à ce modèle axisymétrique est tracée dans la Fig.2.2.1. Tous les modes non-axi-symétriques qui ont été ensuite ajoutés à ce fond axisymétrique ont une masse totale nulle, ce qui signifie que la masse totale du modèle final non-axi-symétrique est la même que celle du modèle axisymétrique. Comme nos orbites ont été calculées strictement dans le plan, nous n'avions besoin que du potentiel de fond dans le plan, $\Phi_0(R)$.

Fonction de distribution d'équilibre axisymétrique

La deuxième étape de notre procédure consistait à choisir une fonction de distribution à l'équilibre pour la population stellaire traceuse dans le plan. Puisque nous nous limitons au plan, nous n'avons pas tenté ici d'être entièrement auto-cohérents (voir, e.g., Binney and Vasiliev, 2023), afin de permettre une forme simple et traitable de la fonction de distribution, à savoir une simple combinaison linéaire de deux fonctions de distribution quasi-isothermales, $f(J_R, J_\varphi) = F_{\rm thin} + \zeta F_{\rm thick}$, avec $\zeta = 0.05$, qui sont 2D dans l'espace des actions, et qui ont toutes deux la forme de l'équation 2.3 (Binney, 2010; Binney and McMillan, 2011), avec $R_{\rm g}$, le rayon de guidage, et Ω, κ, les fréquences circulaire et épicyclique, toutes trois dépendant de l'action azimutale J_φ, h_R, l'échelle de longueur du disque, η, le facteur de normalisation (en unités d'inverse de longueur au carré) de la population traceuse, et enfin la dispersion de vitesse radiale, $\tilde{\sigma}_R$, dépendant du rayon de guidage. En plus, $h_{\sigma,R}$ c'est l'échelle cinématique de la population traceuse. Pour $F_{\rm thin}$, nous avons fixé l'échelle de longueur à $h_R = 2.4$ kpc conformément au potentiel, la dispersion de vitesse à la position du Soleil à $\tilde{\sigma}R, {\rm thin}(R_0) = 30$ kms^{-1}, et l'échelle cinématique à $h\sigma_R = 10$kpc. Pour $F_{\rm thick}$, la seule différence est que nous avons fixé $\tilde{\sigma}_{R,{\rm thick}}(R_0) = 55$kms^{-1}. Notre fonction de distribution correspond à une DF projetée en 4D dans l'espace des phases, c'est-à-dire en unités d'inverse de longueur au carré multiplié par l'inverse de la vitesse au carré, correspondant donc à la DF 6D des populations stellaires du disque modélisées et intégrée sur les hauteurs et les vitesses verticales. La distribution locale des vitesses à $R = R_0$ correspondant à cette DF axisymétrique est représentée dans la Fig.2.7. En pratique, le facteur de normalisation a été ajusté de sorte que le nombre d'étoiles dans le modèle à la position du Soleil soit le même que celui trouvé dans les données à l'intérieur du cylindre de 300pc de rayon et de hauteur $\pm$300 pc autour du Soleil.

Potentiel non-axisymétrique

La troisième étape de notre procédure a consisté à ajouter des modes non-axi-symétriques au potentiel de fond axisymétrique Φ_0. Le potentiel total a été obtenu en ajoutant à $\Phi_0(R)$ la partie réelle de l'équation 2.4 où la phase actuelle et le « pattern speed » de la barre sont respectivement $\varphi_{\rm b,0}$ et $\Omega_{\rm b}$, et celles du mode de bras spiraux, m, sont respectivement $\varphi_{{\rm s},m,0}$ (la phase spirale actuelle à la position solaire) et $\Omega_{{\rm s},m}$. L'amplitude de chaque mode est donnée par $\phi_{{\rm b},m}$ et $\phi_{{\rm s},m}$ pour la barre et les spirales, respectivement. Le temps, t, est tel

qu'actuellement $t = 0$.

Comme indiqué plus haut, l'amplitude des modes du potentiel de la barre est fixée à des valeurs qui reproduisent bien la dynamique de la région du bulbe. Plus précisément, le potentiel de la barre est une superposition de trois modes de Fourier, avec la même forme paramétrique que dans Thomas et al. (2023), ressemblant étroitement aux trois premiers modes pairs du potentiel de la barre dérivés dans Portail et al., 2017. À partir de ce même potentiel, la phase angulaire de la barre a été fixée à $\varphi_{\mathrm{b},0} = 28°$. L'amplitude de chaque mode de la barre, m, est donnée par l'équation 2.5 où $G_{\mathrm{b}}(t) \leq 1$ est la fonction de croissance de la barre, et $A_{\mathrm{b},m}$ est l'amplitude relative du mode de barre donnée par l'équation 2.6 avec $K_{\mathrm{b},m}$ un facteur d'amplitude globale et $R_{\mathrm{b,max}}$ le rayon auquel l'amplitude du mode s'annule. Il est important de noter que nous avons considéré que l'amplitude avait atteint un plateau au temps présent, $G_{\mathrm{b}}(t = 0) = 1$. Les valeurs de $K_{\mathrm{b},m}, a_m$, et b_m pour chacun des modes de la barre sont présentées dans le Tableau2.2. Seule le « pattern speed » de la barre est ajustée à la localisation des structures résonantes dans l'espace des vitesses locales dans le cadre de notre procédure (voir la section suivante).

Le potentiel des bras spiraux que nous proposons est une adaptation du modèle analytique de Cox and Gomez, 2002 décrit dans Monari et al., 2016b, dont l'amplitude est donnée par l'équation 2.7 où $G_{\mathrm{s,m}}(t)$ est la fonction de croissance pour le mode de bras spiraux, m, fixée à $G_{\mathrm{s,m}}(t = 0) = 1$, $p_{\mathrm{s},m}$ est l'angle de pitch, et $A_{\mathrm{s},m}$ est donné par l'équation 2.8 où $\xi_{\mathrm{s},m}$ est le facteur d'amplitude du mode, normalisé à sa valeur $K_{\mathrm{s},m}$ en $R = R_0$, avec une dépendance radiale donnée par l'équation 2.9.

Cette adaptation du potentiel de Cox and Gomez, 2002 a l'avantage d'être facilement généralisable en 3D. Ici, $h_{\mathrm{s},m}$ correspond à l'échelle de hauteur du potentiel spiral, que nous avons fixée à 130pc. Nous avons vérifié que nos résultats ne sont pas très sensibles à ce paramètre et restent similaires pour toute valeur comprise entre 100pc et 300 pc. Enfin, H_m est une fonction de coupure radiale, paramétrée par une coupure interne et une coupure externe, respectivement $R_{\mathrm{s},m,\mathrm{min}}$ et $R_{\mathrm{s},m,\mathrm{max}}$. La fonction est présenté dans l'équation 2.10. Cette coupure est choisie par simplicité, dans un contexte où nous ne vi-

sons pas l'auto-cohérence. Cependant, dans un contexte où le couple densité-potentiel d'un mode spiral est nécessaire à la coupure, il est souhaitable de remplacer la fonction échelon par quelque chose comme $H_m \sim 0.5(1 + \tanh((R - R_{\mathrm{s},m,\mathrm{min}})/\Delta_{\mathrm{cutoff}}))$, où $\Delta_{\mathrm{cutoff}} \to 0$ correspond à notre cas présent.

Ces coupures sont déterminées à partir des vitesses de rotation de la barre et des modes spiraux dans la section suivante. Les paramètres des bras spiraux (pour chaque mode : amplitude, $K_{s,m}$, angle de pitch, $p_{s,m}$, phase actuelle à la position solaire, $\varphi_{\mathrm{s},m,0}$, et vitesse de rotation, $\Omega_{\mathrm{s},m}$) sont ajustés aux données dans la section suivante, en même temps que le « pattern speed » de la barre, Ω_{b}.

B.4 Résultats

Modèle avec barre seule

Avec toutes les composantes paramétriques du potentiel définies ci-dessus, nous étions alors en mesure de lancer nos intégrations rétrogrades afin d'ajuster les paramètres aux données. Comme indiqué plus haut, l'amplitude des modes et la phase du potentiel de la barre sont fixées à des valeurs qui reproduisent bien la dynamique de la région du bulbe. Seule le « pattern speed » de la barre a ensuite été ajustée à la localisation des structures résonantes dans l'espace des vitesses locales, en excluant les bras spiraux du modèle.

Un autre hyperparamètre à ajuster puis à fixer est le temps d'intégration (fictif), T_{int}, dans le cadre de l'intégration rétrograde. Celui-ci n'affectera pas la position des crêtes dans l'espace des vitesses locales, mais influencera leur « netteté » apparente. Comme dans Dehnen (2000), nous avons séparé le temps d'intégration total en deux phases de durée égale : la croissance de la barre et le plateau de son amplitude, avec la fonction de croissance suivante : où $\mathcal{T} \equiv (4t + 3T_{\mathrm{int}})/T_{\mathrm{int}}$. Nous avons choisi d'ajuster ces deux paramètres (le « pattern speed » et le temps d'intégration fictif) à la distribution 1D des étoiles dans le voisinage solaire pour des vitesses azimutales comprises entre $90, \mathrm{km\,s^{-1}} < V_\varphi < 330, \mathrm{km\,s^{-1}}$ à $V_R = 100, \mathrm{km\,s^{-1}}$. Cette distribution est présentée dans la Fig. 2.8. Le choix d'analyser les crêtes à grand V_R permet d'éviter qu'elles soient « contaminées » par l'effet additionnel des bras

spiraux puisque, comme nous le verrons dans la sous-section suivante, ceux-ci déforment principalement l'espace des vitesses locales dans les régions centrales de l'ellipsoïde de vitesses. Cet ajustement du « pattern speed » de la barre a été réalisé dans le voisinage solaire, qui constitue le volume le plus complet, de sorte qu'aucun pic ni vallée n'y soit manquant.

D'un point de vue quantitatif, nous avons comparé la somme des carrés des différences de la distribution 1D des vitesses azimutales dans chaque bin de 2, $\mathrm{km\,s^{-1}}$ entre l'échantillon Gaia RVS du disque et le modèle à barre seule. Seule la position des pics importe ici, c'est pourquoi la renormalisation de la fonction de distribution (DF) n'a été appliquée que dans le petit domaine en V_R considéré dans la Fig.2.8, au lieu de la normalisation de la DF appliquée à l'ensemble de l'espace des vitesses locales dans tous les autres cas. Nous trouvons la meilleure concordance pour $\Omega_\mathrm{b} = 37$, $\mathrm{km\,s^{-1}kpc^{-1}}$, pour un temps d'intégration total (fictif) de 543Myr, correspondant à 3,2 rotations de la barre. Notons toutefois que le pic de vitesse attribuable au groupe en mouvement de Bobylev, ou à la partie inférieure de la bimodalité d'« Hercule » (à $V_\varphi \sim 160\,\mathrm{km\,s^{-1}}$ dans la Fig. 2.8), n'est pas reproduit, et ne l'est jamais par un modèle à barre seule qui reproduit également le chapeau à grand V_φ. Notre meilleure valeur du « pattern speed » place le rayon de corotation de la barre à $R = 6.6$ kpc et son rayon d'OLR à $R = 11$ kpc.

Dans la première colonne de la Fig.2.10, nous présentons la distribution des vitesses (V_R, V_φ) à la position solaire (en fixant la valeur à zéro dans les pixels sans étoiles dans les données à moins de 300pc du Soleil), la distribution locale des actions (J_φ, J_R), ainsi que la vitesse radiale galactocentrique médiane $\tilde{V}R$ en fonction de la position dans le plan galactique. De manière remarquable, la distribution cinématique locale correspondant à ce modèle avec barre seule est déjà très similaire à celle observée, sans aucune contribution supplémentaire des bras spiraux (voir aussi Monari et al., 2019a, pour une conclusion similaire mais moins quantitative). Le succès de ce modèle de barre à reproduire autant de structures ressemblant à la distribution cinématique locale observée provient des signatures des résonances de Lindblad de ses multiples modes. Nous le confirmons dans l'Annexe, où nous fournissons une formule simple basée sur les lignes d'énergie constante dans le formalisme épicyclique amélioré de Dehnen (1999a) afin d'évaluer la localisation approximative de la signature de chaque résonance de la barre dans l'espace des vitesses locales. À $V_R = 100$, $\mathrm{km\,s^{-1}}$, ces localisations approximatives des résonances de la barre sont également indiquées par de petits tirets au-dessus de la Fig.2.8. Cependant, comme cela apparaît clairement dans la troisième ligne de la Fig.2.10, le modèle avec barre seule produit une structure dipolaire des vitesses radiales médianes dans le plan, très différente de celle observée. Cela implique que d'autres ingrédients dynamiques sont nécessaires pour reproduire ce champ de vitesses médian, ce qui est le sujet de la sous-section suivante. Un autre défaut manifeste du modèle avec barre seule, localement, est que le groupe en mouvement de « Sirius » ne se distingue pas dans l'espace des vitesses locales. Quantitativement, si l'on considère la densité d'étoiles dans une bande de $V\varphi$ comprise entre $250\,\mathrm{km\,s^{-1}}$ et $260\,\mathrm{km\,s^{-1}}$ dans l'espace des vitesses locales, et que l'on compare la valeur en $V_R = -12\,\mathrm{km\,s^{-1}}$ à celle en $V_R = 0\,\mathrm{km\,s^{-1}}$, on obtient une augmentation d'environ 25% dans les données à $V_R = -12\,\mathrm{km\,s^{-1}}$ (le pic de « Sirius »), tandis que l'on obtient une diminution de 11% dans le modèle avec barre seule (presque identique au cas axisymétrique). Cela indique que « Sirius » est probablement causé par les bras spiraux.

Ajout des bras spiraux

Étant donné l'échec du modèle à barre seule à reproduire le champ de vitesse radiale médian, l'étape suivante a consisté à ajouter des modes non axisymétriques correspondant aux bras spiraux. Nous avons commencé par ajouter un seul mode au modèle à barre seule (c'est-à-dire avec $\Omega_\mathrm{b} = 37$, $\mathrm{km\,s^{-1}kpc^{-1}}$ fixé), avec une multiplicité $m \in [1, 2, 3, 4]$. Nous avons fixé la hauteur d'échelle à la même valeur que celle du composant gazeux du potentiel de fond, $h_{\mathrm{s},m} = 130$ pc, la coupure externe étant l'OLR de la spirale, et la coupure interne correspondant à la plus grande valeur entre le rayon de corotation de la barre et l'ILR de la spirale (de sorte que la spirale s'étende entre son ILR et son OLR mais ne pénètre pas à l'intérieur de la corotation de la barre). La fonction de croissance $G_{\mathrm{s,m}}(t)$ a la même forme que celle de la barre, et nous avons fixé le temps d'intégration à exactement une rotation complète du mode

de bras spiral. Dans de nombreuses autres tentatives, même en permettant plus d'une rotation et un temps de croissance différent, les meilleurs candidats de la méthode décrite ci-après tendent à converger vers des valeurs proches de celles que nous avons retenues.

L'exploration de l'ensemble de l'espace des paramètres avec la méthode d'intégration rétrograde sur une large portion de l'espace des phases est extrêmement coûteuse en calcul, ce qui nous a conduits à adopter la stratégie suivante pour ajuster le modèle galactique aux données de Gaia. L'ajustement a été réalisé avec la méthode d'évolution différentielle de Storn and Price (1997), une méthode d'optimisation génétique globale implémentée dans la bibliothèque Python `SciPy`. Cet algorithme minimise une fonction objectif, définie comme une fonction d'erreur pondérée $\mathcal{L} = \sum_i (\tilde{V}^{\rm model} R, i - \tilde{V}^{\rm data} R, i)^2 / \sigma_i^2$, comparant les vitesses radiales médianes issues du modèle et des données sur une petite sélection de points (x_i, y_i) avec des poids $1/\sigma_i$. Les vitesses radiales médianes observées $\tilde{V}^{\rm data} R, i$ ont été calculées dans des cases de 250 pc autour du point sélectionné (x_i, y_i), tandis que les vitesses radiales médianes du modèle sont la médiane calculée de la distribution de VR au point sélectionné, c'est-à-dire les valeurs de la DF du modèle dans le plan (V_R, V_φ) intégrées sur V_φ.L'exploration de l'ensemble de l'espace des paramètres avec la méthode d'intégration rétrograde sur une large portion de l'espace des phases est extrêmement coûteuse en calcul, ce qui nous a conduits à adopter la stratégie suivante pour ajuster le modèle galactique aux données de Gaia. L'ajustement a été réalisé avec la méthode d'évolution différentielle de Storn and Price (1997), une méthode d'optimisation génétique globale implémentée dans la bibliothèque Python `SciPy`. Cet algorithme minimise une fonction objectif, définie comme une fonction d'erreur pondérée $\mathcal{L} = \sum_i (\tilde{V}^{\rm model} R, i - \tilde{V}^{\rm data} R, i)^2 / \sigma_i^2$, comparant les vitesses radiales médianes issues du modèle et des données sur une petite sélection de points (x_i, y_i) avec des poids $1/\sigma_i$. Les vitesses radiales médianes observées $\tilde{V}^{\rm data} R, i$ ont été calculées dans des cases de 250 pc autour du point sélectionné (x_i, y_i), tandis que les vitesses radiales médianes du modèle sont la médiane calculée de la distribution de VR au point sélectionné, c'est-à-dire les valeurs de la DF du modèle dans le plan (V_R, V_φ) intégrées sur V_φ. Le choix des points sélectionnés et de leurs poids respectifs a été une étape délicate. Le nombre de points doit être limité afin de réduire le temps de calcul, mais cela implique aussi qu'ils doivent être choisis à des positions « stratégiques » et non pas simplement sur une grille uniforme. De plus, les pondérer simplement par le nombre d'étoiles dans les données donnerait trop de poids au voisinage solaire par rapport à l'ensemble de la zone de l'ajustement. Le premier point auquel nous avons néanmoins attribué le poids le plus élevé, $1/\sigma_0$, est la position solaire (x_0, y_0). Nous devions ensuite choisir des points représentatifs des variations des valeurs (positives et négatives) de la vitesse radiale médiane sur tout le plan. L'ajout de bras spiraux comporte invariablement le risque de ne pas préserver le gradient de vitesse radiale à peu près correct provenant de la barre dans la région autour de $(x_1, y_1) = (7.0\,{\rm kpc}, 3.5\,{\rm kpc})$ et $(x_2, y_2) = (7.0\,{\rm kpc}, 1.0\,{\rm kpc})$, mais il est nécessaire pour inverser le signe de $\tilde{V}_R$ en $(x_3, y_3) = (9.0\,{\rm kpc}, 0.0\,{\rm kpc})$. Ces trois points constituaient nos seconds points les plus importants, tous avec $\sigma_i = 2\sigma_0$. Nous avons ensuite choisi deux paires de points le long d'axes de y constant qui encapsulent les variations positives-négatives dans le champ de vitesses radiales médianes : $(x_4, y_4) = (6.5\,{\rm kpc}, 0.0\,{\rm kpc})$, $(x_5, y_5) = (10.0\,{\rm kpc}, 0.0\,{\rm kpc})$, $(x_6, y_6) = (7.0\,{\rm kpc}, -3.0\,{\rm kpc})$ et $(x_7, y_7) = (10.0\,{\rm kpc}, -3.0\,{\rm kpc})$, avec $\sigma_i = 3\sigma_0$. Afin de capturer la structure spiralée marquée en bas à gauche du plan, nous avons également ajouté deux points, $(x_8, y_8) = (6.0\,{\rm kpc}, -2.5\,{\rm kpc})$ et $(x_9, y_9) = (7.5\,{\rm kpc}, -2.5\,{\rm kpc})$, avec $\sigma_i = 5\sigma_0$. Nous avons enfin imposé une contrainte dans le disque externe, $(x_{10}, y_{10}) = (11.5\,{\rm kpc}, 1.0\,{\rm kpc})$ et $(x_{11}, y_{11}) = (12.0\,{\rm kpc}, 0.0\,{\rm kpc})$, également avec $\sigma_i = 5\sigma_0$. Ceux-ci constituaient les points essentiels de notre ajustement. Nous avons ajouté par-dessus un ensemble de points à faible poids dont la seule fonction était d'aider à guider l'ajustement : $(x_{12}, y_{12}) = (9.0\,{\rm kpc}, -3.0\,{\rm kpc})$, $(x_{13}, y_{13}) = (9.0\,{\rm kpc}, 3.5\,{\rm kpc})$, $(x_{14}, y_{14}) = (10.0\,{\rm kpc}, 3.5\,{\rm kpc})$ et $(x_{15}, y_{15}) = (12.0\,{\rm kpc}, 3.5\,{\rm kpc})$, tous avec $\sigma_i = 100\sigma_0$. Tous les points sélectionnés sont indiqués par des cercles dans le panneau central inférieur de la Fig. 2.10. Cette sélection de points et leurs poids jouent ici le rôle d'un a priori sur les régions les plus importantes de l'espace des configurations.

Pour notre algorithme génétique, définissons maintenant notre population de solutions candidates dans l'espace des paramètres comme $\mathbf{a}i, g$, avec $1 \leq i \leq n$ et $1 \leq g \leq N$. Cela signifie que nous considérons n candidats pour chaque génération, pendant N générations. En pratique, une première génération de solutions candidates est créée en choisissant de manière stochastique de nombreux paramètres candidats dans l'espace des paramètres grâce à un échantillonnage en hypercube latin, tout en essayant de couvrir la majeure partie de l'espace des paramètres dans les bornes spécifiées ci-après. Cette population est ensuite mutée, candidat par candidat, de manière itérative, établissant ainsi une nouvelle génération à chaque itération. À chaque génération g, la mutation de chaque candidat $\mathbf{a}i, g$ est appliquée selon la stratégie « best1bin », avec les étapes suivantes :

- Sélectionner le meilleur candidat de paramètres (celui qui minimise la fonction d'erreur pondérée à la génération courante), $\mathbf{a}_{best,g}$.
- Pour muter chaque candidat $\mathbf{a}_{i,g}$, sélectionner aléatoirement deux autres vecteurs de paramètres candidats, $\mathbf{a}_{j,g}$ et $\mathbf{a}_{k,g}$.
- Prendre un facteur de multiplication fixe (facteur de mutation $\mathcal{M}$) de leur différence en paramètres, $\mathcal{M}\left(\mathbf{a}_{j,g} - \mathbf{a}_{k,g}\right)$, pour obtenir un vecteur $\mathbf{v}_i = \mathbf{a}_{best,g} + \mathcal{M}\left(\mathbf{a}_{j,g} - \mathbf{a}_{k,g}\right)$.
- Le nouveau vecteur d'essai $\mathbf{a}_{i,g+1}$ est alors construit composante par composante, en attribuant la valeur de chaque paramètre soit depuis $\mathbf{v}_i$, soit depuis $\mathbf{a}_{i,g}$ selon qu'une réalisation de la fonction binomiale entre 0 et 1 est inférieure ou supérieure à une valeur de recombinaison choisie $\mathcal{C}$, respectivement.
- Calculer la fonction d'erreur pondérée pour le vecteur d'essai $\mathbf{a}_{i,g+1}$: si ses performances sont meilleures en termes de fonction objectif, il remplace le candidat initial dans la génération suivante, sinon le candidat initial $\mathbf{a}_{i,g}$ reste inchangé à la génération $g + 1$.
- Les critères de convergence sont atteints lorsque l'écart-type des valeurs de la fonction objectif de la population à une génération donnée est inférieur à 1% de la valeur moyenne de la fonction objectif de tous les candidats de la population à cette génération. Le candidat final $\mathbf{a}_{best,g=N}$ est conservé.

Nous avons conservé les valeurs standard des hyperparamètres de l'algorithme, notamment la taille de la population n (15 fois le nombre de paramètres), la valeur de recombinaison $\mathcal{C} = 0.7$, et le facteur de mutation $\mathcal{M}$, une variable aléatoire comprise entre 0.5 et 1. Cette méthode a été choisie car elle est extrêmement efficace pour converger rapidement dans un espace de paramètres de grande dimension. La sélection des points et de leurs poids joue le rôle d'un a priori dans la détermination des régions les plus importantes de l'espace des configurations. Cependant, contrairement à une méthode bayésienne classique, aucun postérieur ni barres d'erreur bien définies ne peuvent être fournis. Nous ne sommes donc pas en mesure de donner des barres d'erreur, et nous ne pouvons exclure que nos meilleurs modèles candidats trouvés ci-après correspondent à des minima locaux dans l'espace des paramètres. De futures améliorations de ce travail devraient aborder cette question, ainsi que prendre en compte une fonction de sélection de Gaia (e.g., Castro-Ginard et al., 2023).

Nous avons d'abord tenté d'ajuster un seul mode de bras spiraux, en permettant aux angles de pitch de varier entre 6° et 30°, à la phase de varier sur l'ensemble des 360°, à l'amplitude du potentiel de varier de zéro jusqu'à 0.2%, et à le « pattern speed » de varier de 10, $\mathrm{km\,s^{-1}}kpc$ jusqu'à le « pattern speed » de la barre : le mode $m = 2$ a donné les meilleurs résultats en termes de fonction objectif parmi $m \in [1, 2, 3, 4]$, avec une vitesse de rotation de 13, $\mathrm{km\,s^{-1}}kpc$. Il s'agit du principal résultat de notre recherche, que nous allons maintenant chercher à affiner. En effet, ce modèle préféré à un seul mode produit clairement un espace des vitesses locales déformé, en particulier un groupe en mouvement de type « Sirius » très déformé par rapport aux observations. Cela n'est pas entièrement surprenant, puisque l'espace des vitesses locales n'a pas été utilisé pour contraindre l'ajustement. Nous avons ensuite modifié la fonction objectif $\mathcal{L}$ avec une contrainte locale, comme suit : $\mathcal{L}' = \mathcal{L} + \sum_{i=1}^{i=2}(\Delta_i^{\mathrm{model}} - \Delta_i^{\mathrm{data}})^2/\sigma_\Delta^2$, où Δ_i est la

position du pic de la distribution 1D de V_R à $V_\varphi, =, 250, \mathrm{km s^{-1}}$ ($i = 1$) et à $V_\varphi, =, 260, \mathrm{km s^{-1}}$ ($i = 2$) au Soleil, et $\sigma_\Delta = 3\sigma_0$ dans les deux cas. L'utilisation de $\mathcal{L}'$, cependant, conduit encore à un meilleur candidat présentant un groupe mobile de type « Sirius » déformé dans l'espace des vitesses locales lorsqu'on considère un seul mode $m = 2$.

Ensuite, afin de possiblement améliorer ce modèle, nous avons tenté un nouvel ajustement en ajoutant un second mode spiral de multiplicité $m = 3$ ou $m = 4$, en plus du premier et de la barre. Nous avons supposé que le bras spiral $m = 2$ possède une plage de vitesses de rotation $10\,\mathrm{km\,s^{-1}} kpc < \Omega_{\mathrm{s},2} < 14\,\mathrm{km\,s^{-1}} kpc$, proche de la valeur trouvée pour l'ajustement à mode unique, que nous cherchons à améliorer. Ensuite, afin de possiblement améliorer ce modèle, nous avons tenté un nouvel ajustement en ajoutant un second mode spiral de multiplicité $m = 3$ ou $m = 4$, en plus du premier et de la barre. Nous avons supposé que le bras spiral $m = 2$ possède une plage de vitesses de rotation $10\,\mathrm{km\,s^{-1}} kpc < \Omega_{\mathrm{s},2} < 14\,\mathrm{km\,s^{-1}} kpc$, proche de la valeur trouvée pour l'ajustement à mode unique, que nous cherchons à améliorer. Pour réduire l'espace des paramètres, l'amplitude du second mode d'ordre supérieur — dont le « pattern speed » et l'angle de pitch sont autorisés à varier respectivement de 10, $\mathrm{km\,s^{-1}} kpc$ jusqu'à le « pattern speed » de la barre et de 6° à 30° — a été fixée avec l'équation proposée par Hamilton (2024), reliant l'amplitude respective des deux modes à leur vitesse de rotation et à leur angle de pitch, à savoir comme étant inversement proportionnelle au produit du carré de leur vitesse de rotation par la tangente de leur angle de pitch (d'où une amplitude plus élevée pour une vitesse de rotation plus faible et un angle de pitch plus petit). Pour réduire davantage l'espace des paramètres, nous avons imposé que la somme des contrastes de densité locale pour les deux modes spiraux soit inférieure à 35%, en vérifiant a posteriori que cette limite ne serait pas atteinte par notre meilleur candidat. Pour calculer le contraste de densité de surface de chaque mode, nous avons pris le rapport entre la densité de surface intégrée au Soleil de la composante baryonique axisymétrique et la densité de surface des bras spiraux correspondant au potentiel de Cox and Gomez (2002) (voir aussi Monari et al., 2016b).

L'ajout de ce second mode $m = 3$ a permis d'atténuer et de régulariser la signature du groupe en mouvement de « Sirius » dans l'espace des vitesses locales, tout en améliorant légèrement la carte de la vitesse radiale médiane. Afin d'affiner davantage les paramètres de ce meilleur candidat trouvé grâce à notre méthode d'optimisation globale, nous avons ensuite effectué une recherche fine par descente de gradient dans un domaine restreint de l'espace des paramètres (large de $1\,\mathrm{km\,s^{-1}} kpc$ en vitesse de rotation, 6° en phase, 2° en angle de pitch, et 0.04% en amplitude potentielle, $K_{\mathrm{s},2}$) autour de notre meilleure solution candidate, à l'aide de l'algorithme Limited-memory Broyden–Fletcher–Goldfarb–Shanno (L-BFGS-B) implémenté dans `Scipy`. La solution ainsi obtenue constitue notre modèle de référence.

Les paramètres finaux de ce modèle de référence sont présentés dans le Tableau 2.2, tandis que sa distribution locale dans l'espace des vitesses et des actions, ainsi que la carte de vitesses radiales médianes, sont présentées dans la troisième colonne de la Fig. 2.10. L'amélioration de la carte des vitesses radiales médianes par rapport au modèle avec barre seule est frappante, mais il existe également des améliorations plus subtiles dans l'espace des vitesses locales, en particulier une meilleure représentation des groupes en mouvement proches du centre de l'ellipsoïde de vitesses. Pour « Sirius », si l'on reconsidère la densité d'étoiles dans une bande de V_φ comprise entre $250\,\mathrm{km\,s^{-1}}$ et $260\,\mathrm{km\,s^{-1}}$, on obtient désormais une augmentation de 5% en $V_R = -12\,\mathrm{km\,s^{-1}}$ par rapport à $V_R = 0\,\mathrm{km\,s^{-1}}$ dans le modèle. Cela reste un pic nettement plus faible que dans les données (∼25%), ce qui nécessitera des investigations supplémentaires, mais constitue une amélioration significative par rapport à la diminution de 11% dans le modèle avec barre seule. Dans la section suivante, nous comparons qualitativement les prédictions de ce modèle de référence à celles d'autres observables.

B.5 Discussions

Le modèle de référence présenté dans le Tableau 2.2 a été ajusté aux données sans a priori sur la position des bras spiraux. Il est maintenant possible de vérifier dans quelle mesure le modèle parvient à retrouver la position des bras spiraux connus de la Galaxie, ainsi que d'évaluer ses performances dans la reproduc-

tion d'autres observables, tels que le champ de vitesses azimutales ou les positions détaillées des groupes en mouvement à travers le disque.

Positions des bras spiraux

Dans la Fig. 4.1, nous présentons la carte globale des vitesses radiales prédite par notre modèle de référence, ainsi que la position de la barre et de la densité maximale des deux modes de bras spiraux ajustés dynamiquement. La ligne continue pour chaque mode spiral dans la Fig. 4.1 correspond au minimum du potentiel spiral, et donc à la densité maximale du bras, jusqu'au rayon de coupure. La correspondance entre densité et potentiel n'est pas bien définie sur le cercle correspondant au rayon de coupure, mais choisir une fonction lisse $\sim (1+\tanh)/2$ au lieu d'une fonction échelon pour $H_m(R)$ dans l'équation 2.10 conduit effectivement à un contraste de densité marqué sur ce cercle jusqu'au point où le potentiel spiral s'annule. Ce contraste de densité marqué est représenté par les lignes pointillées dans la Fig. 4.1. Nous comparons également la position de ces bras aux surdensités d'étoiles jeunes de la séquence principale supérieure identifiées dans Poggio et al. (2021). Comme cela apparaît clairement dans cette figure, le mode $m = 2$ le plus fort correspond bien à la position du bras de la « Crux-Scutum » près de la barre galactique (bien que cette localisation soit aussi souvent considérée comme une continuation du bras du « Carina-Sagittarius »), du bras « Local » près du Soleil, et du bras Extérieur. Cependant, la distribution des étoiles jeunes est une conséquence de la distribution du gaz, tandis que ce que nous retraçons ici est le potentiel. Il est donc particulièrement utile de noter que nos résultats semblent également cohérents avec ceux de Widmark and Naik (2024), qui a trouvé que le bras « Local » constitue une forte surdensité locale, avec un contraste de densité d'environ 20%, proche de la surdensité locale de 24,9% dans notre modèle.

Étant donné que le « pattern speed » du bras spiral $m = 2$ est plus faible que celle de la barre, cela pourrait être interprété comme une déconnexion récente (il y a 52,5 Myr) de la barre dans la région de la « Crux-Scutum », en accord avec les résultats de Vislosky et al. (2024). En revanche, le bras spiral plus faible $m = 3$ correspond bien à la localisation des bras du « Carina-Sagittarius » et de « Perseus ». Il est remarquable qu'un ajustement purement dynamique permette de retrouver en grande partie la position des surdensités de bras spiraux connues dans le disque.

Une autre quantité intéressante à comparer avec les prédictions de notre modèle est la valeur médiane de J_R en fonction de la position dans le disque. En effet, Palicio et al. (2023) ont identifié des structures de bras spiraux dans le disque à partir des valeurs médianes de $\tilde{J}_R$ en fonction de la position. Nous reproduisons une telle carte à partir des données Gaia RVS dans le voisinage solaire étendu, dans la Fig. 4.2, et superposons la position des bras spiraux issus de notre modèle de référence. Nous calculons également les valeurs médianes axisymétriques de $\tilde{J}_R$ à partir de notre modèle, en partant de la même grille de vitesses qu'auparavant à chaque position dans le plan, puis en calculant les actions radiales correspondantes avec `AGAMA` (dans le potentiel axisymétrique de fond), et en prenant la médiane à partir des valeurs de la fonction de distribution. Là encore, l'accord qualitatif a posteriori avec les données est remarquable. Notons que l'augmentation de $\tilde{J}_R$ axisymétrique médian est positivement associée à la présence de bras spiraux dans notre modèle, conformément aux résultats de Debattista et al. (2025) lorsqu'on considère les actions axisymétriques instantanées. Dans les simulations N-corps, il est généralement nécessaire de moyenner les actions sur une échelle de temps suffisamment longue afin de mieux suivre les spirales pour de faibles valeurs (Debattista et al., 2025) de l'action radiale moyenne dans le temps. Dans notre cas, l'essentiel à retenir est l'accord qualitatif a posteriori entre les données et le modèle pour le $\tilde{J}_R$ instantané, sans avoir utilisé cette quantité dans la procédure d'ajustement.

Champ de vitesses azimutales

Une quantité intéressante à examiner, en principe, est la variation de la vitesse azimutale médiane à un rayon galactocentrique fixé, car il s'agit également d'une signature claire de la non-axisymétrie du potentiel. Pour éviter d'être dominé par la fonction de distribution de fond et le potentiel axisymétrique, on peut tracer à partir des données la valeur $\Delta\tilde{V}_\varphi \equiv \tilde{V}_\varphi(x, y) - \tilde{V}_\varphi(R)$, dans le plan (x, y). Cette quantité est présentée dans le panneau de gauche de la Fig. 4.3. Un inconvénient de cette représentation est que la concaténa-

tion azimutale à rayon fixé ne peut être effectuée que dans la région où des données sont disponibles, ce qui explique pourquoi il n'était pas évident d'utiliser une telle quantité comme objectif de l'ajustement lui-même. En revanche, à partir de notre modèle de référence, on peut directement soustraire de la vitesse radiale médiane à chaque position la vitesse radiale médiane obtenue à partir de la fonction de distribution de fond au même endroit. On observe dans le modèle des tendances similaires à celles des données, bien que les deux quantités ne soient pas aisément comparables de manière quantitative.

Vitesse radiale médiane dans le plan azimut–moment angulaire

Une projection intéressante des données de Gaia (voir, par exemple, Friske and Schönrich, 2019; Monari et al., 2019b; Trick et al., 2021; Chiba et al., 2021) est la structure de la vitesse radiale médiane (ou moyenne) dans le plan azimut–moment angulaire. Dans la Fig. 4.4, nous représentons la vitesse radiale médiane dans le plan (J_φ, φ) pour les étoiles situées dans une boîte $[1300, 3000]\,\mathrm{km\,s^{-1}\,kpc} \times [-0.67, 0.67]\,\mathrm{rad}$, avec $5\,\mathrm{kpc} < x < 12\,\mathrm{kpc}$ et $-4\,\mathrm{kpc} < y < 4\,\mathrm{kpc}$. Pour calculer les valeurs médianes dans le modèle, nous fixons d'abord un azimut φ_i tous les 0.01 rad, puis considérons des rayons R_j espacés de 10 pc. Ensuite, pour chaque point, nous calculons la fonction de distribution (DF) avec la méthode de l'intégration à rebours pour différentes vitesses V_R et $V_{\varphi,n} = \frac{J_{\varphi,n}}{R_j}$. Nous fixons ensuite $J_{\varphi,n}$ et additionnons les valeurs de la DF pour tous les rayons R_j, puis nous calculons la vitesse radiale médiane pour chaque $(\varphi_i, J_{\varphi,n})$. L'accord qualitatif avec les données est acceptable, bien que l'on puisse noter que les signatures deviennent faibles à faible J_φ dans le modèle. Cela peut être lié au fait que notre procédure non auto-cohérente n'est pas particulièrement fiable dans la partie très interne du disque proche de la barre. Cela pourrait également révéler que notre barre à vitesse de rotation constante ne suffit pas à expliquer toute la richesse des données dans ce plan (Chiba et al., 2021), et que nous manquons l'effet des perturbations verticales (par ex. Laporte et al., 2019; Laporte et al., 2020), ainsi que des structures accrétées en rotation progrgrade, bien que tout cela nécessite des investigations supplémentaires.

Groupes en mouvement à travers le disque

Dans Bernet et al. (2022) and Bernet et al. (2024), une méthodologie a été développée pour effectuer une recherche à l'aveugle de groupes en mouvement dans les données de Gaia à travers l'ensemble du disque, basée sur l'exécution d'une transformée en ondelettes dans de petits volumes indépendants du disque, suivie d'un regroupement en structures globales grâce à l'algorithme de recherche en largeur (Breadth-first search) issu de la théorie des graphes. En fixant une valeur donnée de V_R, on peut alors, par exemple, observer l'évolution de la localisation des groupes en mouvement dans le plan (R, V_φ) à l'azimut du Soleil, ou dans le plan (φ, V_φ) au rayon du Soleil. Dans la Fig. 4.6, nous superposons les structures identifiées dans Gaia DR3 sur la densité issue de notre modèle. La distribution azimutale des groupes en mouvement (panneaux de droite de la Fig. 4.6) est globalement en accord avec les pentes prédites par notre modèle au rayon solaire, tandis que la distribution radiale à l'azimut solaire (panneaux de gauche de la Fig. 4.6) apparaît également globalement cohérente avec les données, à l'exception de la région à faible $V_\varphi \leq 200\,\mathrm{km\,s^{-1}}$ pour de petits rayons $R \leq 6.5\,\mathrm{kpc}$ (les crêtes du modèle ayant une pente beaucoup trop élevée dans cette zone de l'espace des phases), où l'auto-gravité de la barre exerce probablement un effet non négligeable sur les données.

Fait intéressant, dans le modèle, le groupe en mouvement d'« Hercule » au rayon solaire semble résulter de la fusion de deux crêtes à plus petits rayons, visibles comme des régions sombres dans la Fig. 4.6 dans la densité sous-jacente du modèle : l'une avec une pente compatible avec le gradient radial observé du groupe d'« Hercule », essentiellement causé par la barre, et une autre avec une pente plus forte, due principalement aux bras spiraux. Cela est particulièrement net pour V_R positif, où les deux crêtes sont clairement séparées pour $R < 7$ kpc dans le modèle, tandis que cette séparation semble également laisser une signature similaire dans les données. Pour $V_R = 0$, la séparation est aussi visible, bien qu'elle fusionne avec la continuation interne du groupe en mouvement des « Hyades ». Pour

V_R négatif, l'accord est moins bon, mais dans une région où l'on s'attend à ce qu'« Hercule » domine moins : la seconde crête d'« Hercule » se superpose à celle des « Hyades » à $R \sim 7\,\mathrm{kpc}$ dans le modèle, tandis que dans les données cela n'apparaît que comme une légère courbure vers le haut de la crête des « Hyades », correspondant à la fusion des crêtes dans le modèle. Cette seconde crête d'« Hercule » est clairement un effet des bras spiraux, tandis que la crête principale d'« Hercule » est produite par la barre seule. L'effet conjoint des multiples modes de la barre dans le présent modèle, associé au potentiel axisymétrique de fond utilisé, pourrait expliquer les différences avec Bernet et al. (2024).

Inversement, nous avons appliqué la méthode de Bernet et al. (2022) and Bernet et al. (2024) au modèle et superposé, dans la Fig. 4.7, les groupes détectés sur les données de Gaia à différents rayons à l'azimut du Soleil, ainsi qu'à différents azimuts au rayon solaire. Visuellement, certaines structures apparaissent remarquablement similaires entre le modèle et les données. Un point intéressant à noter est que, bien que non clairement visible à l'œil, le modèle semble bien retrouver une surdensité à la position du Soleil (structure en bas à droite dans le deuxième panneau en partant de la gauche dans la Fig. 4.7), que l'on peut identifier avec l'emplacement de la bimodalité « Bobylev–Hercule-2 » d'« Hercule », bien que beaucoup moins prononcée que dans les données.

Orbites du Soleil

À titre d'exemple d'application de notre modèle, nous proposons de comparer l'orbite planaire du Soleil dans le modèle axisymétrique de fond à celle obtenue dans notre modèle de référence non-axisymétrique. Le résultat est présenté dans la Fig. 4.8. Il est surtout illustratif et ne doit pas être sur-interprété, étant donné que les mouvements verticaux sont négligés. Dans le cas axisymétrique, la période radiale est de 161,5 Myr, et le Soleil est actuellement proche d'atteindre son péri-centre. Le temps écoulé entre le dernier passage au péri-centre et celui que nous sommes sur le point d'atteindre est légèrement plus court dans le modèle non-axisymétrique, à savoir 154,5 Myr. Le précédent passage au péri-centre, qui s'est produit un peu plus tard dans le modèle non-axisymétrique, s'est également effectué plus près du centre galactique que dans le cas axisymétrique. Le dernier apo-centre était très similaire dans les deux modèles, mais l'avant-dernier était plus éloigné dans la Galaxie externe dans le cas non-axisymétrique, pour lequel les amplitudes radiales sont typiquement plus grandes. Si l'on examine l'évolution de la densité de surface à la position du Soleil en fonction du temps, l'image devient plus complexe. Le temps entre le dernier maximum de densité de surface et celui que nous sommes sur le point d'atteindre (soit encore 161,5 Myr dans le cas axisymétrique) est un peu plus long dans le cas non-axisymétrique, à savoir 185 Myr, car nous suivrons temporairement la surdensité du bras « Local » sur notre trajet de retour vers le disque externe. De plus, en remontant à $t \sim -250$ Myr, l'apo-centre qui correspond à un minimum de densité de surface dans le modèle axisymétrique correspond en réalité à un maximum local dans le cas non-axisymétrique, car le Soleil suivait alors également un bras spiral à ce moment-là. Cela pourrait avoir des conséquences intéressantes dans l'étude des phénomènes de sédimentation cyclique sur Terre à longues échelles de temps (par ex. Boulila et al., 2018). Étant donné que l'on s'attend généralement à ce que les bras spiraux résultent d'un cycle récurrent de modes de rainures (« groove modes ») ou de modes de bord (« edge modes »), il est cependant impossible de remonter l'orbite du Soleil sur des échelles de temps supérieures à quelques centaines de Myr, du moins sans recourir à une modélisation chimio-dynamique détaillée de l'évolution de l'ensemble du disque galactique.

Orbites des associations jeunes

Les associations stellaires jeunes ($\sim$ 50 Myr) peuvent généralement être retracées jusqu'à leur position d'origine en intégrant leurs orbites en arrière dans un potentiel galactique donné. Pour illustrer l'importance de prendre en compte les non-axisymétries du potentiel dans une telle procédure, nous intégrons vers l'avant dans le temps, pendant 50 Myr, quatre associations stellaires jeunes archétypales situées à différentes positions dans le disque galactique au sein de notre modèle de référence non-axisymétrique. Chaque association est représentée par 20 étoiles dis« Perseus »s en vitesse et en espace selon des

lois gaussiennes de déviation standard $1\,\mathrm{km\,s^{-1}}$ en V_R et V_φ autour de la vitesse circulaire, et de 2 pc autour des positions $(x, y) = (10.6\,\mathrm{kpc}, -2.4\,\mathrm{kpc})$, $(8.7\,\mathrm{kpc}, -0.3\,\mathrm{kpc})$, $(7.1\,\mathrm{kpc}, 0.4\,\mathrm{kpc})$, $(6.0\,\mathrm{kpc}, -0.5\,\mathrm{kpc})$. Nous les intégrons ensuite en arrière dans le temps, à la fois dans le modèle de référence non-axisymétrique et dans le modèle de fond axisymétrique. Les associations reviennent généralement à une position qui peut être erronée de plus de 150 pc dans le cas axisymétrique, avec une forme allongée très différente de la configuration originale réelle (Fig. 4.9).

B.6 Conclusions

Nous avons utilisé les vitesses planaires d'un échantillon d'étoiles du disque avec une information de phase à 6D provenant de Gaia–StarHorse afin d'ajuster un modèle de potentiel galactique incluant une forme paramétrique détaillée pour la barre et les bras spiraux, en utilisant la méthode de l'intégration à rebours. Les observables ajustées étaient la vitesse radiale galactocentrique médiane, pour une sélection de points dans le plan galactique, complétée par des contraintes additionnelles issues de l'espace des vitesses locales à la position du Soleil. Tous les paramètres du potentiel non-axisymétrique de référence sont résumés dans le Tableau 2.2, au sein du potentiel de fond axisymétrique fixé dans le Tableau 2.1.

Il est remarquable qu'un tel ajustement purement dynamique retrouve de nombreuses localisations connues de surdensités de bras spiraux détectées en photométrie dans le disque (Fig. 4.1). Ces bras spiraux peuvent être interprétés comme des modes de rainure (« groove modes ») ou des modes de bord (« edge modes ») tels que ceux observés dans les simulations N-corps. Dans le voisinage solaire, nous identifions le bras « Local » comme une forte perturbation gravitationnelle, en accord avec les sondes indépendantes du potentiel non-axisymétrique local de Widmark and Naik (2024). Nous retrouvons également la carte observée des actions radiales médianes dans le voisinage solaire étendu (Fig. 4.2), ainsi qu'un bon accord qualitatif avec la variation détaillée en rayon et en azimut des groupes en mouvement identifiés dans les données de Gaia (Fig. 4.6). Ce dernier point est particulièrement remarquable, puisque le modèle n'a pas été directement ajusté à ces structures de l'espace des phases. Le seul groupe en mouvement ajusté localement était « Sirius », qui est totalement absent du modèle « barre seule » : nous notons néanmoins qu'il reste caractérisé par un pic plus faible dans le modèle de référence que dans les données. Bien que notre meilleur modèle candidat puisse correspondre à un minimum local dans l'espace des paramètres — ce dernier étant particulièrement vaste, surtout si l'on autorise la variation des paramètres de la densité axisymétrique de fond et de la fonction de distribution —, nous soutenons néanmoins qu'il peut, pour l'instant, être utilisé comme un potentiel non-axisymétrique de référence pour la Galaxie, par exemple afin d'intégrer avec fiabilité les orbites planaires. Il peut être comparé à d'autres potentiels galactiques récents tels que celui de Hunter et al. (2024). Le code permettant de générer des distributions de l'espace des vitesses locales ainsi que des cartes de vitesses radiales est rendu public.

Les avancées presentés dans cette annexe ne représente qu'une première étape quantitative dans la direction de l'établissement d'un potentiel non-axisymétrique 3D détaillé pour la Voie Lactée. Les améliorations futures de nos investigations consisteront à explorer ses conséquences tridimensionnelles, d'abord dans le cadre d'intégrations directes de particules tests (voir, par ex., Faure et al., 2014; Monari et al., 2016b), puisque les potentiels de barre (Thomas et al., 2023) et de spirales (Cox and Gomez, 2002) peuvent aisément être généralisés en trois dimensions. Notons également que nous avons fait l'hypothèse que les bras spiraux ne peuvent pas exister à l'intérieur de la résonance de corotation de la barre ($R = 6.6$ kpc dans notre modèle de référence), une hypothèse qui pourrait potentiellement être en partie levée : nous avons déjà vérifié que cela n'affecte pas beaucoup notre meilleur modèle candidat. Toutefois, un ajustement correct de ces régions internes du disque galactique nécessiterait de rendre le modèle auto-cohérent. L'absence d'auto-cohérence peut en effet devenir un problème sérieux dans les parties les plus internes de la Galaxie, où la perturbation de la barre est elle-même le traceur. Certaines déficiences de notre modèle à faibles rayons et faibles moments angulaires ont d'ailleurs déjà été identifiées dans la Fig. 4.4 et la Fig. 4.6. Bien que cela dé-

passe le cadre du présent travail, des améliorations futures de notre modèle pourraient s'appuyer sur une adaptation de la méthode auto-cohérente dite « made-to-measure » afin de prendre en compte l'auto-cohérence. Il convient aussi de souligner que le modèle de fond (potentiel axisymétrique et fonction de distribution) n'a pas été ajusté ici, et pourrait en principe également être contraint par les données. Cela augmenterait l'espace des paramètres et pourrait nous amener à utiliser des méthodes d'apprentissage automatique pour explorer efficacement l'ensemble de l'espace des paramètres. Une amélioration parallèle consistera à incorporer une fonction de sélection détaillée dans la procédure d'ajustement (par ex., Castro-Ginard et al., 2023; Khanna et al., 2024), et à calculer un véritable postérieur (avec barres d'erreur) sur les paramètres du meilleur ajustement, tout en tentant peut-être de séparer les populations stellaires en fonctions de distribution distinctes. Enfin, en passant à trois dimensions, il est évident que les perturbations verticales du disque, par exemple celles dues à la galaxie naine du Sagittaire, devront également être prises en compte, de même qu'une éventuelle variation temporelle du « pattern speed » de la barre.

En résumé, le modèle de référence présenté ici, reproduisant un plus grand nombre d'observables que jamais auparavant, constitue une avancée significative dans notre compréhension de la structure non-axisymétrique du disque de la Voie Lactée. Cependant, il est important d'en reconnaître les limites et de continuer à l'améliorer afin d'obtenir une représentation encore plus précise de notre Galaxie.

Bibliography

Al Kazwini, H. et al. (Feb. 2022). "Perturbed distribution functions with accurate action estimates for the Galactic disc". In: A&A 658, A50, A50. arXiv: 2012.06597 [astro-ph.GA].

Amaral, L. H. and J. R. D. Lepine (Apr. 1997). "A self-consistent model of the spiral structure of the Galaxy". In: MNRAS 286.4, pp. 885–894.

Anders, F. et al. (Aug. 2019). "Photo-astrometric distances, extinctions, and astrophysical parameters for Gaia DR2 stars brighter than G = 18". In: A&A 628, A94, A94. arXiv: 1904.11302 [astro-ph.GA].

Anders, F. et al. (Feb. 2022). "Photo-astrometric distances, extinctions, and astrophysical parameters for Gaia EDR3 stars brighter than G = 18.5". In: A&A 658, A91, A91. arXiv: 2111.01860 [astro-ph.GA].

Antoja, T. et al. (Oct. 2008). "Origin and evolution of moving groups. I. Characterization in the observational kinematic-age-metallicity space". In: A&A 490.1, pp. 135–150. arXiv: 0809.0511 [astro-ph].

Antoja, T. et al. (Oct. 2012). "Kinematic groups beyond the solar neighbourhood with RAVE". In: MNRAS 426.1, pp. L1–L5. arXiv: 1205.0546 [astro-ph.GA].

Antoja, T. et al. (Mar. 2014). "Constraints on the Galactic bar from the Hercules stream as traced with RAVE across the Galaxy". In: A&A 563, A60, A60. arXiv: 1309.4272 [astro-ph.GA].

Antoja, T. et al. (Sept. 2018). "A dynamically young and perturbed Milky Way disk". In: Nature 561.7723, pp. 360–362. arXiv: 1804.10196 [astro-ph.GA].

Astropy Collaboration et al. (Aug. 2022). "The Astropy Project: Sustaining and Growing a Community-oriented Open-source Project and the Latest Major Release (v5.0) of the Core Package". In: *apj* 935.2, 167, p. 167. arXiv: 2206.14220 [astro-ph.IM].

Baba, Junichi, Takayuki R. Saitoh, and Keiichi Wada (Jan. 2013). "Dynamics of Non-steady Spiral Arms in Disk Galaxies". In: ApJ 763.1, 46, p. 46. arXiv: 1211.5401 [astro-ph.GA].

Bailer-Jones, C. A. L. (Dec. 2023). "Estimating Distances from Parallaxes. VI. A Method for Inferring Distances and Transverse Velocities from Parallaxes and Proper Motions Demonstrated on Gaia Data Release 3". In: AJ 166.6, 269, p. 269. arXiv: 2311.00374 [astro-ph.GA].

Bailer-Jones, C. A. L. et al. (Aug. 2018a). "Estimating Distance from Parallaxes. IV. Distances to 1.33 Billion Stars in Gaia Data Release 2". In: AJ 156.2, 58, p. 58. arXiv: 1804.10121 [astro-ph.SR].

Bailer-Jones, C. A. L. et al. (Aug. 2018b). "New stellar encounters discovered in the second Gaia data release". In: A&A 616, A37, A37. arXiv: 1805.07581 [astro-ph.SR].

Bailer-Jones, C. A. L. et al. (Mar. 2021). "Estimating Distances from Parallaxes. V. Geometric and Photogeometric Distances to 1.47 Billion Stars in Gaia Early Data Release 3". In: AJ 161.3, 147, p. 147. arXiv: 2012.05220 [astro-ph.SR].

Baranne, A., M. Mayor, and J. L. Poncet (Jan. 1979). "Coravel— A new tool for radial velocity measurements". In: *Vistas in Astronomy* 23.4, pp. 279–316.

Barbillon, M. et al. (Jan. 2025). "Constraints on the history of Galactic spiral arms revealed by Gaia GSP-Spec α-elements". In: A&A 693, A3, A3. arXiv: 2411.10007 [astro-ph.GA].

Belokurov, V. et al. (July 2018). "Co-formation of the disc and the stellar halo". In: MNRAS 478.1, pp. 611–619. arXiv: 1802.03414 [astro-ph.GA].

Benjamin, R. A. et al. (Sept. 2005). "First GLIMPSE Results on the Stellar Structure of the Galaxy". In: ApJ 630.2, pp. L149–L152. arXiv: astro-ph/0508325 [astro-ph].

Beraldo e Silva, Leandro, Walter de Siqueira Pedra, and Monica Valluri (Feb. 2019). "The Discreteness-driven Relaxation of Collisionless Gravitating Systems: Entropy Evolution and the Nyquist-Shannon Theorem". In: ApJ 872.1, 20, p. 20. arXiv: 1812.06901 [astro-ph.GA].

Bernet, M. et al. (Nov. 2022). "From ridges to manifolds: 3D characterization of the

moving groups in the Milky Way disc". In: A&A 667, A116, A116. arXiv: 2206.01216 [astro-ph.GA].

Bernet, M. et al. (June 2024). "Radial and azimuthal gradients of the moving groups in Gaia DR3: The slow and fast bar degeneracy problem". In: A&A 686, A92, A92. arXiv: 2403.02393 [astro-ph.GA].

Bernet, Marcel et al. (May 2025). "Dark matter spiral arms in Milky Way-like halos". In: A&A 697, A214, A214. arXiv: 2503.07753 [astro-ph.GA].

Berski, Filip and Piotr A. Dybczyński (Nov. 2016). "Gliese 710 will pass the Sun even closer. Close approach parameters recalculated based on the first Gaia data release". In: A&A 595, L10, p. L10.

Bienayme, O., A. C. Robin, and M. Creze (June 1987). "The mass density in our galaxy. I. A dynamical model constrained by general star counts". In: A&A 180, pp. 94–110.

Binney, James (Feb. 2010). "Distribution functions for the Milky Way". In: MNRAS 401.4, pp. 2318–2330. arXiv: 0910.1512 [astro-ph.GA].

— (Oct. 2012). "Actions for axisymmetric potentials". In: MNRAS 426.2, pp. 1324–1327. arXiv: 1207.4910 [astro-ph.GA].

— (June 2020). "Trapped orbits and solar-neighbourhood kinematics". In: MNRAS 495.1, pp. 895–904. arXiv: 1912.07023 [astro-ph.GA].

Binney, James, Ortwin Gerhard, and David Spergel (June 1997). "The photometric structure of the inner Galaxy". In: MNRAS 288.2, pp. 365–374. arXiv: astro-ph/9609066 [astro-ph].

Binney, James and Paul McMillan (Mar. 2011). "Models of our Galaxy - II: Models of our Galaxy - II". In: *Monthly Notices of the Royal Astronomical Society* 413.3, pp. 1889–1898.

Binney, James and Ralph Schönrich (Dec. 2018). "The origin of the Gaia phase-plane spiral". In: MNRAS 481.2, pp. 1501–1506. arXiv: 1807.09819 [astro-ph.GA].

Binney, James and Scott Tremaine (2008). *Galactic Dynamics: Second Edition*. Princeton University Press.

Binney, James and Eugene Vasiliev (Apr. 2023). "Self-consistent models of our Galaxy". In: MNRAS 520.2, pp. 1832–1847. arXiv: 2206.03523 [astro-ph.GA].

— (Jan. 2024). "Chemodynamical models of our Galaxy". In: MNRAS 527.2, pp. 1915–1934. arXiv: 2306.11602 [astro-ph.GA].

Binney, James et al. (Sept. 1991). "Understanding the kinematics of Galactic Centre gas." In: MNRAS 252, p. 210.

Bissantz, Nicolai, Peter Englmaier, and Ortwin Gerhard (Apr. 2003). "Gas dynamics in the Milky Way: second pattern speed and large-scale morphology". In: MNRAS 340.3, pp. 949–968. arXiv: astro-ph/0212516 [astro-ph].

Bland-Hawthorn, Joss and Ortwin Gerhard (Sept. 2016). "The Galaxy in Context: Structural, Kinematic, and Integrated Properties". In: ARA&A 54, pp. 529–596. arXiv: 1602.07702 [astro-ph.GA].

Blitz, Leo and David N. Spergel (Oct. 1991). "Direct Evidence for a Bar at the Galactic Center". In: ApJ 379, p. 631.

Bois, Léo et al. (Nov. 2020). "A neural network closure for the Euler-Poisson system based on kinetic simulations". In: *arXiv e-prints*, arXiv:2011.06242, arXiv:2011.06242. arXiv: 2011.06242 [math.NA].

Bougakov, A. et al. (Sept. 2025). "The variation of galactic tides affecting the long-term dynamics of distant trans-Neptunian objects". In: *EPSC-DPS Joint Meeting 2025*. EPSC-DPS2025-1586. Helsinki, Finland.

Boulila, Slah et al. (June 2018). "Long-term cyclicities in Phanerozoic sea-level sedimentary record and their potential drivers". In: *Global and Planetary Change* 165, pp. 128–136.

Boyd, Stephen and Lieven Vandenberghe (2004). *Convex Optimization*. Cambridge University Press.

Callingham, Thomas M. et al. (Apr. 2019). "The mass of the Milky Way from satellite dynamics". In: MNRAS 484.4, pp. 5453–5467. arXiv: 1808.10456 [astro-ph.GA].

Carrillo, I. et al. (Apr. 2018). "Is the Milky Way still breathing? RAVE-Gaia streaming motions". In: MNRAS 475.2, pp. 2679–2696. arXiv: 1710.03763 [astro-ph.GA].

Castro-Ginard, A. et al. (Aug. 2021). "Milky Way spiral arms from open clusters in Gaia

EDR3". In: A&A 652, A162, A162. arXiv: 2105.04590 [astro-ph.GA].

Castro-Ginard, Alfred et al. (Sept. 2023). "Estimating the selection function of Gaia DR3 subsamples". In: A&A 677, A37, A37. arXiv: 2303.17738 [astro-ph.GA].

Chen, Ricky T. Q. (2018). *torchdiffeq*.

Chiba, Masashi and Yuzuru Yoshii (Jan. 1998). "Early Evolution of the Galactic Halo Revealed from Hipparcos Observations of Metal-poor Stars". In: AJ 115.1, pp. 168–192. arXiv: astro-ph/9710151 [astro-ph].

Chiba, Rimpei, Jennifer K. S. Friske, and Ralph Schönrich (Jan. 2021). "Resonance sweeping by a decelerating Galactic bar". In: MNRAS 500.4, pp. 4710–4729. arXiv: 1912.04304 [astro-ph.GA].

Chiba, Rimpei and Ralph Schönrich (Aug. 2021). "Tree-ring structure of Galactic bar resonance". In: MNRAS 505.2, pp. 2412–2426. arXiv: 2102.08388 [astro-ph.GA].

Churchwell, Ed et al. (Mar. 2009). "The Spitzer/GLIMPSE Surveys: A New View of the Milky Way". In: PASP 121.877, p. 213.

Cirasuolo, M. et al. (June 2020). "MOONS: The New Multi-Object Spectrograph for the VLT". In: *The Messenger* 180, pp. 10–17. arXiv: 2009.00628 [astro-ph.IM].

Clarke, Jonathan P. and Ortwin Gerhard (May 2022). "The pattern speed of the Milky Way bar/bulge from VIRAC and Gaia". In: MNRAS 512.2, pp. 2171–2188. arXiv: 2107.10875 [astro-ph.GA].

Clarke, Jonathan P. et al. (Nov. 2019). "The Milky Way bar/bulge in proper motions: a 3D view from VIRAC and Gaia". In: MNRAS 489.3, pp. 3519–3538. arXiv: 1903.02003 [astro-ph.GA].

Clausen, K.F. and M.A.C. Perryman (1990). "The Hipparcos mission". In: *Acta Astronautica* 22, pp. 229–248.

Cox, Donald P. and Gilberto C. Gomez (Oct. 2002). "Analytical Expressions for Spiral Arm Gravitational Potential and Density". In: *The Astrophysical Journal Supplement Series* 142.2, pp. 261–267.

Crézé, M. et al. (Jan. 1998). "The distribution of nearby stars in phase space mapped by Hipparcos. I. The potential well and local dynamical mass". In: A&A 329, pp. 920–936. arXiv: astro-ph/9709022 [astro-ph].

D'Onghia, Elena and J. Alfonso L. Aguerri (Feb. 2020). "Trojans in the Solar Neighborhood". In: ApJ 890.2, 117, p. 117. arXiv: 1907.08484 [astro-ph.GA].

de Jong, R. S. et al. (Mar. 2019). "4MOST: Project overview and information for the First Call for Proposals". In: *The Messenger* 175, pp. 3–11. arXiv: 1903.02464 [astro-ph.IM].

De Rijcke, S. and I. Voulis (Feb. 2016). "Spiral eigenmodes triggered by grooves in the phase space of disc galaxies". In: MNRAS 456.2, pp. 2024–2040. arXiv: 1511.08805 [astro-ph.GA].

De Rijcke, Sven, Jean-Baptiste Fouvry, and Christophe Pichon (Apr. 2019). "Instabilities in disc galaxies: from noise to grooves to spirals". In: MNRAS 484.3, pp. 3198–3208. arXiv: 1812.07002 [astro-ph.GA].

de Salas, Pablo F. and A. Widmark (Oct. 2021). "Dark matter local density determination: recent observations and future prospects". In: *Reports on Progress in Physics* 84.10, 104901, p. 104901. arXiv: 2012.11477 [astro-ph.GA].

de Vaucouleurs, G. (Jan. 1964). "Interpretation of velocity distribution of the inner regions of the Galaxy". In: *The Galaxy and the Magellanic Clouds*. Ed. by Frank J. Kerr. Vol. 20, p. 195.

Debattista, Victor P., Ortwin Gerhard, and Maartje N. Sevenster (Aug. 2002). "The pattern speed of the OH/IR stars in the Milky Way". In: MNRAS 334.2, pp. 355–368. arXiv: astro-ph/0203375 [astro-ph].

Debattista, Victor P. et al. (Feb. 2025). "Azimuthal metallicity variations, spiral structure, and the failure of radial actions based on assuming axisymmetry". In: MNRAS 537.2, pp. 1620–1645. arXiv: 2402.08356 [astro-ph.GA].

Dehnen, Walter (June 1998). "The Distribution of Nearby Stars in Velocity Space Inferred from HIPPARCOS Data". In: AJ 115.6, pp. 2384–2396. arXiv: astro-ph/9803110 [astro-ph].

— (Sept. 1999a). "Approximating Stellar Orbits: Improving on Epicycle Theory". In: AJ 118.3, pp. 1190–1200. arXiv: astro-ph/9906081 [astro-ph].

— (Oct. 1999b). "The Pattern Speed of the Galactic Bar". In: ApJ 524.1, pp. L35–L38. arXiv: astro-ph/9908105 [astro-ph].

— (Feb. 2000). "The Effect of the Outer Lindblad Resonance of the Galactic Bar on the Local Stellar Velocity Distribution". In: AJ 119.2, pp. 800–812. arXiv: astro-ph/9911161 [astro-ph].

Dillamore, Adam M., Vasily Belokurov, and N. Wyn Evans (Aug. 2024). "Radial halo substructure in harmony with the Galactic bar". In: MNRAS 532.4, pp. 4389–4407. arXiv: 2402.14907 [astro-ph.GA].

Dillamore, Adam M. et al. (July 2025). "Dynamical streams in the local stellar halo". In: MNRAS 541.1, pp. 214–233. arXiv: 2503.02926 [astro-ph.GA].

Drimmel, R. (June 2000). "Evidence for a two-armed spiral in the Milky Way". In: A&A 358, pp. L13–L16. arXiv: astro-ph/0005241 [astro-ph].

Drimmel, Ronald and David N. Spergel (July 2001). "Three-dimensional Structure of the Milky Way Disk: The Distribution of Stars and Dust beyond 0.35 R_{solar}". In: ApJ 556.1, pp. 181–202. arXiv: astro-ph/0101259 [astro-ph].

Drimmel, Ronald et al. (June 2024). "The Milky Way as Seen by Classical Cepheids II: Spiral Structure". In: *arXiv e-prints*, arXiv:2406.09127, arXiv:2406.09127. arXiv: 2406.09127 [astro-ph.GA].

Eilers, Anna-Christina et al. (Jan. 2019). "The Circular Velocity Curve of the Milky Way from 5 to 25 kpc". In: ApJ 871.1, 120, p. 120. arXiv: 1810.09466 [astro-ph.GA].

Eilers, Anna-Christina et al. (Sept. 2020). "The Strength of the Dynamical Spiral Perturbation in the Galactic Disk". In: ApJ 900.2, 186, p. 186. arXiv: 2003.01132 [astro-ph.GA].

Englmaier, P., M. Pohl, and N. Bissantz (Jan. 2011). "The Milky Way spiral arm pattern. 3D distribution of molecular gas". In: *Memorie della Societa Astronomica Italiana Supplementi* 18, p. 199. arXiv: 0812.3491 [astro-ph].

Englmaier, Peter and Ortwin Gerhard (Apr. 1999). "Gas dynamics and large-scale morphology of the Milky Way galaxy". In: MNRAS 304.3, pp. 512–534. arXiv: astro-ph/9810208 [astro-ph].

Euclid Collaboration et al. (Mar. 2025). "Euclid Quick Data Release (Q1), A first look at the fraction of bars in massive galaxies at $z < 1$". In: *arXiv e-prints*, arXiv:2503.15311, arXiv:2503.15311. arXiv: 2503.15311 [astro-ph.GA].

Famaey, B. (Aug. 2024). "Some aspects of Galactic Dynamics in the Gaia era". In: *EES2023: Proceedings of the Evry Schatzman School*. Ed. by C. Babusiaux and C. Reylé, p. 69.

Famaey, B. and H. Dejonghe (Apr. 2003). "Three-component Stäckel potentials satisfying recent estimates of Milky Way parameters". In: MNRAS 340.3, pp. 752–762. arXiv: astro-ph/0212059 [astro-ph].

Famaey, B., A. Siebert, and A. Jorissen (May 2008). "On the age heterogeneity of the Pleiades, Hyades, and Sirius moving groups". In: A&A 483.2, pp. 453–459. arXiv: 0712.1470 [astro-ph].

Famaey, B. et al. (Jan. 2005). "Local kinematics of K and M giants from CORAVEL/Hipparcos/Tycho-2 data. Revisiting the concept of superclusters". In: A&A 430, pp. 165–186. arXiv: astro-ph/0409579 [astro-ph].

Famaey, B. et al. (Jan. 2007). "The Hyades stream: an evaporated cluster or an intrusion from the inner disk?" In: A&A 461.3, pp. 957–962. arXiv: astro-ph/0609785 [astro-ph].

Fardal, Mark A., Shuiyao Huang, and Martin D. Weinberg (Sept. 2015). "Generation of mock tidal streams". In: MNRAS 452.1, pp. 301–319. arXiv: 1410.1861 [astro-ph.GA].

Faure, Carole, Arnaud Siebert, and Benoit Famaey (May 2014). "Radial and vertical flows induced by galactic spiral arms: likely contributors to our 'wobbly Galaxy'". In: MNRAS 440.3, pp. 2564–2575. arXiv: 1403.0587 [astro-ph.GA].

Fiteni, Karl et al. (Apr. 2024). "The role of density breaks in driving spiral structure in disc galaxies". In: MNRAS 529.4, pp. 4879–4895. arXiv: 2403.12233 [astro-ph.GA].

Foreman-Mackey, Daniel et al. (Mar. 2013). "emcee: The MCMC Hammer". In: PASP 125.925, p. 306. arXiv: 1202.3665 [astro-ph.IM].

Fouvry, Jean-Baptiste, Pierre-Henri Chavanis, and Christophe Pichon (Oct. 2016). "Func-

tional integral approach to the kinetic theory of inhomogeneous systems". In: *Physica A Statistical Mechanics and its Applications* 459, pp. 117–128. arXiv: 1604.02338 [astro-ph.GA].

Fragkoudi, F. et al. (Sept. 2019). "On the ridges, undulations, and streams in Gaia DR2: linking the topography of phase space to the orbital structure of an N-body bar". In: MNRAS 488.3, pp. 3324–3339. arXiv: 1901.07568 [astro-ph.GA].

Frankel, Neige et al. (June 2020). "Keeping It Cool: Much Orbit Migration, yet Little Heating, in the Galactic Disk". In: ApJ 896.1, 15, p. 15. arXiv: 2002.04622 [astro-ph.GA].

Frankel, Neige et al. (July 2024). "Iron Snails: non-equilibrium dynamics and spiral abundance patterns". In: *arXiv e-prints*, arXiv:2407.07149, arXiv:2407.07149. arXiv: 2407.07149 [astro-ph.GA].

Friske, Jennifer K. S. and Ralph Schönrich (Dec. 2019). "More than just a wrinkle: a wave-like pattern in U_g versus L_z from Gaia data". In: MNRAS 490.4, pp. 5414–5423. arXiv: 1902.09569 [astro-ph.GA].

Fux, R. (May 1999). "3D self-consistent N-body barred models of the Milky Way. II. Gas dynamics". In: A&A 345, pp. 787–812. arXiv: astro-ph/9903154 [astro-ph].

— (July 2001). "Order and chaos in the local disc stellar kinematics induced by the Galactic bar". In: A&A 373, pp. 511–535. arXiv: astro-ph/0105398 [astro-ph].

Gaia Collaboration et al. (Nov. 2016a). "Gaia Data Release 1. Summary of the astrometric, photometric, and survey properties". In: A&A 595, A2, A2. arXiv: 1609.04172 [astro-ph.IM].

Gaia Collaboration et al. (Nov. 2016b). "The Gaia mission". In: A&A 595, A1, A1. arXiv: 1609.04153 [astro-ph.IM].

Gaia Collaboration et al. (Aug. 2018a). "Gaia Data Release 2. Mapping the Milky Way disc kinematics". In: A&A 616, A11, A11. arXiv: 1804.09380 [astro-ph.GA].

Gaia Collaboration et al. (Aug. 2018b). "Gaia Data Release 2. Summary of the contents and survey properties". In: A&A 616, A1, A1. arXiv: 1804.09365 [astro-ph.GA].

Gaia Collaboration et al. (Aug. 2018c). "Gaia Data Release 2. Summary of the contents and survey properties". In: A&A 616, A1, A1. arXiv: 1804.09365 [astro-ph.GA].

Gaia Collaboration et al. (May 2021a). "Gaia Early Data Release 3. Summary of the contents and survey properties". In: A&A 649, A1, A1. arXiv: 2012.01533 [astro-ph.GA].

Gaia Collaboration et al. (May 2021b). "Gaia Early Data Release 3. Summary of the contents and survey properties". In: A&A 649, A1, A1. arXiv: 2012.01533 [astro-ph.GA].

Gaia Collaboration et al. (June 2023a). "Gaia Data Release 3. Chemical cartography of the Milky Way". In: A&A 674, A38, A38. arXiv: 2206.05534 [astro-ph.GA].

Gaia Collaboration et al. (June 2023b). "Gaia Data Release 3. Mapping the asymmetric disc of the Milky Way". In: A&A 674, A37, A37. arXiv: 2206.06207 [astro-ph.GA].

Gaia Collaboration et al. (June 2023c). "Gaia Data Release 3. Summary of the content and survey properties". In: A&A 674, A1, A1. arXiv: 2208.00211 [astro-ph.GA].

Gaia Collaboration et al. (June 2023d). "Gaia Data Release 3. Summary of the content and survey properties". In: A&A 674, A1, A1. arXiv: 2208.00211 [astro-ph.GA].

García-Sánchez, Joan et al. (Feb. 1999). "Stellar Encounters with the Oort Cloud Based on HIPPARCOS Data". In: AJ 117.2, pp. 1042–1055.

Georgelin, Y. M. and Y. P. Georgelin (May 1976). "The spiral structure of our Galaxy determined from H II regions." In: A&A 49, pp. 57–79.

Gerhard, O. E. and M. Vietri (Nov. 1986). "The peculiar shape of the inner galactic rotation curve." In: MNRAS 223, pp. 377–389.

Gilmore, G. and N. Reid (Mar. 1983). "New light on faint stars - III. Galactic structure towards the South Pole and the Galactic thick disc." In: MNRAS 202, pp. 1025–1047.

Gilmore, G. et al. (Mar. 2012). "The Gaia-ESO Public Spectroscopic Survey". In: *The Messenger* 147, pp. 25–31.

Grand, Robert J. J. et al. (Sept. 2023). "An ever-present Gaia snail shell triggered by a dark matter wake". In: MNRAS

524.1, pp. 801–816. arXiv: 2211.08437 [astro-ph.GA].

Haines, Tim et al. (July 2019). "Implications of a Time-varying Galactic Potential for Determinations of the Dynamical Surface Density". In: ApJ 879.1, L15, p. L15. arXiv: 1903.00607 [astro-ph.GA].

Hamilton, Chris (Mar. 2024). "Saturation of spiral instabilities in disc galaxies". In: MNRAS 528.3, pp. 5286–5294. arXiv: 2302.06602 [astro-ph.GA].

Hamilton, Chris and Jean-Baptiste Fouvry (Dec. 2024). "Kinetic theory of stellar systems: A tutorial". In: *Physics of Plasmas* 31.12, 120901, p. 120901. arXiv: 2402.13322 [astro-ph.GA].

Hamilton, Chris, Shaunak Modak, and Scott Tremaine (Aug. 2024a). "Galactokinetics". In: *arXiv e-prints*, arXiv:2408.03366, arXiv:2408.03366. arXiv: 2408.03366 [astro-ph.GA].

— (Nov. 2024b). "Why is the Galactic disk so cool?" In: *arXiv e-prints*, arXiv:2411.08944, arXiv:2411.08944. arXiv: 2411.08944 [astro-ph.GA].

— (July 2025). "Galactokinetics II: Spiral structure". In: *arXiv e-prints*, arXiv:2507.16950, arXiv:2507.16950. arXiv: 2507.16950 [astro-ph.GA].

Hamilton, Chris et al. (Sept. 2023). "Galactic Bar Resonances with Diffusion: An Analytic Model with Implications for Bar-Dark Matter Halo Dynamical Friction". In: ApJ 954.1, 12, p. 12. arXiv: 2208.03855 [astro-ph.GA].

Hayden, Michael R. et al. (Aug. 2015). "Chemical Cartography with APOGEE: Metallicity Distribution Functions and the Chemical Structure of the Milky Way Disk". In: ApJ 808.2, 132, p. 132. arXiv: 1503.02110 [astro-ph.GA].

Haywood, M. (Aug. 2008). "Radial mixing and the transition between the thick and thin Galactic discs". In: MNRAS 388.3, pp. 1175–1184. arXiv: 0805.1822 [astro-ph].

Haywood, M. et al. (Aug. 2018). "In Disguise or Out of Reach: First Clues about In Situ and Accreted Stars in the Stellar Halo of the Milky Way from Gaia DR2". In: ApJ 863.2, 113, p. 113. arXiv: 1805.02617 [astro-ph.GA].

Haywood, Misha et al. (Oct. 2024). "Timing the Milky Way bar formation and the accompanying radial migration episode". In: A&A 690, A147, A147. arXiv: 2403.08963 [astro-ph.GA].

Helmi, Amina et al. (Oct. 2018). "The merger that led to the formation of the Milky Way's inner stellar halo and thick disk". In: Nature 563.7729, pp. 85–88. arXiv: 1806.06038 [astro-ph.GA].

Heyvaerts, J. (Sept. 2010). "A Balescu-Lenard-type kinetic equation for the collisional evolution of stable self-gravitating systems". In: MNRAS 407.1, pp. 355–372.

Hilmi, T. et al. (Sept. 2020). "Fluctuations in galactic bar parameters due to bar-spiral interaction". In: MNRAS 497.1, pp. 933–955. arXiv: 2003.05457 [astro-ph.GA].

Høg, E. et al. (July 1997). "The TYCHO Catalogue". In: A&A 323, pp. L57–L60.

Høg, E. et al. (Mar. 2000). "The Tycho-2 catalogue of the 2.5 million brightest stars". In: A&A 355, pp. L27–L30.

Holmberg, J., C. Flynn, and L. Lindegren (Aug. 1997). "Towards an Improved Model of the Galaxy". In: *Hipparcos - Venice 1997*. Ed. by R. M. Bonnet et al. Vol. 402. ESA Special Publication, pp. 721–726.

Holmberg, Johan and Chris Flynn (Apr. 2000). "The local density of matter mapped by Hipparcos". In: MNRAS 313.2, pp. 209–216. arXiv: astro-ph/9812404 [astro-ph].

Horta Darrington, Danny, Michael S. Petersen, and Jorge Peñarrubia (Apr. 2025). "Disentangling the Galaxy's Gordian knot: evidence from APOGEE-Gaia for a knotted and slower bar in the Milky Way". In: MNRAS 538.2, pp. 998–1018. arXiv: 2402.07986 [astro-ph.GA].

Hou, L. G., J. L. Han, and W. B. Shi (May 2009). "The spiral structure of our Milky Way Galaxy". In: A&A 499.2, pp. 473–482. arXiv: 0903.0721 [astro-ph.GA].

Hunt, Jason A. S. and Jo Bovy (July 2018). "The 4:1 outer Lindblad resonance of a long-slow bar as an explanation for the Hercules stream". In: MNRAS 477.3, pp. 3945–3953. arXiv: 1803.02358 [astro-ph.GA].

Hunt, Jason A. S. and Eugene Vasiliev (June 2025). "Milky Way dynamics in light of Gaia". In: New A Rev. 100,

101721, p. 101721. arXiv: 2501.04075 [astro-ph.GA].

Hunt, Jason A. S. et al. (Dec. 2018). "Transient spiral structure and the disc velocity substructure in Gaia DR2". In: MNRAS 481.3, pp. 3794–3803. arXiv: 1806.02832 [astro-ph.GA].

Hunt, Jason A. S. et al. (Nov. 2019). "Signatures of resonance and phase mixing in the Galactic disc". In: MNRAS 490.1, pp. 1026–1043. arXiv: 1904.10968 [astro-ph.GA].

Hunt, Jason A. S. et al. (Oct. 2022). "Multiple phase spirals suggest multiple origins in Gaia DR3". In: MNRAS 516.1, pp. L7–L11. arXiv: 2206.06125 [astro-ph.GA].

Hunter, Glen H. et al. (Dec. 2024). "Testing kinematic distances under a realistic Galactic potential: Investigating systematic errors in the kinematic distance method arising from a non-axisymmetric potential". In: A&A 692, A216, A216. arXiv: 2403.18000 [astro-ph.GA].

Ibata, R. A., G. Gilmore, and M. J. Irwin (July 1994). "A dwarf satellite galaxy in Sagittarius". In: Nature 370.6486, pp. 194–196.

Ibata, Rodrigo et al. (Feb. 2001). "Galactic Halo Substructure in the Sloan Digital Sky Survey: The Ancient Tidal Stream from the Sagittarius Dwarf Galaxy". In: ApJ 547.2, pp. L133–L136. arXiv: astro-ph/0004255 [astro-ph].

Ibata, Rodrigo et al. (June 2024). "Charting the Galactic Acceleration Field. II. A Global Mass Model of the Milky Way from the STREAMFINDER Atlas of Stellar Streams Detected in Gaia DR3". In: ApJ 967.2, 89, p. 89. arXiv: 2311.17202 [astro-ph.GA].

Ivezić, Željko et al. (Mar. 2019). "LSST: From Science Drivers to Reference Design and Anticipated Data Products". In: ApJ 873.2, 111, p. 111. arXiv: 0805.2366 [astro-ph].

Jerabkova, Tereza et al. (Mar. 2021). "The 800 pc long tidal tails of the Hyades star cluster. Possible discovery of candidate epicyclic overdensities from an open star cluster". In: A&A 647, A137, A137. arXiv: 2103.12080 [astro-ph.GA].

Jiao, Yongjun et al. (Oct. 2023). "Detection of the Keplerian decline in the Milky Way rotation curve". In: A&A 678, A208, A208. arXiv: 2309.00048 [astro-ph.GA].

Jin, Pengzhan et al. (Jan. 2020). "SympNets: Intrinsic structure-preserving symplectic networks for identifying Hamiltonian systems". In: *arXiv e-prints*, arXiv:2001.03750, arXiv:2001.03750. arXiv: 2001.03750 [cs.LG].

Jin, Shoko et al. (May 2024). "The wide-field, multiplexed, spectroscopic facility WEAVE: Survey design, overview, and simulated implementation". In: MNRAS 530.3, pp. 2688–2730. arXiv: 2212.03981 [astro-ph.IM].

Kalnajs, A. J. (Mar. 1977). "Dynamics of flat galaxies. IV. The integral equation for normal modes in matrix form." In: ApJ 212, pp. 637–644.

Khalil, Y. R. et al. (July 2025a). "A non-axisymmetric potential for the Milky Way disk". In: A&A 699, A263, A263. arXiv: 2411.12800 [astro-ph.GA].

— (July 2025b). *SPIBACK: Backward-integration-based non-axisymmetric models of the Milky Way disk*. Astrophysics Source Code Library, record ascl:2507.027.

Khanna, Shourya et al. (Oct. 2024). "GaiaUnlimited: The old stellar disc of the Milky Way as traced by the Red Clump". In: *arXiv e-prints*, arXiv:2410.22036, arXiv:2410.22036. arXiv: 2410.22036 [astro-ph.GA].

Khoperskov, S. et al. (Feb. 2020). "Hic sunt dracones: Cartography of the Milky Way spiral arms and bar resonances with Gaia Data Release 2". In: A&A 634, L8, p. L8. arXiv: 1910.06335 [astro-ph.GA].

Khoperskov, Sergey and Ortwin Gerhard (July 2022). "Chemo-kinematics of the Milky Way spiral arms and bar resonances: Connection to ridges and moving groups in the solar vicinity". In: A&A 663, A38, A38. arXiv: 2111.15211 [astro-ph.GA].

Khoperskov, Sergey et al. (Feb. 2019). "The echo of the bar buckling: Phase-space spirals in Gaia Data Release 2". In: A&A 622, L6, p. L6. arXiv: 1811.09205 [astro-ph.GA].

Khoperskov, Sergey et al. (Nov. 2024). "Rediscovering the Milky Way with orbit superposition approach and APOGEE data II. Chrono-chemo-kinematics of the disc". In: *arXiv e-prints*, arXiv:2411.16866,

arXiv:2411.16866. arXiv: 2411.16866 [astro-ph.GA].

Khoperskov, Sergey et al. (Mar. 2025). "Rediscovering the Milky Way with an orbit superposition approach and APOGEE data: I. Method validation". In: A&A 695, A220, A220. arXiv: 2411.15062 [astro-ph.GA].

Kollmeier, Juna A. et al. (Nov. 2017). "SDSS-V: Pioneering Panoptic Spectroscopy". In: *arXiv e-prints*, arXiv:1711.03234, arXiv:1711.03234. arXiv: 1711.03234 [astro-ph.GA].

Lacroix, Thomas, Martin Stref, and Julien Lavalle (Sept. 2018). "Anatomy of Eddington-like inversion methods in the context of dark matter searches". In: J. Cosmology Astropart. Phys. 2018.9, 040, p. 040. arXiv: 1805.02403 [astro-ph.GA].

Lacroix, Thomas et al. (Oct. 2020). "Predicting the dark matter velocity distribution in galactic structures: tests against hydrodynamic cosmological simulations". In: J. Cosmology Astropart. Phys. 2020.10, 031, p. 031. arXiv: 2005.03955 [astro-ph.GA].

Lagarde, N. et al. (May 2017). "Population synthesis to constrain Galactic and stellar physics. I. Determining age and mass of thin-disc red-giant stars". In: A&A 601, A27, A27. arXiv: 1702.01769 [astro-ph.SR].

Laporte, Chervin F. P. et al. (May 2019). "Footprints of the Sagittarius dwarf galaxy in the Gaia data set". In: MNRAS 485.3, pp. 3134–3152. arXiv: 1808.00451 [astro-ph.GA].

Laporte, Chervin F. P. et al. (Nov. 2020). "Bar resonances and low angular momentum moving groups in the Galaxy revealed by their stellar ages". In: A&A 643, L3, p. L3. arXiv: 2006.13876 [astro-ph.GA].

Lavalle, Julien and Stefano Magni (Jan. 2015). "Making sense of the local Galactic escape speed estimates in direct dark matter searches". In: Phys. Rev. D 91.2, 023510, p. 023510. arXiv: 1411.1325 [astro-ph.CO].

Levine, E. S., Leo Blitz, and Carl Heiles (June 2006). "The Spiral Structure of the Outer Milky Way in Hydrogen". In: *Science* 312.5781, pp. 1773–1777. arXiv: astro-ph/0605728 [astro-ph].

Li, Chengdong et al. (Oct. 2023). "Gaia DR3 features of the phase spiral and its possible relation to internal perturbations". In: MNRAS 524.4, pp. 6331–6344. arXiv: 2303.06393 [astro-ph.GA].

Li, Chengdong et al. (Oct. 2024). "Exploring the impact of a decelerating bar on transforming bulge orbits into disc-like orbits". In: A&A 690, A26, A26. arXiv: 2311.15270 [astro-ph.GA].

Li, Zhi et al. (June 2016). "Gas Dynamics in the Milky Way: A Low Pattern Speed Model". In: ApJ 824.1, 13, p. 13. arXiv: 1603.09650 [astro-ph.GA].

Lin, C. C. and Frank H. Shu (Aug. 1964). "On the Spiral Structure of Disk Galaxies." In: ApJ 140, p. 646.

Lin, C. C., C. Yuan, and Frank H. Shu (Mar. 1969). "On the Spiral Structure of Disk Galaxies. III. Comparison with Observations". In: ApJ 155, p. 721.

Lucchini, Scott, Elena D'Onghia, and J. Alfonso L. Aguerri (June 2024). "The Milky Way bar pattern speed using Hercules and Gaia DR3". In: MNRAS 531.1, pp. L14–L19. arXiv: 2305.04981 [astro-ph.GA].

Luri, X. et al. (Aug. 2018). "Gaia Data Release 2. Using Gaia parallaxes". In: A&A 616, A9, A9. arXiv: 1804.09376 [astro-ph.IM].

Lynden-Bell, D. and A. J. Kalnajs (Jan. 1972). "On the generating mechanism of spiral structure". In: MNRAS 157, p. 1.

Maíz-Apellániz, Jesús (May 2001). "The Spatial Distribution of O-B5 Stars in the Solar Neighborhood as Measured by Hipparcos". In: AJ 121.5, pp. 2737–2742. arXiv: astro-ph/0101310 [astro-ph].

Malhan, Khyati and Rodrigo A. Ibata (July 2018). "STREAMFINDER - I. A new algorithm for detecting stellar streams". In: MNRAS 477.3, pp. 4063–4076. arXiv: 1804.11338 [astro-ph.GA].

— (July 2019). "Constraining the Milky Way halo potential with the GD-1 stellar stream". In: MNRAS 486.3, pp. 2995–3005. arXiv: 1807.05994 [astro-ph.GA].

Malhan, Khyati et al. (Feb. 2022). "The Global Dynamical Atlas of the Milky Way Mergers: Constraints from Gaia EDR3-based Orbits of Globular Clusters, Stellar Streams, and Satellite Galaxies". In: ApJ 926.2, 107, p. 107. arXiv: 2202.07660 [astro-ph.GA].

Masoliver, Jaume and Ana Ros (Mar. 2011). "Integrability and chaos: the classical uncertainty". In: *European Journal of Physics* 32.2, pp. 431–458. arXiv: 1012.4384 [nlin.CD].

Massari, D., H. H. Koppelman, and A. Helmi (Oct. 2019). "Origin of the system of globular clusters in the Milky Way". In: A&A 630, L4, p. L4. arXiv: 1906.08271 [astro-ph.GA].

Mayor, M. (Jan. 1985). "Cross-Correlation Spectroscopy Using CORAVEL". In: *Stellar Radial Velocities*. Ed. by A. G. D. Philip and David W. Latham, pp. 21–34.

Minchev, I. and B. Famaey (Oct. 2010). "A New Mechanism for Radial Migration in Galactic Disks: Spiral-Bar Resonance Overlap". In: ApJ 722.1, pp. 112–121. arXiv: 0911.1794 [astro-ph.GA].

Minchev, I., J. Nordhaus, and A. C. Quillen (July 2007). "New Constraints on the Galactic Bar". In: ApJ 664.1, pp. L31–L34. arXiv: astro-ph/0703805 [astro-ph].

Monari, G. et al. (Sept. 2014). "The Galactic bar and the large scale velocity gradients in the Galactic disk". In: A&A 569, A69, A69. arXiv: 1402.4479 [astro-ph.GA].

Monari, G. et al. (Aug. 2018). "The escape speed curve of the Galaxy obtained from Gaia DR2 implies a heavy Milky Way". In: A&A 616, L9, p. L9. arXiv: 1807.04565 [astro-ph.GA].

Monari, G. et al. (June 2019a). "Signatures of the resonances of a large Galactic bar in local velocity space". In: A&A 626, A41, A41. arXiv: 1812.04151 [astro-ph.GA].

Monari, G. et al. (Dec. 2019b). "Tracing Hercules in Galactic azimuth with Gaia DR2". In: A&A 632, A107, A107. arXiv: 1908.01318 [astro-ph.GA].

Monari, Giacomo, Benoit Famaey, and Arnaud Siebert (Apr. 2016a). "Modelling the Galactic disc: perturbed distribution functions in the presence of spiral arms". In: MNRAS 457.3, pp. 2569–2582. arXiv: 1601.04714 [astro-ph.GA].

Monari, Giacomo et al. (Oct. 2016b). "The effects of bar-spiral coupling on stellar kinematics in the Galaxy". In: MNRAS 461.4, pp. 3835–3846. arXiv: 1606.06785 [astro-ph.GA].

Monari, Giacomo et al. (Nov. 2017a). "Distribution functions for resonantly trapped orbits in the Galactic disc". In: MNRAS 471.4, pp. 4314–4322. arXiv: 1707.05306 [astro-ph.GA].

Monari, Giacomo et al. (Mar. 2017b). "Tracing the Hercules stream with Gaia and LAMOST: new evidence for a fast bar in the Milky Way". In: MNRAS 466.1, pp. L113–L117. arXiv: 1610.05342 [astro-ph.GA].

Morgan, W. W., S. Sharpless, and D. Osterbrock (Apr. 1952). "Some features of galactic structure in the neighborhood of the Sun." In: AJ 57, pp. 3–3.

Myeong, G. C. et al. (Aug. 2018). "The Sausage Globular Clusters". In: ApJ 863.2, L28, p. L28. arXiv: 1805.00453 [astro-ph.GA].

Naidu, Rohan P. et al. (Dec. 2021). "Reconstructing the Last Major Merger of the Milky Way with the H3 Survey". In: ApJ 923.1, 92, p. 92. arXiv: 2103.03251 [astro-ph.GA].

Nelson, Benjamin, Eric B. Ford, and Matthew J. Payne (Jan. 2014). "RUN DMC: An Efficient, Parallel Code for Analyzing Radial Velocity Observations Using N-body Integrations and Differential Evolution Markov Chain Monte Carlo". In: ApJS 210.1, 11, p. 11. arXiv: 1311.5229 [astro-ph.EP].

Nissen, P. E. and W. J. Schuster (Feb. 2010). "Two distinct halo populations in the solar neighborhood. Evidence from stellar abundance ratios and kinematics". In: A&A 511, L10, p. L10. arXiv: 1002.4514 [astro-ph.GA].

Nordström, B. et al. (May 2004). "The Geneva-Copenhagen survey of the Solar neighbourhood. Ages, metallicities, and kinematic properties of ∼14 000 F and G dwarfs". In: A&A 418, pp. 989–1019. arXiv: astro-ph/0405198 [astro-ph].

Oort, J. H., F. J. Kerr, and G. Westerhout (Jan. 1958). "The galactic system as a spiral nebula (Council Note)". In: MNRAS 118, p. 379.

Oria, Pierre-Antoine et al. (June 2022). "Revisiting a Disky Origin for the Faint Branch of the Sagittarius Stellar Stream". In: ApJ 932.2, L14, p. L14. arXiv: 2205.14902 [astro-ph.GA].

Ou, Xiaowei et al. (Feb. 2024). "The dark matter profile of the Milky Way inferred from

its circular velocity curve". In: MNRAS 528.1, pp. 693–710. arXiv: 2303.12838 [astro-ph.GA].

Palicio, P. A. et al. (Feb. 2023). "Spiral-like features in the disc revealed by Gaia DR3 radial actions". In: A&A 670, L7, p. L7. arXiv: 2209.09989 [astro-ph.GA].

Paszke, Adam et al. (2019). "PyTorch: An Imperative Style, High-Performance Deep Learning Library". In: *Advances in Neural Information Processing Systems 32*. Curran Associates, Inc., pp. 8024–8035.

Pérez-Villegas, Angeles et al. (May 2017). "Revisiting the Tale of Hercules: How Stars Orbiting the Lagrange Points Visit the Sun". In: ApJ 840.1, L2, p. L2. arXiv: 1702.06541 [astro-ph.GA].

Perryman (2012). *Astronomical Applications of Astrometry*.

Perryman, M. A. C. et al. (July 1997). "The HIPPARCOS Catalogue". In: A&A 323, pp. L49–L52.

Perryman, M.A.C. (1991). "Hipparcos: Revised mission overview". In: *Advances in Space Research* 11.2, pp. 15–23.

Petač, Mihael et al. (Aug. 2021). "Testing the predictions of axisymmetric distribution functions of galactic dark matter with hydrodynamical simulations". In: J. Cosmology Astropart. Phys. 2021.8, 031, p. 031. arXiv: 2106.01314 [astro-ph.CO].

Peters W. L., III (Feb. 1975). "Models for the inner regions of the Galaxy. I. An elliptical streamline model." In: ApJ 195, pp. 617–629.

Petersen, Michael S., Martin D. Weinberg, and Neal Katz (Dec. 2016). "Dark matter trapping by stellar bars: the shadow bar". In: MNRAS 463.2, pp. 1952–1967. arXiv: 1602.04826 [astro-ph.GA].

Pham, H. -A. (Aug. 1997). "Estimation of the Local Mass Density from an F-Star Sample Observed by HIPPARCOS". In: *Hipparcos - Venice 1997*. Ed. by R. M. Bonnet et al. Vol. 402. ESA Special Publication, pp. 559–562.

Poggio, E. et al. (Mar. 2020). "Evidence of a dynamically evolving Galactic warp". In: *Nature Astronomy* 4, pp. 590–596. arXiv: 1912.10471 [astro-ph.GA].

Poggio, E. et al. (July 2021). "Galactic spiral structure revealed by Gaia EDR3". In: A&A 651, A104, A104. arXiv: 2103.01970 [astro-ph.GA].

Poggio, E. et al. (Oct. 2022). "The chemical signature of the Galactic spiral arms revealed by Gaia DR3". In: A&A 666, L4, p. L4. arXiv: 2206.14849 [astro-ph.GA].

Poggio, E. et al. (July 2025). "The great wave: Evidence of a large-scale vertical corrugation propagating outwards in the Galactic disc". In: A&A 699, A199, A199. arXiv: 2407.18659 [astro-ph.GA].

Pompéia, L. et al. (Aug. 2011). "Chemically tagging the Hyades stream: does it partly originate from the Hyades cluster?" In: MNRAS 415.2, pp. 1138–1154. arXiv: 1101.2583 [astro-ph.GA].

Portail, Matthieu et al. (Feb. 2017). "Dynamical modelling of the galactic bulge and bar: the Milky Way's pattern speed, stellar and dark matter mass distribution". In: MNRAS 465.2, pp. 1621–1644. arXiv: 1608.07954 [astro-ph.GA].

Quillen, A. C. and Ivan Minchev (Aug. 2005). "The Effect of Spiral Structure on the Stellar Velocity Distribution in the Solar Neighborhood". In: AJ 130.2, pp. 576–585. arXiv: astro-ph/0502205 [astro-ph].

Quillen, Alice C. et al. (Oct. 2011). "Structure in phase space associated with spiral and bar density waves in an N-body hybrid galactic disc". In: MNRAS 417.1, pp. 762–784. arXiv: 1010.5745 [astro-ph.GA].

Ramos, P., T. Antoja, and F. Figueras (Nov. 2018). "Riding the kinematic waves in the Milky Way disk with Gaia". In: A&A 619, A72, A72. arXiv: 1805.09790 [astro-ph.GA].

Recio-Blanco, A. et al. (July 2014). "The Gaia-ESO Survey: the Galactic thick to thin disc transition". In: A&A 567, A5, A5. arXiv: 1403.7568 [astro-ph.GA].

Recio-Blanco, A. et al. (June 2023). "Gaia Data Release 3. Analysis of RVS spectra using the General Stellar Parametriser from spectroscopy". In: A&A 674, A29, A29. arXiv: 2206.05541 [astro-ph.GA].

Reddish, J. et al. (May 2022). "The NewHorizon simulation - to bar or not to bar". In: MNRAS 512.1, pp. 160–185. arXiv: 2106.02622 [astro-ph.GA].

Reddy, Bacham E., David L. Lambert, and Carlos Allende Prieto (Apr. 2006).

"Elemental abundance survey of the Galactic thick disc". In: MNRAS 367.4, pp. 1329–1366. arXiv: astro-ph/0512505 [astro-ph].

Reid, M. J. et al. (Nov. 2019). "Trigonometric Parallaxes of High-mass Star-forming Regions: Our View of the Milky Way". In: ApJ 885.2, 131, p. 131. arXiv: 1910.03357 [astro-ph.GA].

Reshetnikov, V. P. et al. (Dec. 2023). "The possible evolution of pitch angles of spiral galaxies". In: A&A 680, L14, p. L14. arXiv: 2311.16915 [astro-ph.GA].

Rivero, A. et al. (June 2025). "Age-Metallicity distributions of Moving Groups in the Solar-Neighbourhood". poster at European Astronomical Society Annual Meeting.

Robin, A. and M. Creze (Mar. 1986). "Stellar populations in the milky way: a synthetic model." In: A&A 157, pp. 71–90.

Robin, A. C. et al. (Oct. 2003). "A synthetic view on structure and evolution of the Milky Way". In: A&A 409, pp. 523–540.

Robin, A. C. et al. (Nov. 2022). "A self-consistent dynamical model of the Milky Way disc adjusted to Gaia data". In: A&A 667, A98, A98. arXiv: 2208.13827 [astro-ph.GA].

Roche, Cian et al. (Sept. 2024a). "The Escape Velocity Profile of the Milky Way from Gaia DR3". In: ApJ 972.1, 70, p. 70. arXiv: 2402.00108 [astro-ph.GA].

— (Sept. 2024b). "The Escape Velocity Profile of the Milky Way from Gaia DR3". In: ApJ 972.1, 70, p. 70. arXiv: 2402.00108 [astro-ph.GA].

Röser, S. et al. (Sept. 2008). "PPM-Extended (PPMX) - a catalogue of positions and proper motions". In: A&A 488.1, pp. 401–408. arXiv: 0806.1009 [astro-ph].

Rozier, Simon et al. (July 2022). "Constraining the Milky Way Halo Kinematics via Its Linear Response to the Large Magellanic Cloud". In: ApJ 933.1, 113, p. 113. arXiv: 2201.05589 [astro-ph.GA].

Rybizki, Jan et al. (July 2020). "A Gaia Early DR3 Mock Stellar Catalog: Galactic Prior and Selection Function". In: PASP 132.1013, 074501, p. 074501. arXiv: 2004.09991 [astro-ph.IM].

The Sage Developers (2025). *SageMath, the Sage Mathematics Software System (Version x.y.z)*. https://www.sagemath.org.

Salomon, Jean-Baptiste et al. (Nov. 2020). "Kinematics and dynamics of Gaia red clump stars. Revisiting north-south asymmetries and dark matter density at large heights". In: A&A 643, A75, A75. arXiv: 2009.04495 [astro-ph.GA].

Sanders, Jason L. and James Binney (Apr. 2016). "A review of action estimation methods for galactic dynamics". In: MNRAS 457.2, pp. 2107–2121. arXiv: 1511.08213 [astro-ph.GA].

Sanders, Jason L., Leigh Smith, and N. Wyn Evans (Oct. 2019). "The pattern speed of the Milky Way bar from transverse velocities". In: MNRAS 488.4, pp. 4552–4564. arXiv: 1903.02009 [astro-ph.GA].

Schönrich, Ralph and Walter Dehnen (Aug. 2018). "Warp, waves, and wrinkles in the Milky Way". In: MNRAS 478.3, pp. 3809–3824. arXiv: 1712.06616 [astro-ph.GA].

Sellwood, J A and J Binney (Jan. 2025). "A comment on "Why is the Galactic disk so cool?", by Hamilton et al". In: *arXiv e-prints*, arXiv:2501.17907, arXiv:2501.17907. arXiv: 2501.17907 [astro-ph.GA].

Sellwood, J. A. (Jan. 1993). "A bar model for the Galactic bulge". In: *Back to the Galaxy*. Ed. by Stephen S. Holt and Francis Verter. Vol. 278. American Institute of Physics Conference Series, pp. 133–136.

— (Nov. 2010). "A recent Lindblad resonance in the solar neighbourhood". In: MNRAS 409.1, pp. 145–155. arXiv: 1001.5197 [astro-ph.GA].

Sellwood, J. A. and J. J. Binney (Nov. 2002). "Radial mixing in galactic discs". In: MNRAS 336.3, pp. 785–796. arXiv: astro-ph/0203510 [astro-ph].

Sellwood, J. A. and R. G. Carlberg (Apr. 2014). "Transient Spirals as Superposed Instabilities". In: ApJ 785.2, 137, p. 137. arXiv: 1403.1135 [astro-ph.GA].

Sellwood, J. A. and Ray G. Carlberg (Oct. 2019). "Spiral instabilities: mechanism for recurrence". In: MNRAS 489.1, pp. 116–131. arXiv: 1906.04191 [astro-ph.GA].

Sellwood, J. A. and Karen L. Masters (Aug. 2022). "Spirals in Galaxies". In: ARA&A 60. arXiv: 2110.05615 [astro-ph.GA].

Shen, Juntai and Xing-Wu Zheng (Oct. 2020). "The bar and spiral arms in the Milky Way: structure and kinematics". In: *Research in Astron. and Astrophys.* 20.10, 159, p. 159. arXiv: 2012.10130 [astro-ph.GA].

Sheth, Kartik et al. (Mar. 2008). "Evolution of the Bar Fraction in COSMOS: Quantifying the Assembly of the Hubble Sequence". In: ApJ 675.2, pp. 1141–1155. arXiv: 0710.4552 [astro-ph].

Siebert, A., O. Bienaymé, and C. Soubiran (Feb. 2003). "Vertical distribution of Galactic disk stars. II. The surface mass density in the Galactic plane". In: A&A 399, pp. 531–541. arXiv: astro-ph/0211328 [astro-ph].

Siebert, A. et al. (Apr. 2011). "Detection of a radial velocity gradient in the extended local disc with RAVE". In: MNRAS 412.3, pp. 2026–2032. arXiv: 1011.4092 [astro-ph.GA].

Siebert, A. et al. (Sept. 2012). "The properties of the local spiral arms from RAVE data: two-dimensional density wave approach". In: MNRAS 425.3, pp. 2335–2342. arXiv: 1207.0363 [astro-ph.GA].

Skowron, D. M. et al. (Dec. 2019). "Mapping the Northern Galactic Disk Warp with Classical Cepheids". In: Acta Astron. 69.4, pp. 305–320. arXiv: 1912.11142 [astro-ph.GA].

Skúladóttir, Ása et al. (June 2025). "Evidence of Gaia Enceladus Experiencing at Least Two Passages around the Milky Way". In: ApJ 986.2, L21, p. L21. arXiv: 2506.00409 [astro-ph.GA].

Sormani, Mattia C., James Binney, and John Magorrian (Dec. 2015). "Gas flow in barred potentials - III. Effects of varying the quadrupole". In: MNRAS 454.2, pp. 1818–1839. arXiv: 1507.03078 [astro-ph.GA].

Steinmetz, M. et al. (Oct. 2006). "The Radial Velocity Experiment (RAVE): First Data Release". In: AJ 132.4, pp. 1645–1668. arXiv: astro-ph/0606211 [astro-ph].

Storn, Rainer and Kenneth Price (Dec. 1997). "Differential Evolution - A Simple and Efficient Heuristic for global Optimization over Continuous Spaces". In: *Journal of Global Optimization* 11, pp. 341–359.

Stref, Martin, Thomas Lacroix, and Julien Lavalle (June 2019). "Remnants of Galactic Subhalos and Their Impact on Indirect Dark-Matter Searches". In: *Galaxies* 7.2, 65, p. 65. arXiv: 1905.02008 [astro-ph.CO].

Syer, D. and S. Tremaine (Sept. 1996). "Made-to-measure N-body systems". In: MNRAS 282.1, pp. 223–233. arXiv: astro-ph/9605061 [astro-ph].

Thomas, Guillaume F. et al. (Oct. 2023). "Impact of the Galactic bar on tidal streams within the Galactic disc. The case of the tidal stream of the Hyades". In: A&A 678, A180, A180. arXiv: 2309.05733 [astro-ph.GA].

Tremaine, S. and M. D. Weinberg (July 1984). "A kinematic method for measuring the pattern speed of barred galaxies." In: ApJ 282, pp. L5–L7.

Tremaine, Scott, Neige Frankel, and Jo Bovy (May 2023). "The origin and fate of the Gaia phase-space snail". In: MNRAS 521.1, pp. 114–123. arXiv: 2212.11990 [astro-ph.GA].

Trick, Wilma H. (Jan. 2022). "Identifying resonances of the Galactic bar in Gaia DR2: II. Clues from angle space". In: MNRAS 509.1, pp. 844–865. arXiv: 2011.01233 [astro-ph.GA].

Trick, Wilma H., Johanna Coronado, and Hans-Walter Rix (Apr. 2019). "The Galactic disc in action space as seen by Gaia DR2". In: MNRAS 484.3, pp. 3291–3306. arXiv: 1805.03653 [astro-ph.GA].

Trick, Wilma H. et al. (Jan. 2021). "Identifying resonances of the Galactic bar in Gaia DR2: I. Clues from action space". In: MNRAS 500.2, pp. 2645–2665. arXiv: 1906.04786 [astro-ph.GA].

Urquhart, J. S. et al. (Jan. 2014). "The RMS survey: galactic distribution of massive star formation". In: MNRAS 437.2, pp. 1791–1807. arXiv: 1310.4758 [astro-ph.GA].

Varghese, Alan John, Zhen Zhang, and George Em Karniadakis (Aug. 2024). "SympGNNs: Symplectic Graph Neural Networks for identifiying high-dimensional Hamiltonian systems and node classification". In: *arXiv e-prints*, arXiv:2408.16698,

arXiv:2408.16698. arXiv: 2408.16698 [cs.LG].

Vasiliev, Eugene (May 2018). *AGAMA: Action-based galaxy modeling framework*. Astrophysics Source Code Library, record ascl:1805.008.

— (Jan. 2019). "AGAMA: action-based galaxy modelling architecture". In: MNRAS 482.2, pp. 1525–1544. arXiv: 1802.08239 [astro-ph.GA].

Vasiliev, Eugene, Vasily Belokurov, and Denis Erkal (Feb. 2021). "Tango for three: Sagittarius, LMC, and the Milky Way". In: MNRAS 501.2, pp. 2279–2304. arXiv: 2009.10726 [astro-ph.GA].

Vauterin, P. and H. Dejonghe (Apr. 1997). "The construction of barred galaxy models using non-linear extensions of linear modes". In: MNRAS 286.4, pp. 812–824.

Vázquez, Ruben A. et al. (Jan. 2008). "Spiral Structure in the Outer Galactic Disk. I. The Third Galactic Quadrant". In: ApJ 672.2, pp. 930–939. arXiv: 0709.3973 [astro-ph].

Virtanen, Pauli et al. (2020). "SciPy 1.0: Fundamental Algorithms for Scientific Computing in Python". In: *Nature Methods* 17, pp. 261–272.

Vislosky, E. et al. (Feb. 2024). "Gaia DR3 data consistent with a short bar connected to a spiral arm". In: MNRAS 528.2, pp. 3576–3591. arXiv: 2312.03854 [astro-ph.GA].

Wegg, Christopher, Ortwin Gerhard, and Matthieu Portail (July 2015). "The structure of the Milky Way's bar outside the bulge". In: MNRAS 450.4, pp. 4050–4069. arXiv: 1504.01401 [astro-ph.GA].

Weiland, J. L. et al. (Apr. 1994). "COBE Diffuse Background Experiment Observations of the Galactic Bulge". In: ApJ 425, p. L81.

Widmark, Axel and Giacomo Monari (Jan. 2019). "The dynamical matter density in the solar neighbourhood inferred from Gaia DR1". In: MNRAS 482.1, pp. 262–277. arXiv: 1711.07504 [astro-ph.GA].

Widmark, Axel and Aneesh P. Naik (June 2024). "First spiral arm detection using dynamical mass measurements of the Milky Way disk". In: A&A 686, A70, A70. arXiv: 2401.04571 [astro-ph.GA].

Widrow, Lawrence M. (June 2023). "Swing amplification and the Gaia phase spirals". In: MNRAS 522.1, pp. 477–487. arXiv: 2302.14524 [astro-ph.GA].

Widrow, Lawrence M. et al. (May 2012). "Galactoseismology: Discovery of Vertical Waves in the Galactic Disk". In: ApJ 750.2, L41, p. L41. arXiv: 1203.6861 [astro-ph.GA].

Williams, M. E. K. et al. (Nov. 2013). "The wobbly Galaxy: kinematics north and south with RAVE red-clump giants". In: MNRAS 436.1, pp. 101–121. arXiv: 1302.2468 [astro-ph.GA].

Xu, Y. et al. (Jan. 2021). "Local spiral structure based on the Gaia EDR3 parallaxes". In: A&A 645, L8, p. L8. arXiv: 2101.00158 [astro-ph.GA].

York, Donald G. et al. (Sept. 2000). "The Sloan Digital Sky Survey: Technical Summary". In: AJ 120.3, pp. 1579–1587. arXiv: astro-ph/0006396 [astro-ph].

Yu, Si-Yue and Luis C. Ho (Sept. 2020). "The Statistical Properties of Spiral Arms in Nearby Disk Galaxies". In: ApJ 900.2, 150, p. 150.

Yuan, Zhen et al. (Nov. 2024). "Could very low-metallicity stars with rotation-dominated orbits have been driven by the bar?" In: A&A 691, L1, p. L1.

Zhang, HanYuan et al. (Apr. 2025). "Observational Constraints of Radial Migration in the Galactic Disk Driven by the Slowing Bar". In: ApJ 983.1, L10, p. L10. arXiv: 2502.02642 [astro-ph.GA].

Zhao, Hongsheng, David N. Spergel, and R. Michael Rich (Dec. 1994). "Signature of Bulge Triaxiality From Kinematics in Baade's Window". In: AJ 108, p. 2154. arXiv: astro-ph/9409024 [astro-ph].

Université de Strasbourg

Yassin Rany KHALIL

Observatoire astronomique de Strasbourg | ObAS

Déchiffrer la dynamique de la barre et des bras spiraux de la Voie lactée avec Gaia

Résumé

Cette thèse utilise les données de la mission Gaia pour modéliser la dynamique de la Voie lactée, incluant la barre et les bras spiraux. Un potentiel Galactique paramétrique est ajusté aux données via une méthode d'intégration rétrograde pour évaluer la fonction de distribution stellaire à quatre dimensions d'espace des phases dans le plan Galactique. Nous avons ainsi été les premiers (et les seuls à ce jour) à réaliser un ajustement direct au champ de vitesses radiales médianes du disque tel que mesuré par Gaia. Il s'agit du modèle dynamique non-axisymétrique le plus réaliste à ce jour pour la Voie Lactée. Ce modèle est ensuite généralisé en trois dimensions spatiales avec des simulations particules tests, ce qui permettra d'étudier les perturbations verticales et le halo de matière noire. Cette approche permettra, à terme, une comparaison étoile par étoile dans l'étude des populations stellaires de la Voie Lactée.

Mots-clés: Galaxie : généralités - Galaxie : cinématique et dynamique - Galaxie : structure - Galaxie : évolution - Galaxie : disque

Deciphering the dynamics of the Milky Way bar and spiral arms with Gaia

Abstract

This thesis uses Gaia data to model the dynamics of the Milky Way, including the bar and spiral arms. A parametric Galactic potential is fitted to the data via a backward integration method to evaluate the four-dimensional phase-space stellar distribution function in the Galactic plane. This allowed me to be the first (and only to date) to achieve a direct fit to the median radial velocity field of the disk as measured by Gaia. This is therefore the most realistic non-axisymmetric dynamical model of the Milky Way to date. This model is then generalized in three spatial dimensions with test particle simulations, which should enable us to study vertical perturbations or the dark matter halo. This approach will eventually enable star-by-star comparisons in the study of stellar populations.

Keywords: Galaxy: general – Galaxy: kinematics and dynamics – Galaxy: structure – Galaxy: evolution – Galaxy: disk